Numerical and Experimental Investigation of the Wind Influence on the Operation of Scaled-Up Open Volumetric Cavity Receivers

Numerische und experimentelle Untersuchung des Windeinflusses auf den Betrieb hochskalierter offener volumetrischer Receiver in Cavity-Bauweise

Von der Fakultät für Maschinenwesen der Rheinisch-Westfälischen Technischen Hochschule Aachen zur Erlangung des akademischen Grades eines Doktors der Ingenieurwissenschaften genehmigte Dissertation

vorgelegt von
Maximilian Philip Drexelius

Berichter: Univ.-Prof. Dr.-Ing. Robert Pitz-Paal
Univ.-Prof. Dr.-Ing. Wolfgang Schröder

Tag der mündlichen Prüfung: 25.09.2024

Acknowledgments

This doctoral thesis and the work leading to it were carried out at the Institute of Solar Research of the German Aerospace Center (DLR) with financial support from the German Federal Ministry for Economic Affairs and Climate Action within the research project FerVoRec (reference number 03EE5027B).

Simulations were performed with computing resources granted by RWTH Aachen University under the projects jara0225 and rwth0796. Additionally, the author gratefully acknowledges the computing time provided to him at the NHR Center NHR4CES at RWTH Aachen University (project number p0020287). This is funded by the Federal Ministry of Education and Research, and the state governments participating on the basis of the resolutions of the GWK for national high performance computing at universities.

My gratitude goes to Univ.-Prof. Dr.-Ing. Robert Pitz-Paal for accepting me as a doctoral student, supervising my work and for the ongoing support and guidance on every step, which led to this thesis.

I also want to thank Univ.-Prof. Dr.-Ing. Wolfgang Schröder for acting as second examiner for my thesis and giving me the opportunity to present my work at his institute.

My gratitude also goes to Univ.-Prof. Dr.-Ing. Bernhard Hoffschmidt and Univ.-Prof. Dr.-Ing. Christian Sattler for their helpful scientific advice during recurring progress meetings.

I further want to thank Peter Schwarzbözel, who dedicated a lot of time and effort to discuss my thesis, new ideas and approaches on a weekly basis and especially for always encouraging me.

My gratitude also goes to Dr.-Ing. Kai Wieghardt for always supporting me in this endeavor and making the wind tunnel campaign possible.

A special thanks goes to Dr.-Ing. Matthias Meinke, who mentored me in the field of computational fluid dynamics with great commitment and offered me valuable advice that was essential in the course of this thesis.

I want to thank my colleague Robin Tim Broeske for the fruitful discussions and for sharing his knowledge with me especially in the field of OpenFOAM.

I further want to express my gratitude to Ralf Uhlig for supporting me during the numerical part of this thesis and always offering me scientific input.

Last but not least, the wind tunnel campaign would not have been possible without the dedication and support of my colleagues at the Institute of Aeroelasticity in Göttingen. Especially i want to thank Dr.-Ing. Nils Paul van Hinsberg, Dr. rer. nat. Marc Braune and Markus Löhr and their team for the support in the planning, execution and evaluation of the experiments. It was a pleasure to work with you.

Abstract

In the transition to an energy system based on renewable energy sources with large contributions of fluctuating feed-in from Photovoltaics and Wind, Concentrating Solar Power (CSP) plants stand out for their ability to provide dispatchable, baseload power. Among the receiver types used in CSP plants, the Open Volumetric Receiver (OVR) offers the potential of high temperature heat for high efficiency power generation or thermochemical processes. In the OVR development return air systems are established, where the air is recirculated to the front after the heat exchange to the subsequent process to utilize the remaining exergy. A cavity shaped receiver design has proven to be beneficial in terms of reduced radiation losses and increased share of recirculated air (air return ratio). This doctoral thesis focuses on investigating the wind influence on large-scale (multi-megawatt) cavity OVRs in terms of (i) wind-induced surface pressure fluctuations and (ii) forced convective heat losses quantified by the air return ratio. Due to the open process, wind-induced pressure fluctuations become a relevant factor in terms of the receiver mass flow, which needs to be maintained in order to prevent thermal stresses at highly irradiated parts of the receiver. In addition to that, ambient wind is expected to disturb the receiver flow within the cavity and induce forced convective heat losses by reduced air return ratios. In this thesis, measurements in a high-pressure wind tunnel are carried out with a model of a solar tower with three separate receiver apertures. In the experiments, Reynolds numbers ranging from 3.49×10^6 to 13.17×10^6 are reached and wind-induced surface pressure fluctuations are evaluated under constant and varying incident angle flow. Furthermore, CFD simulations based on scale-resolving DES were conducted to extend the pressure evaluation to higher wind speeds and to include the receiver flow, which could not be realized within the experiments. The numerical models are validated by a comparison with the experimental results and available literature. The measurements show that incident angles of 45 to 80° relative to the cavity normal axis lead to the highest pressure fluctuations due to flow separation at the cavity opening. They also show that shifts in the incident angle account for RMS values which exceed those under constant incident angle flow by up to one order of magnitude. Based on the results, the impact on the receiver mass flow is evaluated as negligible except for part load conditions, where the mass flow can vary up to 39 %. Forced convective heat losses are evaluated with stationary RANS simulations, which show that the air return ratio, and especially the externally returned air, is sensitive to lateral ambient wind and decreases with increasing wind speed. As measures to reduce forced convective heat losses wind-adjusted return air distributions are derived, which have the potential to significantly increase the air return ratio and are recommended to be incorporated into the receiver design. The use of an aerowindow has a limited potential due to the size of the receiver.

Zusammenfassung

Im Rahmen der Energiewende hin zu einem auf erneuerbaren Energien basierenden Energiesystem mit hohen Anteilen fluktuierender Einspeisung aus Photovoltaik und Wind zeichnen sich solarthermische Kraftwerke (CSP) durch die Bereitstellung von disponierbarer, grundlastfähiger Energie aus. Unter den in CSP-Kraftwerken eingesetzten Receivertypen, bietet der offene volumetrische Receiver (OVR) das Potenzial von Hochtemperaturwärme für effiziente Stromerzeugung oder thermochemische Prozesse. Im OVR wird die Luft nach dem Wärmeaustausch vor den Receiver zurückgeführt, um die verbleibende Exergie zu nutzen. Das Cavity-Design hat sich als vorteilhaft erwiesen, da es die Strahlungsverluste reduziert und den Anteil der rückgeführten Luft erhöht. Diese Dissertation konzentriert sich auf die Untersuchung des Windeinflusses auf Multi-Megawatt Cavity OVRs im Hinblick auf (i) windinduzierte Druckschwankungen und (ii) erzwungene konvektive Wärmeverluste, quantifiziert durch die Rückführrate. Aufgrund des offenen Prozesses beeinflussen Druckschwankungen den Receiver-Massenstrom, der aufrechterhalten werden muss, um thermische Spannungen in stark bestrahlten Teilen des Receivers zu vermeiden. Zusätzlich ist zu erwarten, dass Wind die Receiverströmung in der Cavity stört und die Rückführrate verringert. Im Rahmen dieser Arbeit wurden Messungen in einem Hochdruckwindkanal mit einem Modell eines Solarturms mit drei separaten Receivern durchgeführt. Darin wurden Reynoldszahlen im Bereich von 3.49×10^6 bis 13.17×10^6 erreicht und Drücke bei konstanten und variierenden Anströmwinkeln ausgewertet. Zusätzlich wurden skalenauflösende CFD-Simulationen (Detached-eddy simulations) durchgeführt, um die Druckauswertung um höhere Windgeschwindigkeiten zu erweitern und die Receiverströmung einzubeziehen, die in den Experimenten nicht realisiert werden konnte. Die numerischen Modelle werden durch einen Vergleich mit den Experimenten und verfügbarer Literatur validiert. Die Messungen zeigen, dass Anströmwinkel von 45 bis 80° relativ zur Cavity-Normalen aufgrund der Strömungsablösung an der Cavity zu den höchsten Druckschwankungen führen. Sie zeigen auch, dass wechselnde Anströmwinkel zu Druckschwankungen führen, die jene bei konstantem Anströmwinkel um bis zu eine Größenordnung übersteigen. Auf Grundlage der Ergebnisse werden die Auswirkungen auf den Massenstrom als vernachlässigbar eingeschätzt, außer bei Teillastbedingungen, bei denen der Massenstrom um bis zu 39 % schwankt. Die erzwungenen konvektiven Verluste werden mit stationären RANS-Simulationen bewertet, aus denen hervorgeht, dass die Rückführrate mit zunehmender Windgeschwindigkeit abnimmt und insbesondere am Rand des Receivers rückgeführte Luft vom Wind verdrängt wird. Als Maßnahmen zur Verringerung dieser Verluste werden windangepasste Rückluftverteilungen abgeleitet, die das Potenzial haben, die Rückführrate signifikant zu erhöhen und in das Konzept integriert werden sollten. Der Einsatz eines Luftvorhangs ist aufgrund der Größe des Receivers ineffektiv.

Contents

Nomenclature

Abbreviations and Acronyms

ARR	Air return ratio
CFD	Computational fluid dynamics
CFL	Courant-Friedrichs-Lewy
CSP	Concentrating solar power
$DDES$	Delayed detached-eddy simulation
DES	Detached-eddy simulation
DFT	Discrete Fourier transform
DIT	Decaying isotropic turbulence
DLR	German Aerospace Center
DNI	Direct normal irradiation
DNS	Direct numerical simulation
FFT	Fast Fourier transform
HDG	High Pressure Wind Tunnel Göttingen
$HiTRec$	High-Temperature Receiver
LES	Large-eddy simulation
MSD	Modelled stress depletion
OVR	Open volumetric receiver
PDF	Probability distribution function
$PISO$	Pressure implicit with splitting of operators
PIV	Particle image velocimetry
PSA	Plataforma Solar de Almería
PSD	Power spectral density

$RANS$	Reynolds-averaged Navier-Stokes
RMS	Root mean square
$SAURAN$	Southern African Universities Radiometric Network
$SBES$	Stress-blended eddy simulation
SGS	Subgrid scale
$SIMPLE$	Semi-Implicit Method for Pressure Linked Equations
SLA	Stereolithography
STJ	Solar Tower Jülich
$STPP$	Solar tower power plant

Roman symbols

A	m^2	Reference area
B	–	Velocity decay rate
C_l	–	Lift coefficient
C_d	–	Drag coefficient
C_p	–	Pressure coefficient
C_s	–	Smagorinsky coefficient
C_{DES}	–	DES model constant
D	m	Characteristic length
D_T	$\frac{\mathrm{m}^2}{\mathrm{s}}$	Diffusion coefficient
E	J	Energy
E	–	Roughness parameter
F_d	N	Drag force
G	–	Filter function
H	J	Enthalpy
I	%	Turbulence intensity
K	$\frac{\mathrm{m}^2}{\mathrm{s}^2}$	Kinetic energy
K_p	–	Proportional controller coefficient

M	$\frac{\mathrm{g}}{\mathrm{mol}}$	Mole mass
M_{pitch}	$\mathrm{N\,m}$	Pitch moment
Ma	–	Mach number
N	–	Amount of sampling values
R	$\frac{\mathrm{J}}{\mathrm{mol\,K}}$	Universal gas constant
R_a	m	Average surface roughness
Re	–	Reynolds number
S_A	–	FFT amplitude scale factor
S_{pp}	$\frac{\mathrm{Pa}}{\mathrm{Hz}}$	Power spectral density of the pressure
Sc	–	Schmidt number
St	–	Strouhal number
T	s	Period
T	K	Temperature
V_c	m^3	Cell volume
X	–	Fourier transform
Z	–	Compressibility factor
$\dot{Q}$	W	Heat flux
$\dot{m}$	$\frac{\mathrm{kg}}{\mathrm{s}}$	Mass flow
$\hat{c}_k$	–	Fourier coefficients
$\mathbf{D}(\mathbf{u})$	$\frac{1}{\mathrm{s}}$	Rate of strain tensor
$\mathbf{I}$	–	Unit tensor
$\mathbf{T}$	$\frac{\mathrm{kg}}{\mathrm{m\,s}^2}$	Stress Tensor
$\mathbf{g}$	$\frac{\mathrm{m}^2}{\mathrm{s}}$	Gravitational acceleration vector
$\mathbf{u}$	$\frac{\mathrm{m}}{\mathrm{s}}$	Velocity vector
$\tilde{d}$	m	DES length scale
c	$\frac{\mathrm{m}}{\mathrm{s}}$	Speed of sound
c_p	$\frac{\mathrm{J}}{\mathrm{kg\,K}}$	Specific heat capacity
d	m	Cylinder diameter
d	m	Aerowindow outlet diameter

d	m	Wall distance
e	$\frac{\mathrm{J}}{\mathrm{kg}}$	Specific internal energy
elr	–	External return air factor
f	Hz	Frequency
f_d	–	DDES boundary layer shield function
f_s	Hz	Sampling frequency
h	m	Wind tunnel width
h	$\frac{\mathrm{J}}{\mathrm{kg}}$	Specific enthalpy
i	–	Imaginary unit
k	$\frac{1}{\mathrm{m}}$	wave number
k	$\frac{\mathrm{m}^2}{\mathrm{s}^2}$	Turbulent kinetic energy
l_0	m	Integral length scale
l_m	m	mixing length
m	Hz	Discrete frequency
m	kg	Mass
p	Pa	Pressure
p_{rgh}	Pa	Modified pressure
s	$\frac{\mathrm{kPa}}{\mathrm{mV}}$	Sensor sensitivity
t	s	Time
t_n	–	Integral controller coefficient
u	$\frac{\mathrm{m}}{\mathrm{s}}$	Characteristic velocity
u_τ	$\frac{\mathrm{m}}{\mathrm{s}}$	Friction velocity
u	$\frac{\mathrm{m}}{\mathrm{s}}$	Velocity component in the coordinate direction x
v	$\frac{\mathrm{m}}{\mathrm{s}}$	Velocity component in the coordinate direction y
w	$\frac{\mathrm{m}}{\mathrm{s}}$	Velocity component in the coordinate direction z
$w\,[n]$	–	Windowing function
$x(t)$	–	Time signal
x, y, z	m	Cartesian coordinates
$x\,[t]$	–	Discrete time signal

y_+	–	Non-dimensional wall distance
z_0	m	Aerodynamic roughness length
z_d	m	Zero-plane displacement

Greek symbols

Δ	m	Filter width
Φ		Flow quantity
Φ'		Fluctuation term
Π	–	Non-dimensional variable
α	$\frac{\mathrm{m}^2}{\mathrm{s}}$	Thermal diffusivity
α	–	Relaxation factor
$\bar{\Phi}$		Reynolds Average
β	$^\circ$	Aerowindow jet outflow angle
δ	m	Boundary layer height
ϵ	–	Turbulence model mode
ϵ	$\frac{\mathrm{m}^2}{\mathrm{s}^3}$	Rate of dissipation of turbulent kinetic energy
η	m	Kolmogorov scale
γ	–	Boolean return air field
κ	–	von Kármán's constant
κ	$\frac{\mathrm{W}}{\mathrm{m\,K}}$	Thermal conductivity
μ	$\frac{\mathrm{kg}}{\mathrm{m\,s}}$	Dynamic viscosity
ν	$\frac{\mathrm{m}^2}{\mathrm{s}}$	Kinematic viscosity
ν_t	$\frac{\mathrm{m}^2}{\mathrm{s}}$	Turbulent / eddy (kinematic) viscosity
ω	$\frac{1}{\mathrm{s}}$	Vorticity
ω	Hz	Angular frequency
ω_d	–	Non-dimensional vorticity
ϕ	$^\circ$	Incident angle
ρ	$\frac{\mathrm{kg}}{\mathrm{m}^3}$	Density

σ		Variance / Uncertainty
τ	$\frac{\mathrm{kg\,m}}{\mathrm{s}^2}$	Reynolds stresses
τ_w	$\frac{\mathrm{kg\,m}}{\mathrm{s}^2}$	Wall shear stress
θ	$^\circ$	Angular probe position
$\tilde{\nu}$	$\frac{\mathrm{m}^2}{\mathrm{s}}$	SA model eddy viscosity
ξ	$-$	Return air concentration
ζ	$-$	Pressure loss coefficient
ζ_N	$-$	Nozzle coefficient

Subscripts and Superscripts

F	Full scale
M	Model
$Mean$	Mean
N	Nozzle
RMS	Root mean square
∞	Free stream / Ambient
air	Air
arr	Air return ratio
c	Centerline
c	Caloric
$corr$	Corrected
eff	Effective
elr	External return air
fan	Fan
h	Hot air
ilr	Internal return air
in	Inlet
inc	Intercepted radiation

jet	Jet
k	Kulite
log	Logarithmic layer
$loss$	Loss
out	Outlet
p	Patch
r	Return air
rad	Radiation
rec	Receiver
rel	Relative
s	Sensor
s	Static
set	Set
t	Turbulent
tot	Total
vis	Viscous sublayer

1 Introduction

The introduction gives a brief overview on solar tower power plants and their main components with a focus on the most common receiver types. Their advantages and disadvantages will be discussed compared to the open volumetric receiver, whose development,functionality and challenges will be presented in detail. Regarding the challenges, the influence of ambient wind on the OVR operation will be highlighted, as it is the focus of this work. After that, previous studies regarding fields of research which are relevant to the topics of this thesis are summarized and presented. At first, numerical and experimental studies on bluff body flows are presented and the Reynolds-dependent flow regimes in a circular cylinder flow are discussed. Then the studies about wind influence on cavity receivers in general and on the open volumetric receiver (OVR) are presented. The literature review is concluded with studies on countermeasures to reduce the wind influence on forced convective heat losses in cavity receivers. The Introduction is concluded with a summary of the objectives and the outline of this thesis.

1.1 Solar Tower Power Plants and Common Receiver Technologies

Solar tower power plants (STPP) belong to the point-focusing technologies within the field of concentrating solar power (CSP) with the aim to convert direct solar irradiation into usable end energy. The schematic layout of a STPP for electrical power generation is displayed in fig. 1.1 where the dotted line denotes the steam power cycle and the solid line denotes the cycle of the primary heat transfer fluid. In STPPs the solar irradiation is reflected by mirrors, so called heliostats, onto the receiver which is placed on the solar tower. The heliostats are equipped with drives that allow a rotation of the mirror surface along two axes in order to track the sun position during the day. In a commercial plant, hundreds up to thousands of heliostats are foreseen to achieve a high concentration factor which is defined as the ratio between the area of collected sunlight and the area of the solar receiver onto which it is concentrated.

The function of the receiver is to absorb the concentrated irradiation from the heliostat field and transfer it via convection or conduction (depending on the receiver type) to the heat transfer medium. In the concept displayed in fig. 1.1 the energy is further transferred to the heat storage or via a heat exchanger to the secondary cycle, which in this case constitutes a steam Rankine cycle for power generation. The implementation of a thermal storage in the plant design is optional and offers the possibility of a more flexible, dispatchable energy output. The storage shall not be the focus here, but as discussed in detail in [1] a variety of thermal storage concepts exist which can be grouped

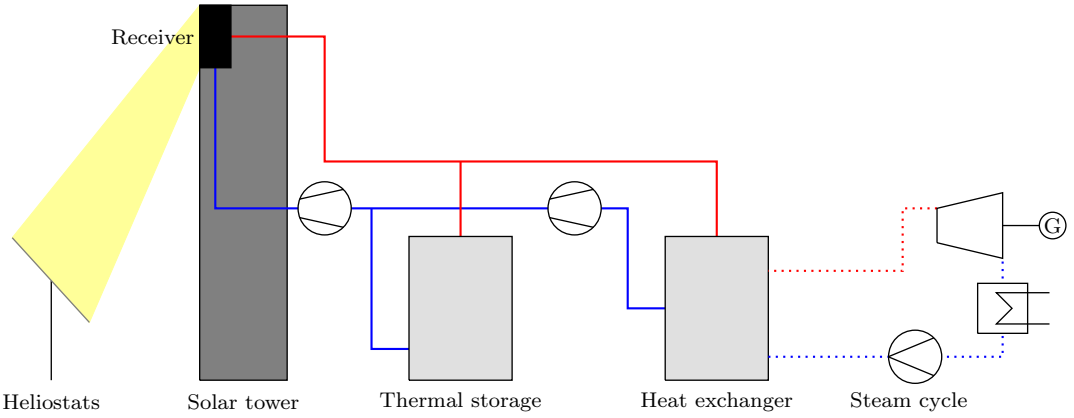

Figure 1.1: Schematic layout of a Solar tower power plant (STPP) containing a primary cycle (solid line) and a secondary cycle, in this case, Rankine cycle (dotted line).

by the working principle in latent, sensible and thermochemical heat storage.

The receiver constitutes a main component of the STPP of which a variety of concepts exist. The receiver types can be grouped in terms of the heat transfer medium, whether heat is transferred directly or indirectly (cf. [2]) and based on the shape of the receiver (external or cavity).

The most common receiver type is the tube receiver which consists of tube panels where molten salt, water or sodium [2] is circulated as the heat transfer medium. The tube receiver is also referred to as an closed-loop surface receiver in this work. In contrast to the open volumetric receiver presented later, the heat in this receiver concept is transferred indirectly via convection from the irradiated tubes. A main advantage is the direct storability of the heat transfer medium so no further heat transfer losses occur in the heat storage. In molten salt applications the maximum achievable outlet temperature is restricted by the thermal stability of the heat transfer medium. For a typical mixture of 60 % NaNO3 and 40 % KNO3 (% by weight) the operating temperature is limited to a maximum of 600 °C before degradation sets in. In addition to the upper temperature limitation, molten salt requires external heating when the plant is not under operation to prevent solidification when temperatures drop below approximately 220°. The main focuses of research according to Mehos [3] is to achieve higher operating temperatures to increase the power block efficiency. This leads to further research demand in terms of materials that sustain higher flux densities and temperatures and coatings to reduce radiation losses due to infrared emission as those losses correlate to T^4.

Another receiver type, called direct absorption receivers, is characterized by the fact that the heat transfer medium e.g. falling particles, or liquid films are directly exposed to the concentrated irradiation. In contrast to tube receivers much higher temperatures up to 2000 °C [2] can be achieved, because the restrictions posed by thermal stresses within the tubes and by the thermal stability of the heat transfer medium itself do not apply here. According to Mehos [3] the mayor challenges lie in the particle flow control

and containment, erosion and attrition, and conveyance. As presented in Ho [4] particle loss occurs due to attrition and mainly wind, which is why in directly irradiated particle receivers mostly cavity shaped receivers are foreseen in order to shield the particle flow from ambient wind.

1.2 The Open Volumetric Receiver

Another type of receiver within the field of indirectly heated receivers is the volumetric air receiver on which Ávila-Marín [5] gives a comprehensive overview regarding the different types and their development. In this section the open volumetric receiver (OVR) will be discussed, the general concept and its advantages compared to other receiver types will be pointed out and the important steps in the OVR development will be highlighted concluding with challenges of the technology leading to the topic of this thesis.

The OVR consists of a porous structure typically made of ceramic or metallic materials. The geometric shape varies between irregular foams, wire mesh or regular structured channels. The aim is to achieve a high porosity which allows the solar irradiation to penetrate the material. This way the radiation losses due to emission are reduced compared to external surface-receivers, like for example tube receivers. Also, the irradiation-absorbing surface and also the effective heat transfer surface is substantially larger than the front surface of the absorber (cf. [6]). The increase in the heat transfer surface is necessary to compensate the major drawback of air as the heat transfer medium which e.g. compared to molten salt is a lower heat transfer coefficient. Furthermore, the heat capacity of air is lower compared to molten salt which leads to relatively high mass flows in order to achieve comparable thermal energy outputs.

The absorbed irradiation is then transferred via convection to the working fluid, in this case air, which is drawn in the porous absorber structure by fans within the air system. Depending on the material of the porous structure, working temperatures of up to 1000 °C for metallic structures and even up to 1200 °C for SiSiC ceramics are achievable (cf. [5]). In contrast to other common receiver types mentioned before the OVR is an open process subject to the ambient conditions.

In the following part the important steps in the OVR development are briefly summarized which consequently lead to the investigation of up-scaled solar tower plant concepts as the one presented in section 2.1.1, on which this thesis is based on. The development of open volumetric receivers started in the 1980s and 1990s among others with the work by Fricker [7] who developed an open volumetric absorber based on metal-wire structures. The receiver concept was further scaled up towards a 2.5 MW_{th} receiver, which has been tested at the Plataforma Solar de Almeria (PSA) in the context of the Phoebus-TSA project. During those tests absorber efficiencis of 85 % at 700 °C receiver air outlet temperatures were recorded [5]. The HiTRec ("High Temperature Receiver") technology was developed at DLR starting in 1995 with the work by Hoffschmidt [6], who evaluated various ceramic receiver materials. The HiTRec receiver is a modular and scalable receiver based on a ceramic honeycomb structure with rectangular channels made of siliconized silicon carbide (SiSiC). As displayed on the left side of fig. 1.2, one

absorber module has a frontal surface of about 0.14 m × 0.14 m. The channels in the porous part of the absorber have a channel width of approximately 1 mm.

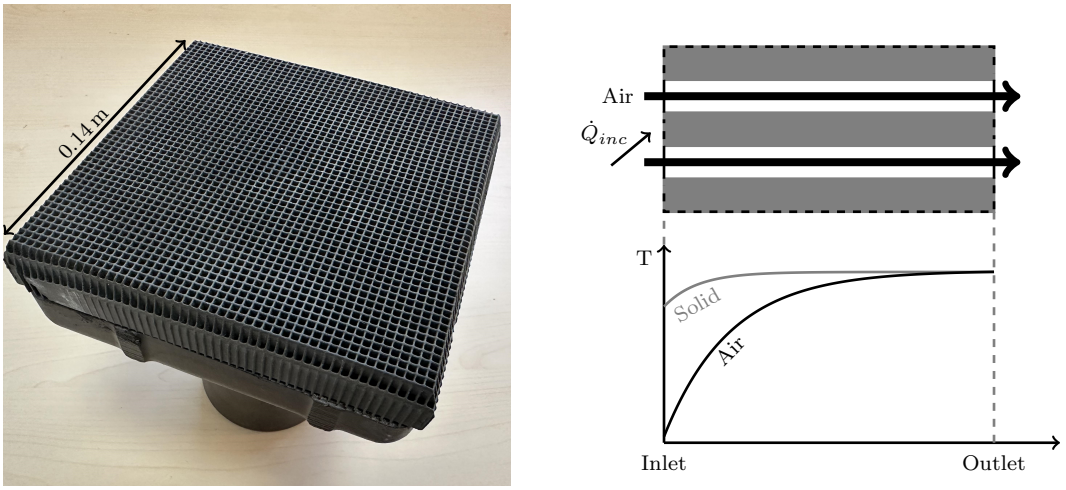

Figure 1.2: On the left an image of one HiTRec absorber module is depicted, showing the porous material and the cup on which the material is placed. On the right side the volumetric effect is visualized by the theoretical temperature profiles of the solid structure and air during irradiation.

In theory the open volumetric receiver offers the name-giving volumetric effect [8]. In e.g. tube receivers the outlet temperature of the working fluid is always lower than the surface temperature of the tube. The porous structure of the OVR leads to an absorption of a large part of the incoming irradiation inside the volume. Therefore, the OVR can achieve outlet temperatures of the heat transfer fluid which are higher than the front temperature of the absorber, which is called the volumetric effect and visualized in the right side of fig. 1.2.

The HitRec concept, its design and the supporting structure has been tested and improved in various projects at receiver levels of 200 kW_{th} [9] up to 3 MW_{th} [10]. The ongoing tests lead to the construction of the Solar Tower Jülich (STJ) demonstration plant [11], which has a tower height of 55 m and incorporates a receiver based on the HiTRec technology with an aperture area of ≈ 23 m^2 delivering 1.5 MW electrical power.

Within the receiver development a substantial effort is put into optimizing the porous structures of the OVR from uniform structures like the HiTRec up to non-uniform, 3D-shaped structures which are facilitated by the increasing progress in additive manufacturing techniques. Those non-uniform receiver structures allow the local adjustment of the receiver properties to optimize the thermal efficiency of the receiver (e.g. [12], [13]).

In addition to the development of the absorber structure itself, the design of the air return system poses an important field in the OVR research and development. Open volumetric receiver concepts incorporate an air return system where the air is returned back to the front after the heat is transferred to a subsequent secondary cycle (e.g. heat

storage, or Rankine cycle). For a Rankine cycle the return air temperature typically varies between 110 and 270 °C [14]. The return air is also called warm air in the context of this thesis, in contrast to the hot air which denotes the air being drawn into the receiver. From an energetic point of view it is desirable to recirculate as much of the return air as possible. In general, the rate of returned warm air with respect to the total return air mass flow is quantified by the air return ratio (ARR). At the STJ, Tiddens [15] employed a measurement of the ARR based on a tracer gas method, where helium was circulated within the air circuit and the ARR was determined by a mass spectrometer measurement of the helium fraction. With this method air return ratios between 67.7 and 68.6 % were measured at the STJ.

In the basic HiTRec concept, the air is returned through gaps between the absorber modules (cf. fig. 1.3) in order to cool the supporting structure of the receiver. In this thesis, this flow path is called the internal air return. In a further investigation on the air return ratio at the STJ, Stadler et al. [16] numerically investigated the potential of incorporating an external air return where a fraction of the returned warm air is returned from lateral outlets adjacent to the receiver. A partial external air return has proven to be advantageous compared to a fully internal air return in terms of the overall parasitic losses. By reducing the internal return air mass flow the overall pressure drop can be reduced. [16] showed that for the STJ a reduction in parasitic losses of up to 34 % can be achieved when increasing the fraction of externally returned air from 0 to 40 %. The calculated air return ratio was mostly unaffected by the adjustment in the external return air fraction in this configuration.

In order to visualize the return air flows in an OVR, in fig. 1.3 the sketches of two different receiver concepts are shown. On the left side a conventional closed-loop tube receiver in an external configuration is shown and on the right side an open volumetric air receiver based on the HiTRec technology in a cavity concept is shown. In the detailed

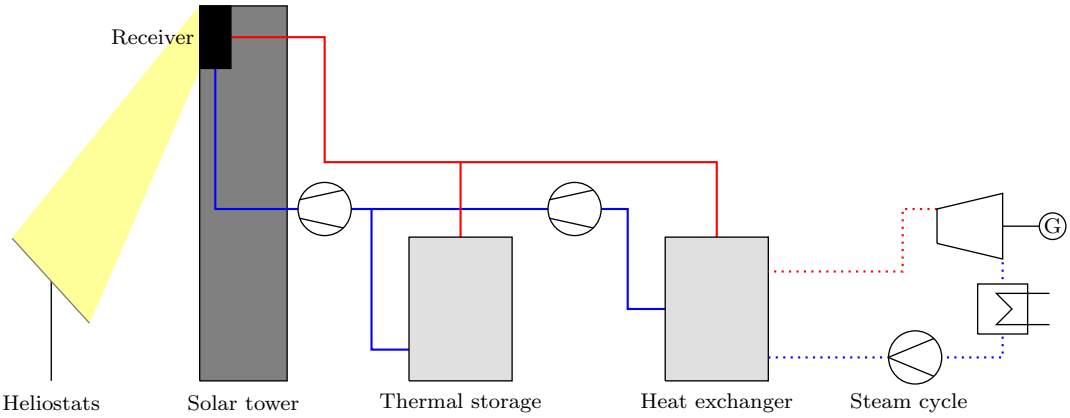

Figure 1.3: Schematic sketch of a closed-loop tube receiver in an external configuration (left) and an open volumetric receiver based on the HiTRec absorber in a cavity configuration (right), visualizing the air return system.

views, the heat transfer fluid is visualized by the colored arrows. The (e.g.) molten salt

in the tube receiver heats up due to convection in the irradiated tubes. In the OVR, the return air is visualized by the blue arrows. It is returned internally through gaps between the absorber cups, which draw in a mixture of ambient and return air, that heats up convectively inside the porous structure. In addition to the internal air return, an external air return can be foreseen, in this example realised via outlets below the receiver.

In recent research projects (e.g. [17]) an up-scaling of the technology and its efficiency potential is investigated. As presented in detail in section 2.1.1, tower concepts with heights up to 200 m and widths of approximately 30 m are foreseen to address the need for higher power outputs. At those heights, the influence of ambient wind naturally increases due to the increase in wind speed with height. The impact of ambient wind on the receiver efficiency and the operation of the OVR has so far not been investigated for scaled-up cavity receivers and will be the focus of this thesis. Ambient wind contributes to the convective heat losses in the OVR due to the interaction with the return air, leading to reduced air return ratios and therefore a reduction in the receiver inlet temperature. In contrast to closed-loop receivers like tube receivers, the OVR is subject to the ambient conditions, which leads to an additional influence of wind-induced surface pressure fluctuations. Due to the open process, changes in the pressure at the receiver surface potentially disturb the receiver mass low, as it is prescribed by the pressure difference between the fan in the air system and the ambient pressure at the receiver surface. Wind-induced mass flow drops during operation may lead to critical increases in the absorber temperature or temperature gradients leading to material failure. In order to evaluate the impact on the operational safety, the characteristics of wind-induced pressure fluctuations in the temporal and spectral domain need to be evaluated for a given receiver design.

1.3 Previous Studies

In this thesis, the wind influence on the open volumetric cavity receiver will be investigated by means of experimental and numerical methods. The literature review includes both numerical and experimental studies. At first the flow around bluff bodies will be characterized based on the example of a circular cylinder flow and its flow regimes are defined. Furthermore, the state of the research regarding bluff body flows by means of numerical simulations will be presented which is considered in the choice of the numerical methods applied and described in section 3.3. After that, relevant investigations of the wind influence on cavity receivers in general regardless of the receiver technology will be evaluated and the observations and implications will be summarized. In addition, known studies of the wind influence specifically on open volumetric receivers will be discussed. The literature review concludes with studies on countermeasures to reduce the wind influence on cavity receivers.

1.3.1 Numerical and Experimental Studies on Bluff Body Flow

Ambient wind flow around solar tower power plants falls into the field of bluff body flows (cf. the schematic of an OVR cavity receiver in fig. 1.3), which according to Roshko [18] are characterized by large areas of flow separation, typically vortex shedding and large drag coefficients. In addition to the definition based on the flow characteristics, Mockett [19] further defines a bluff body as the opposite to a streamlined body.

The circular cylinder poses a fundamental test case of bluff body flow in both numerical simulations and experiments. It can be observed that the flow experiences different states shown e.g. in the drag coefficient C_d and Strouhal number $St = \frac{fD}{u_\infty}$ both depending on the Reynolds number $Re = \frac{\rho u D}{\mu}$. The Strouhal number constitutes the dominant frequency f, which is non-dimensionalized by the characteristic length D and free stream velocity u_∞. As stated by Schewe [20], the pursuit of large Reynolds numbers in experimental studies is often accompanied by huge blocking ratios due to large probe bodies, which results in high levels of scatter in the results. It is acknowledged that besides the Reynolds number, the stability of the flow is influenced by additional parameters such as turbulence intensity of the wind tunnel, the Mach number and surface roughness [20]. Due to the influence of those parameters the specifications of the boundaries of the flow regimes vary in literature but can be summarized as follows (cf. [20], [21] and [18]).

The subcritical state reaches up to $Re \leq 3 \times 10^5$ which is characterized by a laminar boundary layer separation and fully turbulent vortex shedding in the wake at $St \approx 0.2$.

The critical state, in which a separation bubble followed by a turbulent reattachment of the boundary layer occurs, takes place at $Re = 3.5 \times 10^5$ and shows a discontinuous transition in the Strouhal number from 0.2 to values of 0.3 and further to 0.48. Furthermore C_d decreases strongly as the final separation point moves further downstream (cf. [20] and [18]). In [21] the critical regime was observed to occur for $3.5 \times 10^5 \leq Re \leq 1.5 \times 10^6$ and is said to be very sensitive with regards to the surface roughness and free stream turbulence.

The critical state is followed by the supercritical regime beginning at $Re = 3.5 \times 10^5$. In this regime the separation point moves downstream on the cylinder due to the turbulent boundary layer, which is able to sustain flow separation longer (cf. [22]). In this regime the Strouhal number is constant in the beginning at ≈ 0.48 and decreases slowly down to 0.4 with a constant drag coefficient until the transitional regime is reached.

In the transitional regime, which ranges from $1 \times 10^6 \lesssim Re \lesssim 3 \times 10^6$ (cf. [23]), the drag coefficient increases again accompanied by a chaotic flow separation.

The transcritical regime starts at $Re \geq 3 \times 10^6$ and is characterized by a periodic flow separation with Strouhal number greater than 0.2 and a drag coefficient which can be observed to plateau. In this state the laminar-turbulent transition occurs in the attached boundary layer (c.f. [23]) and the point of separation moves downstream on the cylinder with increasing Reynolds number.

Roshko [24] investigates the bluffness of a body and its effect on the flow around it and concludes that bluffer bodies experience higher drag (under the prerequisite of an equal frontal area) and that the flow is diverged more strongly resulting in a wider wake. At the same time, it can be observed that e.g. bluffer cylinders experience lower Strouhal

numbers.

As mentioned above the free stream turbulence is expected to influence the characteristics and the stability of the cylinder flow. According to Bearman [25] there are three effects regarding the free stream turbulence in bluff body flows. The first is an accelerated transition to turbulence in shear layers, which results in an upstream shift of the separation point in separated shear layers (in the subcritical flow regime). The second effect is the distortion of the turbulence in the free stream itself by the presence of the bluff body due to the mean flow around the bluff body. The third effect is an enhanced mixing under increased free stream turbulence which in wall bounded flows affects the outer part of the boundary layer. Free (not wall bounded) shear layers are generally more affected by changes in the free stream turbulence as the "spreading rate of a shear layer will be increased by the action of the normal component" of the free stream turbulence [25].

The investigation of the wind flow around the solar tower in this study takes place under Reynolds number above 3.5×10^6 (c.f. table 3.2) which indicates a flow state within the transcritical regime when the tower width is applied in the calculation of the Reynolds number. This implies turbulent boundary layers and a Reynolds-independence of the drag coefficient.

In the following, relevant findings obtained from numerical studies of bluff body flow with different turbulence modeling approaches (which are discussed in detail section 2.3.3 and section 3.3.4) are presented and their applicability and influence on the results are discussed.

A reduction in the spatial dimensions to a 2D simulation is an appealing approach when modeling flow processes as it reduces computational costs significantly. The application of two-dimensional models to simulate the flow around bluff bodies has been investigated in a variety of studies which emphasize the deficiencies of this simplification. For example Mittal and Balachandar [26] investigated the effect of three-dimensionality on the lift and drag of a circular cylinder under a comparatively low Reynolds number of 525. They found that the drag coefficient computed from two-dimensional simulations is significantly higher than what is obtained from experiments as the pressure distribution does not match. These observations are also reflected in the work by Jordan and Ragab [27] who investigated a circular cylinder flow for $Re \leq 140000$ with 2D and 3D Large-eddy simulations (LES). They found that the 2D simulation overestimates the pressure coefficient and Strouhal number while it underestimates the formulation length of the primary vortices. The over-prediction of the drag force in two-dimensional simulations is directly traced to higher Reynolds stresses in the wake [26].

In the presence of various turbulence modeling approaches, Spalart [28] states that it is very unlikely for a RANS model to be capable of providing the accuracy needed in the variety of separated and vortical flows, as the nonlinear interaction of at least the largest eddies with the mean flow has to be modeled. This statement is supported by a variety of studies of which some are mentioned in the following.

For example Ashton et al. [29] numerically investigated the flow around the Ahmed Car Body which is a canonical test case in the field of bluff body flow and for the evaluation of turbulence models. It could be shown that the Spalart-Allmaras Detached-

eddy Simulation (SA-DES) models pose a clear improvement over RANS models in the prediction of both the turbulent kinetic energy and the streamwise velocity. The main deficiency in the RANS model was the under-prediction of turbulence in the separated shear layers.

The Detached-Eddy Simulation has gained popularity since it was first proposed in 1997 by Spalart et al. [30] with applications in cases of heavily separated flow and has been investigated in a variety of studies e.g. in the projects FLOWMANIA [31] and DESider [32]. DES is an approach promising to overcome the computational costs of LES especially imposed in wall bounded flows. Due to the inherently smaller scales of turbulence in the vicinity of the wall, that region has to be resolved way finer than the wall distant field. The computational cost can be reduced significantly by modeling the boundary layer with RANS while treating the wall distant flow with LES and therefore resolving the large scales of turbulence.

The sensitivity on the background RANS model to the results obtained with DES simulations is generally considered to be very low [32] when an accurate prediction of the separation point is not difficult. This applies to e.g. cases of "massively-separated flow with geometry-induced separation" where, as stated in Mockett [19], the sensitivity of DES to the underlying RANS model is negligible. This also applies to the flow around the solar tower in this study as the points of flow separation are generally prescribed by the non-continuous geometrical features of the tower.

Further studies applying the DES modeling approach to bluff body flows are presented below. Mockett et al. [33] studied the flow around a circular cylinder with an aspect ration of 4.8 for a Reynolds number of 1.40×10^5. The CFD simulations, based on the SA-DES model, were compared to Particle Image Velocimetry (PIV) measurements in a wind tunnel and showed great agreement in the time-averaged and unsteady quantities of the velocity field. Squires et al. [34] studied the massively separated flow over a circular cylinder for a Reynolds number of 8.00×10^6 and compared the base DES model by Spalart [30] with the improved Delayed Detached-eddy simulation (DDES) model [35]. Compared to measurements under the same conditions, both CFD models showed very good agreement in the averaged drag coefficient, shedding Strouhal number (St) and angle of separation. Also, the pressure coefficient calculated by both models was in the range of the experimental results.

In the context of solar power applications scale resolving simulations are applied in the investigation of wind-induced structural loadings on heliostats. For example in Wolmarans and Raig [36] a hybrid RANS-LES approach namely Stress Blended Eddy Simulation (SBES) was used to calculate the pressure distribution on a heliostat model. In contrast to a RANS model which could only predict the mean wind loads, with the (partly) scale-resolving SBES model a great agreement in the mean and peak loading distribution compared to experimental results could be obtained.

As concluded by Mockett [19] the application of hybrid RANS-LES approaches is especially suitable for situations of strongly-separated flow where (U)RANS approaches tend to provide poor results and for applications where the resolution of unsteady turbulent motion is required to determine the quantities of interest which applies to e.g. surface pressure fluctuations at the open volumetric receiver.

The results and observations from the numerical studies mentioned above are essential in the choice of the turbulence modeling approach applied to the flow simulations in this thesis. The application of the DES approach shows great agreement in the time-averaged and instantaneous quantities for cases of strong vortex shedding and flow separation, while at the same time reducing the grid requirements in the boundary layer region compared to a fully LES. In LES the boundary layer requires especially fine discretization due to the inherently smaller eddies in the vicinity of the wall. The application of the statistical RANS modeling in the wall region reduces those requirements and enables a (partly) scale resolving simulation of the flow around the solar tower. Based on these arguments, the application of the DES model is considered appropriate to evaluate the instantaneous pressure fluctuations induced by ambient wind at the open volumetric receiver.

1.3.2 Wind Influence on Cavity Receivers

In the studies that focus on the wind influence on cavity receivers the evaluation of forced or mixed convective heat losses has been the subject for different receiver types based on experimental and numerical methods. A majority of studies focus on convective losses in closed-loop surface receivers (e.g. parabolic dish or molten-salt) and particle receivers (cf. section 1.3.4).

A very common analytical model to estimate convective heat losses in closed surface cavity receivers is the Clausing model [37]. According to Clausing [37] the fluid within the cavity can be split into a stagnation zone of heated air at the upper part of the cavity and a cold convective zone below due to the density differences. The size of the stagnation zone increases with an increasing inclination angle, which means a more downward facing receiver.

Numerous studies focused on small scale cavities as in parabolic dish concentrators both by means of numerical and experimental methods. Prakash et al. [38] experimentally and numerically investigated the convective losses on a downward facing cavity receiver in a parabolic dish with an inner diameter of 0.3 m for various inclination angles under side and head-on wind. It was found that the convective losses are generally higher under wind and increase with wind speed at all inclination angles except for side-wind on a downward facing cavity where the wind acts as a natural wind barrier.

Flesch et al. [39] conducted experiments in a cryogenic wind tunnel to evaluate the mixed convective heat losses in a cylindrical cavity surface receiver with a diameter of $\approx 2.4\,\mathrm{m}$. Reynolds numbers of up to 5.2×10^5 could be reached with inner cavity wall temperatures of around 730 °C. In such a system the main mechanism of influence is a wind inflicted reduction of the high temperature stagnation zone within the receiver cavity. It was shown that the wind influence becomes more relevant for increasing receiver inclination angles as the stagnation zone in those cases is larger and more affected by ambient wind.

Siegrist et al. [40] experimentally evaluated forced convective heat losses on a large-scale cavity receiver with an inner diameter of 15 m. Due to the fluid properties in a high-pressure wind tunnel Reynolds numbers up to 8.0×10^6 were reached. The

largest forced convective heat losses could be observed during frontal wind with a lateral inclination of 60° to 80° relative to the aperture normal axis. Regarding the inclination angle the results support the findings by Flesch et al. [39] mentioned above.

In contrast to the open volumetric receiver, the convective losses in cavity shaped surface receivers occur due to an interaction with the hot air stagnation zone and not due to the interference with the open process and losses of return air in the OVR. Despite the differences in the physical effect, some findings can be transferred to the application in the OVR. A strong directional dependency of the convective losses can be observed, which is also expected in the OVR cavity design and should be considered in the parameter design of the experiments and simulations. What could be observed and has to be investigated if it applies to the scaled-up OVR is that side wind could be shown to act as a natural barrier in smaller cavity receivers.

1.3.3 Wind Influence on the Open Volumetric Receiver

The investigations of the wind influence on open volumetric receivers so far are based on 2D and 3D CFD simulations. At this point, the studies only cover simulations of up to several receiver modules due to the inherent discrepancy in scales between the open volumetric structure with channel widths in the order of 1 mm and larger receivers in the order of 10 m, which makes a numerical investigation of those systems extensively expensive.

The air return ratio of the OVR has been investigated by Marcos et al. [41] with numerical simulations to quantify the ARR and optimize the geometry and return air system of the HiTRec receiver considering ambient wind. Among the different configurations a partial air return through a ringlike structure adjacent to the receiver cups has proven promising compared to an air return solely through the gaps between each module as it was originally foreseen in the HiTRec concept. The work concludes that lateral wind should be considered in the design of an OVR to account for the impact on the air return ratio.

Roldan et al. [42] investigated the wind influence on three HiTRec-II cups with 2D RANS simulations. The study covered wind speeds ranging from 0 to 8 $\frac{\mathrm{m}}{\mathrm{s}}$ and incident angles ranging from side to head-on wind. The quantity of interest in this study was the air outlet temperature and it could be shown that in this receiver configuration side wind leads to the strongest decrease in the air outlet temperature following a second-order degree polynomial function with respect to the wind speed.

As part of his dissertation, Maldonado Quinto [43] investigated the wind influence on the convective heat losses for one up to four vertically placed HiTRec modules in stationary 3D RANS simulations. The results indicate a high sensitivity of the air return ratio to side-wind as the ARR under side wind conditions decreases exponentially from approximately 60 to 30 % with increasing wind speeds. The minimal value was reached at wind speeds of around 6 $\frac{\mathrm{m}}{\mathrm{s}}$ and for further increases in wind speed the correlation shows an asymptotic behavior.

1.3.4 Countermeasures to Reduce the Wind Influence on Cavity Receivers

There are several investigations on measures to protect cavity receivers against wind influence which are mostly based on air curtains or so called aerowindows and fully or partial closure of the receiver aperture by windows. All the following studies address closed-loop surface or particle receivers. No studies on countermeasures to reduce the wind influence on open volumetric receiver systems are known to the author.

Tan et al. [44] investigated the wind influence on the performance of solid particle receivers with and without the protection of an air curtain which, within the model, is placed on the upper edge of the cavity with a downward facing outflow. It could be shown that the aerowindow can prohibit the heated air at the receiver surface from escaping and the ambient air from entering the cavity. The application of an aerowindow decreases convective losses for most cases especially for low wind speed cases (compared to the jet outflow velocity). It is also pointed out that care needs to be taken in the application of the aerowindow to prevent unintended disturbance of the heated air within the cavity which could be observed under wind conditions of direct inflow.

Amsbeck et al. [45] numerically investigated the efficiency of a surface receiver based on tubes arranged in a cavity with a circular opening and a diameter of 0.9 m. With the application of a segmented fused silica windows, which fully encloses the aperture, the convective losses could be reduced by 92.2 %. The losses due to thermal emission are reduced as well with a wavelength-sensitive coating of the window. Despite an increase in reflective losses due to the window the overall efficiency of the receiver is increased from 67.7 to 80.8 % under windless conditions. When ambient wind is considered the effectiveness of the silica window is expected to be even higher.

In contrast to a fully enclosed cavity, Flesch et al. [46] investigated a partial window (experimentally and numerically) and also the application of an aerowindow (numerically) at a cavity surface receiver. The cavity has a circular opening with a diameter of 2.4 m (0.66 m in the scaled model). With the application of a partial window at the upper side of the cavity a reduction in the convective losses under wind of 10 to 30 % could be achieved with a higher effectiveness at larger wind speeds. Regarding the aerowindow it could be shown that for a carefully chosen jet velocity the momentum of the jet is able to seal the cavity against ambient wind in most cases leading to a reduction in convective losses. Additionally, it was observed that for high wind speeds the effect of an natural air curtain occurs under lateral wind which prevents the hot air from leaving the cavity and it is recommended to design the cavity in a way that it redirects ambient wind to pass the cavity opening from an lateral angle. The application of a silica window is a very effective measure to reduce losses for relatively small receivers but with increasing aperture areas the application becomes impracticable mainly due to the mechanical restrictions of the material solely due to the weight of the window in addition to thermal stresses under irradiation. This applies to the receiver configuration investigated in this thesis, where a full or even partial window is not applicable due to the size of the aperture with a diameter of approximately 14 m.

As part of his dissertation Siegrist [47] investigated the effect of different structural adjustments placed around the cylindrical cavity opening of a receiver with a diameter

of 15 m. The structural measures consisted of a porous mesh or solid porches which are attached in a ring around the aperture opening with the aim to deflect the flow or cause a reduction of the momentum. The measures could be shown to decrease convective heat losses for specific angles, while for less favorable angles of attack the convective heat losses were effectively increased. The results underline the difficulty of finding a reduction measure which is universally effective for different wind incident angles.

1.4 Objectives of this Study and Outline

In this section the gaps in the state-of-the-art are identified, then the objectives are formulated followed by the structure and scope of this thesis.

As presented in section 1.3.2, so far, closed loop surface receivers have been the the main focus of research and wind-induced convective losses have been evaluated by various authors. The inherent discrepancy in scales between the open volumetric receiver geometry with channels in the order of 1 mm (as visualized in fig. 1.2) and tower diameters in the order of 10 m in industrial scales, which requires numerical domains in the order of 100 m to model ambient wind, results in intensively large computational resources. Therefore, the numerical investigations of the wind influence on open volumetric receivers have been restricted to a limited amount of receiver modules far from scaled-up industrial power plants. The modeling approach developed by Stadler et al. [14], which will be explained in detail in section 3.3.5 lays the foundation for simulations of larger OVRs and the evaluation of their efficiency potential, which to this date has been limited to evaluations without considering ambient wind.

The main objective of this thesis is to extend the evaluation of the large-scale open volumetric cavity-receiver concept by the influence of ambient wind and identify and quantify wind-induced effects on the operation. The relevant parameters influenced by ambient wind are (i) wind-induced surface pressure fluctuations and (ii) forced convective heat losses quantified by the air return ratio. Due to the open process of the OVR, where ambient air is drawn into the receiver as the heat transfer medium, changes in the ambient pressure in the vicinity of the receiver influence the receiver mass flow. Especially at highly irradiated areas of the receiver, the receiver mass flow and return air flow are important to be maintained in order to prevent thermal stresses within the receiver structure. Strong fluctuations in the receiver mass flow induce thermal stresses and sudden drops in the receiver mass flow potentially lead to overheating of the structure. In this context wind-induced surface pressure fluctuations are investigated in this thesis.

In addition to the surface pressure, ambient wind influences the efficiency of the OVR in terms of forced convective heat losses. As mentioned before, in contrast to closed-loop surface receivers, the relevant loss mechanism in terms of convective losses at the OVR is a wind-induced reduction in the air return ratio leading to reduced inlet temperatures of the receiver.

The objectives mentioned above are investigated in this thesis by means of experimental and numerical methods. In the context of this thesis a wind tunnel campaign

was planned and performed in order to evaluate the wind-induced surface pressure fluctuations at the cavity receiver. The measurements were conducted in a high-pressure wind tunnel in order to achieve comparatively high Reynolds numbers ranging from 3.49×10^6 to 13.17×10^6 which have to be expected during the operation of such a solar tower power plant. It was presumed that the pressure fluctuations are primarily influenced by ambient wind and not the mere operation of the receiver. Due to this assumption and primarily due to the inability to incorporate the receiver flow in the scaled ($\approx$ 1:290) wind tunnel model in the high-pressure wind tunnel environment, the receiver flow is not considered in the experiments. Pressure fluctuations are evaluated under constant incident angle flow and varying incident angles. Within the experimental campaign passive countermeasures by adjusting the surface structure next to the cavity opening are applied and the effectiveness in terms of reducing surface pressure fluctuations are evaluated. The experimental results obtained under constant incident angle flow are further utilized for the model validation of the CFD simulations conducted in this thesis.

Furthermore, CFD simulations were conducted with different turbulence modeling approaches. For the evaluation of wind-induced surface pressure fluctuations transient Detached-eddy simulations (DES) were conducted, while the evaluation of the forced convective heat losses is conducted via stationary RANS simulations. The DES are applied in the determination of the pressure fluctuations, because based on the literature review, it is expected to be necessary to (at least party) resolve the turbulent scales of motion when fluctuations in the flow field are of interest. Within the evaluation of surface pressure fluctuations the simulations extend the experimental results to higher wind speeds up to 14 $\frac{\mathrm{m}}{\mathrm{s}}$, which could not be achieved in the experiments due to the operational limits of the wind tunnel. In addition to that, the receiver flow is incorporated in the numerical model to evaluate its influence on the surface pressure and the interaction with ambient wind.

In addition to the surface pressure, the impact on forced convective heat losses is evaluated numerically. Forced convective losses in the OVR are quantified by the loss of return air which under windless conditions occurs due to the convective updraft induced by the density differences between ambient air and the return air. Under the presence of wind those losses are expected to be enhanced due to the interaction of the receiver flow with ambient wind. In the numerical part of the thesis the forced convective heat losses are investigated for windless conditions and lateral wind with wind speeds of 4 and 8 $\frac{\mathrm{m}}{\mathrm{s}}$. In contrast to experimental approaches, where the determination of the air return ratio is very difficult, in the simulations the ARR can be quantified by the implementation of a scalar transport equation which furthermore enables to distinguish between internally and externally returned air. What is investigated furthermore are countermeasures to reduce forced convective losses by incorporating wind-adjusted return air distributions and an aerowindow adjacent to the receiver cavity opening.

The thesis is structured in the way that after the introduction, the fundamentals are presented, starting with the power plant concept, on which this thesis is based on. The fundamentals part further includes the relevant background on the experimental and numerical methods, which are applied in this work. Within the methods part,

the characterization of ambient wind is presented which poses a fundamental boundary condition for the experimental and numerical work in this thesis. Furthermore, the experimental methods are presented including a detailed description of the wind tunnel, the measurement equipment and an uncertainty analysis of the obtained quantities. In the chapter regarding the numerical methods the models, discretization methods, turbulence modeling approaches, boundary conditions, encountered limitations and an uncertainty analysis are presented. After that, the experimental and numerical results are presented and evaluated from various perspectives including a model validation. Within the discussion of the results the main findings are presented, the limitations are discussed and implications on the cavity receiver operation are drawn based upon the results which were obtained. Finally, this thesis concludes with a summary of the methods and results that were obtained and an outlook on possible future research in this field.

2 Fundamentals

In this chapter the fundamentals relevant to this work and to the applied methods are presented. At first the reference plant concept will be presented on which the measurements and simulations in this thesis are based on. Afterwards the losses in the proposed cavity receiver design are assessed. Later on, the fundamentals regarding the wind tunnel experiments in this work are presented including the concept of similitude and the measurement principle of the sensors which are used. This chapter concludes with the numerical fundamentals including the governing equations, fundamentals of discretization, turbulence modeling, numerical visualization of coherent structures and the boundary layer theory.

2.1 Reference Power Plant Concept and Efficiency and Losses in the Cavity Design

In this section the reference plant concept which incorporates cavity shaped open volumetric receivers will be presented as in this study the wind influence on this particular receiver design will be investigated. This section concludes with the definition of the receiver efficiency and an estimation of the receiver losses which occur under operation.

2.1.1 Reference Power Plant Concept

Currently, the STJ [11] is the largest OVR power plant in operation. The receiver has a convex shape, has an aperture area of 23 m^2, consists of more than 1000 HiTRec cups and delivers a nominal electrical power of 1.5 MW.

In recent research projects a further upscaling of the technology and the efficiency potential of such a design has been investigated. Based on the work in those projects, in [48] and [49] an OVR design has been proposed where the solar tower incorporates three separate receiver apertures with a combined nominal thermal power of 240 MW_{th} and a nominal electrical output of 50 MW_{el}. The tower has a height of around 200 m and the heliostat field contains 41,338 units to provide the necessary concentrated irradiation. The receivers are designed in a concave cavity shape, which based on numerical results (cf. [49]), leads to a reduction in radiation losses and an increased air return ratio.

In fig. 2.1, which was adopted from Schwarzbözl et al. [48], an artistic sketch of the reference plant including the heliostat field is visualized. In a close-up view the CAD model of the tower, showing the main receiver is depicted. The main, southern cavity (as visualized in fig. 2.1) is larger than the north-western and north-eastern cavities which are designed equally. The southern receiver has an aperture height of 11.0 m while the north-eastern and north-western receiver have an aperture height of 9.6 m. This results in aperture areas of 156.7 m^2 for the southern cavity and 113.6 m^2 for the northern cavities. Due to the concave form of the receiver the surface area is larger than the aperture area with around 229.7 m^2 and 166.5 m^2 respectively. Each of the three receivers is segmented into vertical units called subreceivers whose hot air streams are merged with the other subreceivers within the air system in the tower. The three cavity centers are placed at a height of 187 m.

To ensure comparability to the prior investigations, in this thesis the design point conditions at the main cavity are chosen with a target hot air temperature $T_{h,out}$ of 670 °C and an intercepted irradiation $\dot{Q}_{inc}$ (also denoted as intercept) of 125 MW. The return air temperature is determined by the downstream Rankine steam block and for this study a return air temperature $T_{r,in}$ at the outlet of the steam block of 270 °C is presumed. In the design point an internal and external air return is foreseen with an equal distribution of the respective mass flows. The externally returned air is recirculated from below the receiver through a ringlike outlet surface which extends across the width of the receiver.

In the design of the receiver the mass flow distribution is adopted to the irradiation at the receiver as visualized in fig. 3.19. To set the desired mass flow distribution orifices

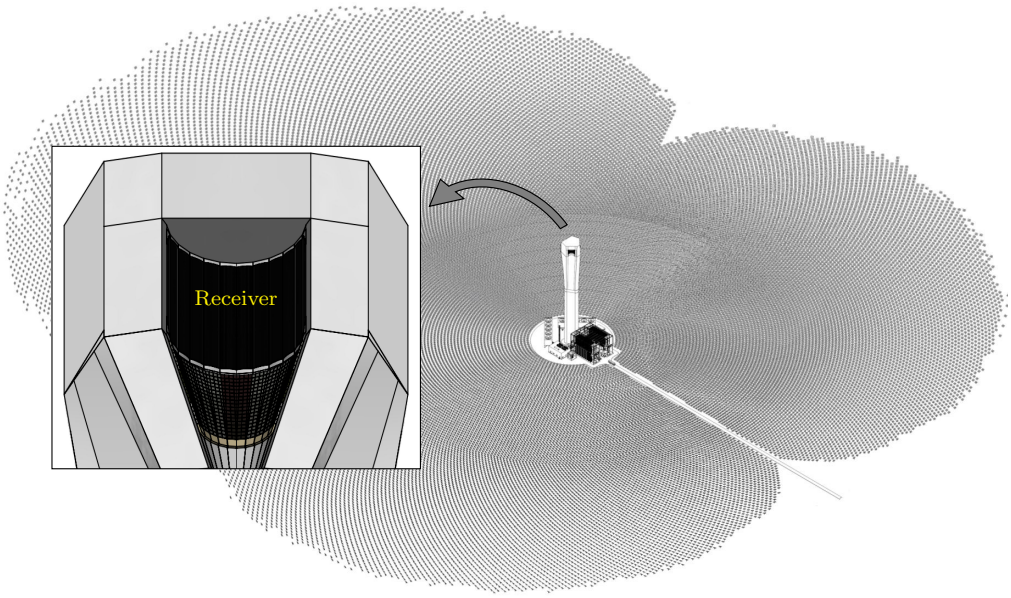

Figure 2.1: Artistic sketch of reference plant layout with a three-face open volumetric cavity receiver and a tower height of 200 m (adopted from Schwarzbözl et al. [48]). The heliostat field consists of 41,338 units placed on 1.7 km × 1.5 km. The main receiver is shown in the detailed view.

are foreseen in the air system behind the absorber modules.

Based on numerical investigations (cf. [14]) a receiver efficiency of around 84.3 % with air return ratios of about 84.8 % at a target hot air and return air temperature of 670 °C and 270 °C respectively are expected for the proposed scaled up cavity design. The receiver efficiency is defined as in eq. (2.1) as the enthalpy difference between the receiver inlet and outlet in relation to the intercepted irradiation at the receiver aperture area.

Within the concept, the reference plant is located in Vanrhynsdorp, South Africa. The location was considered in the heliostat field layout and aim point distribution that was conducted with the raytracing software STRAL [50]. The distribution of intercepted irradiation within the numerical investigation in this thesis is adopted from prior work.

2.1.2 Receiver Efficiency and Losses in the Cavity Design

In this section the assessment of the receiver efficiency and losses within the cavity design is presented and evaluated based on the numerical results published in Stadler et al. [14]. Within the Solar Tower Power Plant optical losses occur due to a misalignment of heliostats or blocking and shading between neighboring heliostats. Those losses resulting in a reduction of the concentrated irradiation at the receiver are typically allocated to the heliostat field and not the receiver itself (cf. [45]).

The losses attributed to the receiver can be grouped into radiation losses, convective

losses and internal heat losses due to convective heat transfer between the hot air and return air stream which results in a lower hot air outlet temperature. The internal losses do not appear in the energy balance in eq. (2.1) and schematic in fig. 2.2. Within the schematic the relevant components of the absorber module are visualized and named with the porous absorber structure, which is fitted into the cup that is placed onto a pipe. The orifices, which pose the dominant pressure loss in the absorber module, are dimensioned to set the mass flow distribution at the receiver as visualized in fig. 3.19.

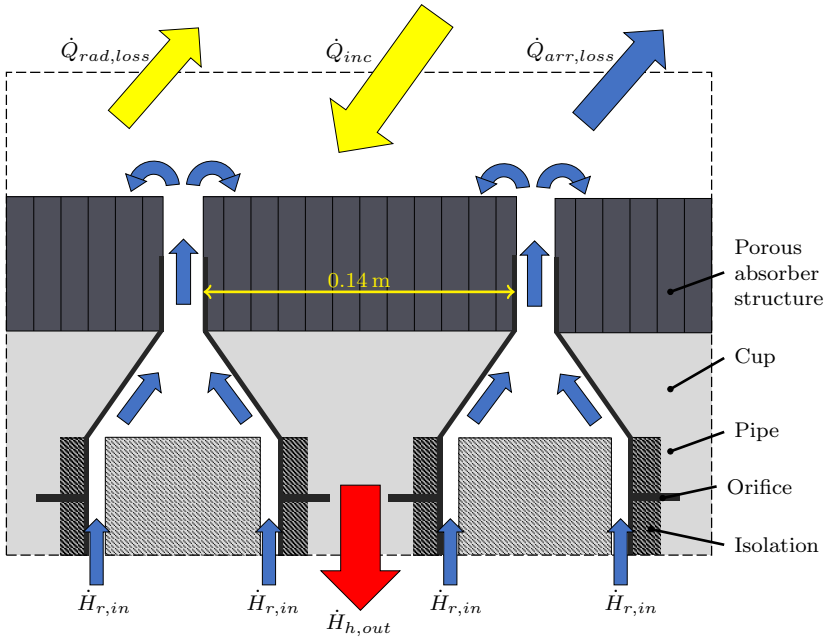

Figure 2.2: Schematic of the open volumetric air receiver including the relevant enthalpy and energy flows, which are considered in the energy balance for the receiver efficiency in eq. (2.1) (adopted from Drexelius et al. [51]).

The receiver efficiency η_{rec} can be evaluated based on the quantities visualized in fig. 2.2 by an energy balance over the receiver module as in eq. (2.1).

$$\eta_{rec} = \frac{\dot{H}_{h,out} - \dot{H}_{r,in}}{\dot{Q}_{inc}} = 1 - \frac{\dot{Q}_{rad,loss} + \dot{Q}_{arr,loss}}{\dot{Q}_{inc}} \tag{2.1}$$

Radiation losses $\dot{Q}_{rad,loss}$ occur via thermal emission based on the surface temperature of the receiver and reflection of incoming irradiation. Open volumetric receivers are designed to absorb the incoming irradiation deep within the structure to reduce the amount of radiation which is emitted towards the ambient and lost. Radiation losses further depend on the shape of the receiver. External facing receivers like the STJ receiver are subject to higher radiation losses than cavity shaped receivers as parts of the emitted irradiation is recaptured by the receiver based on the view factors of the geometry.

In contrast to a tube receiver where natural convection at the tube surfaces contributes to the convective losses, at the OVR ambient air close to the receiver surface is drawn into the receiver. Therefore convective losses only occur due to incomplete air return denoted as $\dot{Q}_{arr,loss}$, which are quantified by the air return ratio (ARR). The ARR can be defined in multiple ways either by a mass balance or derived from an energy balances over the receiver.

Based on substance it can be defined as the return air concentration (from here on denoted as ARR) which is the way the ARR is calculated in the CFD models applied in this work. For the total air return ratio the ARR based on substance can be denoted as in eq. (2.2) (in analogy to [16])

$$ARR = \frac{\dot{m}_{returned}}{\dot{m}_{tot}} \tag{2.2}$$

with the recirculated return air mass flow $\dot{m}_{returned}$ and the total receiver mass flow $\dot{m}_{tot}$. The air return ratio can also be defined based on a caloric approach as in eq. (2.3), derived from an energy balance over the receiver assuming a constant specific heat capacity, as for example defined in [52] or [16],

$$ARR_c = \frac{T_{h,in} - T_\infty}{T_{r,out} - T_\infty} \tag{2.3}$$

with the inlet temperature of the air drawn into the receiver $T_{h,in}$, the ambient temperature T_∞ and the return air temperature $T_{r,out}$ leaving the receiver. It shall be noted that in the definition in eq. (2.3) irradiation is not considered.

At the convex STJ receiver a receiver efficiency of approximately 71 % with air return ratios of 60 % are reported based on numerical simulations by Stadler et al. [14].

As stated in section 2.1.1, for the cavity receiver a receiver efficiency of 84.3 % with air return ratios of 84.8 % at design point conditions are reported based on numerical simulations by Stadler et al. [49]. Of the losses approximately 66 % can be attributed to radiation losses while the remaining part is attributed to convective losses due to incomplete air return (under windless conditions).

In part load with lower target temperatures the radiation losses naturally decrease in accordance to the receiver surface temperature which is also influenced by the return air outlet temperature. At the cavity reicever design studied in Stadler et al. [49], an increased air return ratio of 4 to 6 percentage points was observed, when 50 % of the return air mass flow was returned via outlets located below the receiver, compared to a solely internal air return.

The impact of the ARR on convective losses and the receiver efficiency heavily depends on the return air temperature. Based on the definition of the ARR in eq. (2.3) a reduction in the ARR from a complete air return to an ARR of 90 % results in thermal losses of 1.5 MW at a return air temperature of 100 °C and 5.1 MW at a return air temperature of 270 °C which corresponds to a reduction in the receiver efficiency of 1.2 percentage points and 4.1 percentage points respectively (based on an assumed mass flow of 200 $\frac{\text{kg}}{\text{s}}$ and intercepted irradiation of 125 MW). This simple approximation underlines the importance of a high air return ratio in the open volumetric receiver which needs to be

maintained under the presence of wind. Marcos et al. [41] state that receiver efficiencies of 90.0 % should be aspired and lateral wind as well as the receiver geometry needs to be considered carefully in the receiver design.

2.2 Experimental Fundamentals

This section gives a brief overview on the concept of similitude which is essential for the construction of the wind tunnel model, the choice of the experimental parameters and to transfer the results obtained within the experimental environment to the full-scale application. Furthermore, the measurement principles of the measurement equipment that was used is presented in brevity.

2.2.1 Dimensional Analysis and Concept of Similitude

In the preparation and design of every experiment the concept of similitude plays an important role. In order to transform the results from the model environment to the real scale environment, it needs to be assured that both bodies and the physics which act upon those bodies are similar. For the identification of relevant parameters to a problem, dimensional analysis can be utilized in order to reduce the number of variables to a minimum number of independent variables. The most common approach in this context is the so-called Π-theorem by Buckingham [53] in which the set of parameters is represented by non-dimensional variables Π_i. The Π-theorem states that within a system of n quantities Q_n, $i = n - k$ independent non-dimensional variables Π_i exist if the system inherits k arbitrary fundamental units with each Π_i in the form of

$$\Pi_i = \prod_{j=1}^{n} Q_j^{a_j} \tag{2.4}$$

If we now consider two physical systems, a system S and a transformed system S' the two systems are similar in a physical sense if the variables Q and Q' within each system behave similar provided the behavior is describable by the same physical equation (cf. [53]). If this is the case, the same set of non-dimensional variables will result by the presented approach and it follows that the non-dimensional quantities Π_i in each system have to be equal if physical similarity is provided.

In the experiments within this thesis, the transient surface pressure under wind will be determined and the variables relevant to the flow are the density ρ, the velocity $\mathbf{u}$, the characteristic length D, the dynamic viscosity μ, the pressure difference to the free stream static pressure $p - p_\infty$, the speed of sound c and the frequency f. The drag force F_d will further be utilized in the estimation of the blockage factor (cf. eq. (3.12)), which is why it is included in the set of variables. Those variables inherit three fundamental units, namely the mass, time and length, which leads to five independent non-dimensional variables Π_i in order to describe the system.

The five non-dimensional variables, which are determined that way, are summarized in table 2.1. For convenience, the non-dimensional variable related to the drag force F_d is related to the cross-sectional area A of the model instead of D^2, as shown in table 2.1.

The speed of sound c is non-dimensionalized by the free stream velocity u_∞ which leads to the Mach number Ma. Based on the Mach number the flow regime can be specified into subsonic, transonic, supersonic and hypersonic flow. Ma is assessed in this

context in order to determine whether compressibility effects have to be considered. In Wolowicz et al. [54] it is shown that the rate of change in pressure with density under the assumption of adiabatic flow is related to the Mach number in a way that compressibility effects are negligible for Mach numbers less than 0.2. It shall be mentioned that in experimental set ups where the flow is significantly obstructed, the local mach number can vary significantly from the free stream value.

The pressure difference to the free stream static pressure $p-p_\infty$ is non-dimensionalized by the free-stream dynamic pressure $\frac{\rho_\infty}{2}u_\infty^2$.

The Reynolds number (Re) relates the inertial forces to the viscous forces acting on a body and influences for example the point of transition from a laminar to a turbulent boundary layer, the thickness of and the velocity profile in a boundary layer and also the point of flow separation (cf. [54]).

The frequency in any measured quantity is non-dimensionalized by the Strouhal number St with the characteristic length D and the free stream velocity u_∞.

The non-dimensional parameters, which are relevant to the experiments conducted in this work, are summarized in table 2.1.

Table 2.1: Non-dimensional variables of relevance to the experiments in this thesis.

Non-dimensional variable	Name	Physical meaning or definition
$Re = \frac{\rho_\infty u_\infty D}{\mu_\infty}$	Reynolds number	$\frac{inertial\ forces}{viscous\ forces}$
$Ma = \frac{u_\infty}{c_\infty}$	Mach number	$\frac{flow\ velocity}{speed\ of\ sound}$
$St = \frac{fD}{u_\infty}$	Strouhal number	nondimensional frequency
$C_p = \frac{p-p_\infty}{\frac{\rho_\infty}{2}u_\infty^2}$	Pressure coefficient	$\frac{pressure\ forces}{inertial\ forces}$
$C_d = \frac{F_d/A}{\frac{\rho_\infty}{2}u_\infty^2}$	Drag coefficient	$\frac{drag\ forces}{inertial\ forces}$

Wolowicz et al. [54] state the importance of the concept of similitude in regards to experimental data as "one of the prime factors necessary to determine the limitations of data obtained from a model is the degree to which the similitude requirements have been met". As defined by Kline [55] physical similitude can conceptually be broken down to geometrical, kinematic and dynamic similitude, which refers to a similarity in geometric dimensioning, in the velocity ratios and the ratios of forces acting upon the model compared to the real scale design.

The concept of similitude has been applied in this thesis in the design of the wind tunnel model which is based on geometric similitude. Furthermore it is applied to the evaluation of measurement data and the transfer from the model scale to the real scale environment, which applies to the wind tunnel parameters and the evaluation of pressure signals in the time and frequency domain.

2.2.2 Measurement Principles

The equipment used in the measurements will be described in detail in section 3.2.3 and the uncertainty of the experimental results is approximated in section 3.2.4. This

section briefly describes the measurement principle of the pressure transducers used in the experiment.

Within the receiver cavities piezoresistive pressure transducers (Kulite XCQ-080) are instrumented whose measurement principle is described in detail in Buttgenbach et al.[56]. The pressure sensors instrumented in the wind tunnel model work based on the principle of piezoresistive differential pressure transducers. As differential pressure sensors they measure the pressure difference between two sources, the reference pressure and the local pressure at the measurement location. This is considered in the positioning of the sensors to comply with the definition of the pressure coefficient in table 2.1. The two applied pressures are connected to a silicon-based membrane which is strained when a pressure difference is applied. The membrane is coated with a wheatstone bridge (cf. [56]) whose electrical resistance changes under the deflection of the membrane measured in the voltage drop across the bridge. The voltage across the bridge is monitored and converted to a pressure value based on calibration curves. As will be discussed in section 3.2.4 the uncertainty of the pressure measurement is evaluated based on the sensor sensitivity, which is why it is important to understand the working principle.

2.3 Numerical Fundamentals

In this section the fundamental background regarding the numerical simulation of ambient wind flow around a solar tower is described. At first the governing equations that describe the flow phenomenon and the approaches to solve those equations numerically via discretization are presented. In the following, the fundamentals of turbulence modeling are described in detailed, including the concept of the energy cascade and modeling approaches which have developed in the field of turbulent flow simulations. This section is concluded with the boundary theory and the numerical approximation of boundary layer flows.

2.3.1 Governing Equations

The flow problem in this work is described by the Navier-Stokes equations, which include the conservation of mass, momentum and energy. A derivation of those equations can be found in e.g. [57] or [22]. The most general form assumes a compressible fluid which is applied for the cases where the receiver flow under irradiation from the heliostat field is considered. Due to the high temperature variations (25 to 700 °C), the assumption of an incompressible flow does not apply here. In contrast to that, in the simulations without irradiation and receiver flow an incompressible fluid is assumed which is why the governing equations for both cases are presented in the following.

The conservation of mass or continuity equation is described by the partial differential equation in eq. (2.5) formulated in the divergence form

$$\frac{\partial \rho}{\partial t} + \nabla \cdot (\rho \mathbf{u}) = 0 \tag{2.5}$$

with the fluid density ρ and the velocity vector $\mathbf{u}$. For a compressible flow the mass inside a control volume can change due to the advective flows across the boundaries.

For an incompressible fluid with a constant density ρ the continuity equation simplifies to eq. (2.6).

$$\nabla \cdot \mathbf{u} = 0 \tag{2.6}$$

The second fundamental equation to describe fluid dynamics is the momentum equation derived from Newton's second law of motion. It states that the change in impulse of a fluid inside a control volume equals the sum of all forces F_{sys} acting on the system eq. (2.7).

$$\frac{dm\mathbf{u}}{dt} = \sum_{sys} F_{sys} \tag{2.7}$$

In this case the forces include the body force due to gravity, the pressure forces on the boundaries and the friction forces due to viscosity. This leads to eq. (2.8) in the divergence form

$$\frac{\partial \rho \mathbf{u}}{\partial t} + \nabla \cdot (\rho \mathbf{u}\mathbf{u}^{\mathbf{T}}) = -\nabla p + \rho \mathbf{g} + \nabla \cdot \mathbf{T} \tag{2.8}$$

with the gravitational acceleration $\mathbf{g}$, the static pressure p, the dynamic viscosity μ and the stress tensor $\mathbf{T}$.

For a Newtonian fluid the stress tensor $\mathbf{T}$ can be determined by eq. (2.9)

$$\mathbf{T} = 2\mu\mathbf{D}(\mathbf{u}) - \frac{2}{3}\mu\nabla\cdot\mathbf{u}\mathbf{I} \tag{2.9}$$

with a linear dependency on the rate of strain tensor $\mathbf{D}(\mathbf{u})$ which is defined as in eq. (2.10).

$$\mathbf{D}(\mathbf{u}) = \frac{1}{2}(\nabla\mathbf{u} + (\nabla\mathbf{u})^T) \tag{2.10}$$

For the cases of incompressible flow, the body force due to gravitation is neglected as the density is constant which gives the simplified momentum equation in eq. (2.11).

$$\frac{\partial\mathbf{u}}{\partial t} + u\cdot\nabla\mathbf{u} = -\frac{1}{\rho}\nabla p + \nu\nabla^2\mathbf{u} \tag{2.11}$$

For the cases of incompressible flow, the problem is fully described by the continuity eq. (2.6) and momentum equation eq. (2.11). For the cases of compressible flow, the energy equation based on the first law of thermodynamics is added as the third governing equation. The volumetric internal energy e is formulated via the volumetric enthalpy h: $e = h - \frac{p}{\rho}$ which gives the energy equation as in eq. (2.12)

$$\frac{\partial(\rho h)}{\partial t} + \nabla\cdot(\rho\mathbf{u}h) + \frac{\partial\rho K}{\partial t} + \nabla\cdot(\rho\mathbf{u}K) - \frac{\partial p}{\partial t} = \nabla(\alpha\nabla h) + \rho\mathbf{u}g \tag{2.12}$$

with the kinetic energy $K = \frac{1}{2}|\mathbf{u}|^2$ and the thermal diffusivity α. In eq. (2.12) volumetric heat sources are omitted as they do not occur in the flow problem at hand. To close this set of equations, the equation of state for an ideal gas is assumed as $p = \rho\frac{R}{M_{air}}T$ with the Temperature T, the universal gas constant $R = 8.314\,\frac{\mathrm{J}}{\mathrm{mol\,K}}$ and the mole mass of dry air $M_{air} = 28.9616\,\frac{\mathrm{g}}{\mathrm{mol}}$. The temperature field T is calculated by the enthalpy $h = c_p T$ with the specific heat capacity c_p (cf. definition of the thermophysical properties in Appendix E).

With the given set of equations, the velocity, pressure, temperature, enthalpy and density fields can be determined. As discussed in section 1.4 one objective of this thesis is to evaluate the wind influence on the air return ratio (ARR) which introduces a further unknown variable that needs to be determined. The ARR is numerically determined by the mass flow weighted average of the concentration of return air at the receiver inlet. As will be presented in section 3.3.5 the receiver surface is divided into inlet (hot air, $\gamma = 0$) and outlet cells (return air, $\gamma = 1$), which gives a cell-wise mass flow weighted average of the return air concentration ξ as in eq. (2.13) where j denotes the cells and n_j the amount of cells on the receiver patch.

$$ARR = \frac{\sum_{j=0}^{n_j}(1-\gamma_j)\dot{m}_j\xi_j}{\sum_{j=0}^{n_j}(1-\gamma_j)\dot{m}_j} \tag{2.13}$$

The concentration is mathematically described as a passive scalar which itself does not influence the other quantities. Therefore it is calculated by a compressible scalar transport equation (advection-diffusion equation) eq. (2.14) as presented in [57].

$$\frac{\partial(\rho\xi)}{\partial t} + \nabla \cdot (\rho u \xi) = \nabla \cdot (\rho D_T \nabla \xi) \tag{2.14}$$

It includes the advective transport of the concentration ξ and the diffusion due to the local diffusion coefficient $D_T = \mu_{eff}/\rho Sc$ based on the effective dynamic viscosity μ_{eff}. The Schmidt number Sc is assumed to equal unity in accordance to the assumptions by Stadler et al. [14]. The effective dynamic viscosity μ_{eff} is composed of the laminar and turbulent dynamic viscosity.

The transport equation is calculated separately for the internal and external air return by setting the respective inlet value of ξ to 1 while setting ξ at the other air return boundary to 0. This allows a distinction between both return air systems and to evaluate the wind influence on each separately. The total air return ratio is simply calculated by a mass flow-weighted addition. The solution of the scalar transport equation is incorporated in the solver of the flow field and solved after a converged solution in the steady state simulations is reached or after each time iteration for the transient simulations respectively.

2.3.2 Discretization

In the discretization the set of partial differential equations presented in section 2.3.1 is transformed to a set of algebraic equations [19]. As presented in Ferziger and Perić [57] the most widely used methods to discretize the equations are the finite differences, finite volumes and finite elements method. In OpenFOAM, which is used in this thesis to solve the equations, the finite volume method is applied and will be described in the following part (cf. [57] or [58] for a detailed description of the other methods).

In the finite volume method, the flow domain is divided into a finite number of enclosed volumes and the equations are integrated over these finite volumes. The volume integrals of the divergence terms in the set of equations can be transformed to surface integrals by applying Gauss's divergence theorem. It states that the volume integral of the divergence of a quantity Φ over a finite volume V equals the surface integral over the enclosed surfaces S of the volume as denoted in eq. (2.15).

$$\int_V \nabla(\rho \mathbf{u} \Phi)\, dV = \oint_s \rho \mathbf{u} \Phi\, \mathbf{n}\, dS \tag{2.15}$$

With this method, which is applied on each finite volume and for the whole domain by summation of each volume, a set of integral equations is obtained. In order to obtain algebraic equations from the surface and volume integrals each term is numerically integrated by quadrature formulas. While volume integrals are easily determined by the cell centered values the discretization of the surface integrals (e.g. the convective terms at the boundaries of each volume) requires the determination of the values at the bounding surfaces of each volume. For this, interpolation schemes as functions of the

cell center values are applied. A variety of interpolation schemes exist with different accuracy depending on the formulation and the resulting truncation error. A very common interpolation scheme is the upwind scheme which utilizes the upstream cell center value depending on the flow direction for the bounding quantities. As described in [57], this approach is unconditionally stable but numerically diffusive as the truncation error of the Taylor series is of first order. A more accurate scheme is the linear interpolation which includes two neighboring cell center values which due to the truncation error is second order accurate. For a detailed review of of the finite volume discretization and additional interpolation schemes the reader is referred to Ferziger and Perić [57].

In unsteady simulations a temporal discretization of the partial derivatives with respect to time is necessary. The temporal discretization can be viewed as a finite-difference scheme along the temporal coordinate. In [57] different methods to discretize the temporal derivatives are presented, which are based on marching methods. They differ in terms of how many time steps are included in the approximation, commonly ranging from two to three-level-methods. The methods can further be characterized in explicit and implicit methods, where in explicit methods the approximation solely depends on the current and past time steps, while in implicit methods the approximation includes the future time step $n+1$. For example, in eq. (2.16) the approximation based on the two-level Euler backward method is presented.

$$\frac{\partial \Phi}{\partial t} = \frac{\Phi^n - \Phi^{n-1}}{\Delta t} \tag{2.16}$$

Euler's backward method is explicit as it only includes the current and the past time step. The temporal discretization is characterized by the time step size Δt, which raises the question of stability with respect to how large the time step can be chosen.

A common non-dimensional parameter to determine the time step width and evaluate the stability of the temporal discretization is the Courant–Friedrichs–Lewy number (CFL number, cf. [59]), in this work is defined as in eq. (2.17).

$$CFL = \frac{u\Delta t}{\Delta x} = \frac{\Delta t}{2V} \sum_{faces} |u_i A_i| \tag{2.17}$$

In the physical sense the CFL number is a measure of how far information is transported with the velocity u along the cell width Δx in one time step Δt. Consequently, CFL numbers larger than one indicate that during a time step the information is traveled further than one cell distance. Numerically it can be seen as a parameter to evaluate the balance between the spatial and temporal resolution [19]. The requirements on the CFL number depend on whether implicit or explicit temporal schemes are used (cf. [57] for detailed description on temporal discretization schemes). In general, CFL numbers ≤ 1 ensure numerical stability for implicit temporal schemes.

For scale resolving simulations as DNS or LES recommendations on appropriate time steps can be derived from investigations on this topic in literature. Choi and Moin [60] investigated different time steps in a plane channel flow with an implicit temporal discretization scheme. It could be shown that the relevant turbulent properties converge

for $CFL \leq 1$. Mockett [19] investigated the sensitivity of the solution of the flow around a cylinder with a DES utilizing two different time steps. It was observed that for $CFL > 1$ the formation of turbulent structures in the shear layer of separated flow is oppressed, which is attributed to time filtering effects due to the coarser time step. This underlines the general guideline for CLF numbers less than 1 especially in the regions of resolved turbulence, which is in alignment with the recommendation by Spalart and Streett [61] advising local CFL numbers of ≤ 1 based on rough accuracy driven estimates.

The discretization schemes used for the approximation of the spatial and temporal derivatives in this work are summarized in section 3.3.3.

2.3.3 Turbulence Modelling

In this section the fundamental concept of turbulence will be presented starting with the turbulent energy cascade. Then the numerical approaches to simulate turbulent flow and the differences and limitations of each one will be discussed.

Turbulent energy cascade

When we assume a fully turbulent flow at large Reynolds numbers, the concept of the energy cascade introduced by Richardson [62] can be applied. It describes turbulence as a cascade where larger eddies break down to smaller eddies due to instabilities. During the break down energy is transferred from larger to smaller scales. The large eddies are characterized by a large length scale and a consequently large Reynolds number. Therefore the effects of viscosity are negligibly small at these scales (cf. [63]). During the energy transfer towards smaller eddies they become smaller up to a point where the kinetic energy of the eddies becomes small compared to the molecular viscosity and dissipation further determines the energy transfer. Kolmogorov [64] further specified the concept of the energy cascade[1] by formulating three hypotheses. The first hypothesis addresses the smallest scales of turbulence and states that in contrast to large scale motion, which is anisotropic and determined by the boundary conditions of the flow, the small-scale turbulence is locally isotropic at sufficiently large Reynolds numbers. It is argued that the directional differences are lost during the eddy-breakdown towards smaller scales (cf. [63], [64] or [65]). The second hypothesis further states that the smallest scales of turbulence are determined by the turbulent dissipation rate ϵ at which they receive energy from larger scales and the molecular viscosity ν. The third hypothesis states that at scales l larger than the smallest Kolmogorov scales η but smaller than the turbulent length scale l_0 the statistics have a universal form only dependent on the dissipation rate ϵ. It is argued that at those scales, based on the Reynolds number the turbulence dissipation from larger scales overcompensates viscous effects. The range where the third hypothesis is applied is called the inertial subrange and is characterized by a linear decrease of the turbulent kinetic energy proportional to $\epsilon^{2/3}k^{-5/3}$. In fig. 2.3

[1] The original publication by Kolmogorov published in 1941 in russian was translated and republished in 1991 in the Proceedings of the Royal Society.

the wavelength spectrum of the turbulent kinetic energy is displayed based on measurement data of decaying isotropic turbulence by Comte-Bellot and Corrsin [66].

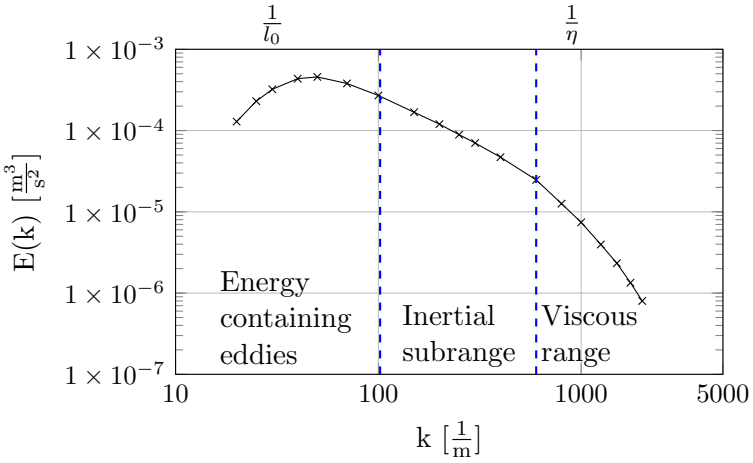

Figure 2.3: Wavelength spectrum of the turbulent kinetic energy k based on measurement data of decaying isotropic turbulence by Comte-Bellot and Corrsin [66].

In fig. 2.3 the different regions in the turbulence spectrum are marked, which contain the region determined by the energy containing eddies inserted by the boundary conditions, the inertial subrange where the turbulent kinetic energy decays in a universally observed manner and the viscous range dominated by the molecular viscosity.

Turbulent flow simulation and modeling approaches

In a direct numerical simulation (DNS) the entire range of scales within the turbulent flow is directly resolved without utilizing turbulence modeling, which makes it the most intuitive approach. Based on the Kolmogorov hypotheses it can be shown (cf. [63]) that the ratio between the smallest η to the largest scales l_0 is proportional to the Reynolds number by $\eta/l_0 \propto Re^{-3/4}$. As the separation between the smallest and largest scales grows with Re, so does the requirement on grid refinement in order to resolves the smaller scales and with it the requirement of refinement in the time step due to numerical stability and physical reasons (cf. CFL number in section 2.3.2). The necessity to resolve the smallest scales in turbulence to this date restricts DNS to applications with simple geometries and low Reynolds number flows. Nevertheless, DNS is especially useful in the development of turbulence models as a ground truth for validation and calibration of model parameters.

To overcome or reduce the cost of resolving the small-scale turbulence, modeling approaches have evolved which are based on statistical turbulence modeling (RANS), partially modeling the turbulent scales (LES) and combined approaches (DES). The most common approach to model turbulent flow without resolving the scales of motion is the RANS approach. This concept is based on the Reynolds decomposition (cf. [67]) leading to the Reynolds-averaged Navier-Stokes equations. The idea is to solve the Navier-Stokes

equations presented in section 2.3.1 for averaged fields which is achieved by decomposing the turbulent flow fields Φ into an average component $\bar{\Phi}(x, y, z)$ and a fluctuating component $\Phi'(x, y, z, t)$. Depending on the problem the averaging can be achieved by e.g. time averaging, ensemble averaging or favre averaging (cf. [57]) which is used in flows where considerable density fluctuations ρ' are present. As presented in detail in e.g. [65] the application of the Reynolds decomposition introduces an additional nonlinear term in the momentum equation which consists of the fluctuating components of the velocity field - the so called Reynolds stresses. Those fluctuating components are unknown and pose an additional variable to the Navier-Stokes equations forming the closure problem in the RANS approach. The closure of the RANS equations is achieved by approximations, which relate the Reynolds stresses to known parameters as the mean flow [57]. Wilcox [65] gives a comprehensive overview of the existing RANS models ranging from simple algebraic models to models based on multiple additional partial differential equations.

In linear eddy viscosity models the Reynolds stresses τ are related to the mean flow in analogy to the Newtonian stresses (cf. eq. (2.9)), but via the turbulent eddy viscosity ν_t. This approach is based on the Boussinesq stress-strain relationship [68] and denotes as

$$\tau = 2\nu_t \mathbf{D}(\mathbf{u}) - \frac{2}{3} k \mathbf{I} \tag{2.18}$$

with the rate of strain tensor $\mathbf{D}(\mathbf{u})$ defined in eq. (2.10) and the turbulent kinetic energy k in the fluctuating velocity field.

$$k = \frac{1}{2}\overline{u_i' u_i'} = \frac{1}{2}(\overline{u'^2} + \overline{v'^2} + \overline{w'^2}) \tag{2.19}$$

The simplest linear eddy viscosity models are algebraic models based on Prandtls mixing length theory [69], which applies the algebraic equation as in eq. (2.20)

$$\nu_t = l_m^2 \frac{d\overline{u}}{dy} \tag{2.20}$$

to calculate the eddy viscosity ν_t by the mixing length l_m, which as postulated by Prandtl is proportional to the wall distance. More advanced classes of eddy-viscosity models, so called one- or two-equation models, use the respective amount of differential equations to describe the turbulence quantities from which the eddy viscosity is derived.

The modeling approach in this work is based on the one equation eddy viscosity Spalart-Allmaras RANS (SA-RANS) model presented by Spalart and Allmaras [70] and will be described in detail. In the SA-RANS model formulation in OpenFOAM the k-term in eq. (2.18) is omitted. The model is based on the modified turbulence viscosity $\tilde{\nu}$ and the eddy viscosity ν_t, which is needed to close the Navier-Stokes equations, is calculated by eq. (2.21).

$$\nu_t = \tilde{\nu} f_{v1} \quad \text{with} \quad f_{v1} = \frac{\chi^3}{\chi^3 + c_{v1}^3} \quad \text{and} \quad \chi = \frac{\tilde{\nu}}{\nu} \tag{2.21}$$

$\tilde{\nu}$ is obtained by the following transport equation [70]

$$\frac{\partial(\tilde{\nu})}{\partial t} + \nabla \cdot (u\tilde{\nu}) = c_{b1}\rho\tilde{S}\tilde{\nu} - c_{w1}f_w\rho\frac{\tilde{\nu}^2}{d^2} + \frac{1}{\sigma}[\nabla((\nu+\tilde{\nu})\nabla\tilde{\nu}) + c_{b2}(\nabla\tilde{\nu})^2] \tag{2.22}$$

with $\tilde{S}$ defined as

$$\tilde{S} \equiv \Omega + \frac{\tilde{\nu}}{\kappa^2 d^2} f_{v2} \tag{2.23}$$

with Ω as the magnitude of the vorticity, d as the closest distance to the wall and κ as the thermal conductivity. The full set of equations of the model parameters can be found in Appendix D.

In terms of computational cost and modeling accuracy LES lies between RANS and DNS. LES poses an approach to directly solve the Navier-Stokes equations for the large-scale motion by applying a filtering operation, while modeling the small scale turbulence. This can be achieved with the application of an explicit or implicit filter. Compared to RANS modeling LES promises to be more accurate especially "when the large-scale flows of interest are intrinsically time dependent" [71] which can especially be expected for bluff body flows [63]. Depending on the resolution LES can be grouped into LES with near-wall resolution in which the spatial resolution is fine enough to resolve a large enough portion of the turbulence everywhere in the field, LES with wall-modeling where this resolution is only achieved in the wall-far field or the so-called very-large-eddy simulation where the spatial resolution is too coarse to resolve the bulk in the turbulent energy spectrum. According to Pope [63] within the concept of explicit filtering the steps include a filtering operation which divides the field into a filtered, fully resolved component $\overline{\mathbf{u}}(x,y,z,t)$ and a residual component $\mathbf{u}'(x,y,z,t)$ which is modeled. Applied on the Navier-Stokes equations this yields a residual stress term in the momentum equation that is closed by a subgrid scale (SGS) model and the solution of the filtered equations provides a solution of the large-scale turbulent motion.

The filtering is achieved by aplying a low-pass filter on the velocity field $\mathbf{u}$ which can be formulated in the most general way according to Leonard [72] by a convolution of the velocity field $\mathbf{u}$ with a filter function $G(x,x')$ to yield the filtered value $\overline{\mathbf{u}}$ in the filtered space x'.

$$\overline{\mathbf{u}} = \int G(x,x')\mathbf{u}(x')dx' \tag{2.24}$$

One of the most common filters is the box filter introduced by Deardorff [73] where $\overline{\mathbf{u}}$ is the average of $\mathbf{u}(x')$ in the interval with the width Δ. Another prominent filter used in LES is the Gaussian filter with a mean zero and a variance of $\sigma^2 = \frac{\Delta^2}{12}$ (for a detailed summary of filter functions cf. [74] or [63]). Independent on which filtering function is used, the filter introduces a filter width Δ which determines up until which length scale the field is resolved while smaller turbulent motion is excluded from the filtered velocity field and captured by the SGS model. The residual stress term can be interpreted as an addition of diffusion to the filtered equations to represent the effect of unresolved turbulent motion.

Among the SGS models the Smagorinsky model (cf. [75]) is the most common which relates the residual stress to the filtered rate of strain tensor $\overline{\mathbf{D}(\mathbf{u})}$ in analogy to the algebraic linear eddy-viscosity models described before.

$$\tau_r = -2\nu_t \overline{\mathbf{D}(\mathbf{u})} \tag{2.25}$$

The eddy viscosity ν_t is derived from a dimensional analysis and an important distinction in the model definition compared to the RANS eddy viscosity models lies in the dependency of the length scale l_s on the filter width Δ as in eq. (2.26).

$$\nu_t = l_s^2 \overline{D} = (C_s \Delta)^2 \overline{D} \tag{2.26}$$

Additionally the model constant, the so called Smagorinsky coefficient C_s is introduced.

In addition to the explicit filtering operation there are further approaches with implicit filtering where no actual filter is applied on the governing equations. In this approach the filtering occurs implicitly due to the spatial discretization as scales smaller than the grid resolution intrinsically can not be resolved. Therefore, the finite volume discretization itself acts as a filter on the solution.

Implicit filtering has the advantage of resolving the flow up to the grid resolution whereas for explicit filtering the filter width necessarily has to be larger than the grid spacing. On the other hand this leads to a lower accuracy in the small resolved scales in implicit filtering as those structures approach the grid size (cf. [19]). In addition to that, in implicit filtering the exact behavior of the filter is unknown and depends on the discretization schemes that are appplied (cf. [19]).

Another approach to solve the Navier-Stokes equations for turbulent flow, which represents a hybrid approach between LES and RANS, is the Detached-eddy Simulation (DES), which was first proposed by Spalart et al. [30]. DES was introduced to combine the advantages of both modeling approaches by applying a RANS formulation in the boundary layer field, while using the LES approach in the far field. Applying the RANS formulation in the near-wall field drastically reduces the mesh requirements as it is no longer necessary to resolve the inherently smaller turbulent scales in the boundary layer by applying the Reynolds averaging and modeling the fluctuating fields in that area. On the other hand, the flow field far from the wall, where (e.g. in a bluff body flow) separation and vortex shedding occurs, is partially resolved by the LES approach. In the DES approach the model has to distinguish between those two areas, which can be achieved by a strict definition of modeling zones (zonal DES, e.g. cf. [76]) or via a dynamic formulation based on the grid sizing and wall distance as in the Spalart-Allmaras DES model (SA-DES, [30]) whose detailed model formulation will be presented in section 3.3.4. In general the SA-DES model is modified to act as SGS model in the wall-far field by introducing the cell width Δ in the formulation of the destruction term in the transport equation for the adjusted eddy viscosity $\tilde{\nu}$. This enables a distinction between the ordinary SA-RANS model within a close distance to the wall and a Smagorinsky-like LES model far from the wall. It is important to mention that in general the grid requirements in the far field are the same as for a regular LES.

To conclude this section a comparison of the computational costs of DES, LES and DNS is presented based on a literature review which emphasizes the motivation behind the modeling approach of the LES and further the DES. As presented in Wilcox [65] the computational costs of the simulation of the flow over a backward-facing step by DNS and by LES, both at a relatively small Reynolds number of 5000 (based on the step height) are compared. For this example the LES required 3 % of the grid points compared to the DNS and the computing time was 2 % of that for the DNS, while the agreement with experimental data was equally good. Although it is not further specified if the computational time accounts for core-hours or pure simulation time the reduction in the mesh requirement already emphasizes the potential of the LES compared to the approach of fully resolving the flow with a DNS.

Compared to a fully LES, in DES the wall layer is modeled in a statistical sense with the RANS approach. As presented in Piomelli et al. [77] based on the estimation by Chapman [78] the number of grid points necessary to resolve the wall layer is porportional to $Re_L^{1.8}$ while modeling the wall layer (as within the DES approach) only requires $Re_L^{0.4}$ grid points. As a comparison, in Piomelli et al. [77] the number of grid points necessary to resolve the wall layer flow by means of DNS is estimated to increase with $Re_L^{2.2}$ which underlines the motivation behind the turbulence modeling approaches.

2.3.4 Boundary Layer Modelling

As presented in table 2.1 the Reynolds number relates the inertial forces to the viscous forces. When a flow around e.g. a flat plate is considered, at the wall the no-slip conditions applies, whereas in the free stream region the free stream velocity and Reynolds number applies. In typical applications the inertial forces dominate within the wall-far field. When the wall distance decreases at some point the inertial and viscous forces will be of the same order and when the wall distance further decreases towards the wall, the viscous forces will dominate due to the no-slip condition. Between the free flow and the wall, a velocity profile emerges which is characterized in the boundary layer theory. To describe and characterize the boundary layer additional parameters need to be introduced. Based on dimensional analysis (cf. [65]) a velocity scale, the so called friction velocity u_τ can be derived from the wall shear stress τ_w and the density ρ as in eq. (2.27).

$$u_\tau = \sqrt{\frac{\tau_w}{\rho}} \tag{2.27}$$

Based on the friction velocity the non-dimensional wall distance y_+ is defined by

$$y_+ = \frac{y u_\tau}{\nu} \tag{2.28}$$

with the wall distance y and the kinematic viscosity ν.

The wall boundary layer can conceptionally be grouped into different sections based on the non-dimensional wall distance (cf. [79] or [80]). The region closest to the wall, the so-called viscous sublayer is placed in approximately $y_+ \leq 5$. For this region it

can be shown, based on the assumption of a constant shear stress τ_w inside this region, that the velocity follows $u = u_\tau y_+$. In the viscous sublayer the flow is dominated by the viscous effects. Further away from the wall the buffer layer emerges which is valid for aproximately $5 \leq y_+ \leq 30$. In this layer the viscous and turbulent stresses are of similar order and the velocity profile is generally difficult to describe (cf. [80]). The region for even greater wall distances with $y_+ \geq 30$ is called the logarithmic layer where the velocity matches the so-called log-law. Here the velocity is approximated with a logarithmic dependency on y_+. The flow in this region is dominated by turbulent stresses and the velocity increases gradually up until the free stream velocity.

Typical boundary layer heights are very small and to approximately discretize the velocity gradient within the boundary layer by placing the first node inside the viscous sublayer poses the necessity for a great amount of cell layers within the boundary layer. As presented in Siegrist [47] the turbulent boundary layer height δ_t at the position x can be approximated by

$$\frac{\delta_t}{x} \approx \frac{0.385}{Re_x^{1/5}} \tag{2.29}$$

Instead of resolving the boundary layer down to the viscous sublayer, wall functions can be applied where the first node is typically placed in the logarithmic layer and the gap to the wall is covered by correlations. In addition to that, approaches have evolved where blending functions are used to blend between the viscious sublayer and the logarithmic layer allowing a less restrictive placement of the first node (cf. section 3.3.2).

2.3.5 Flow Visualization Techniques

Different approaches in the visualization of vortical structures exist in literature, which are mostly based on the evaluation of the velocity gradient tensor and e.g. discussed in Dong et al. [81]. The visualization applied in this work is based on the λ_2-criterion as proposed by Jeong and Hussain [82]. In theory a vortex core can be defined by the presence of a pressure minimum in the balance between the centrifugal and pressure force. Different proposals exist regarding the definition of the pressure minimum and the λ_2-criterion is only strictly valid for steady inviscid planar flow (cf. [82]) as exceptions exist in three-dimensional viscous flow. Based on taking the gradient of the Navier Stokes equations and further neglecting the time-dependent and viscous term in the acquired equation eq. (2.30) can be derived [82]

$$S^2 + \Omega^2 = -\frac{1}{\rho}\Delta p \tag{2.30}$$

with S as the symmetric and Ω as the antisymmetric part of the velocity gradient tensor. As postulated by Jeong and Hussain [82] the presence of a local pressure minimum requires two positive eigenvalues of the pressure tensor which, due to eq. (2.30), can be determined by the eigenvalues of $S^2 + \Omega^2$. In an application on three-dimensional flows (cf. e.g. [81]) it can be seen that depending on the λ_2 value the structure of the iso-surfaces can break down and non-physical vortex structures can be observed. Still the

method is chosen due to its simplicity and its ability to visualize the impact of different turbulence modeling approaches on the vortical structures.

3 Methods

In this section the methods applied in the experimental and numerical work in this thesis are presented. At first the characterization of ambient wind is discussed and applied for weather data at the defined reference power plant location. The results are further utilized in the definition of the numerical and experimental parameters regarding the inlet wind conditions. After that, the experimental methods are described including the wind tunnel model, the experimental parameters, the applied measurement equipment and the wind tunnel parameters in general. The uncertainty of the experimental results is assessed with an uncertainty analysis based on the GUM method [83]. The section continues with the discussion of the applied numerical methods including the numerical domain, a discussion on the numerical grid and its resolution, the applied discretization and solution methods and the applied turbulence model. After that, the boundary and initial conditions are presented in detail including the modeling of ambient wind and the receiver flow, which is followed by a discussion on the limitations of the applied methods and an uncertainty analysis of the numerical results.

3.1 Characterization of Ambient Wind

As described in Pfahl et al. [84], wind can be characterized by the profile of the mean velocity u and turbulence intensity I, a probability distribution function (PDF) of wind speed and direction and the power spectral density of the velocity fluctuations. All of those characteristics vary on the location and especially on the terrain condition.

In this thesis the characterization of wind is especially important in the context of model development and the definition of the simulation and measurement parameters. The characterization of wind in this chapter focuses on identifying the predominant wind directions and speeds at the reference power plant site. Additionally, the wind direction variability will be analyzed, as during the experiments dynamically changing wind directions are considered (cf. section 3.2.2).

As described in section 2.1.1 the reference plant under investigation is located in Vanrhynsdorp, South Africa. Therefore weather data at this location has been analyzed, obtained from the Southern African Universities Radiometric Network (SAURAN, cf. [85]). The measurement data was recorded in 2018 on a minutely basis and includes wind direction and wind speed. The weather station is operated at a height of 10 m and the topography is reported as an "enclosure on rural farmland". For the operation of the OVR the wind condition at receiver height is of particular interest and therefore the measured values have to be extrapolated based on an assumed boundary layer profile. As presented in Kent et al. [86] different approaches of modeling the velocity profile in an atmospheric boundary layer exist. For this study Prandtl's logarithmic law is applied following eq. (3.1):

$$u(z) = \frac{u_\tau}{\kappa} ln(\frac{z - z_d}{z_0}) \tag{3.1}$$

with u_τ as the friction velocity and κ as the von Kármán's constant. As those parameters are constant, the extrapolation solely depends on the zero-plane displacement z_d and the aerodynamic roughness length z_0 which is determined by the surface roughness conditions (for further explanation cf. [86]). For the given rural terrain at the measurement location z_d and z_0 are assumed to equal 0.33 m and 0.03 m respectively. Based on eq. (3.1) and the assumptions regarding the roughness parameters the velocities at the middle of the receivers (187 m) are obtained. All data presented in this context are based on this approach of extrapolation and the velocities refer to the receiver height.

To get a visual impression on the predominant incident angles ϕ a wind rose plot is suitable as shown in fig. 3.1. It becomes visible that the predominant wind direction at the reference location varies between a southern and south-western incident angle. When applying a coarser discretization with a step size of 45° the maximum shifts to a south-western incident angle.

Furthermore, the frequency distribution of the extrapolated wind speed at receiver height is visualized in fig. 3.2 in an absolute and cumulative manner. Based on the evaluation of each data point at receiver height, approximately 90 % of the yearly values are below 14 $\frac{\text{m}}{\text{s}}$ with a peak in the distribution at around 4 $\frac{\text{m}}{\text{s}}$ average wind speed.

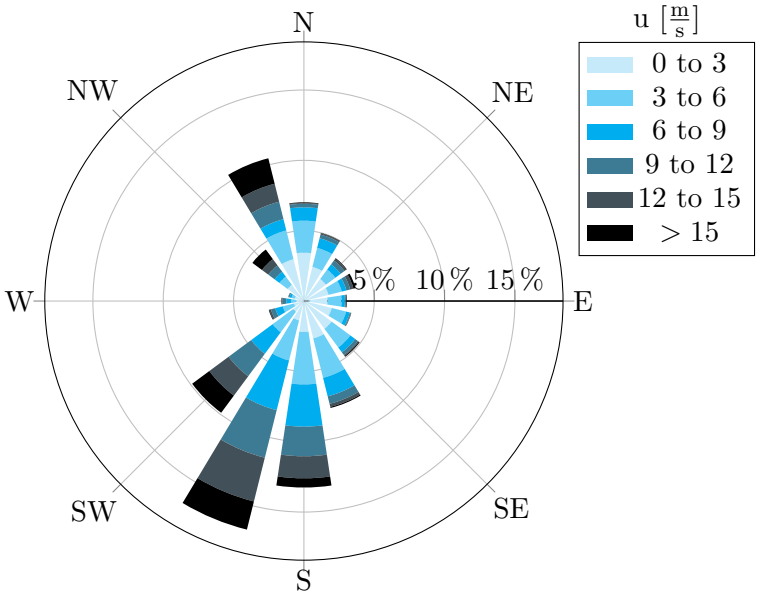

Figure 3.1: Wind rose diagram of the wind speed u, which has been extrapolated to the mean receiver height (based on the minutely SAURAN data from 2018 at Vanrhynsdorp, South Africa (cf. [85])).

To increase the relevance of the data set, only those time periods should be included when operating the power plant is advisable with regard to the solar irradiation. The DNI (direct normal irradiance) quantifies the amount of irradiation on a unit area perpendicular to the sun excluding diffuse solar radiation, which can not be using in concentrating solar systems. Only those measurement points where the DNI extends the necessary limit for an efficient operation of the tower should be included. Regarding the DNI the missing data rate in the SAURAN data almost reached 50 % which is why this criterion is not further considered. As an estimate, the frequency distribution can be analyzed during predefined solar hours of the day. In fig. 3.2 the data has been analyzed as well including only data points between 9 am and 18 pm, which in this context is defined as solar hours. During solar hours the frequency distribution further shifts towards higher wind speeds, but the characteristic peak velocity and upper boundary remain the same.

Another aspect that narrows the operating range of the power plant is the structural integrity of the heliostats. The maximum permissible wind speed varies depending on the heliostat model but according to Pfahl et al. [84] and Augsburger [87] 10 $\frac{\mathrm{m}}{\mathrm{s}}$ wind speed is a typical maximum threshold for the operation of the heliostat drives. Based on the extrapolation via eq. (3.1) at a heliostat height of around 3 m, when assuming a shut-off velocity of 10 $\frac{\mathrm{m}}{\mathrm{s}}$, wind speeds at the receiver height of up to 19.5 $\frac{\mathrm{m}}{\mathrm{s}}$ should technically be considered at most.

In fig. 3.3 the data on wind speed is evaluated with regards to seasonal effects based on a contour plot showing the magnitude of wind speed with respect to the solar time

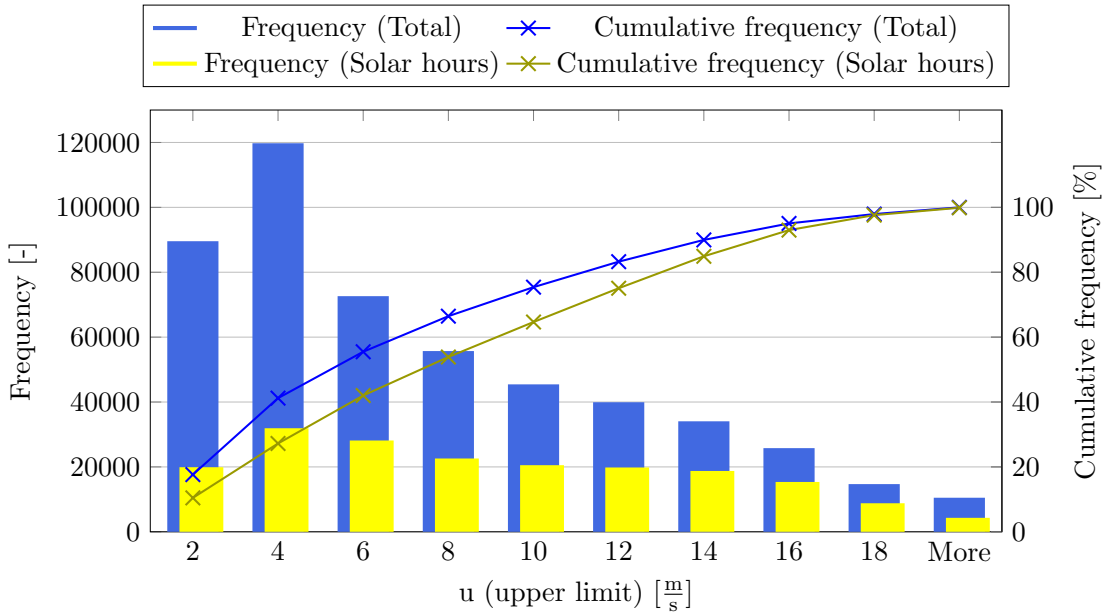

Figure 3.2: Absolute and cumulative frequency distribution of extrapolated wind speed less or equal to the given threshold in total and during solar hours (based on the minutely SAURAN data from 2018 at Vanrhynsdorp, South Africa (cf. [85])).

and date within the year 2018. This visualization is chosen to further demonstrate seasonal effects regarding the wind conditions. It can be seen that during months of high irradiation, which at the reference plant location are roughly between December and March, especially high wind speeds are observed. This further underlines the importance of ambient wind on the receiver operation.

Another important aspect in the characterization of wind is the direction variability and its dependency on wind speed. Wind direction variability in this context is defined as the magnitude of change in the incident angle $\Delta\phi$ in a given period of time. As mentioned in Saucier and Brundidge [88] and Mahrt [89] it can generally be observed that wind direction variability decreases with wind speed.

Based on the SAURAN data the minutely change in the wind direction can be correlated to the wind speed. During data processing care needs to be taken when changes in wind direction occur at the point of discontinuity in the scale ($0° = 360°$). To account for this, as described in Mahrt [89], changes in wind direction that exceed 180° are reduced by 360° or increased by 360° if they are lower than $-180°$. Based on this assumption the wind direction variability and its dependency on wind speed is visualized for the year 2018 in fig. 3.4. To increase clarity only every 100th data point is shown.

At the reference location the expected behavior of a higher direction variability at lower wind speeds can be observed. Based on minutely data, the variability of wind direction lies way below $\pm 50°$ for wind speeds greater than $4\,\frac{\mathrm{m}}{\mathrm{s}}$ which agrees very well

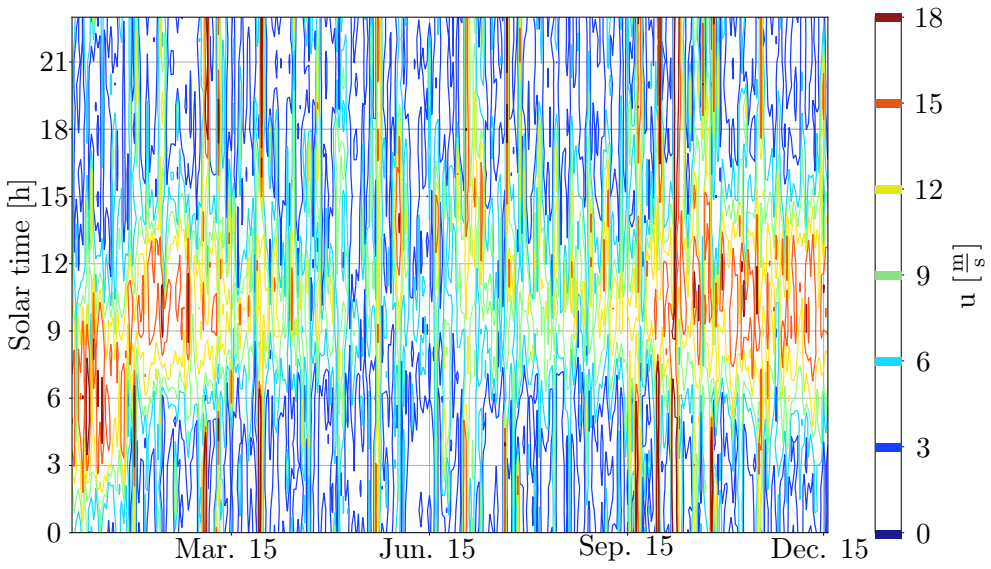

Figure 3.3: Seasonal weather data evaluation based on a contour plot of the wind speed with regards to the solar time and date (based on the minutely SAURAN data from 2018 at Vanrhynsdorp, South Africa (cf. [85])).

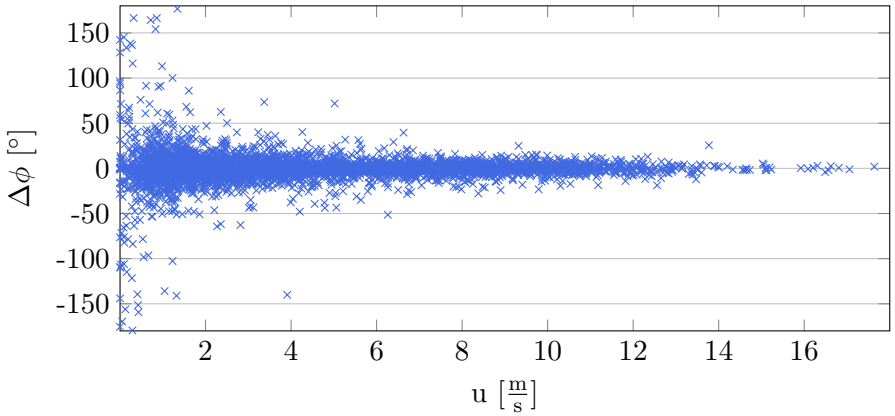

Figure 3.4: Dependency of the wind direction variability on wind speed (based on the minutely SAURAN data from 2018 at Vanrhynsdorp, South Africa (cf. [85])).

with minutely data at different sites as e.g. analyzed in Mahrt [89].

Based on the wind direction variability shown in fig. 3.4, the standard deviation in wind direction change between adjacent time steps $\sigma(\Delta\phi)$ at different wind speeds can be evaluated as visualized in fig. 3.5. $\sigma(\Delta\phi)$ decreases strongly with wind speed and falls below values of 10° for wind speeds greater than 4 $\frac{\mathrm{m}}{\mathrm{s}}$ at the given location, based on minutely data. The standard deviation in this data set can be approximated by the hyperbolic function $25.84u^{-0.695}$. As mentioned in Joffre and Laurila [90] minutely

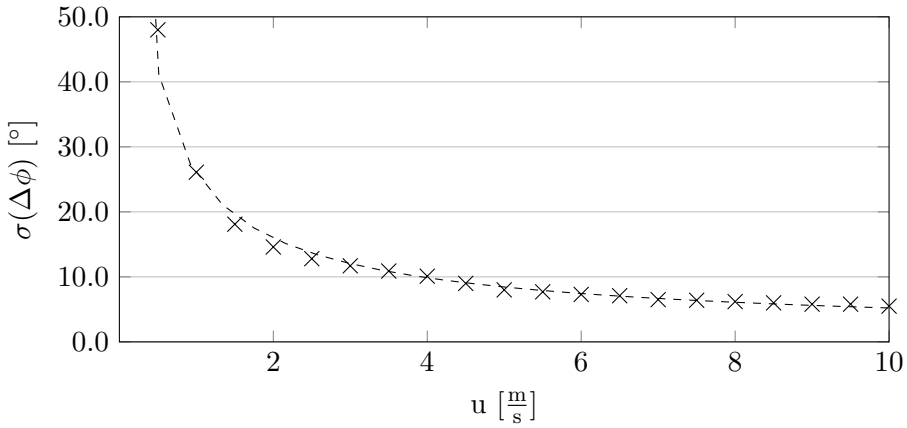

Figure 3.5: Standard deviation of the wind direction variability depending on wind speed (based on the minutely SAURAN data from 2018 at Vanrhynsdorp, South Africa (cf. [85])).

measurements miss spectral contributions of high frequency gusts, which is why a slightly larger standard deviation can be assumed for data with a higher temporal resolution.

In order to gain more insight on the short term characteristics of ambient wind, data obtained at the Solar Tower Jülich (STJ) with a sampling frequency of 1 Hz is evaluated. In fig. 3.6 the incident angle change within consecutive data points is evaluated including the correction of discontinuities mentioned above. The data includes five days of measurement under wind speeds ranging from 0.2 to 16.8 $\frac{\mathrm{m}}{\mathrm{s}}$. Displayed are the relative frequencies of changes in incident angles exceeding a certain difference in the incident angle and therefore characterizing the wind direction variability.

Based on this data it can be observed that for 92 % of the data the secondly variation in the incident angles is below 20° between consecutive data points which is slightly higher than the results obtained based on minutely data.

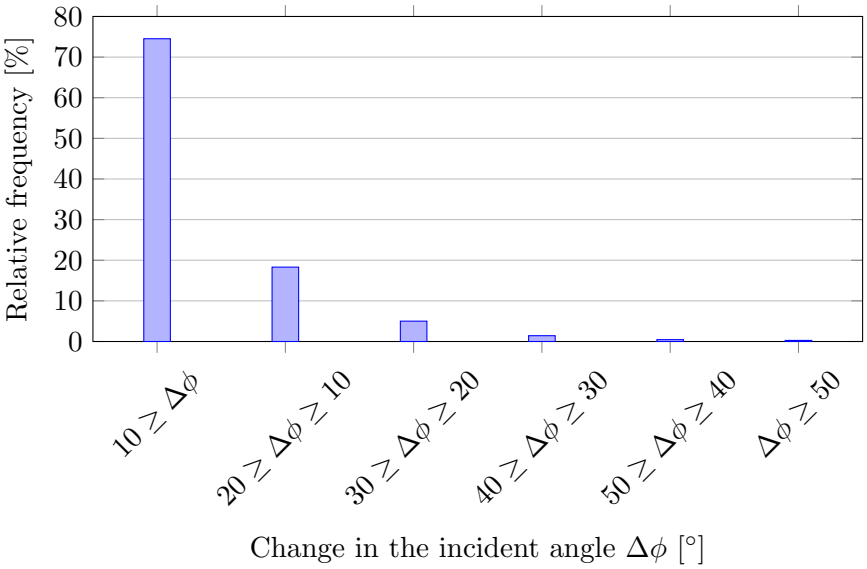

Figure 3.6: Relative frequencies of changes in incident angles exceeding a certain difference in the incident angle $\Delta\phi$ based on secondly data obtained at the STJ.

3.2 Experimental Methods

In this section the experimental methods are described in detail including the wind tunnel model, the measurement equipment applied at the model and the wind tunnel parameters. This section is concluded by an uncertainty analysis of the measured quantities. Parts of the experimental methods described in this section were already published previously by the author and colleagues in a journal paper (cf. [51]).

3.2.1 Wind Tunnel Model

The wind tunnel model is based on the reference plant concept presented in section 2.1.1 with a global scale factor of $\approx 1:290$. The choice of the scale factor is influenced by a set of boundary conditions and opposing requirements. As presented in section 3.1 during operation at the potential plant site, wind speeds up to 14 $\frac{\mathrm{m}}{\mathrm{s}}$ should be considered, which equals a Reynolds number of 36.61×10^6. Reynolds numbers of that magnitude are difficult to achieve in experimental set-ups. On one hand a large-scale factor and therefore large model is desirable, while on the other hand the model size is limited by the blockage effect experienced by every model in a bounded wind tunnel. The blockage factor is defined as the ratio of the cross-sectional area of the model perpendicular to the flow-direction related to the cross-sectional area of the test section and should be low enough to avoid wall-induced flow interference (cf. section 3.2.4 for a detailed explanation and evaluation of the blockage effect).

In fig. 3.7 the wind tunnel model is displayed mounted in the test section and in a close up view from northern direction. An important parameter in the design and construction of the model is the surface roughness which has a strong influence on the flow–structure interaction. The surface roughness strongly influences the boundary layer characteristic and separation (cf. [91]) and was chosen to be as smooth as possible to enable a comparison to the CFD simulations. The model has been milled of an aluminum alloy (EN AW 7022 [AlZn5Mg3Cu – 3.4345]) and was polished to achieve an average surface roughness of $R_a \leq 0.0016\,\mathrm{mm}$.

In fig. 3.8 the upper part of the model is displayed (south-view) and how the transient pressure probes p_k are arranged within each cavity (left). Furthermore, on the right-hand side the distribution of static pressure probes p_s around the model and the definition of the incident angle ϕ is visualized.

The static pressure probes are located at the angular positions as in table 3.1 with $\phi = 0.0°$ referring to a southern incident angle.

Table 3.1: Angular positions of the static pressure probes at the model.

probe	p_{s0}	p_{s1}	p_{s2}	p_{s3}	p_{s4}	p_{s5}	p_{s6}	p_{s7}	p_{s8}	p_{s9}	p_{s10}
angle [°]	0.0	43.4	72.3	99.6	135.0	170.7	189.3	225.0	260.4	287.7	316.6

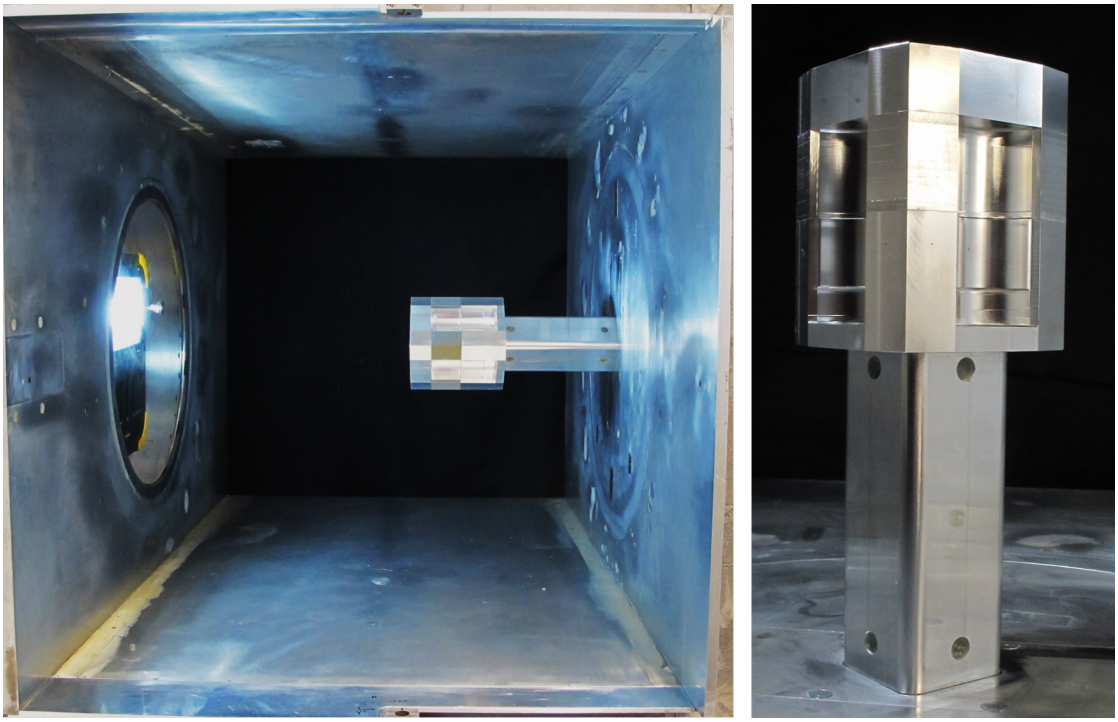

Figure 3.7: Pictures of the wind tunnel model during the test campaign mounted in the test section (left) and in a detailed view from a northern direction (right).

3.2.2 Wind Tunnel and Experimental Parameters

The experiments were conducted in the closed-circuit High-pressure wind tunnel (HDG) operated by the DLR in Göttingen. The wind tunnel can technically be operated under a pressure ranging from atmospheric up to 10 MPa at ambient temperature. Under those conditions, densities of 1.2 to 117.8 $\frac{\mathrm{kg}}{\mathrm{m}^3}$ (at 25 °C) can be realized. During the test series the fan speed ranges from 5 to 35 $\frac{\mathrm{m}}{\mathrm{s}}$.

The test section where the model is placed in has a cross section of 0.6 m × 0.6 m and a length of 1 m (cf. fig. 3.7) and can be accessed via a lock system without depressurizing the whole tunnel. The model is mounted horizontally on a three-component piezoelectric force-measuring element (Kistler Instrumente, Type 9067) (cf. section 3.2.3) which is placed outside the side wall of the tunnel. The force balance allows to constantly monitor the forces and moments that act on the model during the experiments. The model and the force balance itself are mounted on a rotatable table which enables the rotation of the model and the investigation under various incident angles. The rotatable table has an angular accuracy of ±0.03° (cf. [92]), which allows relatively small increments in the incident angle.

During the experiments the tunnel pressure was held constant at 6 MPa, limited by the measurement equipment. Due to wall friction, which increases with Reynolds number, the temperature in the tunnel tends to increase especially during longer periods

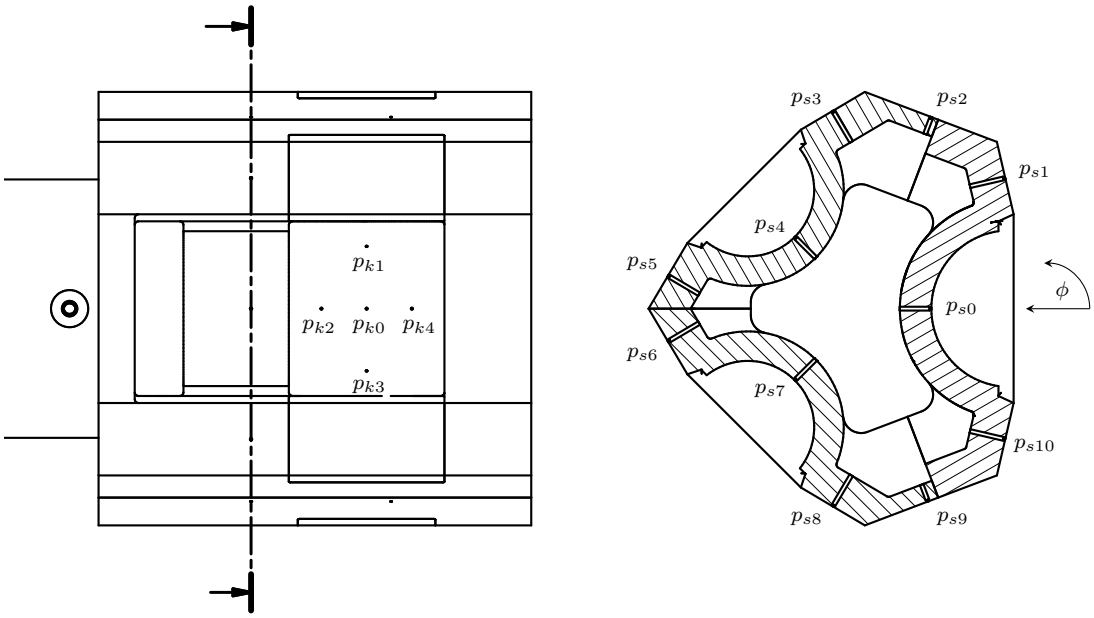

Figure 3.8: South view of the model ($\phi = 0°$) with the distribution of the dynamic pressure probes p_k in the southern cavity (left). Horizontal cut through the upper part of the tower to display the locations of the static pressure probes p_s (right).

of operation and varied in the inflow region between 20.4 °C and 40.8 °C during the experiments. To ensure constant inflow Reynolds numbers the tunnel fan is controlled via a PID controller (cf. section 3.2.3), that compensates the temperature variability. Under nominal conditions (at 6 MPa and 25 °C) the investigated Reynolds numbers, corresponding fan speeds and translated free stream velocities in the full scale application $u_{\infty,F}$ are summarized in table 3.2.

Table 3.2: Wind tunnel parameters under nominal conditions at 6 MPa and 25 °C.

Re [−]	fan speed $[\frac{\mathrm{m}}{\mathrm{s}}]$	$u_{\infty,F}$ $[\frac{\mathrm{m}}{\mathrm{s}}]$
3.49×10^6	8.0	1.3
5.23×10^6	12.0	2.0
7.85×10^6	18.0	3.0
10.46×10^6	24.0	4.0
13.17×10^6	30.0	5.0

The free stream turbulence intensity was not measured during these measurements, but is known to increase slightly with pressure and is reported to be at a maximum value of about 0.8 % at 10 MPa tunnel pressure (cf. [92]). During the whole test series

the inflow Mach number ranged from 0.02 to 0.09 which is way below the value of 0.2 for which compressibility effects need to be considered in the concept of similitude (cf. [54]).

The experiments in this study can be grouped into two test series:

(1) Stationary measurement under constant incident angles to investigate pressure fluctuations induced by flow separation at the tower.

(2) Dynamic measurement during rotation of the tower to investigate the effect of changing incident angles on the surface pressure in the cavities.

In the first test series, measurements were conducted under 17 different flow directions while utilizing the symmetry of the tower. The incident angle is varied from 0° to 180° in steps of 11.25°. The first test series was conducted for all five Reynolds numbers displayed in table 3.2. For each Reynolds number and flow direction a measurement time of 60 s was chosen since this has proven to be sufficient in terms of statistical convergence of the RMS (root mean square) pressure values, defined as in eq. (3.2), with the length N of the signal p and its time averaged value $\bar{p}$.

$$p_{RMS} = \sqrt{\frac{1}{N-1}\sum_{i=1}^{N}(p_i - \bar{p})^2} \tag{3.2}$$

For example in fig. 3.9 the convergence plot of the RMS and mean value is evaluated based on a sliding window approach with a step-wise increased window length at the highest Reynolds number of 13.17×10^6 and an incident angle of 45°. The results are normalized by the values based on the full measurement time of 60 s.

As visual in fig. 3.9 the mean pressure converges a lot faster with increasing window size than the RMS value. For the RMS value an evaluation time of $18 - 48$ s is necessary to reduce the relative deviation below 1 %. The mean value reaches the same accuracy in less than 18 s of evaluation time for the worse case and for the other cases an evaluation time of 2 s already yields results with comparable statistical accuracy.

In the second test series changing incident angles are investigated at the two highest Reynolds numbers 10.46×10^6 and 13.17×10^6. As described in section 3.1 there is a general dependency of the variability of wind direction in regards to wind speed as the variability decreases strongly with wind speed. The area of high variability lies within the range of wind speeds that are achievable in the wind tunnel ($\leq 5\,\frac{\mathrm{m}}{\mathrm{s}}$). During this test series the model was rotated at four different angular velocities of 20, 30, 40 and 45 $\frac{^\circ}{\mathrm{s}}$. The angular velocity is limited by the maximum rotational speed of the rotatable table, which is at 45 $\frac{^\circ}{\mathrm{s}}$. Because of the instrumentation of the pressure probes, the rotation had to be carried out back and forth between 0° to 180°.

In fig. 3.10 the RMS value based on a sliding window width ranging from 10 to 150 repetitions of a rotation between 0 and 180° is shown.

Based on the results of the sliding window RMS values, measurement of this kind was repeated 100 times to ensure statistical convergence of the RMS pressure values. In order to avoid hysteresis effects in the flow field, the tower rested at the end position of rotation before rotating back.

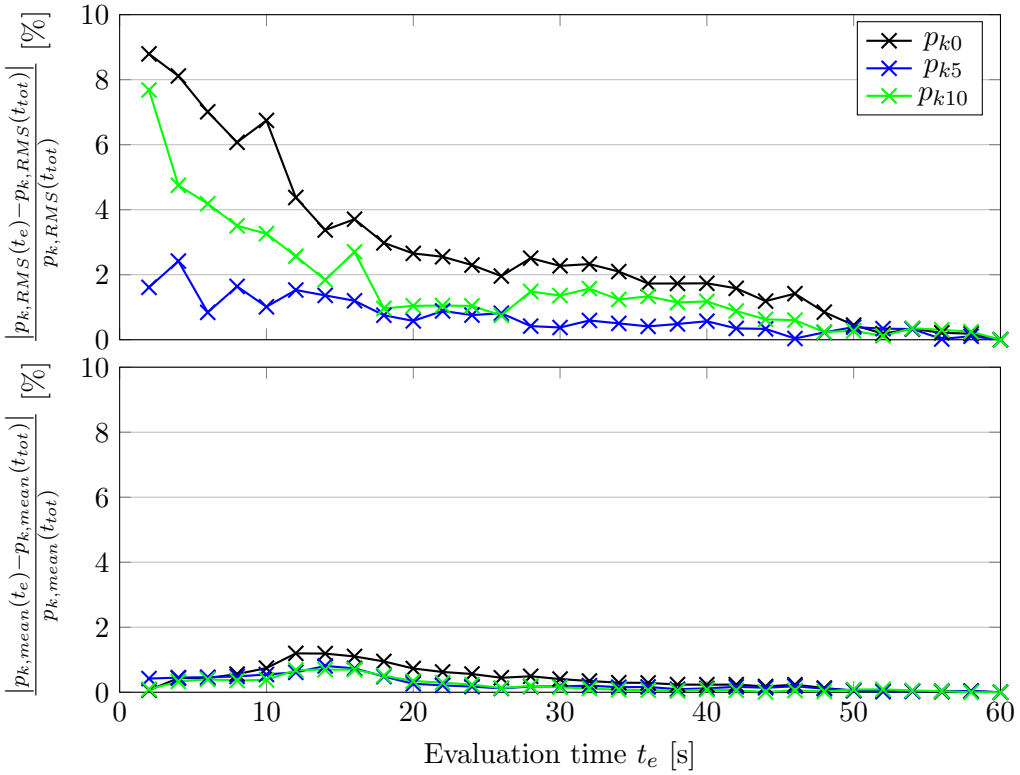

Figure 3.9: Relative deviation of the RMS and mean value based on varying evaluation times compared to the RMS value based on an evaluation time of 60 s at p_{k0}, p_{k5} and p_{k10} at an incident angle of 45° and a Reynolds number of 13.17×10^6.

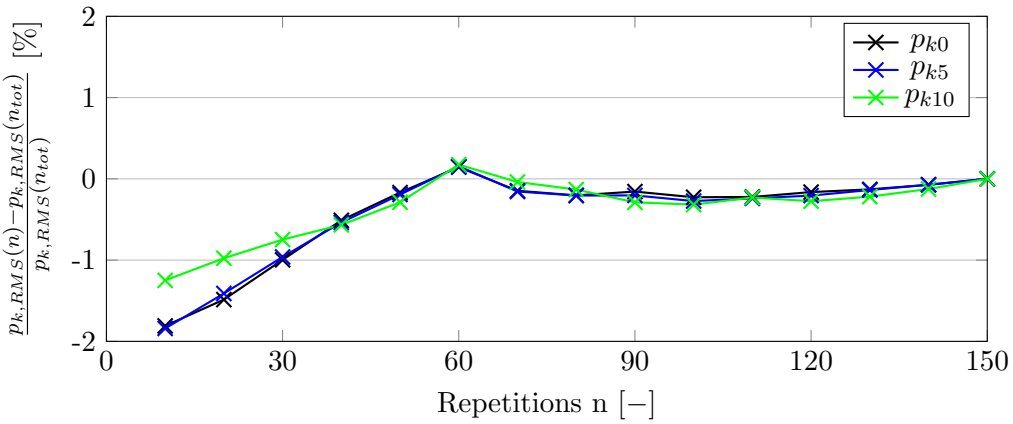

Figure 3.10: Relative deviation of the RMS value based on the number of rotations from 0 to 180° at p_{k0}, p_{k5} and p_{k10} with an angular velocity of 20 $\frac{°}{s}$ at a Reynolds number of 10.46×10^6.

3.2.3 Measurement Equipment at the Model and Wind Tunnel

This section presents the measurement equipment and quantities that will be recorded during the experimental measurements. In fig. 3.11 a sketch of the wind tunnel with the locations of the measurement quantities discussed in this section is shown. Furthermore, the test section, where the model is placed in is marked by the dashed lines.

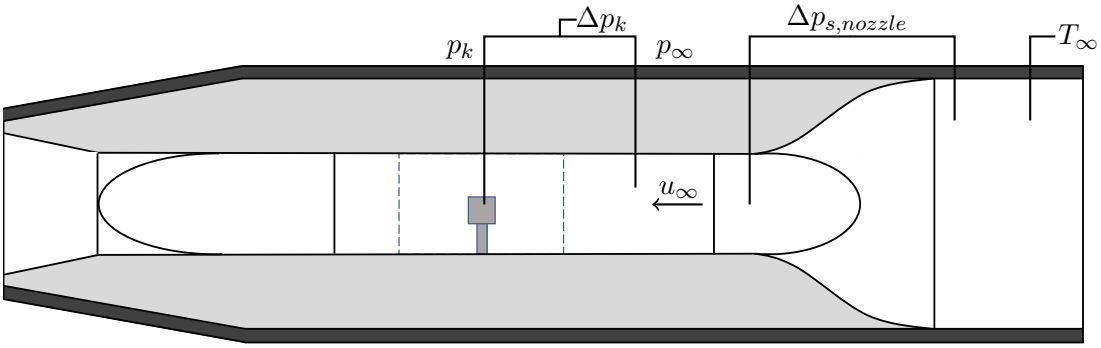

Figure 3.11: Sketch of the wind tunnel including the test section (dashed lines) and the measurement locations of model and tunnel parameters.

As shown in fig. 3.8 at the model two types of pressure probes were instrumented. In the cavities differential pressure transducers (Kulite XCQ-080) are instrumented to measure the transient surface pressure. The arrangement of the pressure transducers inside the cavities can be seen in fig. 3.8. The pressure reference tubes were connected to the inlet area in front of the test section so that the measured pressure at the probe location represents the differential pressure with respect to the incident flow. Based on this, the dimensionless pressure coefficient C_p is evaluated according to eq. (3.3)

$$C_p = \frac{\Delta p_k}{q_\infty} \tag{3.3}$$

with the dynamic pressure q_∞. The dynamic pressure can be calculated via eq. (3.4) with the inflow density ρ_∞ and velocity u_∞ or via the nozzle pressure gradient Δp_N.

$$q_\infty = \frac{1}{2}\rho_\infty u_\infty = \Delta p_N \tag{3.4}$$

The nozzle pressure gradient Δp_N is calculated by the measured static pressure difference across the nozzle multiplied by a calibrated nozzle pressure coefficient $\zeta_N = 1.0404$, which leads to the dynamic pressure in eq. (3.5).

$$q_\infty = \zeta_N \Delta p_{s,N} \tag{3.5}$$

Additionally, at the upper part of the model eleven differential pressure transducers (Type ESP-HD, Pressure Systems) are placed at a uniform height in the center of each facade of the model. In contrast to the pressure transducers in the cavity, they only

monitored the average pressure during the measurement. The pressure transducers were the same models as used in [91]. All pressure taps (both dynamic and static) have an inner diameter of 0.5 mm.

As described in section 3.2.2, the Reynolds number is kept constant during the measurement via a PID-controlled fan to account for variations in the flow parameters that lead to a deviation from the nominal Reynolds number defined by eq. (3.6) with the reference length D.

$$Re_\infty = \frac{\rho_\infty u_\infty D}{\mu_\infty} \tag{3.6}$$

Due to the high operating pressure in the tunnel the inflow density ρ_∞ and dynamic viscosity μ_∞ are calculated via the modified ideal gas equation with the gas deviation factor Z. The inflow temperature T_∞ is measured with four independent PT100 temperature sensors and u_∞ is derived from the dynamic pressure (cf. eq. (3.4)).

The Mach number in the inflow region Ma_∞ is also derived from the dynamic pressure.

$$Ma_\infty = \frac{u_\infty}{c} \tag{3.7}$$

The unsteady forces acting on the model during the experiments is measured with a 3-component piezoelectric force transducer (Type 9067, Kistler Instruments) which is described in detail by Schewe [93] and van Hinsberg et al. [92]. The force balance was mainly used to monitor the aerodynamic loads on the model during the operation of the tunnel but also in the data post processing in order to identify the time periods of rotations within the investigation of varying incident angles. As described in section 3.2.2 due to the instrumentation the tower had to be rotated back and forth in order to avoid torsion and damage to the cables belonging to the measurement equipment. Between each rotation the tower was rested to avoid hysteresis and because the start had to be initiated manually, the rest time is not equal. For the pressure evaluation a synthetic time series has been created in a post-processing step which excludes the time where the tower was rested between rotation. In order to identify the start and end of a rotation the pitch moment is analyzed which is calculated from the forces recorded by the piezoelectric force balance. Data from all measurement equipment was monitored with a sampling rate of 1000 Hz.

In addition to the quantitative measurement surface oil flow visualization was conducted as a measure to visualize the near surface flow field and to quantify the boundary layer height to assess this parameter in the discussion of systematic errors. Furthermore, the results are compared to CFD results in a validation of the flow field (cf. section 4.2.1). In this method the surface of the tower is coated with a Petroleum-based paint containing Titanium-Dioxide particles. When air flows over the coated surface, streaks of the particles remain which indicate streamlines at the surface. What makes this method so appealing is the simplicity and the possibility of flow visualization without the need for optical access to the test section of the wind tunnel. On the other hand as pointed out by Tamura and Fujii [94] the oil technique has the tendency to smoothen the streamlines due to the viscosity of the oil which differs from the air viscosity in the tunnel. It must be kept in mind that this method can only give an impression on time-averaged surface streamlines instead of instantaneous flow fields.

3.2.4 Uncertainty Analysis

In the following section an uncertainty estimation of the measured and derived quantities will be presented. In order to translate the measured quantities from the wind tunnel environment to the full-scale tower it is important to measure the dimensionless parameters with high accuracy. The uncertainty analysis can be grouped into a description and estimation of systematic errors and the quantitative evaluation of the uncertainty in the relevant measured quantities. The quantitative uncertainty analysis is evaluated according to the procedure presented in the GUM:1995 (ISO 2008) norm [83] and following that, uncertainties of quantities that are derived from other measured quantities are determined by the Gaussian uncertainty propagation. The uncertainty of the function f depending on n uncorrelated variables x_1, x_2, ..., x_n is defined as in eq. (3.8) (cf. [95])

$$\sigma_f = \sqrt{\left(\frac{\partial f}{\partial x_1}\right)^2 {\sigma_{x_1}}^2 + \left(\frac{\partial f}{\partial x_2}\right)^2 {\sigma_{x_2}}^2 + ... + \left(\frac{\partial f}{\partial x_n}\right)^2 {\sigma_{x_n}}^2} \tag{3.8}$$

In order to compare the experimental results to the CFD simulations of the full size tower the concept of similitude needs to be applied (cf. section 2.2.1). The surface pressure in the full-size environment $p_F(x,t)$ is calculated via the pressure coefficient C_p according to eq. (3.9)

$$\frac{\Delta p_M(x,t)}{q_{\infty,M}} = C_p = \frac{p_F(x,t) - p_{\infty,F}}{q_{\infty,F}} \tag{3.9}$$

and is calculated with the measured differential pressure $\Delta p_M(x,t)$ and dynamic pressure $q_{\infty,M}$. As stated in eq. (3.5) the dynamic pressure $q_{\infty,M}$ is derived from the static nozzle pressure difference. The pressure difference between both sections is measured with a CPT6100 15 PSI differential pressure sensor and according to manufacturer specifications the relative uncertainty for the given pressure range lies within $\pm 0.02\,\%$.

The absolute uncertainty in the difference pressure $\Delta p_M(x,t)$ in the receiver cavities measured by the differential pressure transducers is evaluated in a calibration process which is described in detail by Braune [96] who used the same equipment. During the calibration process the sensor sensitivity is evaluated in the relevant pressure range with a linear regression of the differential pressure over the voltage signal. The uncertainty of the sensor sensitivity is then evaluated by the deviation between the calibration values and the regression. The choice of a linear regression here is a conservative estimate as a cubic regression would capture nonlinear behavior leading to a smaller deviation (cf. [96]). Based on the calibration an uncertainty in the sensor sensitivity s of $\sigma_s = 0.0003\,\frac{\mathrm{kPa}}{\mathrm{mV}}$ is determined which results in an absolute uncertainty of the differential pressure according to eq. (3.10).

$$\sigma_{\Delta p}(\Delta p) = \sigma_s \left|\frac{\Delta p}{s}\right| \tag{3.10}$$

Depending on the pressure range, the absolute uncertainty in the differential pressure measurement varies between 2 an 30 Pa which equates to a relative uncertainty of $0.09\,\%$.

According to the procedure in [83] the combined standard uncertainty of the pressure coefficient σ_{C_p} can be calculated as the positive square root of the combined variance via eq. (3.11). To increase readability the subscript M for measurement is omitted in eq. (3.11).

$$\sigma_{C_p} = \sqrt{\left(\frac{\partial C_p}{\partial \Delta p}\right)^2 {\sigma_{\Delta p}}^2 + \left(\frac{\partial C_p}{\partial q_\infty}\right)^2 {\sigma_{q_\infty}}^2} = \frac{\Delta p}{q_\infty}\sqrt{\frac{\sigma_s^2}{s^2} + \frac{\sigma_{q_\infty}^2}{q_\infty^2}} \tag{3.11}$$

Based on this approach, the absolute uncertainty in C_p for the cavity pressure varies between 0.00094 and 0.00101 and therefore the relative uncertainty in the derived surface pressure in the full-size environment $p_F(x,t)$ varies between 0.089 and 0.090 %. With a coverage factor of 2 this yields a relative uncertainty between 0.178 and 0.180 % at 95 % confidence level.

As described in section 3.2.3 in addition to the pressure measurement in the receiver cavities, pressure transducers were placed at the upper part of the tower to evaluate the time-averaged pressure coefficient C_p. According to van Hinsberg [91] where the exact same equipment was used, those pressure transducers have a relative uncertainty of 2 % at 95 % confidence level. With the uncertainty in the dynamic pressure this gives a combined uncertainty of the pressure coefficient for those pressure transducers based on eq. (3.8) of 2.00 % .

In the following part the systematic uncertainties will be described and quantified where possible. The Reynolds number is an essential non-dimensional parameter but its uncertainty is not calculated via uncertainty propagation for several reasons. As described in section 3.2.3 the calculation of the Reynolds number is based on real gas correlations with the compressibility factor Z which is an approximation with an uncertainty that cannot be quantified in this context. Additionally, it can safely be assumed that the uncertainty in the measurement of the underlying quantities is negligible compared to the influence on Re due to the blockage effect which leads to the discussion of systematical uncertainties due to the wind tunnel and model design.

The blockage effect describes the contraction of streamlines between the model and the side walls of the tunnel caused by the mere presence of the model. The local necking of streamlines results in an increased velocity and Reynolds number compared to the free stream conditions. It is quantified by the blockage factor which can be defined as the cross-sectional area of the model in relation to the cross-sectional area of the test section. Besides to the potential deviation from the desired free stream Reynolds number undesired wall model interference induced flow phenomena can occur for large blockage factors. With a scale factor of approximately 1 : 290 the model introduces an area averaged blockage ratio of 16.6 % which has been chosen as a reasonable compromise between the desire for large Reynolds numbers and the necessity to keep the blockage factor low. To account for this effect, a correction of the local Reynolds number in the area of contraction can be applied based on the correlation by Allen and Vincenti [97] for a circular cylinder (as applied in [98]). The corrected velocity u_{corr} is determined via a correlation based on the blockage factor $\frac{d}{h}$ with the cylinder diameter d and the wind tunnel width h, the measured velocity u and measured drag coefficient C_d as in

eq. (3.12).

$$\frac{u_{corr}}{u} = 1 + \frac{1}{4} C_d \left(\frac{d}{h}\right) + 0.82 \left(\frac{d}{h}\right)^2 \tag{3.12}$$

The drag coefficient is calculated following the definition in table 2.1 with the drag force F_d measured by the piezoelectric force balance, the projected surface area of the tower and the dynamic pressure q. To account for the different model widths at the lower and upper part of the model, the blockage factor is calculated by the area averaged tower width of approximately 0.1 m which gives a blockage factor of 16.6 % with a tunnel width of 0.6 m. For a case of an incident angle of $\phi = 0.0°$ with a free stream Reynolds number of 3.49×10^6 and 13.17×10^6 this yields a relative deviation in the velocity of around 7.3 % for both cases.

Due to the limitations in the applicability of the correction as presented in Roshko [98] and furthermore as the results presented in section 4.1 show that the dimensionless quantities of interest are relatively Reynolds-independent in the Re-range that is investigated, the presented Reynolds numbers are uncorrected. E.g. in the case of a cylinder flow the exact knowledge of the corrected Reynolds number is far more important as a shift in the Reynolds number leads to a variation of the separation point (cf. [92]). This aspect is not that important to the given experiment as the separation is determined by the tower geometry and the sharp corners at which the boundary layer can no longer follow the geometry curvature leading to flow separation.

A systematic error which effects the pressure measurement is the temperature drift during the operation of the tunnel. The differential pressure sensors in the cavity have a passive temperature compensation which reduces thermal drift but to further reduce this influence and compensate for the temperature drift a correction is applied based on the assumption of a linear pressure drift over time. To quantify the drift in the measured differential pressure, before and after a certain period of measurement time a 60 s measurement without fan operation is recorded to determine the drift in the resting pressure. The difference in pressure at each probe is averaged during each control measurement and the pressure signal between the control measurements is corrected based on the linear drift which is observed. This correction is applied on the differential surface pressure p_k and also on the dynamic pressure q which also drifts due to the temperature changes during operation.

According to van Hinsberg [91], the lift C_l and drag coefficients C_d are obtained by the force balance with an 0.5 % accuracy at a 95 % confidence level.

The wind tunnel model is mounted on the force balance which is placed outside of the tunnel and covered with the side wall. In order to avoid force transmission from the tower to the side wall, a gap of approximately 1 mm is foreseen between the tower and the side wall. A leakage flow has to be expected in this area (cf. left side wall in fig. 3.12). The leakage flow was not measured but its influence on pressure measurements at the tower top can be assumed to be negligible.

At the side wall where the wind tunnel model is mounted, the wall boundary layer is a further systematic source of error. With the surface-oil flow visualization methods in

this study the boundary layer height and the extent of the area of recirculation at the bottom of the tower can be quantified. As displayed in fig. 3.12 the wall boundary layer height at an inflow Reynolds number of 10.46×10^6 was quantified as being less than $0.24D$ and therefore the influence on the measurement which takes place at the upper part of the tower is negligible. The observation regarding the side wall boundary layer

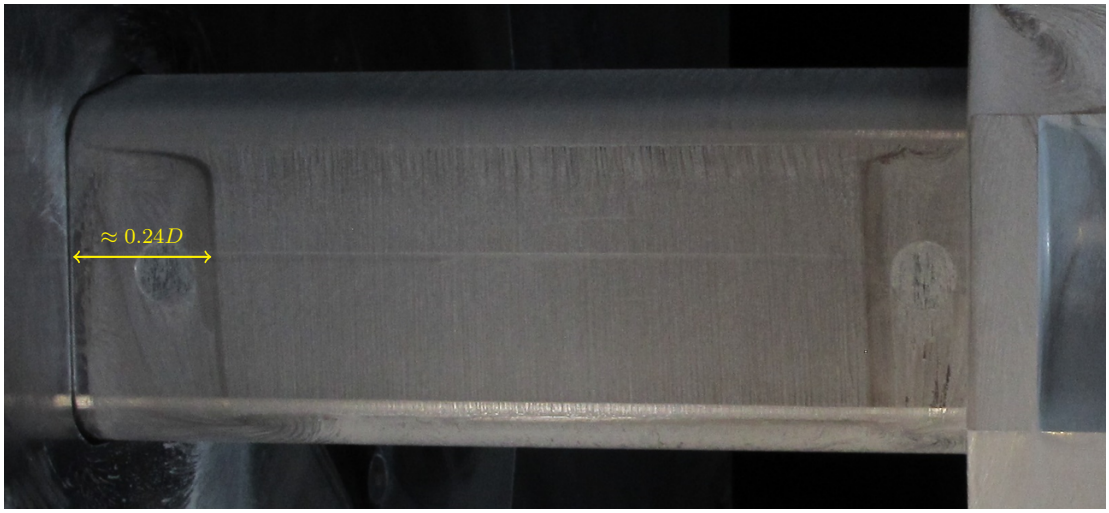

Figure 3.12: Surface-oil flow patterns from a stationary flow at $\phi = 45°$ and $Re = 10.46 \times 10^6$ at the lower part of the model adjacent to the tunnel wall.

height are in alignment with the observations by van Hinsberg et al. [92] who observed a boundary layer height at lower Reynolds numbers in the same wind tunnel of less than 6 cm. Regarding the uniformity of the free stream velocity profile, van Hinsberg et al. [92] showed that the relative dynamic pressure variation across the test section at the model position is below 0.3 %.

In table 3.3 the expanded uncertainties of the measured quantities based on a 95 % confidence level are summarized.

Table 3.3: Calculated uncertainties of the measured and derived quantities at a 95 % confidence level.

Quantity	Symbol	Form	Standard uncertainty
Inflow dynamic pressure	q_∞	rel	0.02 %
Inflow temperature	T_∞	abs	0.2 K
Inflow pressure	p_∞	rel	0.02 %
Reynolds number	Re	rel	7.3 %[1]
Wind incident angle	ϕ	abs	0.03°
Static surface pressure	p_s	rel	2.00 %
Static pressure coefficient	$c_{p,s}$	rel	2.00 %
Kulite surface pressure	p_k	rel	0.176 %
Kulite pressure coefficient	$c_{p,k}$	rel	0.180 %
Drag and lift coefficient	C_d and C_l	rel	0.5 %

[1] based on the velocity correction proposed by Allen and Vincenti [97] and not calculated via uncertainty propagation.

3.3 Numerical Methods

The relevant fundamentals regarding the numerical simulations in this study were introduced in section 2.3. In this section the details regarding the modeling assumptions, model domain, boundary conditions for each model and the applied turbulence models are presented. The limitations of the CFD model, which were encountered in parts of the simulations, are also discussed. This section is concluded with an uncertainty analysis of the quantities obtained by the CFD simulations, namely the surface pressure and the air return ratio in the open volumetric cavity receiver.

3.3.1 Computational Domain

The tower geometry, the size of the tower and the receiver design have already been presented in section 2.1.1. In the CFD models the upper 50 m of the tower have been included. This distance is safely sufficient to prevent the flow at the receiver from being influenced by an interaction with the bottom boundary patch.

In this work, two different CFD models regarding the wind incident angle, numerical domain and boundary conditions are used. The first model (SE-model) includes the whole tower with the purpose to investigate the flow interaction with the tower under a constant incident angle and the resulting pressure fluctuations at the receiver surfaces. Based on the evaluation of the weather data at the reference location in section 3.1 the model is designed for a south-eastern incident angle as this wind direction occurs most frequently. In the first model the irradiation, the receiver hot air and return air flow are not included which enables a direct comparison to the wind tunnel measurements in this work.

The second model (E-model) is designed for a case of a western incident angle (90.0°) and is mainly used to investigate the wind-influence on the receiver flow in the cavity design and also to include the receiver flow in the discussion on wind-induced pressure fluctuations. In order to model the receiver flow, the computational domain within the cavity has a much higher spatial resolution to capture the smaller scales of the receiver flow and to enable a finer surface discretization on the receiver. In order to maintain manageable computational costs, the geometry is simplified by a symmetry axis which is assumed along the east-western axis. Based on the surface oil flow visualization in the measurement the symmetry plane is placed along the stagnation line of the upper part of the tower as displayed in the lower part of fig. 3.13. In addition to the symmetry assumption the domain size has been slightly reduced.

The assumption of symmetry along the east-western axis of the receiver imposes an unphysical constraint on the resolved scales in parts of the flow which interact with the symmetry plane. It is argued though that the resolved turbulence is only of interest inside the receiver cavity and not in the wake of the tower whose physics are naturally altered by the symmetry plane. In the wake the eddies emerging from the flow separation at the tower are disturbed by the symmetry plane as on contact the normal component of the flow is set to zero to prevent flux through the symmetry plane hindering the natural movement and decay of vortices in the wake. It is argued that the symmetry plane is

able to yield comparable results within the receiver cavity as long as the symmetry plane is placed in the stagnation line of the tower and as long as the boundary layer at the wind facing part of the tower is able to emerge as without the symmetry plane.

In general, the numerical domain needs to be large enough to prevent unintended flow interference of the boundary conditions at the lateral boundaries with the flow around the bluff body. The upstream region needs to be large enough to ensure a developed inflow. The length of the downstream region needs to ensure a sufficient relaxation of the vortices arising from the bluff body in order to prevent back-flow at the outlet boundary.

In fig. 3.13, sketches of the numerical domain for both models are shown with the respective dimensions of the domain (given in multiples of the characteristic diameter D). In addition, the boundary patch names are displayed whose boundary conditions are presented in section 3.3.5.

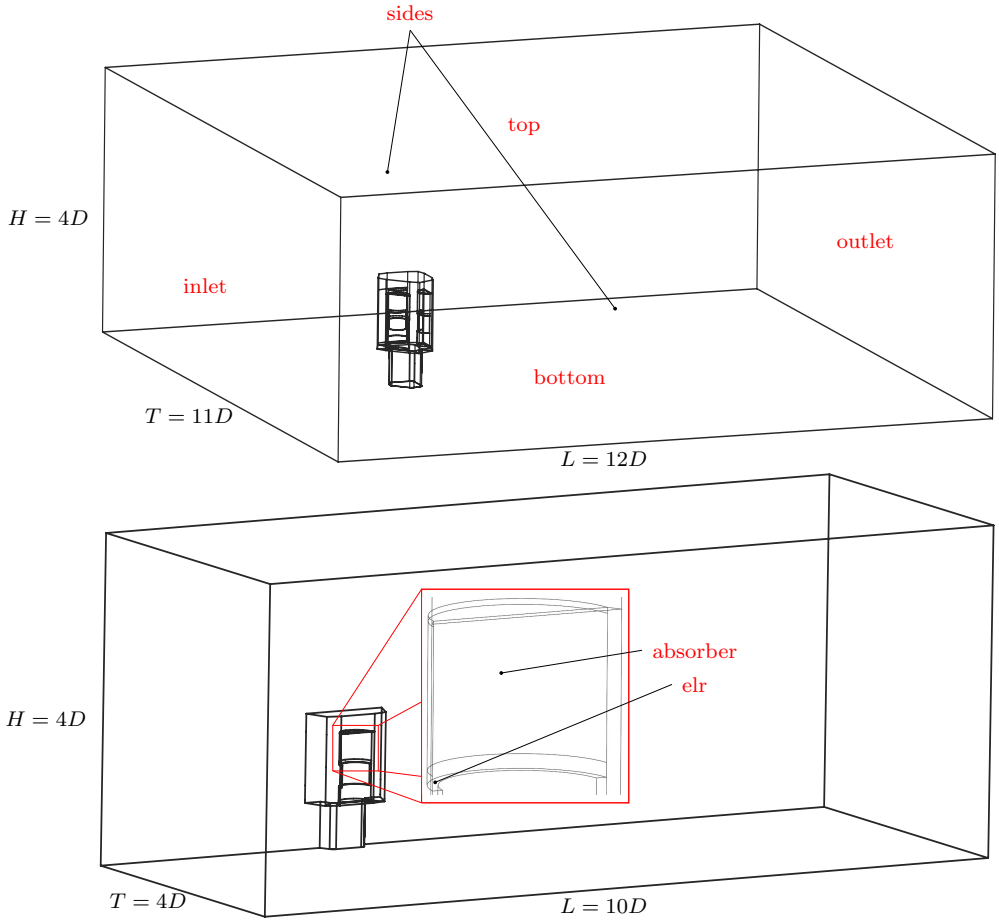

Figure 3.13: Model domains for the SE-Model (upper sketch) and the E-Model (lower sketch) with the domain sizes related to the characteristic tower diameter D. Additionally, the patch names are displayed in red.

As shown in fig. 3.13, for the SE-model a domain length of 12D (with around 3D in

the upstream and 9D in the downstream region), a domain width of 11D and height of 4D has been chosen.

For the E-model a shorter domain length of 10D has been chosen with an upstream region length of 3D and a downstream region length of 7D. Due to the symmetry, the domain width could be drastically reduced to 4D and the height of 4D has been chosen as within the SE-model. Also, it must be mentioned that the characteristic width of the tower in the E-model is smaller compared to the SE-model, but the characteristic diameter D of the whole tower has been chosen here for consistency and comparability.

Based on the projected surface area, the blockage factor in the measurement corresponds to 16.6 % and in the SE-model to 2.5 %. Due to the symmetry assumption, the blockage factor in the E-model is further reduced to 0.9 %.

3.3.2 Mesh and Resolution

The numerical grids have been created with a block-structured hexahedral meshing approach in ICEM CFD 2020R (cf. [99]) where the blocks are fitted to the geometry of the tower.

In fig. 3.14 the surface mesh of the southern cavity and a slice through the internal mesh is shown exemplary for the SE-model. For clarity only every second node of the mesh is visualized. In the left part of fig. 3.14 the surface mesh of the tower from a southern view is displayed. The boundary layer mesh is wrapped around the tower as can be seen in the right part of fig. 3.14, where a slice normal to the southern receiver (along the south-northern axis) is shown. This approach prevents highly anisotropic cells in the boundary layer from propagating into the area of the computational domain in which the LES mode is applied.

The SE-model, which includes the whole tower, contains $\approx$ 192 million elements with a surface resolution of $\leq$ 10 cm. The detailed cavity model (E-model) contains $\approx$ 258 million elements due to the higher density within the cavity and the finer surface resolution of $\leq$ 5 cm. The computational grid of the E-model is created based on the same blocking topology as the SE-model mesh with the same boundary layer treatment.

In LES the mesh resolution plays a key role as it limits which part of the turbulent spectrum is directly resolved and which part is modeled by the subgrid scale model (cf. section 2.3.3). For the DES model used in this work this is even more relevant as an implicit filtering based on the grid size is applied in the LES regions of the domain (cf. section 3.3.4).

In general, a certain amount of cells are necessary to resolve turbulent motion like eddies. Subsequently smaller grid spacing is required to resolve smaller eddies, which equate to smaller scales of turbulence being resolved. Following the concept of the energy cascade (as presented in section 2.3.3) the large scale turbulent kinetic energy has an anisotropic and flow dependent form, whereas at smaller scales turbulence is more homogeneous and isentropic, which makes it easier to model. It must be ensured that turbulence scales are resolved which lie within the inertial subrange and in general as much of the turbulent kinetic energy as possible should be resolved. Of course, the possibilities of mesh refinement are limited by the computational resources. In the

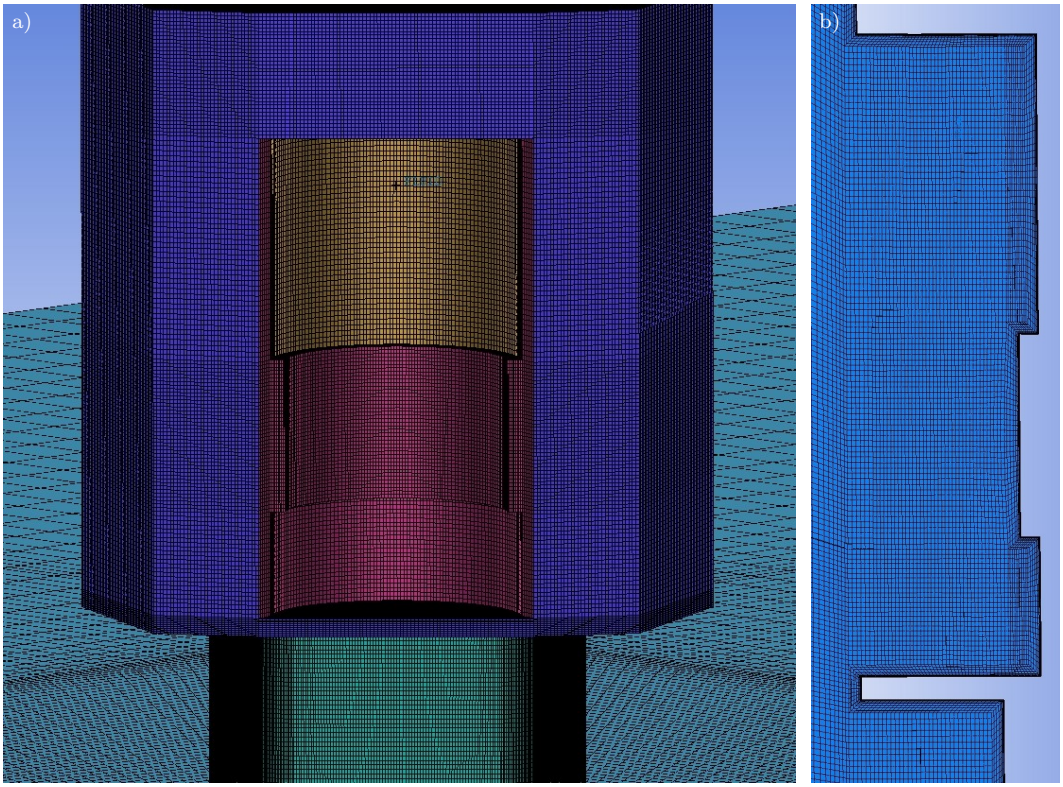

Figure 3.14: a) Surface mesh of the tower from a southern view point and b) A vertical slice of the internal mesh at the middle of the southern receiver in the wall normal direction. In both illustrations only every second node is visualized for clarity.

following paragraph an approach to estimate the required element size for scale resolving simulations is discussed. The approach is based on the integral length scale l_0 at which the peak in the energy spectrum occurs (cf. [63]). It is considered as the characteristic length of the largest, energy containing motions of turbulent flow. For a scale resolving simulation it is important to ensure a grid sizing in the region of interest which is small enough to resolve up to those eddy sizes which yield a certain amount of the turbulent kinetic energy in the spectrum. For LES it is recommended to resolve at least 80 % (cf. [63]) of the energy spectrum which is estimated to be the case for 5 cells across the integral length scales (cf. [100]).

In order to analyze this, the integral length scale l_0 is related to the local grid sizing Δ. According to Mockett [19] or Pope [63] the integral length scale can be determined by eq. (3.13) with the turbulent kinetic energy k and the rate of dissipation of turbulent kinetic energy ϵ based on dimensional analysis.

$$l_0 = \frac{k^{1.5}}{\epsilon} \tag{3.13}$$

In fig. 3.15 the ratio of the integral length scale l_0 to the local grid sizing Δ is visualized on a horizontal slice at the receiver center height.

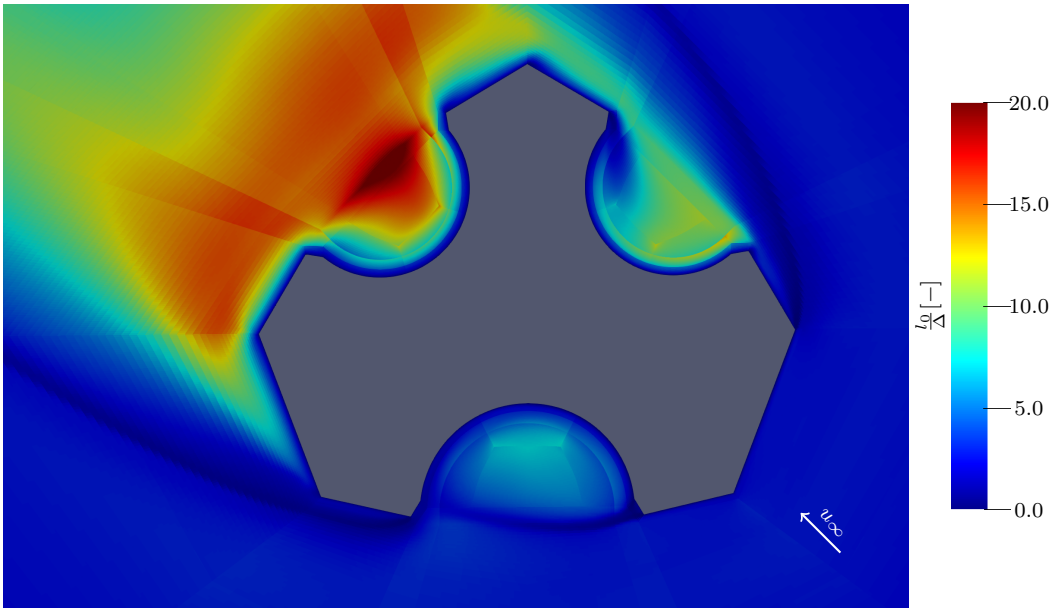

Figure 3.15: Integral length scale to grid size ratio $\frac{l_0}{\Delta}$ calculated by a precursor RANS simulation for the SE-model at 4 $\frac{\text{m}}{\text{s}}$ wind.

Due to the size of the problem and the structured meshing approach the achievable minimal cell size is limited by the computational resources. Within the model a uniform grid sizing has been chosen at each cavity due to the structured meshing approach but as fig. 3.15 reveals a variable grid sizing in each cavity is desirable as the integral length scale varies between the cavities. In the north-western cavity, which is in the wake for the given incident angle, the grid spacing allows for up to 21 cells across the local integral length scale. In the north-eastern cavity, which is under parallel flow, the integral length scale ratio varies between values of 9 to 11 in the windward side of the cavity and lesser values of 2 to 4 in the leeward side of the cavity, where the separated flow partially enters the cavity. In the southern cavity $\frac{l_0}{\Delta}$ varies between values of 2 to 7. From the evaluation of the integral length scale it can be concluded that due to the size of the problem and the limitations in computational resources the grid resolution of the model is rather coarse for an LES in the southern cavity, parts of the north-eastern cavity and especially in the areas where the boundary layer separates, which has to be considered in the evaluation of the results in section 4.2.

Another important aspect is the treatment of the boundary layer mesh at the walls and especially the wall normal distance of the first cell layer. As discussed in section 2.3.4, the normal wall distance of the mesh prescribes the treatment of the boundary conditions that can be applied, as will be presented in section 3.3.5. In the mesh generation a growth rate of around 1.1 was applied in the boundary layer mesh with an average non-

dimensional wall distance y_+ of approximately 5 ranging from 0.2 to values of 31 based on the precursor RANS simulation for the 4 $\frac{\mathrm{m}}{\mathrm{s}}$ case with the SE-model. For the 14 $\frac{\mathrm{m}}{\mathrm{s}}$ the mesh was adjusted to the higher wind speed with average y_+ values of approximately 4 ranging from 0.2 to 21, also based on the results by the precursor RANS simulation. Within the receiver cavities the y_+ values for both cases are well below 9.

In section 3.3.5 the basic concepts of boundary layer modeling have been described and in this work a wall function for the eddy viscosity ν_t is applied. In OpenFOAM a variety of wall functions are implemented (cf. [101]) and in this work a wall function is used, which is based on the work by Popovac and Hanjalic [102]. The wall function uses a blending scheme which removes the strict requirements on the positioning of the first wall boundary layer cell as discussed in section 2.3.4, which is very convenient as it ensures the applicability of the wall function in the whole domain. Especially in flows around complex bodies, it can be difficult to ensure the positioning of the first node within a specific part of the boundary layer as the local flow conditions vary along the complex surface. As presented above, the non-dimensional wall distance y_+ varies along the body and it is not ensured to be within the viscous sublayer at all faces of the body. In the applied wall function the eddy viscosity is blended between the viscous sublayer and logarithmic layer by a binomial function according to eq. (3.14)

$$\nu_t = ((\nu_{t,vis})^n + (\nu_{t,log})^n)^{(1/n)} \tag{3.14}$$

with the binomial blending exponent n and $\nu_{t,vis} = 0$ in the viscous sublayer, as the viscous forces outweigh the inertial forces in that region. The eddy viscosity in the logarithmic layer is calculated by

$$\nu_{t,log} = \nu_w \left(\frac{y_+ \kappa}{ln(E y_+)} - 1 \right) \tag{3.15}$$

with the von Kármán constant $\kappa = 0.41$ and the roughness parameter E set to 9.81.

The wall function by Popovac and Hanjalic [102] has proven to reproduce great agreement on several cases compared to experimental results and is deemed to be especially suitable for flow simulations in complex configurations like in this study.

3.3.3 Discretization and Solution Method

As described in section 2.3.2 the underlying set of partial differential equations (cf. section 2.3.1) is discretized with the finite volume method to yield a set of algebraic equations for each volume. As the equations are not independent from one another, an iterative solution method is necessary. To solve the equations, the open source CFD tool OpenFOAM version 6 [103] is used. For the iterative solution of the stationary simulations the SIMPLE algorithm (Semi Implicit Method for Pressure Linked Equations) is applied, which was introduced by Patankar and Spalding [104] and is for example described in detail in Versteeg and Malalasekera [79]. In brevity the SIMPLE algorithm assumes an initial pressure field and velocity field obtained from previous iterations or user defined initial values. With those fields the discretized momentum equations are

solved to obtained a prediction of the intermediate velocity field. After that a pressure correction equation is constructed to obtain the deviation in the pressure field based on the intermediate velocity. The pressure field is then updated while applying the user-prescribed under-relaxation (c.f. explanation below). Based on the new pressure field, the velocity field is corrected to obey the continuity equation. Those steps are repeated in an iterative manner until the deviations between the initial and corrected quantities reach the convergence criterion.

For the transient simulations the PIMPLE algorithm is used which combines the aforementioned SIMPLE algorithm and the PISO algorithm which stands for Pressure Implicit with Splitting of Operator and was introduced by Issa [105]. Within the PIMPLE algorithm the SIMPLE algorithm is incorporated to achieve the steady state solution for each time step while applying under-relaxation within the internal iterations of each time step despite for the final iteration, which is solved without relaxation. When convergence within a time step with regards to the required residuals is achieved the algorithm marches on in time based on the prescribed time step.

In section 2.3.2 the concept of discretization was introduced. In the following part the schemes are presented which are used in the discretization step and displayed in detail in Appendix F. In OpenFOAM the discretization schemes can be prescribed independently for each flow quantity and term in the equation.

For the gradient terms in the set of equations presented in section 2.3.1 a linear Gaussian integration has been applied which is second order accurate.

For the convection terms in the equations different schemes have been applied depending on the flow quantity. For the convection of the velocity (e.g. in the momentum equation) a flux blending scheme is used which combines a non-dissipative central differencing and a linear-upwind scheme to stabilize the solution while maintaining second-order accuracy. The Linear-Upwind Stabilised Transport (LUST) scheme blends with the weight factors of 0.25 for the upwind and 0.75 for the linear discretization uniformly throughout the whole domain. The convection term of the return air concentration ξ_{elr} and ξ_{ilr}, the SA model eddy viscosity $\tilde{\nu}$, the kinetic energy term K and the enthalpy h are discretized with an upwind differencing scheme, which as described in section 2.3.2 is first order accurate. The convection terms of the remaining quantities are discretized with a central differencing scheme based on a linear interpolation which is second order accurate.

The Laplacian or diffusive terms are discretized in the same way for all flow quantities with a linear Gaussian scheme with a limiter to stabilize the solution.

In eq. (3.16) the method used in the discretization of the temporal derivatives is presented, which is commonly referred to as the backward scheme.

$$\frac{\partial \Phi}{\partial t} = \frac{\frac{3}{2}\Phi^{n+1} - 2\Phi^{n} + \frac{1}{2}\Phi^{n-1}}{\Delta t} \tag{3.16}$$

This scheme is implicit as it includes quantities at the future time step and is second order accurate.

As presented in section 2.3.2, the CFL number is a measure of the temporal resolution in relation to the spatial resolution. Based on the recommendations presented in

section 2.3.2, the CFL number in the DES is limited to $CFL \leq 1$ in the entire numerical domain. In fig. 3.16 the CFL number is evaluated in a horizontal plane at the middle of the receivers for the cases SE4 at the time step $t = 133.6\,\mathrm{s}$ and SE14 at the time step $t = 39.3\,\mathrm{s}$.

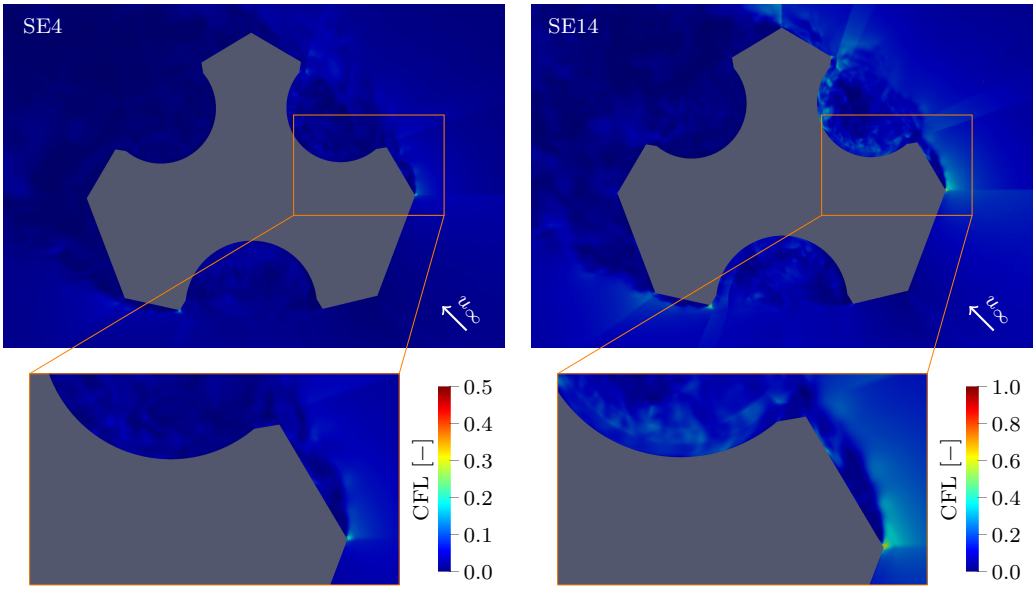

Figure 3.16: CFL number on horizontal cut planes at receiver center height evaluated for the DES cases: SE4 at $t = 133.6\,\mathrm{s}$ and SE14 at $t = 39.3\,\mathrm{s}$.

As visual in fig. 3.16 in the SE4 case (left) the CFL number is way below 0.2 in the areas of separated flows. The highest CFL numbers occur at the edge of the tower, where the flow separation takes place with values way below 0.4. In the SE14 case the CFL number in the cavity and the areas of separation in general are below 0.4 while the highest CFL number in the area of separation is around 0.6. Overall this gives confidence in the chosen time step to be small enough to yield time-step independent results with the DES of those cases.

In order to control the iterative solution process described above convergence criteria are necessary to determine when the iterative process can be stopped. Due to the discretization and the truncation errors in the discretization schemes (cf. [57]) the discretized equations are not exact and a residual term remains in the solution process. Within OpenFOAM a target residual for each quantity can be prescribed. In this work a target residual has been set for the pressure, velocity, air return ratios and the remaining quantities of 1×10^{-6}, 1×10^{-8}, 1×10^{-6} and 1×10^{-4} respectively. To assess the convergence of the solution the change in the quantities of interest is further evaluated. The residual alone does not ensure convergence as it is averaged over all grid points.

As mentioned in the description of the SIMPLE algorithm above, relaxation can be applied in order to speed-up or slow down the solution in iterative solvers. While a fast convergence is desirable, underrelaxation can avoid instabilities and subsequently

divergence in iterative solution methods. The basic idea is to limit the amount which a variable can change from one iteration to the next. Based on [106] the under-relaxation of a quantity Φ from an iteration or time step $n-1$ towards the next step n can be written as

$$\Phi^n = \Phi^{(n-1)} + \alpha_\Phi(\Phi^n - \Phi^{(n-1)}) \tag{3.17}$$

with the under-relaxation factor $0 \leq \alpha_\Phi \leq 1$. As eq. (3.17) shows, Φ^n becomes equal to Φ^{n-1} and the result satisfies the original discretized equation when the iteration converges. In the steady-state simulations in this study relaxation factors for p and u of 0.4 and 0.6 respectively are applied, whereas the other quantities are less under-relaxed with a factor of 0.8. In the transient simulation the same relaxation factors are applied on the internal iterations within each time step and the final iteration is calculated without relaxation.

3.3.4 Turbulence Modelling and Model Calibration

As introduced in section 2.3.3 for the stationary RANS simulations the SA-RANS model is used, whose full set of equations and model parameters can be found in Appendix D. For the transient DES in this study the SA-DDES model (cf. [35]) is used which is based on and poses a revision of the SA-DES model, that was introduced by Spalart et al. [30]. Compared to the SA-RANS model, it replaces the wall distance d in the destruction term in the transport equation for $\tilde{\nu}$ with the so-called DES-length scale $\tilde{d}$ which is defined as in eq. (3.18)

$$\tilde{d} \equiv min(d, C_{DES}\Delta) \tag{3.18}$$

with the filter width Δ and a model constant C_{DES}. This leads to a destruction term in the transport equation of $\tilde{\nu}$ in the form of

$$-c_{w1} f_w \left(\frac{\tilde{\nu}}{\tilde{d}}\right)^2 \tag{3.19}$$

with the model constants c_{w1} and function f_w as specified in Appendix D. The modification in the SA-RANS destruction term yields a model that still behaves as the SA-RANS model for $d << \Delta$. It can be shown that, when the production term balances the destruction term, the model simplifies to an effective Smagorinsky-type model as the SA-eddy viscosity then is proportional to the rate of strain tensor and the square of the filter width ($\tilde{\nu} \propto \mathbf{D}(\mathbf{u})\Delta^2$) just as the sub-grid scale turbulent viscosity in the Smagorinsky LES model (cf. [75] and eq. (2.26)). This makes it behave as an SGS model when $d >> \Delta$ which applies in the flow field far from the wall, where it switches to a LES-like formulation related to the filter width Δ (cf. [30]).

Due to the definition of the DES-length scale in the (D)DES model no explicit filtering and no additional SGS model is necessary but instead the discretization of the domain and the numerical dissipation serve as an implicit SGS model.

Different possibilities of defining the filter width Δ in eq. (3.18) exist (cf. [107]), which influence the transitional behavior between the RANS and LES mode. In this work the filter width is defined by the third root of the cell volume ($\Delta \equiv \sqrt[3]{V_c}$).

As discussed by Spalart et al. [35] the original formulation of the SA-DES model has difficulties with "modelled stress depletion" (MSD) (cf. [32] and [35]) due to an activation of the LES mode inside the boundary layer caused either by thick boundary layers or very fine grid spacing parallel to the wall. This can lead to an activation of the LES mode within the boundary, where the resolved stresses are under-predicted due to the lack of fluctuating components in the velocity field, which leads to an under-prediction of the skin friction. Ultimately this stress depletion can lead to a premature flow separation.

In order to prevent MSD, the DES length scale $\tilde{d}$ is adjusted according to eq. (3.20)

$$\tilde{d} \equiv d - f_d \, max(0, d - C_{DES}\Delta) \tag{3.20}$$

while setting the delay function f_d to 0 in order to yield RANS mode and setting f_d to 1 in order to yield LES mode (cf. eq. (3.18)). The definition of f_d along with the full set of closure coefficients and auxiliary relations is summarized in Appendix D.2. Essentially it introduces a parameter which relates the model length scale, which depends on the eddy-viscosity field, to the wall distance. With this adjustment the model can refuse the LES mode when f_d indicates that the corresponding grid point lies within a boundary layer, whereas the DES formulation is solely dependent on the grid.

The transition from RANS to LES mode is monitored within the simulations as demonstrated in fig. 3.17, where the simulation mode is visualized by a boolean flag ϵ wherein 1 denotes LES mode and 0 denotes RANS mode to ensure an appropriate switch in the model. The intermediate values between 0 and 1 in fig. 3.17 are caused by the interpolation on the cut plane. Within the separated flow region LES mode is active in the entire domain as intended. The thickness of the RANS mode zone at the tower wall varies depending on the location at the tower. At the inward side of the tower the RANS mode zone is the smallest with a rather uniform thickness of less than 0.02 m, while the thickness varies between 0.03 and 0.06 m within the cavities.

As presented in eq. (3.18), the SA-(D)DES model introduces C_{DES} as an adjustable model constant. As stated in Yan et al. [108] mathematical derivations of C_{DES} yield different results based on the approach that is used, which is why a numerical approach for the calibration is seen as essential. Therefore C_{DES} has been calibrated beforehand with simulations of the canonical case of decaying isotropic turbulence (DIT) in a cubical domain (cf. e.g. [32]). The case has been simulated with the SA-DDES model and the results have been compared to measurement data by Comte-Bellot and Corrsin [66] at different time steps of decay and to the results obtained with an LES model based on an eddy viscosity SGS model. The kinetic energy spectrum is evaluated at those time steps and the qualitative agreement of the SA-DES model with the measured kinetic energy spectrum was deemed to be sufficient with the value of 0.65 for C_{DES} which has been further used. The details on the simulation set up, boundary conditions and the visualization of the spectral results are shown in Appendix D.3.

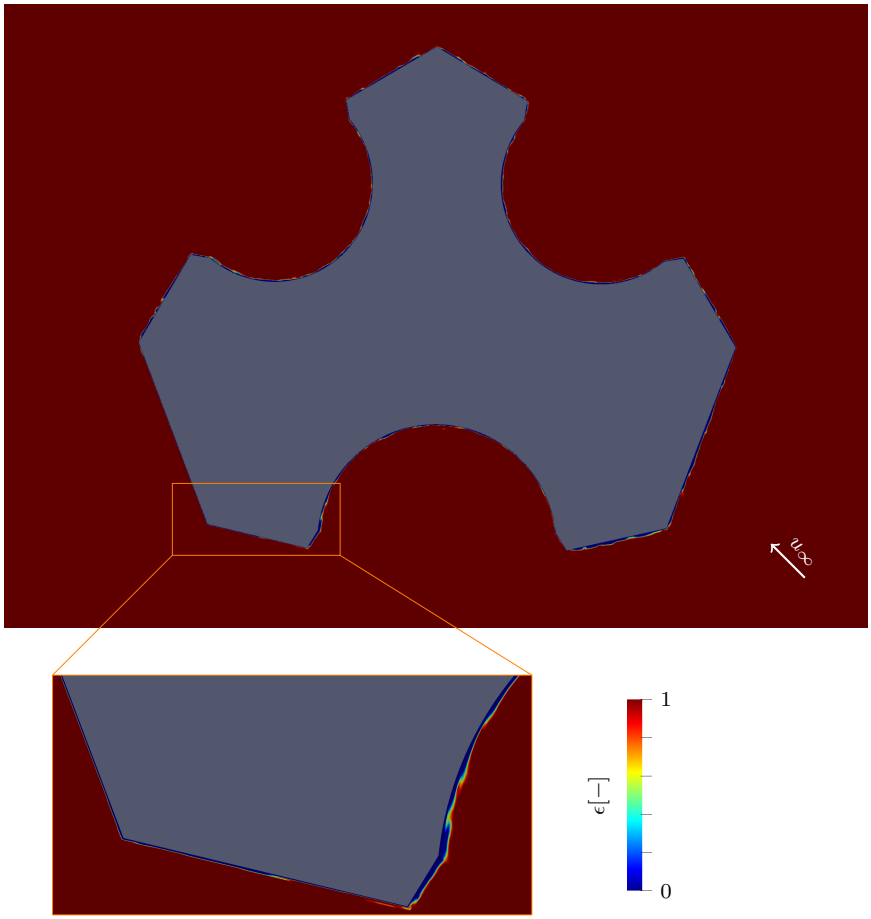

Figure 3.17: Exemplary evaluation of the turbulence model modes for the DES case with the SE-model at 4 $\frac{\text{m}}{\text{s}}$ wind speed at $t = 133.6\,\text{s}$. $\epsilon = 0$ denotes RANS mode while $\epsilon = 1$ denotes LES mode.

3.3.5 Boundary and Initial Conditions

In this section the boundary and initial conditions are presented for the SE-model, which includes the whole tower and the E-model, where only the southern cavity is included. Due to the different approaches depending on whether the receiver flow is considered or not, the boundary conditions will be presented separately. The simulations, where the receiver flow is not considered, were conducted with ambient wind, whereas the simulations where the receiver flow is considered, were conducted with and without the influence of ambient wind.

Boundary Conditions for the Incompressible Cases

As presented in section 2.3.1 the governing equations simplify significantly when incompressible flow is assumed. Furthermore, the amount of variables that need to be prescribed at the domain boundaries reduce to the static pressure p, the velocity vector $\mathbf{u}$, the SA-eddy viscosity $\tilde{\nu}$ and the eddy viscosity ν_t. The models used to determine the thermophysical properties, namely the density ρ, dynamic viscosity μ and specific heat capacity c_p are based on tabulated data of dry air [109] and are summarized in Appendix E.

Regarding the pressure, at the ambient inlet a Neumann boundary condition with a zero gradient is assigned while at the outlet a Dirichlet boundary condition for the total pressure p_{tot} is assigned and the static pressure p is then calculated via eq. (3.21).

$$p = p_{tot} - \frac{1}{2}\rho|\mathbf{u}|^2 \tag{3.21}$$

The lateral ambient patches are treated as symmetry patches for each variable. In this model without the consideration of the receiver and return air flow the whole tower is modeled as a wall and consequently a Neumann pressure boundary condition with a zero gradient is assigned on the whole tower.

Regarding the velocity vector $\mathbf{u}$, at the ambient inlet a uniform free stream velocity u_∞ is prescribed for each case as this poses a realistic assumption for the comparison to the wind tunnel experiment. It was decided not to apply a logarithmic velocity profile at the inlet because the relative difference in velocity along the receiver height under the assumption of a logarithmic profile accounts for less than 1.07 %. The low deviation is caused by the velocity gradient in the log-profile which flattens considerably with height. If the receiver is placed at a lower height, this assumption would cause a larger error. At the outlet a mixed condition is applied, that treats outflow as a Neumann velocity boundary condition with a zero gradient while for potential back flow into the domain a velocity calculated from the bounding cell value in the patch-normal direction is prescribed. This allows the treatment of back flow, which in practice does not occur due to the size of the downstream domain. At the tower surface a no-slip velocity boundary condition is prescribed.

For the SA-eddy viscosity $\tilde{\nu}$ a fixed value at the inlet is prescribed while on the tower walls a fixed value of zero is applied (according to the recommendations by Spalart and Allmaras [70]). At the inlet a free stream value of around $\tilde{\nu}_\infty = 3\nu$ was chosen based on the recommendation by Spalart and Allmaras [70] and Allmaras et al. [110]. But as discussed in Spalart and Allmaras [70] the turbulence model is insensitive to the free stream value, "provided that they are much smaller than the values in the turbulent region". At the outlet a mixed condition in analogy to the velocity boundary condition is prescribed.

For the eddy viscosity ν_t the tower walls are treated with a wall function called nutUWallFunction which is based on the proposal by Popovac and Hanjalic [102]. The wall function blends between an integration to the wall and a generalized wall function which makes it especially applicable in the case. Due to the complex flow situation y_+

varies between values corresponding to the buffer and logarithmic layer, which makes the usage of a conventional wall function unappealing (as discussed in section 2.3.4). At the ambient in- and outlet ν_t is calculated by the turbulence model via eq. (D.5).

To conclude, the set of boundary conditions used for the incompressible cases is summarized in table 3.4.

Table 3.4: Boundary conditions applied in the incompressible simulations without the consideration of the receiver operation (SE-model).

patch	p	$\mathbf{u}$	$\tilde{\nu}$	ν_t
ambient inlet	$\frac{\partial p}{\partial n} = 0$	$\mathbf{u} = \mathbf{u}_\infty$	$\tilde{\nu} = \tilde{\nu}_\infty$	calculated
ambient outlet	$p_{tot} = p_\infty$	$\frac{\partial \mathbf{u}}{\partial n} = 0$	$\frac{\partial \tilde{\nu}}{\partial n} = 0$	calculated
ambient sides	symmetry	symmetry	symmetry	symmetry
tower walls	$\frac{\partial p}{\partial n} = 0$	$\mathbf{u} = 0$	$\tilde{\nu} = 0$	$\nu_t = f(\mathbf{u}, y_+, ...)$

Boundary Conditions for the Compressible Cases

For the cases where the irradiation, the receiver flow and return air flow are considered, the compressible Navier Stokes equations are solved. Therefore, the set of variables in addition to the static pressure p, the velocity vector $\mathbf{u}$, the SA-eddy viscosity $\tilde{\nu}$ and the eddy viscosity ν_t further include the temperature T and the return air concentration ξ. Consequently, the tower is now not treated as a wall at the receiver patch and the patch where the external return air enters the domain.

With this model, transient DES and stationary RANS simulations have been conducted to simulate the impact of ambient wind on the receiver. In the context of the investigation of different external return air distributions and their impact on the convective losses, simulations under windless conditions have been conducted as well as a reference (cf. section 4.2.4).

At first, the boundary conditions for the ambient patches are described. In the compressible cases the hydrostatic pressure contribution cannot be neglected. In OpenFOAM the static pressure p is substituted by the modified pressure p_{rgh} in the momentum equation, which is defined as in eq. (3.22).

$$p_{rgh} = p - \rho(\mathbf{gh}) \tag{3.22}$$

The static pressure p is then calculated from the modified pressure p_{rgh}. For the cases under windless conditions the total pressure $p_{rgh,tot}$ is prescribed at each ambient patch. For the simulations under wind, the lateral ambient patches are treated with a symmetry condition for all variables. At the ambient inlet a Neumann pressure boundary condition with a zero gradient is assigned while at the outlet the total pressure is prescribed as in the cases under windless conditions.

For the cases under wind the boundary conditions for the velocity vector $\mathbf{u}$, the SA-eddy viscosity $\tilde{\nu}$ and the eddy viscosity ν_t are defined in the same way as in the incompressible cases. For the windless cases the velocity at each ambient patch is defined by a mixed condition that treats outflow as a Neumann velocity boundary condition with a zero gradient, while for inflow the velocity is calculated from the bounding cell value in the patch-normal direction. For the SA-eddy viscosity $\tilde{\nu}$ a mixed condition is applied on the ambient patches that sets the inflow value to $\tilde{\nu}_\infty$ and prescribes a zero gradient Neumann condition for potential outflow. The eddy viscosity ν_t is calculated by the turbulence model at each ambient patch under windless conditions.

At the ambient patches a free stream temperature of $T_\infty = 298.15\,\mathrm{K}$ is defined, which is used as a Dirichlet condition on the ambient inlet patch for the cases under wind. At the outlet in analogy to the velocity condition a mixed condition is applied, which assigns a zero gradient for outflow and a fixed inlet value of T_∞ for inflow. For the cases under windless conditions this mixed boundary conditions is applied on all ambient patches.

The return air concentration as a passive scalar is numerically treated in the same way as the temperature with a free stream value of $\xi_\infty = 0$.

The boundary conditions on those parts of the tower that are still modeled as walls are defined identically to the incompressible cases for p_{rgh} (in analogy to p), $\mathbf{u}$, $\tilde{\nu}$ and ν_t. The additional variables T and ξ are treated with Neumann boundary conditions with a zero gradient.

In the following part the boundary conditions regarding the receiver and the part of the tower where the external return air enters the domain are described. These boundary conditions are adopted from Schwager et al. [17] and were also published and validated with experimental data of the return air ratio at the STJ in Stadler et al. [49]. To this date, the boundary conditions whave only been used in windless conditions as in Schwarzbözl et al. [48] where the efficiency of a similar cavity shaped receiver is numerically investigated.

In this modeling approach the receiver is treated as a continuous cylindrical patch instead of resolving the actual geometry of the absorber modules and return air channels. This simplification allows to overcome the difference in scales between the porous receiver structure and the size of the numerical domain and enables a simulation of large-scale open volumetric receivers.

In order to model the hot air, which enters the receiver and the return air, which in the real geometry, is returned in the gaps between the HiTRec cups, the receiver patch has to be divided into cells for each flow direction. Furthermore, boundary conditions that represent the respective behavior need to be implemented. The division into hot and return air cells is based on the agglomerate approach presented in Stadler et al. [49]. An algorithm is implemented, which divides the surface mesh on the receiver patch into n_r agglomerates in the circumferential direction and n_z agglomerates in the vertical direction. For each agglomerate, starting in the middle, cells are added to the set of return air cells until the prescribed area ratio between return and hot air is reached in an iterative matter. The area ratio is chosen to match the area ratio in the actual receiver geometry to ensure comparability in the hot and return air velocities between the modeled and actual geometry. In fig. 3.18 the resulting distribution of return air

cells (colored in black) and hot air cells (colored in grey) is shown for the model in this study. In addition, on the left side of fig. 3.18 the outflow of the internal and external return air is visualized with a glyph representation colored in the outflow velocity. As

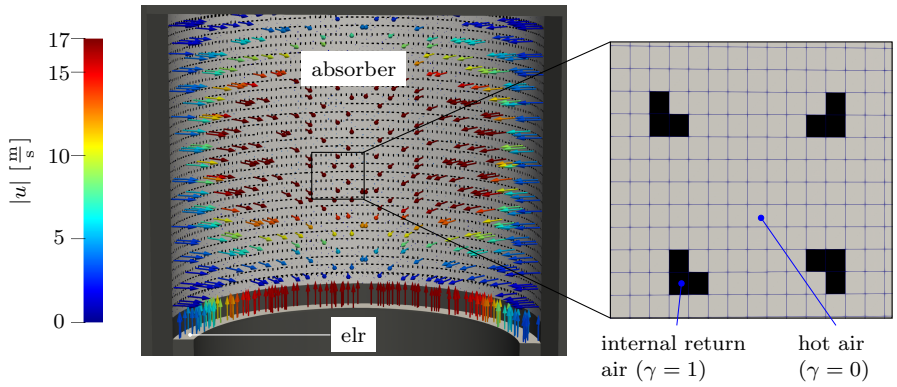

Figure 3.18: Distribution of return air cells (colored in black) and hot air cells (colored in grey) at the southern receiver. On the left side, the flow paths of the return air through the internal and external air return are visualized in a glyph representation colored in the outflow velocity.

shown in Stadler et al. [49] the number of agglomerates influences the calculated air return ratio and the efficiency, which tend to increase with the amount of agglomerates. Therefore, the number of agglomerates and its influence on the results will be discussed in the uncertainty analysis in section 3.3.7.

The receiver design point (as discussed in section 2.1.1) is defined with a hot air target temperature of 670 °C at a total intercept of 125 MW. As the numerical domain ends at the outer receiver surface, the hot air temperature calculated by the model corresponds to the inlet temperature of the absorber modules. Therefore, in order to estimate and establish the target temperature, the boundary condition needs to be able to calculate the hot air temperature after the heat exchange in the open volumetric structure which is not part of the CFD model. Also, the return air temperature is determined by the receiver type and its heat exchange between the hot and return air stream. In order to calculate the hot air temperature after the receiver and the return air temperature entering the CFD domain, a characteristic map of the absorber modules is used. It is based on a 1D model developed by Ahlbrink et al. [111] where the heat transfer within the absorber module is modeled in detail for a variety of input parameters. Under stationary conditions the model calculates the return air temperature as it leaves the absorber and the hot air temperature after the heat exchange in the model as a function of the hot and return air mass flows, the intercepted irradiation $\dot{Q}_{inc}$, the return air temperature as it enters the absorber (which is prescribed by the heat exchanger) and the hot air temperature on the patch. Based on these parameters the respective return air temperature which is included in the temperature boundary condition and the hot air temperature leaving the porous structure are calculated for each agglomerate. As new

receiver structures with different heat transfer characteristics are developed (cf. [13]) the characteristic map can be exchanged within the model.

As mentioned in section 2.1.1 the intercept of concentrated radiation at the receiver surface has been calculated with the raytracing software STRAL and is used in the boundary conditions of the receiver as a tabular input. The irradiation is interpolated on the receiver surface mesh in the preprocessing and assumed constant during the simulations. The mass flow through the absorber is prescribed by the pressure difference between the ambient air and the fan pressure. The mass flow distribution across the receiver is established via orifices with different diameters that represent the dominating pressure loss in the absorber module. This distribution is adapted to the distribution of the irradiation with an optimization method by Ahlbrink et al. [112], which is solely used as an input in this study.

In the CFD model the mass flow distribution is realized by introducing pressure loss coefficients in the hot air ζ_h and return air path ζ_r. As the orifice is the dominant pressure loss, a second-order dependency between the mass flow and pressure is assumed, leading to the velocity boundary condition at the receiver in eq. (3.23).

$$\mathbf{U} = \mathbf{n}\left(\sqrt{\frac{p_p - p_{fan,h}}{\zeta_h \frac{\rho_p}{2}}}(1-\gamma) + \sqrt{\frac{p_{fan,r} - p_p}{\zeta_r \frac{\rho_r}{2}}}\gamma\right) \tag{3.23}$$

The distinction between return and hot air cells at the receiver is made by the γ field which equals $\gamma = 0$ for the hot air cells and $\gamma = 1$ for the return air cells. For the hot air path the density at the patch ρ_p is used whereas for the return air path the density ρ_r at return air temperature $T_{r,out}$ is used. Herein an artificial fan pressure is introduced for each flow path that determines the mass flow and velocity respectively.

In fig. 3.19 the interpolated intercept and mass flow distribution at the design point hot air outlet temperature of 670.0 °C is shown as calculated by the predecessor simulation without ambient wind. As visual in fig. 3.19 the intercept varies significantly across the

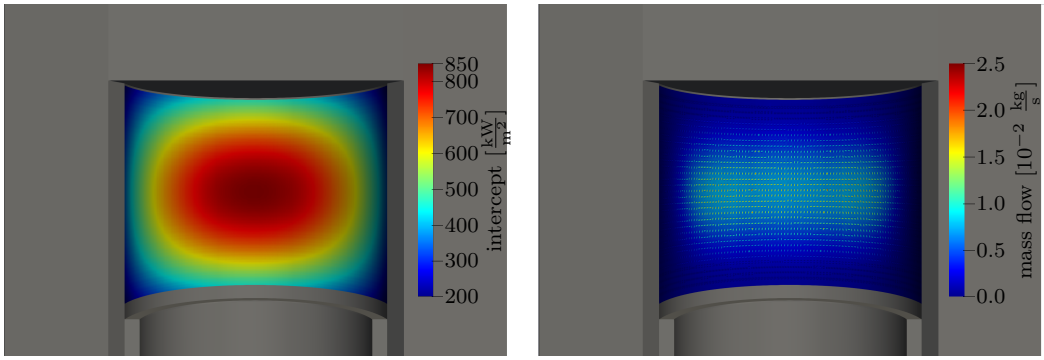

Figure 3.19: Design point irradiation and mass flow distribution at the main receiver.

receiver with peak values of around 1000 $\frac{\mathrm{kW}}{\mathrm{m}^2}$ at the center. The mass flow distribution is designed to follow the intercept distribution qualitatively.

For the temperature boundary condition at the receiver the distinction between hot and return air cells is also made by the γ field. For hot air cells a Neumann condition with a zero gradient is applied which sets the outlet temperature to the internal cell value T_p while the return air temperature is determined by the characteristic map mentioned above and the calculated temperature is prescribed as the fixed value $T_{r,out}$. This gives a formulation of the temperature boundary condition as in eq. (3.24).

$$T = T_p(1-\gamma) + T_{r,out}\gamma \tag{3.24}$$

As for the receiver temperature, for the remaining variables at the receiver mixed conditions are applied due to the occurrence of opposite flow directions at the receiver boundary. For the modified pressure p_{rgh} a Neumann boundary condition is applied which sets the pressure gradient to the provided value such that the flux on the boundary matches that specified by the velocity boundary condition (cf. fixedFluxPressure in [103]). For the SA-eddy viscosity $\tilde{\nu}$ a mixed condition is applied that prescribes a fixed value for the return air entering the domain with a value of $\tilde{\nu}_r = 3\nu(T_{r,out})$ and a Neumann zero gradient condition on the hot air cells. The eddy viscosity ν_t at the receiver boundary is calculated by the turbulence model. For the return air concentration ξ a mixed condition is applied that sets a fixed value of $\xi = 1$ at the return air cells which corresponds to a concentration of 100 %. At the hot air cells a Neumann zero gradient boundary condition is applied for the air return ratio.

In addition to the internal air return, the receiver concept contains the possibility of an external air return quantified by the factor elr, which is defined as the ratio of the mass flow which is returned externally in relation to the total hot air mass flow. According to this definition the mass flow which is returned internally $\dot{m}_{ilr}$ and externally $\dot{m}_{elr}$ are defined as

$$\begin{aligned} \dot{m}_{ilr} &= (1-elr)\dot{m}_h \\ \dot{m}_{elr} &= (elr)\dot{m}_h \end{aligned} \tag{3.25}$$

At design point conditions an equal distribution of $elr = 0.5$ is prescribed, but the boundary condition allows for altered distributions. The velocity at the elr boundary patch is treated with a fixed value condition based on the prescribed mass flow. For the temperature, SA-eddy viscosity $\tilde{\nu}$ and ξ boundary condition fixed value conditions with $T_{elr} = T_{r,in}$, $\tilde{\nu}_{elr} = 3\nu(T_{r,in})$ and $\xi_{elr} = 1$ are prescribed respectively. The eddy viscosity ν_t is calculated by the turbulence model and the pressure is treated with a Neumann zero gradient condition. The outlet temperature of the externally returned air here corresponds to the temperature of the internally returned air before it enters the absorber module $T_{r,in}$.

With the receiver boundary conditions presented above, a predecessor simulation is conducted with a stationary RANS approach under windless conditions to establish the nominal design point distribution of all relevant variables. For this simulation the target hot air temperature is established by adjusting the fan pressures $p_{fan,r}$ and $p_{fan,h}$ in eq. (3.23) with a PI controller. The hot air fan pressure $p_{fan,h}$ is controlled to achieve the set hot air temperature $T_{h,set}$ under the given irradiation while the return air fan pressure $p_{fan,r}$ is controlled to match the given set return air mass flow $\dot{m}_{ilr,set}$. The

PI controller is fed with the averaged hot air temperature $\overline{T_{h,out}}$, which is obtained by a mass flow weighted average of the hot air outlet temperatures $T_{h,out}$ obtained by the characteristic map of the absorber for each cell as in eq. (3.26).

$$\overline{T_{h,out}} = \frac{\int_i T_{h,out}\dot{m}_i(1-\gamma)}{\int_i \dot{m}_i(1-\gamma)} \tag{3.26}$$

The deviation from the set point is defined as in eq. (3.27)

$$\begin{aligned} \sigma_h &= 0.975\sigma_h + \left(\overline{T_{h,out}} - T_{h,set}\right) \\ \sigma_r &= 0.975\sigma_r + \left(\dot{m}_{ilr} - \dot{m}_{ilr,set}\right) \end{aligned} \tag{3.27}$$

with the current internal return air mass flow $\dot{m}_{ilr}$ defined as the sum over all return air cells on the absorber patch. With the given deviation from the set points the fan pressures are further adjusted according to the PI controller as defined in eq. (3.28).

$$\begin{aligned} p_{fan,h} &= p_{fan,h}\left(1 - K_p\left(\frac{\sigma_h}{t_n T_{h,set}} + \left(\frac{\overline{T_{h,out}}}{T_{h,set}} - 1\right)\right)\right) \\ p_{fan,r} &= p_{fan,r}\left(1 - K_p\left(\frac{\sigma_r}{t_n \dot{m}_{ilr,set}} + \left(\frac{\dot{m}_{ilr}}{\dot{m}_{r,set}} - 1\right)\right)\right) \end{aligned} \tag{3.28}$$

With the controller parameters set to $K_p = 0.001$ and $t_n = 40$ the stationary design hot air temperature $T_{h,out}$ can be set with a very high accuracy for windless conditions (deviation from the set value of less than 0.1 K).

To conclude this section, the set of boundary conditions applied in the compressible cases without consideration of wind are summarized in table 3.5.

Table 3.5: Boundary conditions applied in the compressible simulations without the consideration of ambient wind (E-model).

patch	p_{rgh}	$\mathbf{u}$	$\tilde{\nu}$	ν_t	T	ξ
ambient patches	$p_{rgh,tot} = p_\infty$	$in: \mathbf{u} = n\mathbf{u}_i$ $out: \frac{\partial \mathbf{u}}{\partial n} = 0$	$in: \tilde{\nu} = \tilde{\nu}_\infty$ $out: \frac{\partial \tilde{\nu}}{\partial n} = 0$	calculated	$in: T = T_\infty$ $out: \frac{\partial T}{\partial n} = 0$	$in: \xi = 0$ $out: \frac{\partial \xi}{\partial n} = 0$
tower walls	$\frac{\partial p_{rgh}}{\partial n} = 0$	$\mathbf{u} = 0$	$\tilde{\nu} = 0$	$\nu_t = f(\mathbf{u}, y_+, ...)$	$\frac{\partial T}{\partial n} = 0$	$\frac{\partial \xi}{\partial n} = 0$
receiver	$\frac{\partial p_{rgh}}{\partial n} = f(\mathbf{u})$	$\mathbf{u} = \mathbf{u}(\rho, p_p, p_{fan}, \zeta)$	$in: \tilde{\nu} = \tilde{\nu}_{absorber}$ $out: \frac{\partial \tilde{\nu}}{\partial n} = 0$	calculated	$in: T = T_{ilr,out}$ $out: \frac{\partial T}{\partial n} = 0$	$in: \xi = 1$ $out: \frac{\partial \xi}{\partial n} = 0$
elr	$\frac{\partial p_{rgh}}{\partial n} = f(\mathbf{u})$	$\mathbf{u} = \mathbf{u}(\dot{m}_{elr})$	$\tilde{\nu} = \tilde{\nu}_{elr}$	calculated	$T = T_{ilr,in}$	$\xi = 1$

In table 3.6 the boundary conditions described above are summed up for the compressible cases when ambient wind is considered. During the simulations with wind the temperature-controller is not used in order to investigate the influence on a non-controlled system rather than evaluating the controller which was only designed to establish the target state without external interference in a steady state simulation.

For the simulations under wind a simplification was made with respect to the receiver velocity and temperature boundary conditions. The pressure-linked velocity boundary

condition in eq. (3.23) has shown to yield numerical unstable behavior under the consideration of wind regarding the pressure field inside the domain. The numerical instabilities in the form of pressure waves with amplitudes exceeding physical bounds are presumed to be caused by the initial transients which remain present inside the domain even after comparatively long simulation times.

Therefore, a simplification was made for the simulations under wind regarding the receiver boundary condition, where the volumetric flow rate is held constant based on the reference distribution calculated under windless conditions. Based on the experimental evaluation of the pressure fluctuations under constant incident angles (cf. fig. 4.2) this assumption poses a relatively small error, as the pressure drop in the air system of the receiver is atleast one order of magnitude larger than local fluctuations in the surface pressure which are expected under constant incident angle wind at the investigated wind speeds. For example based on the experimental results at the wind speed of 4 $\frac{\mathrm{m}}{\mathrm{s}}$ pressure RMS values of $\leq 2\,\mathrm{Pa}$ are to be expected at a lateral incident angle (cf. fig. 4.2). Based on the absorber boundary condition in eq. (3.23) the receiver inlet velocity only varies by 0.14 % when a change in the ambient pressure of 2 Pa is assumed which underlines the validity of the simplification as the error in the receiver velocity is negligible.

The simplification in the receiver boundary condition effectively reduced the numerical pressure fluctuations and, as evaluated in section 3.3.6, the presence of the symmetry plane along the east-western axis of the tower is presumed to at least cause the persistence of those fluctuations. The temperature boundary condition at the receiver has been simplified in the sense that the 1D-absorber model by Ahlbrink et al. [111] is no longer implemented to calculate the return air outlet temperature and instead the temperature distribution on the absorber outlet faces is assumed constant (based on the predecessor reference simulation under windless conditions) which drastically reduces the computational time.

Table 3.6: Boundary conditions applied in the compressible simulations when ambient wind is considered (E-model).

patch	p_{rgh}	$\mathbf{u}$	$\tilde{\nu}$	ν_t	T	ξ
ambient inlet	$\frac{\partial p_{rgh}}{\partial n} = f(\mathbf{u})$	$\mathbf{u} = \mathbf{u}_\infty$	$\tilde{\nu} = \tilde{\nu}_\infty$	calculated	$T = T_\infty$	$\xi = 0$
ambient outlet	$p_{rgh,0} = p_\infty$	$\frac{\partial \mathbf{u}}{\partial n} = 0$	$\frac{\partial \tilde{\nu}}{\partial n} = 0$	calculated	$\frac{\partial T}{\partial n} = 0$	$\frac{\partial \xi}{\partial n} = 0$
ambient sides	symmetry	symmetry	symmetry	symmetry	symmetry	symmetry
tower walls	$\frac{\partial p_{rgh}}{\partial n} = 0$	$\mathbf{u} = 0$	$\tilde{\nu} = 0$	$\nu_t = f(\mathbf{u}, y_+, ...)$	$\frac{\partial T}{\partial n} = 0$	$\frac{\partial \xi}{\partial n} = 0$
receiver	$\frac{\partial p_{rgh}}{\partial n} = f(\mathbf{u})$	$\mathbf{u} = \mathbf{u}_{absorber}$	$in : \tilde{\nu} = \tilde{\nu}_{absorber}$ $out : \frac{\partial \tilde{\nu}}{\partial n} = 0$	calculated	$in : T = T_{ilr,out}$ $out : \frac{\partial T}{\partial n} = 0$	$in : \xi = 1$ $out : \frac{\partial \xi}{\partial n} = 0$
elr	$\frac{\partial p_{rgh}}{\partial n} = f(\mathbf{u})$	$\mathbf{u} = \mathbf{u}(\dot{m}_{elr})$	$\tilde{\nu} = \tilde{\nu}_{elr}$	calculated	$T = T_{ilr,in}$	$\xi = 1$

Regarding the initial conditions, the stationary RANS simulations have been started from solutions obtained with a potential flow simulation. In the parameter study of varying elr distributions, the converged solution of the reference distribution with the

respective wind speed has been used as the initial solution for each case. For the transient DES in this study precursor steady state RANS solutions of each case were used as an initial value to decrease the initial transients, which are excluded from the evaluation of the results.

3.3.6 Limitations of the CFD Model

During the development and tests with the approach used in the E-model, limitations were encountered regarding the stability of the methods and especially the boundary conditions. The process of refining the model was very time- and resource-consuming and led to relatively short simulation times with the final E-model of less than 12 s (cf. fig. 4.31). In this section the steps in the development and the corresponding observations will be summarized briefly.

In the beginning, the numerical domain was significantly smaller compared to the domain presented in fig. 3.13. The domain had a length of around 5D, a width of 3D and a height of 2D (instead of 10D, 4D and 4D respectively in the final E-model). With this model, simulations excluding and including the receiver flow were performed in order to validate the model with the experimental results and further include the receiver operation with the receiver velocity boundary condition in eq. (3.23) in the discussion of wind-induced pressure fluctuations. With the validation case an offset in the average pressure within the cavity is observed, which is attributed to the change in the aerodynamic resistance of the tower due to the assumption of symmetry along the east-western tower axis, which geometrical does not constitute an actual symmetry axis. In addition to the offset in the mean pressure a low-frequency fluctuation within the signal was observed, which tended to increase in amplitude with increasing simulation time. In the simulation which included the receiver flow under a free stream velocity of $u_\infty = 4\,\frac{\mathrm{m}}{\mathrm{s}}$ relatively high RMS values were recorded with RMS values up to 30 Pa. An increase in the free stream velocity up to $8\,\frac{\mathrm{m}}{\mathrm{s}}$ led to pressure amplitudes in the domain of $\geq 500\,\mathrm{Pa}$, which are clearly not caused by the physics of the problem but are rather related to numerically induced fluctuations due to the applied methods.

In order to overcome this nonphysical behavior, two steps in the modeling approach have been conducted. Firstly, the receiver velocity boundary condition has been simplified as described in section 3.3.5 by assuming a constant volumetric velocity distribution based on the reference case without wind. Secondly, the dimensions of the numerical domain have been significantly increased as mentioned above in order to reduce the influence of the symmetry conditions of the lateral ambient patches.

With the increased domain size and simplified receiver boundary conditions, which constitute the final E-model, further simulations with and without considering the receiver flow are conducted, whose results will be presented and discussed in section 4.2.1 and section 4.2.3. In this section the impact of the modeling adjustments on the described limitations of the model will be discussed.

At first the case without receiver flow is considered. Due to the adjustments in increasing the numerical domain the overlaying low-frequency pressure fluctuations observed in the smaller domain do no longer increase in amplitude with increasing simulation

time and are of significantly lower amplitude, but still persist as visualized in the time series in fig. 3.20 (E4DDES). In order to isolate the influence of the symmetry plane along the east-western axis a further case is evaluated, where the numerical domain is mirrored along that symmetry plane and by that the symmetry plane through the tower is removed. The pressure time series obtained with this mirrored model are additionally visualized in fig. 3.20 for the cavity center probe p_{k0} and the probe in the stagnation point of the tower p_{k16}.

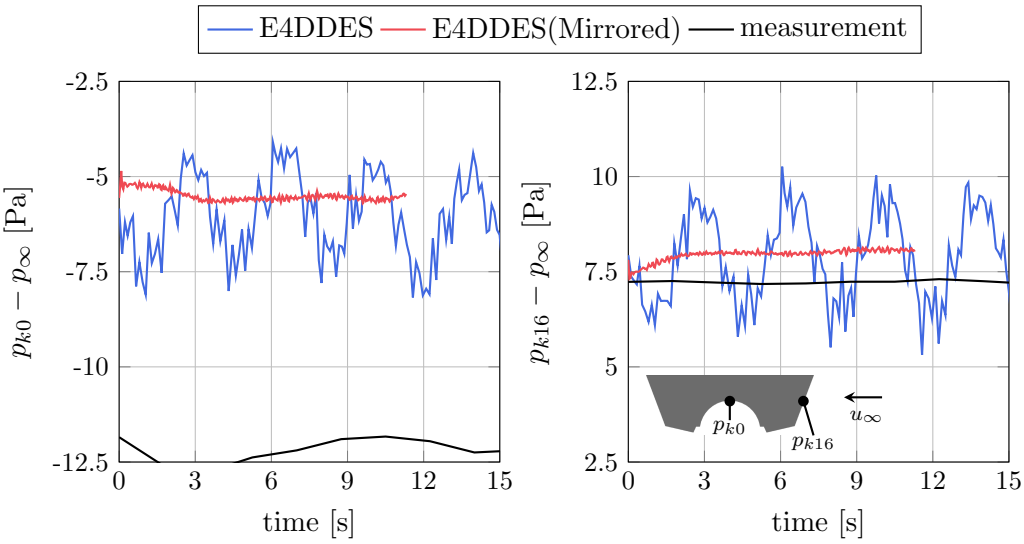

Figure 3.20: Pressure time series obtained with the E4DDES model and a mirrored version, in which the symmetry plane along the east-western tower axis is omitted (E4DDES(Mirrored)).

As visual in fig. 3.20 there is an offset in the mean pressure within the receiver cavity compared to the measurement. Averaged over all cavity probes, this offsets accounts for $\approx$ 6.2 Pa (average of p_{k0} to p_{k4}). In the stagnation point of the flow (p_{k16}) that offset is not nearly as pronounced with a difference of $\approx$ 0.5 Pa which leads to the conclusion that the difference in the average pressure is caused by the deviation in the aerodynamic resistance of the tower due to the application of the symmetry plane as the tower geometry is not symmetric along that axis. In can be seen that the pressure signal incorporates an overlaying fluctuation, which is not observed within the measurement and therefore attributed to the modeling errors in the E-model. The fluctuation is apparent at all probe positions regardless of the location and has an average amplitude of around 2.3 Pa and based on the FFT shown in fig. 4.25 a dominant frequency of 0.27 Hz. As the fluctuation does not occur with the mirrored model, it is attributed to the flow interaction with the symmetry plane along the east-western axis of the tower.

In the following part the effect of the modeling assumptions and the adjustment of the boundary conditions is discussed in terms of the simulations which include the receiver flow. Due to the simplification in the receiver boundary condition the pressure fluctua-

tions within the cavity are reduced from 30 (as mentioned above) to 10.5 Pa as shown in fig. 4.32. In the pressure time series of the DDES which includes the receiver flow with wind (fig. 4.31) it becomes clear that the pressure at the receiver surface under 4 $\frac{\mathrm{m}}{\mathrm{s}}$ wind is mainly prescribed by the receiver flow itself and the low-frequency fluctuation observed within the E-model without the receiver flow cannot be recognized in the time series data (cf. fig. 4.31). This observation leads to the conclusion that the low frequency fluctuation is suppressed by the presence of the receiver flow inside the cavity.

As a final remark it shall be mentioned that those transient fluctuations naturally do not occur within the stationary RANS approach which is applied in the estimation of forced convective heat losses (cf. section 4.2.3 and section 4.2.5) which is why those investigations are not affected by the limitations described above. Consequently, those simulations are carried out with the model based on the smaller domain (cf. grid independence study in section 3.3.7).

3.3.7 Uncertainty Analysis

The uncertainty in the numerical solution can be grouped into contributions due to the iterative process, the discretization and modeling assumptions. For example in Versteeg and Malalasekera [79] and Ferziger and Perić [57] the uncertainties arising in CFD simulations are discussed in detail and will be presented and described briefly at first. Then the individual uncertainties are discussed and quantified for the CFD models used in this study where possible, which differ in modeling assumptions and discretization with respect to space and time.

Iteration Error

Due to the discretization and linearization a set of coupled linear equations (cf. section 2.3.2) is obtained, which is solved in an iterative manner for each time step or iteration.

The iteration error is defined as the difference between the exact solution of the discretized equations and the iterative solution. The iterative solution is obtained after the user-prescribed convergence criterion is reached. The exact solution of the discretized equations can never be reached due the computational accuracy (round-off errors). Furthermore, it is not feasible to aim for the exact solution as it is sufficient to minimize the iterative error to a level relating to the other uncertainties, which typically are way above the round-off error (cf. [57]). According to Ferziger and Perić [57] the iteration error should at least be one order of magnitude lower than the discretization error. In Ferziger and Perić [113] different methods to estimate the iteration error are described. It can be shown that the rate of change in the iteration error is related to the rate of change in the normalized residual except for the beginning of the iteration. The residuals of the equations within the E- and SE-model simulations were reduced by at least three to four orders of magnitude within each iteration or time step. Based on the reduction in residuals and assuming an iteration error of 100 % at the beginning of the iteration, the estimated iteration error is in the order of 0.01 % to 0.1 %.

Discretization Error

As discussed in section 2.3.2, the solution in space and time is discretized on a finite number of cells and time steps for which the set of coupled linear equations is solved. Assuming a converged iteration with a negligible iteration error, the solution still varies from the exact solution of the initial set of differential equations due to the discretization and interpolation from the computing points to the cell faces. According to e.g. Ferziger and Perić [57] this deviation is defined as the discretization error. The deviation depends on the level of discretization and varies within the numerical domain depending on the gradients in the flow quantities as areas of little to no change in quantities allow coarser discretization. An estimate of the discretization error can be obtained by the comparison of numerical solutions obtained from systematically refined grids, which applies to a discretization in space and time (in case of a transient simulation). In the context of grid refinement, the order of accuracy of the approximation schemes which are applied, defines to which order the discretization error can be reduced with a grid refinement (cf. [57]).

With the E-model, where the receiver flow is considered, a grid independence study without wind for the receiver operation at design point conditions (cf. section 2.1.1) is conducted. As later on adjusted external return air velocity distributions are investigated, it shall be mentioned here that for the grid independence study a uniform elr distribution has been prescribed. Three different grid levels have been created whose parameters and integral quantities are summarized in table 3.7 for which the discretization error is evaluated. The receiver efficiency η_{rec} within the grid independence study

Table 3.7: Mesh parameters and results of the grid independence study at design point conditions with an hot air temperature of 670 °C and an intercept of 125 MW under windless conditions.

elements	absorber resolution	ARR_{tot}	η_{rec}
52,134,064	7 cm	84.8 %	80.9 %
126,409,452	5 cm	86.0 %	81.5 %
220,475,454	4 cm	86.4 %	81.6 %
Extrapolation	-	86.8 %	81.7 %

is calculated based on an energy balance across the receiver including the temperature difference in return and hot air which is calculated by the 1D model by Ahlbrink et al. [111] with respect to the intercepted irradiation. Based on the Richardson's extrapolation (cf. [114] and [115]) an extrapolated return air ratio ARR_{tot} of 86.8 % and receiver efficiency η_{rec} of 81.7 % is calculated which gives an absolute discretization error in those quantities of 0.8 percentage points for ARR_{tot} and 0.2 percentage points for η_{rec} when the mesh with 126,409,452 elements is used. As the deviation in the quantities of interest is sufficiently low, this mesh density was chosen for the investigation in this study.

As discussed in Stadler et al. [14] the number of agglomerates within the receiver

approximation especially influences the air return ratio and subsequently the receiver efficiency, which tends to increase with the number of agglomerates. Therefore, in addition to the grid independence study, the number of agglomerates has been varied as well for the mesh discretization level determined by the grid independence study. Due to the varying number of agglomerates and the iterative determination of return air cells (described in section 3.3.5) the area ratio varies slightly between the cases in table 3.8. Based on the discretization level of the receiver surface, the number of agglomerates is

Table 3.8: Parameters and results of the agglomerate study at design point conditions with an hot air temperature of 670 °C and an intercept of 125 MW under windless conditions.

Amount of agglomerates	Area ratio	ARR_{tot}	$T_{h,in}$
1140	7.96 %	86.9 %	536.3 K
1968	8.13 %	87.3 %	537.9 K
3200	8.04 %	86.0 %	535.4 K
4940	8.07 %	87.6 %	538.6 K

limited upwards by the amount of return air cells remaining within each agglomerate, while still maintaining the prescribed area ratio. At the case with 4940 agglomerates most of the agglomerates only contain two return air cells which is not advisable due to the numerical stability (cf. [16]). The absolute deviation in ARR_{tot} is less than 1.3 percentage points within the remaining cases. For this study a discretization with 3200 agglomerates has been chosen as the deviation remains within an acceptable range.

For the SE-model, which contains the whole tower to evaluate the pressure fluctuations under wind, a grid independence study was omitted due to the computational costs of the transient DES and the significantly larger domain. Instead, a comparison with experimental data (cf. section 4.2.1) is made to estimate the uncertainties in the model in predicting the quantities of interest, namely the surface pressure at the receiver. Due to the lack of a grid independence study, the uncertainties in the results can only be given in total and not separately attributed to the discretization and modeling uncertainties which will be addressed below.

In addition, an evaluation of the integral length scale was conducted to evaluate the resolution of turbulent scales as presented in section 3.3.2, which will be included in the discussion of the combined model uncertainty.

In the transient DES with the SE-model the temporal discretization needs to be evaluated as well. As presented in section 3.3.3 the CFL number as a measure of temporal resolution in relation to the spatial resolution is way below 0.4 in the areas of separated flow and within the cavities. In the areas where the flow separation takes place and the largest velocities occur the CFL number is way below 0.6 which fulfills the widely acknowledged recommendation of $CFL \leq 1$ in the context of LES. This recommendation was given by Spalart and Streett [61] and also investigated by Mockett [19] where it could be observed in the DES of a cylinder flow that a coarsening in the time step can

lead to a suppression of vortical structures due to time filtering effects, which supports the recommendation of $CFL \leq 1$. Instead of conducting a time step independence study, this recommendation is applied for the transient simulations in this work.

Modeling Uncertainties

The modeling error is defined as the difference between the exact solution of the mathematical model, which includes modeling assumptions and the actual flow (cf. [57]).

Sources of error are introduced in the mathematical model by assumptions and simplifications which are in general applied within the representation of the geometry by the numerical grid, assumptions within the turbulence modeling, the boundary conditions and the determination of the thermophysical properties and other auxiliary relations.

Those contributions to the modeling uncertainty will be assessed in the following part. In this study basically two numerical models have been used which differ in the geometrical representation of the tower (cf. section 3.3.1) and the boundary conditions which are applied depending on whether the receiver and return air flow is considered (E-model) or not (SE-model) (cf. section 3.3.5). Firstly, the individual contributions to the modeling error will be addressed and then concluded for the individual quantities of interest namely the surface pressure and the air return ratio with each model.

A universal source of uncertainty is the approximation of the geometry and especially the surface roughness, which within the numerical model is idealized as a smooth surface. As defined in Schlichting and Gersten [80] there is no difference compared to the ideal smooth surface as long as the roughness elements are still completely within the purely viscous sublayer. The numerical results are compared to the wind tunnel experiments, which were obtained with a model based on polished aluminum alloy with a surface roughness of around $R_a \leq 1.6 \mu m$ as described in section 3.2.1. Based on estimations for turbulent flow over a flat plate (cf. [80]), this lies well within the viscous sublayer and is therefore negligible in the estimation of modeling errors by comparison to the results obtained within the wind tunnel measurements.

In the following, the modeling uncertainty introduced by the turbulence model will be discussed. Regarding the surface pressure distribution, the turbulence model needs to be able to accurately predict the velocity fluctuations induced by the flow separation at the tower geometry, which is also influenced by the discretization as it prescribes the range of scales which are resolved by the LES part of the DDES solution.

Regarding the air return ratio further the mixing of return air with ambient air needs to be modeled adequately. The investigation and parameter study of the wind influence on the air return ratio is conducted with stationary RANS simulations as discussed in section 4.2.4 but also a comparison of the RANS results to results obtained with the DDES approach are shown in table 4.7 and fig. 4.34. It could be shown that, while the temporal fluctuations are lost in the stationary RANS simulation, the time-averaged quantities match within a deviation of 1.1 percentage points for the receiver-averaged air return ratio as shown in table 4.7. Furthermore, also the local distribution of the ARR is determined very accurately with similar deviations (cf. fig. 4.34) which allows the simplification with the RANS approach for the evaluation of the time-averaged ARR.

In general, the uncertainty due to the turbulence model can only be quantified for a given application with a comparison to DNS or sufficiently accurate experimental data, which will be addressed and discussed in detail in section 4.2.1 and briefly summarized at the end of this section.

The thermophysical properties pose a further source of uncertainty within the models. As presented in section 3.3.5 within the SE-model where the flow around the tower is modeled without the consideration of the receiver operation, the assumption of incompressibility is applied in the mathematical model and constant thermophysical properties are assumed (cf. section 2.3.1). The error introduced in the assumption of constant thermophysical properties is estimated by the simulation in the E-model where the energy balance is considered with temperature-dependent fluid properties. Within the E-model in a case without receiver operation the fluid temperature during lateral wind around the tower at $4\,\frac{\mathrm{m}}{\mathrm{s}}$ varies around less than 2 K. Based on the approach to determine the fluid properties presented in Appendix E this leads to deviations which can safely be assumed negligible compared to the uncertainties due to the turbulence model and the discretization. Within the E-model the fluid properties are assumed temperature-dependent and are interpolated from tabulated data as presented in Appendix E. The interpolation itself is a regression which introduces uncertainties due to the deviation from the underlying data which in this case is negligibly small with R-squared values above 0.99.

A further source of uncertainties attributed to the boundary conditions are boundary effects due to the finite dimensions of the domain. When the dimensions of the numerical domain are chosen too small in an external flow simulation the boundary conditions applied on the bounding surfaces may influence the flow phenomenon under investigation. The numerical domains of the models in this study are visualized in fig. 3.13 and based on the projected surface area, the blockage factor in the SE-model accounts for 2.5 % while the blockage factor in the E-model is further reduced to 0.9 %, which is why the influence of the lateral boundaries is deemed negligible compared to the other contributions of uncertainty. Attention needs to be directed to the assumption of symmetry along the east-western axis of the tower within the E-model. The symmetry plane hinders the evolution of the turbulent wake behind the tower, but as argued in the beginning of section 3.3.1 the resolution of the wake and its effect back on the flow within the cavity is assumed to be negligible. Under the restrictions in terms of computational resources and time a representation with the whole tower with the increased spatial resolution was not feasible as it would have resulted in meshes in the order of 500 mio. cells with the structured meshing approach. The impact of the symmetry plane along the east-western tower axis on the evaluation of the surface pressure (as already shown in section 3.3.6) will be summarized below.

In the context of the boundary conditions the inflow parameters in both models and the receiver and return air boundary conditions applied in the E-model need to be discussed as well. The ambient inflow conditions for both models are equal with a uniform inlet velocity and uniform eddy viscosity. Within the wind tunnel experiments it was not possible to measure the spatial distribution of the inflow turbulence, but in measurements by van Hinsberg et al. [92] the dynamic pressure variation across

the test section in the same wind tunnel was evaluated to be less than 0.3 %. It can be assumed that the largest deviations are observed in the vicinity of the tunnel walls with a comparatively more uniform distribution in the center where the upper part of the model is placed. In the simulations a uniform inlet velocity free of any free stream turbulence is applied which does introduce an uncertainty in the comparison to the experimental data that contributed to the uncertainty of the surface pressure evaluation.

The receiver and return air boundary conditions within the E-model are simplified with the agglomerate approach described in section 3.3.5. Instead of resolving the honeycomb structure of the receiver modules and the return air channels between each module which are in the order of 1 mm, the receiver surface is simplified as a cylindrical surface with a coarser resolution while still maintaining the return air and hot air mass flows and velocities by prescribing the same area ratio between in and outflow cells in comparison to the actual geometry of the HiTRec receiver.

The agglomerate approach itself has been validated by a comparison of the receiver-averaged air return ratio obtained from steady state RANS simulations of the STJ by Stadler et al. [14] under windless conditions to experimental data for the receiver obtained by Tiddens et al. [15].

A reasonable accuracy within the experimental uncertainties was found and deviations are attributed to drifts of the measured quantities compared to the stationary conditions in the simulation, uncertainties in the measurement of the irradiation and wind influence which was not considered in the simulation. In the experiments the ARR was measured by injecting helium in the air stream as a tracer gas and measuring the mole fraction of helium in the circulating air. Due to the fact that only two data points were recorded within the measurement it is hardly possible to quantify the inherent uncertainty of the modeling approach. Nevertheless, in order to quantify the uncertainty of the receiver modeling approach with regards to the determination of the air return ratio at the cavity receiver within this study, the results are directly compared to the results published by Stadler et al. [49]. The cavity receivers match in shape, size and opening angle of the receiver surface while only the outer shell geometry differs, which is not expected to influence the receiver operation under windless conditions, on which the comparison is based on. The model in this study yields comparable results in the total air return ratio and receiver efficiency for the same design point conditions with an absolute deviation in the ARR of 1.2 percentage points which lies within the uncertainty of the agglomerate and grid independence study and an absolute deviation in the receiver efficiency of 2.8 percentage points. The deviation in the receiver efficiency is attributed to differences in the intercepted irradiation, which is interpolated on the surface mesh within the pre-processing.

The level of agreement is deemed sufficient especially as the absolute level of air return ratio is of lesser interest compared to relative difference due to adjustments in the parameter study in section 4.2.4.

The uncertainty in the evaluation of the surface pressure with the SE model is mainly influenced by the assumption of uniform wind conditions (velocity and turbulence), the turbulence modeling itself and the discretization error, which as mentioned before could not be quantified due to limitations in computational resources. Based on the com-

parison to the experimental data a combined uncertainty can be evaluated based on the deviations in the results. A qualitative comparison based on surface flow visualization techniques and a quantitative comparison based on the surface pressure within the respective cavities will be presented and discussed in section 4.2.

As discussed in section 3.3.6 the surface pressure evaluation with the E-model is further influenced by the assumption of symmetry along the east-western tower axis. Due to the assumption of symmetry along the east-western axis of the tower, which does not constitute a symmetry axis in a geometrical sense, the aerodynamic behavior of the tower is altered, which shows in an additional deviation in the average pressure, as already visual in the time series data in fig. 3.20. The comparison of results in the temporal and spectral domain will be discussed in detail in section 4.2.1.

As a final remark the impact of the agglomerate approach on the surface pressure fluctuations is discussed. Within this approach the internal return air flow, which can be abstracted as several jets, is inherently coarsened compared to the geometry of the HiTRec receiver. In Meloni et al. [116] jet-induced pressure fluctuations are evaluated in an experimental set-up, where a subsonic circular jet is placed tangential to a flat plate. The authors investigate the effect of different jet Reynolds numbers on the surface pressure fluctuations at the flat plate by varying the exhaust diameter. Depending on the distance to the exhaust outlet and whether the jet shear layer interacts with the wall, different dependencies of the wall pressure fluctuations on the Reynolds number (or exhaust diameter) are obtained. For example, in the region close to the nozzle outlet, where the shear layer of the jet not yet interacts with the wall, a quadratic dependence of the intensity of the pressure fluctuations on the nozzle exhaust diameter can be observed. With increasing distance, the dependency on the exhaust diameter diminishes.

Within the receiver model, the integral mass flow ratios between the model and the real geometry agree. Due to the coarsening in the modeling approach, locally the return air jets are larger within the model, which (following the observation in [116]) leads to the conclusion that the pressure fluctuations calculated by the model pose a conservative estimate for the receiver flow induced pressure fluctuations. The dependence on the receiver discretization can only be quantified by a transient grid independence study based on e.g. the numerical grids in table 3.8, which was not achievable due to the restrictions in computational resources within this work.

4 Results

In this chapter, the results obtained with the numerical models and the wind tunnel experiments based on the methods discussed in chapter 3 are presented. At first the experimental results regarding wind induced surface pressure fluctuations are presented. The experiments cover cases with constant incident angles and measurement during changes in the incident angle. Additionally, the near surface flow field is evaluated via surface oil flow visualization and qualitatively compared to the numerical results. The numerical results can be grouped into two parts, the evaluation of wind-induced surface pressure fluctuations and the evaluation of forced convective heat losses. The impact on the surface pressure is at first evaluated without considering the receiver flow in order to ensure comparability to the measurements where the receiver flow could not be realized. The numerical model is validated in a qualitative and quantitative comparison with the experimental data and furthermore, larger wind speeds that could not be obtained in the wind tunnel are evaluated. In a next step the receiver flow is numerically included and its impact on the surface pressure under wind will be evaluated within the uncertainties of the model. The forced convective heat losses are evaluated under design point conditions and further active countermeasures, namely a wind-adjusted external return air distribution and the application of an aerowindow are numerically investigated.

Parts of the experimental results presented in this section were already published previously by the author and colleagues in a journal paper (cf. [51]). Also, parts of the numerical results regarding the wind influence on the air return ratio were published previously by the author and colleagues in a journal paper (cf. [117]). Furthermore, the numerical and experimental results are evaluated and the operational implications compared to molten salt receivers are assessed in a conference proceedings paper (cf. [118]).

4.1 Experimental Measurements

In this section the results obtained during the wind tunnel experiments are presented. During the cases of constant incident angle flow, Reynolds numbers from 3.49×10^6 to 13.17×10^6 were reached, limited due to operational limits of the wind tunnel. In total 17 incident angles ranging from 0 to 180° are covered, utilizing the symmetry of the tower. The impact of changing incident angles on the surface pressure is evaluated by measurements during rotation of the model, which were conducted under Reynolds numbers of 10.46×10^6 and 13.17×10^6 for angular velocities of 20 to 45 $\frac{°}{s}$. In addition, a passive countermeasure and its impact on the surface pressure fluctuations is evaluated. In this approach attachments are applied on the side walls next to the cavity opening in order to alter the flow separation in that area.

4.1.1 Surface Pressure Evaluation Under Constant Incident Angles

In this section the measurement under constant incident angles, as introduced in section 3.2.2, is evaluated. The measurements include static pressure measurements which are placed around the whole tower and compared to measurements on a circular cylinder under comparable Reynolds numbers obtained from literature. After that, the dependence of the mean and RMS of the pressure within the receiver cavities on the incident angle and the Reynolds number is evaluated. The local deviations within a single cavity are discussed followed by a spectral analysis based on an FFT. In the temporal and spectral analysis, critical incident angles are identified in terms of RMS values and peaks in the frequency spectrum.

Static Pressure Probe Evaluation

In this part, the pressure distribution at the static pressure probes (cf. fig. 3.8) is compared to results obtained in a circular cylinder flow. Based on the definition of flow regimes presented in section 1.3.1 the measurements in this study are located in the transcritical regime with Reynolds numbers ranging from 3.49×10^6 to 13.17×10^6.

Data in the transcritical regime is generally difficult to obtain with a high accuracy. Large blockage factors due to large models (as defined in section 3.2.4) or high velocities, which introduce compressibility effects, lead to a large scatter in the data (as discussed in [91] and [20]).

In fig. 4.1 the time-averaged pressure distribution at the static pressure probes p_s (cf. fig. 3.8) is shown for an incident angle of $\phi = 0.0$ and 90.0° for all Reynolds numbers under investigation. Herein, a representation over the relative angular probe position θ_{rel} is chosen, which is defined as the difference between the local angle θ of the probe p_s and the angle of attack ϕ, so that $\theta_{rel} = 0.0°$ in fig. 4.1 corresponds to head-on wind for both cases. The locations of the static pressure probes regarding the angle at the model are summarized in table 3.1. In addition the pressure coefficient of a circular cylinder at $Re = 14.08 \times 10^6$ as published in Jones et al. [119] is shown. The profile of the static pressure coefficient in the cylinder flow is symmetric as expected for a circular cylinder

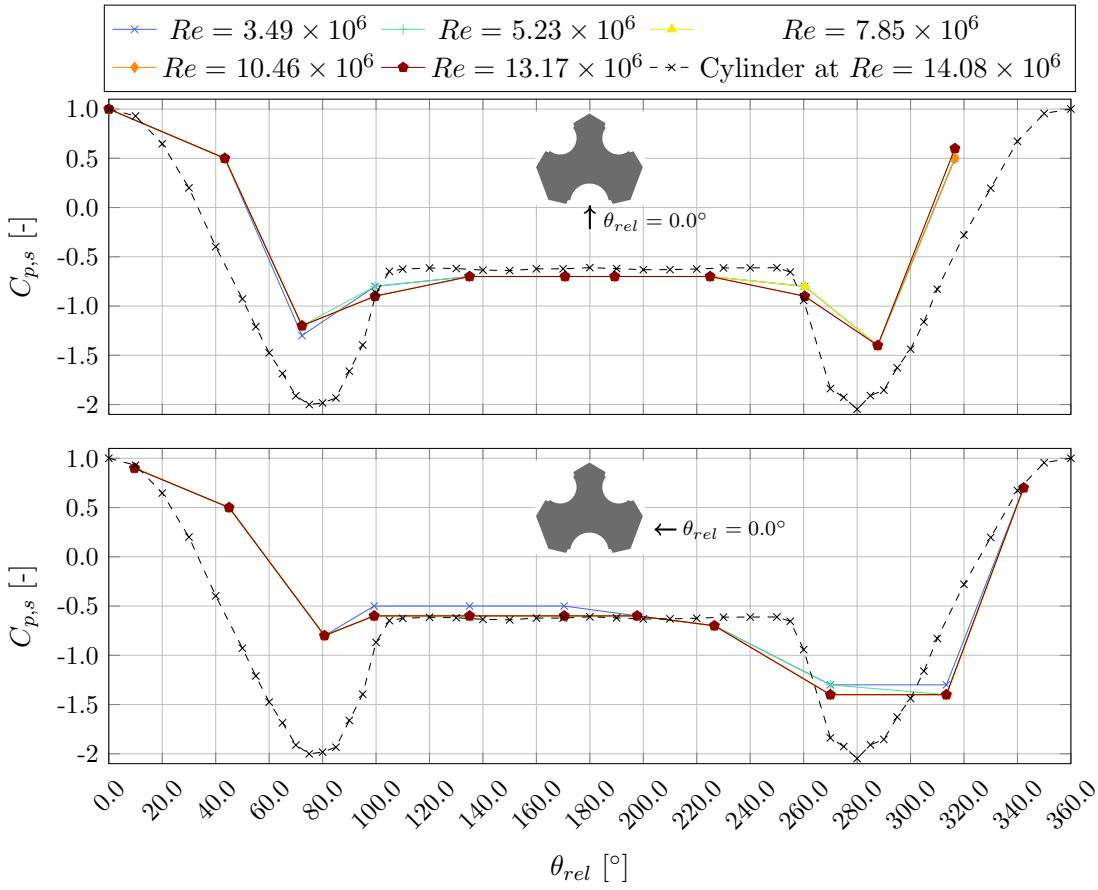

Figure 4.1: Surface distribution of the pressure coefficient $C_{p,s}$ at the static pressure probes p_s (cf. fig. 3.8) and for a case of transcritical flow around a circular cylinder at $Re = 14.08 \times 10^6$ based on data by Jones et al. [119].

in the transcritical regime, with drops in the pressure coefficient to -2 at approximately $\pm 80°$.

For an incident angle of $\phi = 0.0°$ (cf. upper part of fig. 4.1), the pressure coefficient distribution on the solar tower model is qualitatively similar to the flow around a circular cylinder as measured in Jones et al. [119]. Quantitatively, the C_p value in the wake ($100.0° \leq \phi \leq 260.0°$) is in a range comparable to the cylinder flow. At the negative pressure peaks clear differences can be observed, as they are less pronounced at the tower model. In contrast to the cylinder flow, the tower contour is not continuous, but features sharp edges that influence the area where in the cylinder flow the boundary layer accelerates until the point of separation. For an incident angle of $\phi = 90.0°$ (cf. lower part of fig. 4.1) the asymmetry of the tower and the influence of the cavity on the time-averaged pressure coefficient become visible. Due to the geometrical asymmetry the pressure drops are asymmetric as well. The level of the pressure drop at the southern cavity ($260.0° \leq \phi \leq 320.0°$) is close to the case of a flow around a cylindrical cylinder,

but in contrast to that the pressure drop here is caused by the flow separation at the cavity opening. Also the pressure plateau is on a slightly higher level with an average C_p of -0.6 compared to the incident angle of $\phi = 0.0°$ with an average value of -0.7.

Mean and RMS Pressure Dependence on the Incident Angle at the Cavity Receiver

First of all, the measurements will be evaluated to show the dependence of the mean and RMS pressure on the incident angle for each Reynolds number. At first only the probes in the middle of the respective cavities are evaluated while in fig. 4.4 the local variability within the cavities will be discussed. According to the angle definition in fig. 3.8, an angle of 0.0° equates to wind from the south and 90.0° represents wind from the east. The pressure transducers are arranged in a cross as exemplary shown for the southern cavity in fig. 3.8. The probes p_{k0} to p_{k4} are placed in the southern cavity, the probes p_{k5} to p_{k9} in the north-eastern and p_{k10} to p_{k14} in the north-western cavity.

Figure 4.2 shows the RMS values of the pressure signal at the center position of the southern and north-eastern cavity (p_{k0} and p_{k5}) for each Reynolds number and angle of attack.

For a case of constant incident angle flow, pressure fluctuations at the cavity surface result from fluctuations in the flow field, which in certain cases are amplified by flow separation at the tower geometry and the flow-surface interaction of the emerging eddies. Due to the rotation of the tower which was limited to 0 - 180° the north-western cavity does not experience e.g. head-on wind. Due to the symmetry along the north-southern tower axis and the exact same size of the northern cavities still every relative flow angle regarding those cavities can be evaluated. The same applies to the southern cavity. Due to the probe position at the tower, the peak pressure fluctuations at each cavity occur under different flow directions. As the measurement at p_{k0} and p_{k5} shows, head-on wind leads to the lowest pressure fluctuations ranging from 0.01 to 0.24 Pa. In table 4.1 the peak RMS values and under which incident angle they occur are summed up for each probe in the southern and north-eastern cavity. The largest RMS values can be observed under angles ranging from ±45.0° to ±78.8° relative to the cavity center axis (p_{k0}: 56.3°, p_{k5}: 45.0°). Under those incident angles the flow separation at the cavity opening leads to comparatively high pressure fluctuations at the probe positions inside the cavity. At the largest Reynolds number, which corresponds to a scaled wind speed of 5 $\frac{\mathrm{m}}{\mathrm{s}}$, the RMS values reach 2.02 Pa in the southern cavity at p_{k3} under a relative incident angle of 67.5° and in the north-eastern cavity 1.73 Pa at p_{k8} under a relative incident angle of 45.0°.

In fig. 4.3 the time-averaged relative pressure ($p_k - p_\infty$) at the center probe of each cavity is displayed for each incident angle ϕ and Reynolds number. The probes p_{k0} and p_{k5} experience head-on wind during the experiments at 0.0° and 135.0°, respectively which leads to the highest relative mean pressure at $Re = 13.17$ of approximately 16.0 Pa. In all cavities a minimum relative pressure of approximately -20.0 Pa occurs under side wind conditions as for this flow situation the local acceleration at the receiver surface is the highest.

In the following part the local deviation in the RMS and mean pressure within each cavity is further evaluated. The pressure fluctuation for cases at a constant incident

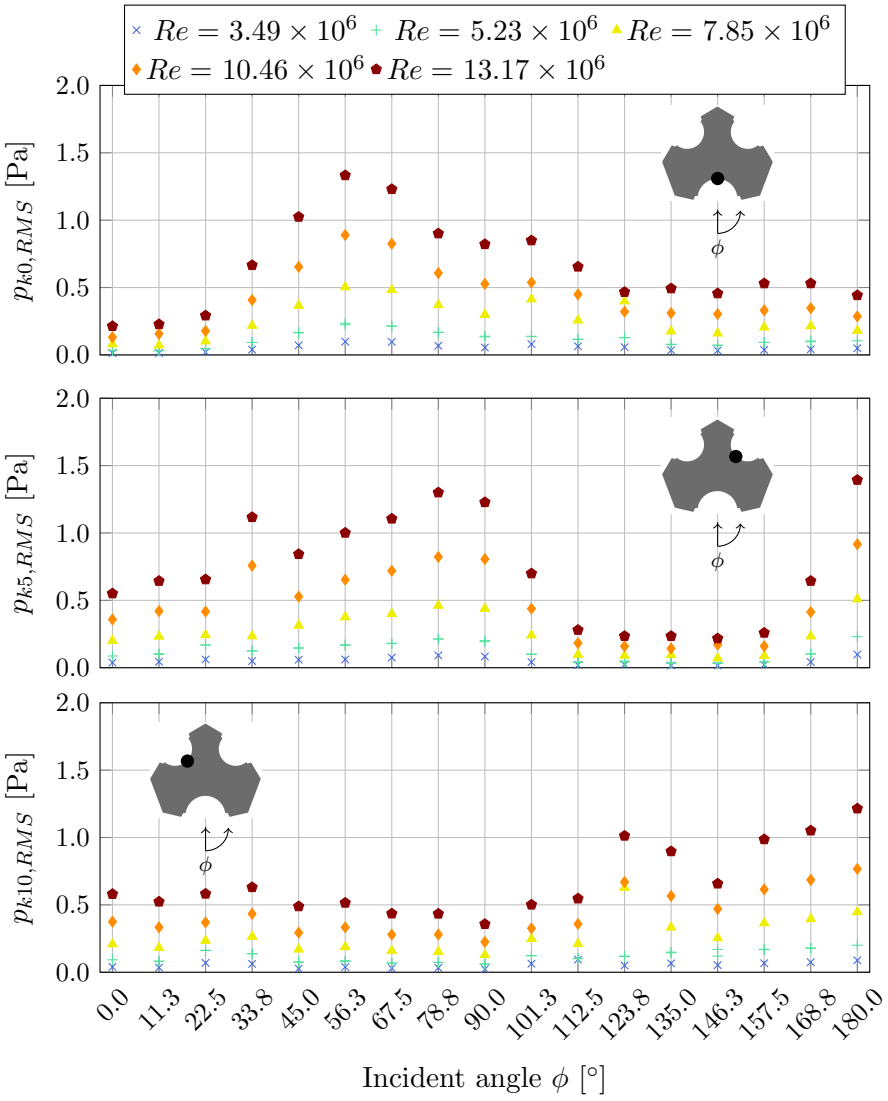

Figure 4.2: Distribution of the RMS value of the pressure signal as a function of the incident angle ϕ and Reynolds number for the center probe position of each cavity.

angle are mainly caused by flow separation at the receiver edges. The relative position in the cavity towards the receiver edge is therefore expected to have a major impact on the severity of pressure fluctuations. Regarding the RMS values the trends in the dependency on wind direction are consistent for each probe in the cavity. The peak RMS values occur at the probes that are located at the lateral positions of the cavity. In fig. 4.4 the RMS pressure values for each probe within the southern (top) and north-eastern cavity (bottom) are displayed during inflow at the highest Reynolds number for each incident angle ϕ. In the southern cavity the RMS peaks at the lateral probe

Table 4.1: Peak RMS pressure values at each probe inside the southern and north-eastern cavity and the corresponding incident angle ϕ for each Reynolds number.

probe and angle	3.49×10^6	5.23×10^6	7.85×10^6	10.46×10^6	13.17×10^6
p_{k0} at $\phi = 56.3°$	0.10 Pa	0.23 Pa	0.50 Pa	0.89 Pa	1.33 Pa
p_{k1} at $\phi = 67.5°$	0.15 Pa	0.36 Pa	0.76 Pa	1.34 Pa	2.02 Pa
p_{k2} at $\phi = 67.5°$	0.10 Pa	0.22 Pa	0.50 Pa	0.87 Pa	1.37 Pa
p_{k3} at $\phi = 56.3°$	0.14 Pa	0.34 Pa	0.76 Pa	1.40 Pa	2.20 Pa
p_{k4} at $\phi = 78.8°$	0.09 Pa	0.21 Pa	0.46 Pa	0.83 Pa	1.30 Pa
p_{k5} at $\phi = 180.0°$	0.10 Pa	0.23 Pa	0.51 Pa	0.92 Pa	1.39 Pa
p_{k6} at $\phi = 78.8°$	0.10 Pa	0.25 Pa	0.57 Pa	1.02 Pa	1.68 Pa
p_{k7} at $\phi = 56.3°$	0.07 Pa	0.20 Pa	0.44 Pa	0.75 Pa	1.21 Pa
p_{k8} at $\phi = 180.0°$	0.10 Pa	0.24 Pa	0.58 Pa	1.07 Pa	1.73 Pa
p_{k9} at $\phi = 180.0°$	0.11 Pa	0.25 Pa	0.57 Pa	0.99 Pa	1.52 Pa

positions (p_{k1} and p_{k3}) are about 40 % larger than those in the center of the cavity. In the north-eastern cavity the largest RMS values also occur at the wind facing side position in the cavity, with RMS values that are approximately 29 % larger compared to the center position. For a wind direction of 180° the RMS peak in the north-eastern cavity occurs at p_{k8} which is also at the wind facing side position in the cavity, with an RMS value 24.0 % larger than at the center probe for that wind direction.

In the following, the local variability in mean pressure is discussed. For the receiver operation local differences in mean pressure due to wind are relevant as they may introduce local deviations from the design receiver mass flow. In fig. 4.5 the mean pressure in the southern and north-eastern cavity is presented for each flow direction and a Reynolds number of 13.17×10^6.

The variability in the mean pressure is in agreement with the variability in the RMS value as far as the angle range is concerned, which again is caused by the flow separation at the cavity opening. At the southern cavity the local variability in the mean pressure is a lot higher with the largest deviation of 6.15 Pa at $\phi = 56.3°$, while at the north-eastern cavity the largest deviation only accounts for 2.95 Pa at $\phi = 180.0°$. The difference is attributed to differently shaped cavity side-walls.

Over all when analyzing the mean and RMS pressure values at different flow directions it can be concluded that the highest deviations in RMS and mean value within a cavity occur in the angle range between 45.0° and 78.8° relative to the cavity normal axis (cf. fig. 4.4 and fig. 4.5). In the main cavity those local differences in RMS and mean value are significantly higher. Especially at probe p_{k3}, which is located on the windward side of the cavity, the difference between the cavity-averaged value regarding mean and RMS pressure is the highest. At a flow direction of $\phi = 56.3°$ the RMS value on the windward side is 65 % above the average value of the probes in the center and the mean value is −3.9 Pa below the cavity average.

In the following part the frequency analysis of the surface pressure measurement will be

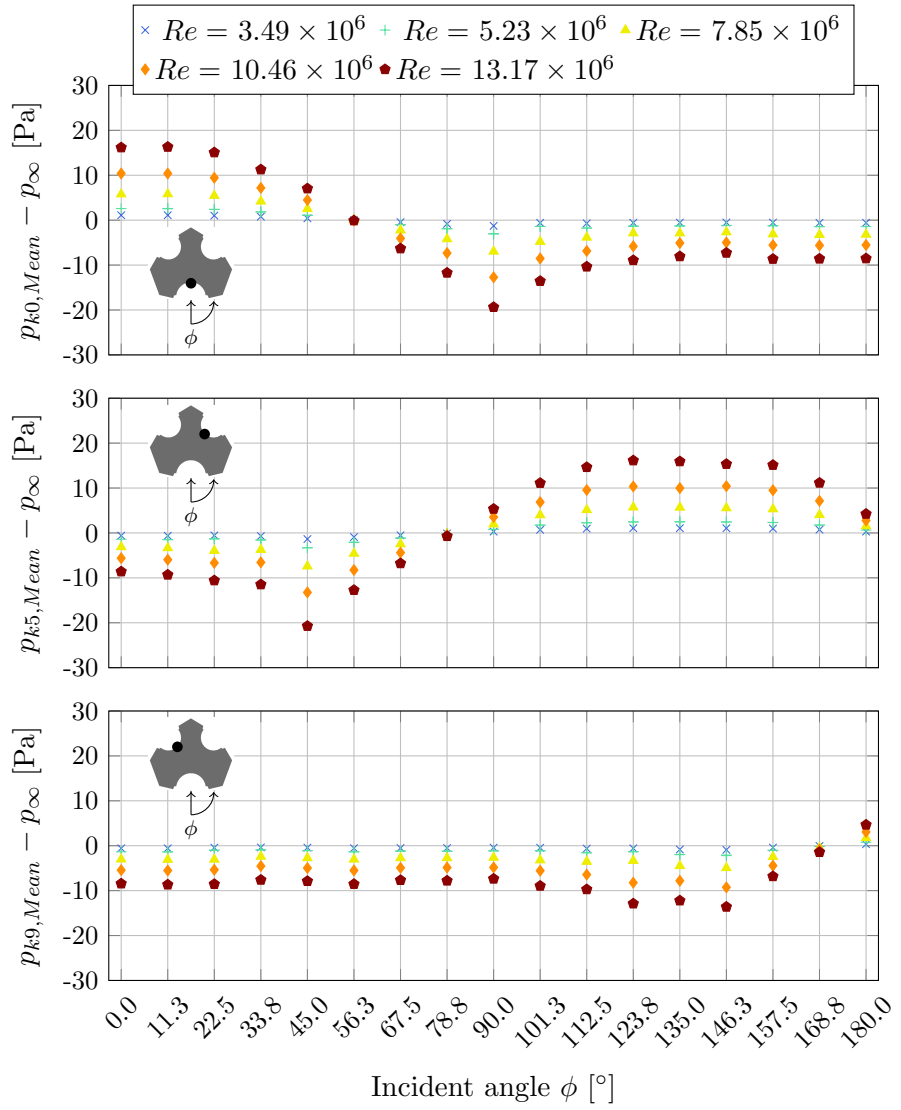

Figure 4.3: Distribution of the relative mean pressure ($p_k - p_\infty$) as a function of the incident angle ϕ and Reynolds number for the center probe position of south and north-east cavity

discussed in order to identify dominant frequencies in the signal. Because of the complex 3D-geometry a rather complex system of flow separation and vortices is expected with a strong dependency on the incident angle. The translation from the time-domain to the frequency-domain is made based on a FFT with Welch's method (cf. Appendix B). In order to reduce noise, the time signal is split into 24 segments with 50 % overlap and a Hann windowing function is applied. For each cavity the flow situations can be grouped in:

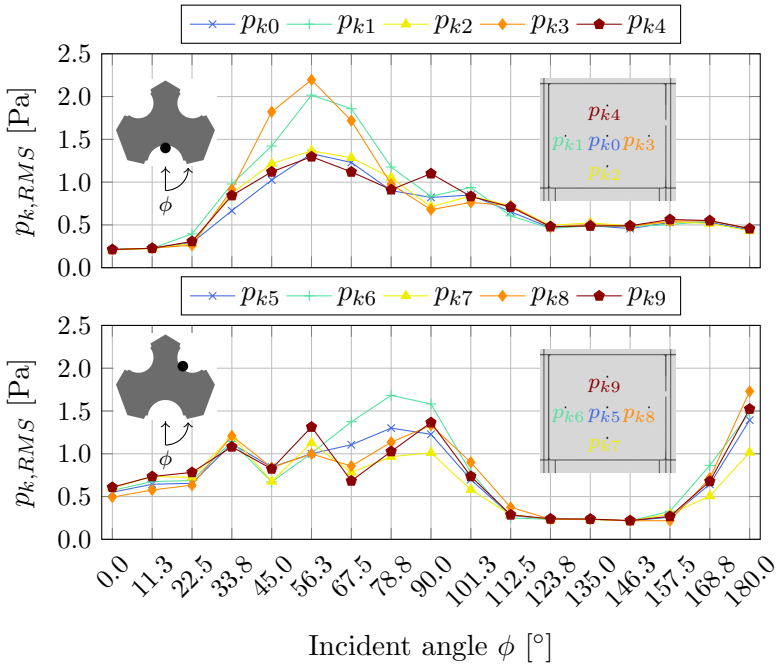

Figure 4.4: Local distribution of the pressure RMS value at each probe within the southern (p_{k0} to p_{k4}) and north-eastern cavity (p_{k5} to p_{k9}) as a function of the incident angle ϕ for a Reynolds number of 13.17×10^6.

(1) Head-on wind into the cavity (e.g. p_{k0} at $\phi = 0.0°$)

(2) Flow parallel to the cavity opening (e.g. p_{k5} at $\phi = 45.0°$)

(3) The cavity being in the wake of the tower (e.g. p_{k10} at $\phi = 45.0°$)

(4) Flow between 45.0° and 78.8° relative to the cavity normal axis (critical incident angles w.r.t. the RMS value) (e.g. p_{k0} at $\phi = 78.8°$)

Figure 4.6 shows the pressure spectral density for probes at these flow situations over the dimensionless frequency $\frac{fD}{u_\infty}$. A representation via the dimensionless frequency is chosen to increase the readability when spectra at different Reynolds numbers are shown together. The dimensionless frequency is calculated with the projected tower width D at southern flow direction $\phi = 0.0$ as the projected tower width only varies slightly with changes in flow direction (e.g. 0.12 m for $\phi = 0.0°$, 0.11 m for $\phi = 45.0°$ and 0.10 m for $\phi = 90.0°$). As the flow separation at the lower part of the tower is not expected to influence the pressure measurement in the receiver cavities which are presented in the spectral plot, the calculation of the reference length only considers the upper part of the tower. The flow around a circular cylinder can be grouped into different regimes depending on the Reynolds number as presented in section 1.3.1 where the flow experiences different states based on the relation of inertial to viscous forces and in terms of the boundary layer (laminar or transient) which influences the points of flow separation

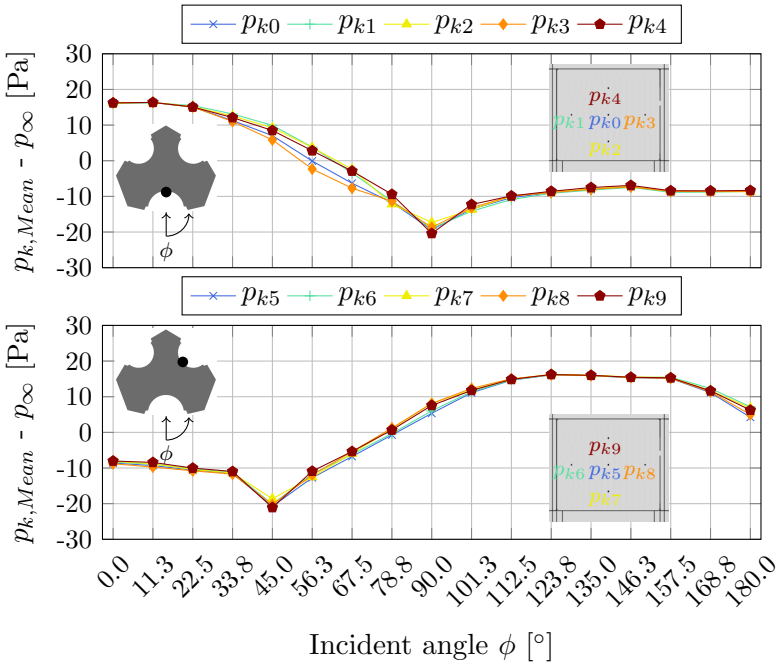

Figure 4.5: Local distribution of the mean pressure at each probe within the south (p_{k0} to p_{k4}) and north-east cavity (p_{k5} to p_{k9}) as a function of the incident angle ϕ for a Reynolds number of 13.17×10^6.

where the boundary layer at the cylinder surface can no longer follow the curvature and separates. At the Reynolds number under investigation a flow state within the trans-critical regime is expected which is characterized by Strouhal numbers ≥ 0.2 which e.g. in [20] are observed to slightly increase with Reynolds number and converge towards a value of around 0.3 (cf. [119]).

In the top left sub-figure in fig. 4.6, the power spectrum of head-on wind at the southern cavity is displayed. A lot of peaks occur in the spectrum, indicating that the energy is distributed over a lot of frequencies, as the wall pressure in this flow situation is not influenced by periodic vortex shedding at a particular frequency.

The top right plot shows a case of flow parallel to the north-eastern cavity. For this flow situation no peaks in the power spectrum can be observed which can potentially be caused by two things. Either there is a large dispersion in the flow separation or the pressure probe is not exposed to flow separation because of the shielding effect of the cavity shape for the given free flow velocities. In order to isolate the cause of the observation, additional measurements of the flow field via Particle Image Velocimetry (PIV) or CFD simulations would be necessary.

The mid left plot shows the power spectrum of a probe in the wake of the flow. The peak at a Strouhal number of 0.75 at $\mathrm{Re} = 3.49 \times 10^6$ can be assigned to the grid frequency of 50 Hz and can therefore be ignored in the flow analysis. The same peak can be identified in both top and bottom plots. In the mid left plot, for the Reynolds

numbers of 13.17×10^6 and 10.46×10^6 a peak at a St of 0.53 and 0.66 can be observed, respectively. The origin of this peak cannot be further specified but it is assumed that the peak is not caused by a flow phenomenon as the height of the peak is a lot smaller compared to the peaks in the bottom left and bottom right plot.

The mid right plot shows a case of 45.0° flow relative to the north-east cavity axis. In this situation clear peaks due to vortex shedding can be observed for all Reynolds numbers at a Strouhal number of approximately 0.27 (cf. table 4.2).

In the bottom plots, cases of a flow direction of 78.8° relative to the cavity axis are shown for the southern (left) and north-western cavity (right). A qualitatively similar behavior in the power spectrum can be observed with differences in the Strouhal number potentially caused by the fact that the edge at the southern cavity is bulkier compared to northern tip of the tower. Despite the non-symmetry in the tower geometry, the flow situation is similar in terms of the angle of attack towards the side wall near the cavity (cf. fig. 3.8) which leads to a comparable flow acceleration at that wall and flow separation at the edge of the cavity. The resulting periodic flow separation occurs at Strouhal numbers of 0.40 to 0.50.

In the bottom left case the second harmonic of the vortex shedding frequency can be observed at a Strouhal number of 0.78 to 0.88. Table 4.2 sums up the peak frequencies and displays the corresponding Strouhal numbers for the cases in the two bottom plots and the cases in the mid right plot. For the cases in table 4.2 the Strouhal number is Reynolds-independent within a deviation of ± 0.02 to ± 0.04, as to be expected for the flow being at the transcritical flow regime at $Re \geq 3 \times 10^6$. The reason for the slight displacement with respect to the Reynolds number cannot be identified for sure based on the data available. It is attributed however to the blockage effect, as it changes continuously with the flow velocity. The peak frequencies in table 4.2 correspond to the real scale application as they are calculated by the Strouhal numbers with a tower width of the reference plant of 35 m and the full scale wind speed corresponding to the Reynolds number of each case and therefore.

Table 4.2: Peak full-scale frequencies and corresponding Strouhal numbers (f/St) in the pressure power spectrum for selected cases from fig. 4.6.

probe and angle	$Re = 3.49 \times 10^6$	$Re = 5.23 \times 10^6$	$Re = 7.85 \times 10^6$	$Re = 10.46 \times 10^6$	$Re = 13.17 \times 10^6$
p_{k5} at $\phi = 180.0°$	0.009 Hz/0.25	0.016 Hz/0.28	0.021 Hz/0.25	0.033 Hz/0.29	0.039 Hz/0.27
p_{k0} at $\phi = 78.75°$	0.016 Hz/0.44	0.025 Hz/0.43	0.035 Hz/0.41	0.046 Hz/0.40	0.056 Hz/0.39
p_{k10} at $\phi = 146.25°$	0.018 Hz/0.48	0.028 Hz/0.49	0.042 Hz/0.49	0.058 Hz/0.50	0.071 Hz/0.50

When comparing those results to the flow around a circular cylinder (e.g. [119], [98], [20] or [91]), it should be noted that the Strouhal numbers which can be observed in fig. 4.6 are caused by the flow separation at the cavity edge. The location of the separation line here is determined by the geometry and does not vary with the Reynolds number, which is very much in contrast to the Strouhal numbers observed at a flow around a circular cylinder. But if the comparison with a flow around a circular cylinder in the transcritical Reynolds number region is taken as a basis (e.g. [119], [20]), it can be assumed that the Strouhal number will remain constant at higher flow velocities.

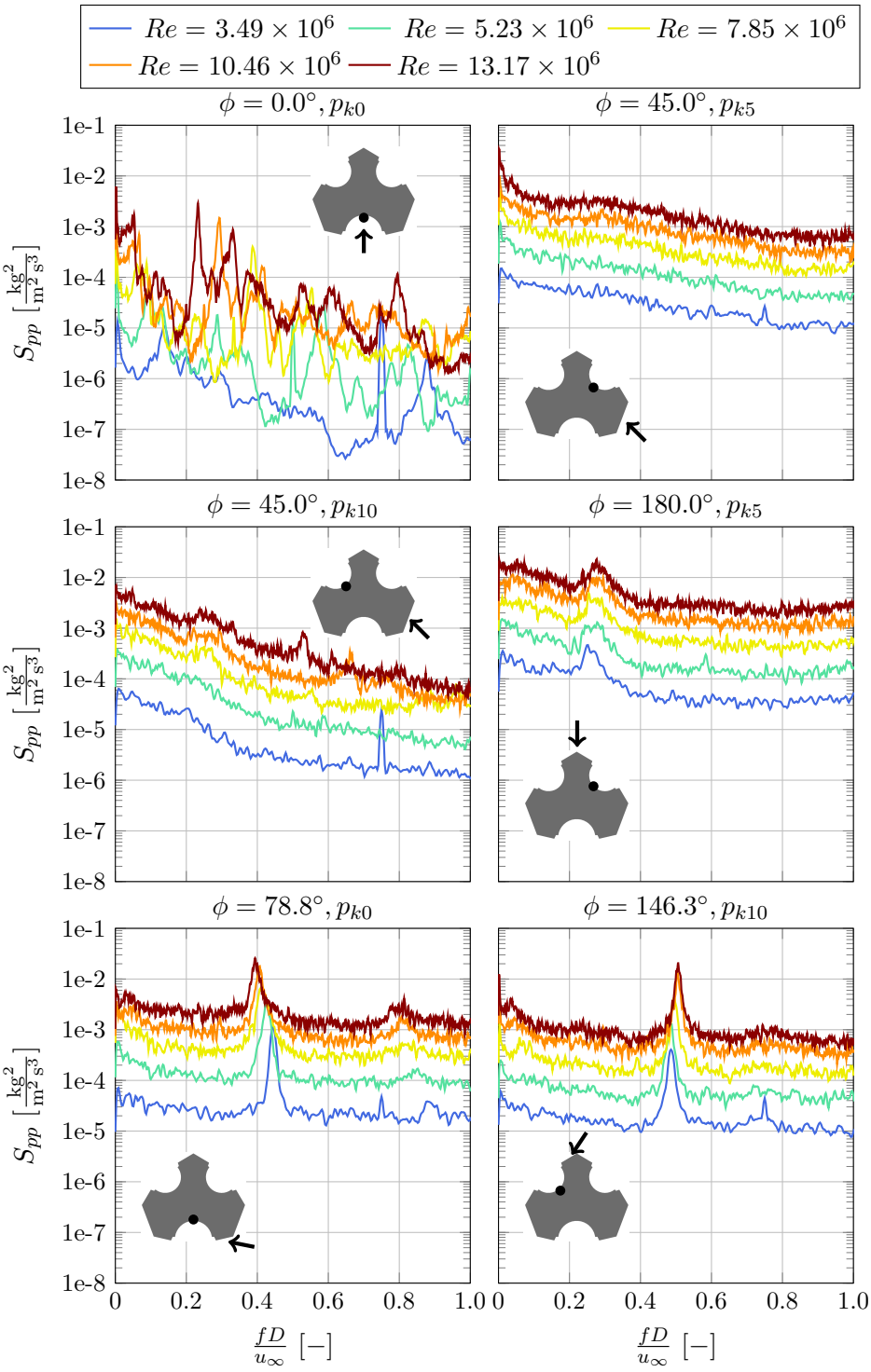

Figure 4.6: Power spectral density of the pressure S_{pp} for six representative flow situations at each Reynolds number.

In fig. 4.7 the local variability of the surface pressure with respect to the spectral distribution is evaluated at the southern cavity. The power spectral density S_{pp} of the pressure signal at each southern cavity probe (p_{k0} - p_{k4}) is visualized under the incident angle of 78.8 and 90.0° at the highest Reynolds number investigated (13.17×10^6). In order to increase readability the S_{pp} signal which was obtained by the original pressure signal is filtered with the Savitzky-Golay filter (cf. [120]) based on a window length of 51 with third-order polynomial functions within each window. This way the noise in the spectral distribution is reduced without altering the peak locations.

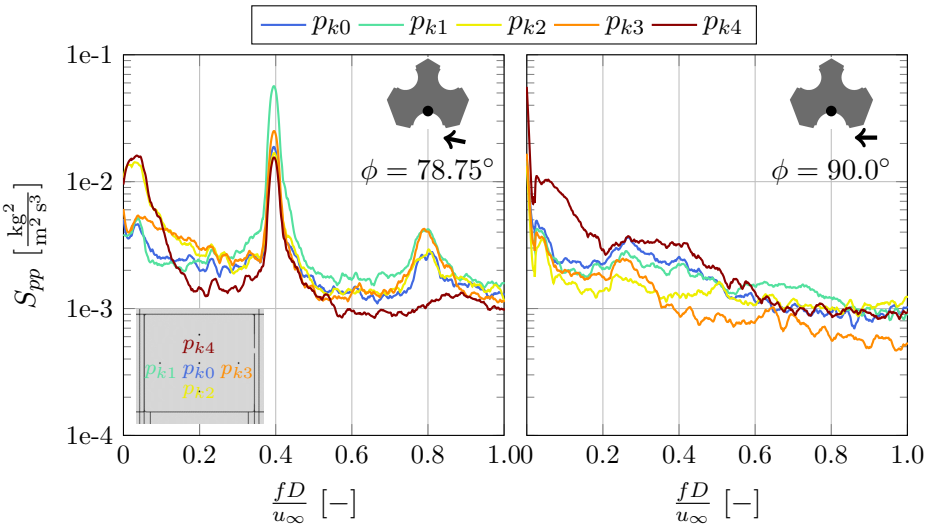

Figure 4.7: Local variability of the power spectral density of the pressure S_{pp} within the southern cavity at two incident angles (78.8 and 90.0°) at the highest Reynolds number investigated (13.17×10^6). The S_{pp} is filtered with a Savitzky-Golay filter to increase the readability.

As already shown in fig. 4.6 the strongest peak in the frequency spectrum at the center of the southern cavity is at a Strouhal number of around 0.4. As visual in fig. 4.7 this peak is clearly visual at all probe positions within the cavity but at the leeward side of the cavity (p_{k1}) the peak is pronounced the most. This indicates a stronger amplitude in the signal which is in alignment with the evaluation of the RMS values within the cavity (cf. fig. 4.4). At $St = 0.8$ the second harmonic of the main peak is pronounced at each probe position except for upper probe within the cavity p_{k4}. In the right side of fig. 4.6 the S_{pp} at each probe within the southern cavity is displayed under side-wind conditions. At this incident angle the flow separation does not directly impinge on the probe positions and therefore the peaks in the pressure spectrum are not nearly as pronounces as under an incident angle of 78.8°. Only a slight peak at a Strouhal number of around 0.25 can be observed at the probe positions p_{k0}, p_{k1} and p_{k3}. This further emphasizes the high sensitivity of the surface pressure fluctuations on the incident angle due to the complex geometry of the tower which defines the vortex shedding under wind.

In fig. 4.8 the Reynolds dependency of the RMS values for p_{k3} is displayed for selected

flow directions. The directions include head-on wind ($\phi = 0.0°$), side-wind ($\phi = 90.0°$), the direction where the probe is positioned in the wake of the tower ($\phi = 180.0°$) and flow directions, under which the highest RMS values are observed ($45.0° \leq \phi \leq 78.8°$). Figure 4.8 emphasizes that the RMS dependency on the Reynolds number at the

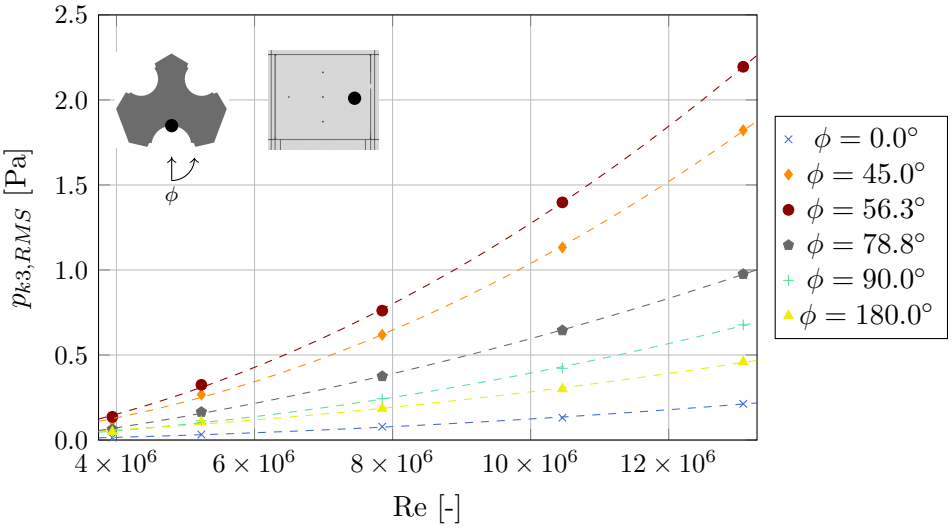

Figure 4.8: Dependency of the RMS pressure value on the Reynolds number for the probe p_{k3} and the interpolation based on second order polynomial functions.

probes shown can be approximated via second order polynomial functions in the range of measurement which are included via dashed lines for each probe position. Depending on the flow direction a relative increase in the RMS value from 9.5 (for 180.0° flow at p_{k3}) to 16.1 times (for 56.3° flow at p_{k3}) can be observed in the Reynolds number range under investigation.

Summary: Mean and RMS Pressure Dependence on the Incident Angle at Constant Incident Angle Flow

As part of the experiments in the wind tunnel, the impact of constant incident angle flow on the surface pressure inside the receiver cavities is investigated at Reynolds numbers ranging from 3.49×10^6 to 13.17×10^6, which equals wind speeds from 1.3 to 5 $\frac{\text{m}}{\text{s}}$ in the real-scale application. The model has been rotated between 17 different incident angles ranging from 0° (southern flow direction) to 180° (northern flow direction). The surface pressure is measured at five positions within each receiver cavity with piezoresistive pressure transducers. During the investigation a critical incident angle range between approximately 45 and 80° relative to the cavity normal axis can be identified. At those incident angles RMS values up to 2.2 Pa occur, which are caused by the flow surface interaction of eddies emerging from the flow separation at the tower geometry. The local deviation in the RMS value at given incident angles is particularly high at the incident angle range, where the cavity is subject to flow separation. The lateral parts of

the receiver are subject to RMS values, which exceed those in the center by almost 65 %. A second-degree polynomial dependence of the measured RMS values on the Reynolds number can be observed and an extrapolation towards higher wind speeds of 14 $\frac{\mathrm{m}}{\mathrm{s}}$ leads to RMS values up to 8 Pa at the lateral parts of the receiver. In a spectral evaluation based on Welch's FFT dominant frequencies can be obtained incident angles at which the probe position is subject to flow separation. The dominant frequencies increase almost linearly with Re from 0.009 (at 1.3 $\frac{\mathrm{m}}{\mathrm{s}}$) and 0.071 Hz (at 5.0 $\frac{\mathrm{m}}{\mathrm{s}}$).

4.1.2 Surface Pressure Evaluation During Varying Incident Angles

The aim of this test series is to evaluate the effect of shifts in wind direction on the surface pressure within the receiver cavities. The surface pressure has been evaluated during changes in the incident angle by a rotation of the model during the measurement. The model has been rotated back and forth over an angle range of 180° from a southern to a northern incident angle and rested between direction changes to avoid hysteresis. As the start of each rotation had to be set manually by the operator, the pause time is not equal for each test series and the signal had to be post-processed to erase those parts of the signal. In order to identify the start and end of rotation, the force balance data was analyzed and the beginning and end of the rotation is identified in the time series of the pitch moment, as displayed in fig. C.2.

For this test series the test parameters cover the two largest Reynolds numbers in this study 10.46×10^6 and 13.17×10^6 and four different rotational speeds of 20, 30, 40 and 45 $\frac{^\circ}{\mathrm{s}}$ to evaluate the influence of the angular velocity on the surface pressure.

Figure 4.9 shows a part of the pressure signal at the southern cavity for a rotation starting from 0.0° at a rotational speed of 20 and 40 $\frac{^\circ}{\mathrm{s}}$ at a Reynolds number of 13.17×10^6. For comparison with the stationary measurements the pressure under constant incident angle flow at 0.0 and 90.0° is displayed as well. As visual in fig. 4.9, during rotation the surface pressure varies between the maximum dynamic pressure during head-on flow and the minimal pressure which occurs under approximately side-wind conditions.

As already shown in the time series in fig. 4.9, a change in the incident angle leads to much higher changes in the average pressure compared to the separation induced pressure fluctuations at stationary incident angles.

In the following part, the RMS value of the pressure signal during the rotation of the model is evaluated for each Reynolds number and angular velocity under investigation. The RMS values are averaged over 100 cycles of rotation. Due to the symmetry of the tower, the same results at the north-eastern and north-western cavity would be obtained if the same relative angle range was covered. For that reason, the data from the north-western cavity is not shown in this section and instead the north-eastern cavity is evaluated. In fig. 4.10 the RMS values of the pressure during a rotation from head-on to side-wind is shown for the the probes south cavity (p_{k0} to p_{k4}: $0.0 - 90.0°$) and the north-east cavity (p_{k5} to p_{k9}: $45.0 - 135.0°$) for the different angular velocities defined in section 3.2.2. In addition, the maximum RMS values during the stationary measurements are plotted at each probe location for a Reynolds number of 13.17×10^6.

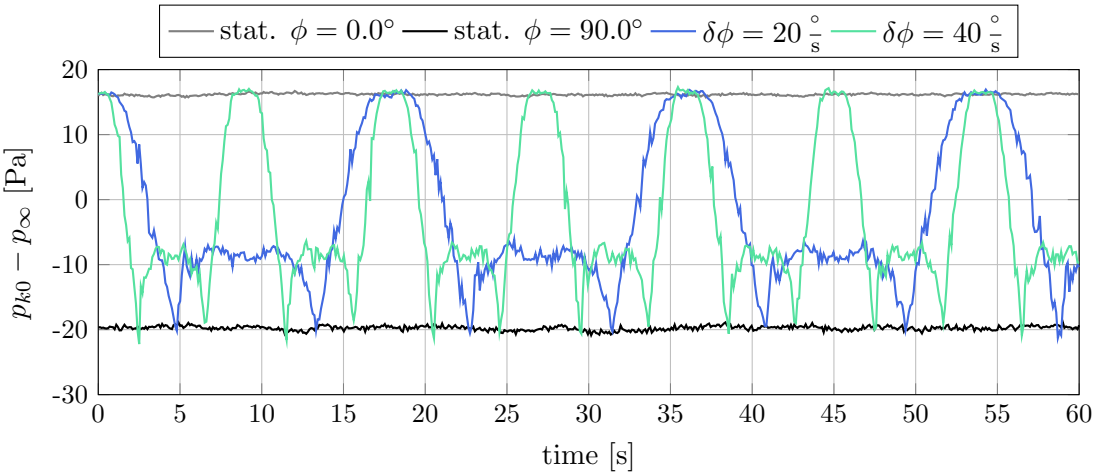

Figure 4.9: Extract of the pressure signal at probe p_{k0} during the rotation of the tower at two different rotational speeds (20 and $40\,\frac{°}{s}$) at a Reynolds number of 13.17×10^6. In addition, the pressure signals at probe p_{k0} during stationary flow at $\phi = 0.0°$ and 90.0° at $Re = 13.17 \times 10^6$ are shown.

The data in fig. 4.10 suggests a slight dependence of the RMS values on angular velocity, as the RMS values consistently over all probes decrease with increasing angular velocity. The RMS values during a rotation with $20\,\frac{°}{s}$ are on average about 7.4 % larger compared to a rotation at $40\,\frac{°}{s}$. For the southern and north-eastern cavity, the RMS values at the upper probes (p_{k4} and p_{k9}, respectively) are 5.8 % and 2.3 %, respectively higher than the cavity average value, whereas the RMS values at the bottom probes (p_{k2} and p_{k7}) are 4.9 % and 5.2 %, respectively lower.

To analyze the local differences in the instantaneous pressure during rotation, the time series of the pressure difference between probe p_{k1} and p_{k3} is shown in fig. 4.11. The local differences in the instantaneous pressure under the dynamic measurement correspond to the differences in mean pressure under a steady-state measurement as shown in fig. 4.5. Additionally, at the times where the incident angle lies within 45.0 and 78.8° (e.g. $2.3\,\text{s} \leq t \leq 3.9\,\text{s}$) the pressure probes are exposed to the flow separation at the cavity opening, which leads to superimposed high frequency fluctuations in the signal. A drop in the pressure difference can be observed as the incident angle is approaching the side wind situation at the angle of around 80.0°. For the case with an angular velocity of $40\,\frac{°}{s}$ the gradient in pressure difference is steeper, but the overall amplitude is only slightly influenced by the angular velocity. As can be seen in the time series data in fig. 4.9 as well, the gradient in the local pressure difference is determined by the angular velocity.

As mentioned in the characterization of ambient wind in section 3.1, it is very unlikely that the OVR will experience a change in wind direction during operation where the incident angle varies between head-on to side-wind in a short period of time. Therefore, in fig. 4.12 the RMS value during a change of flow direction is evaluated with respect to

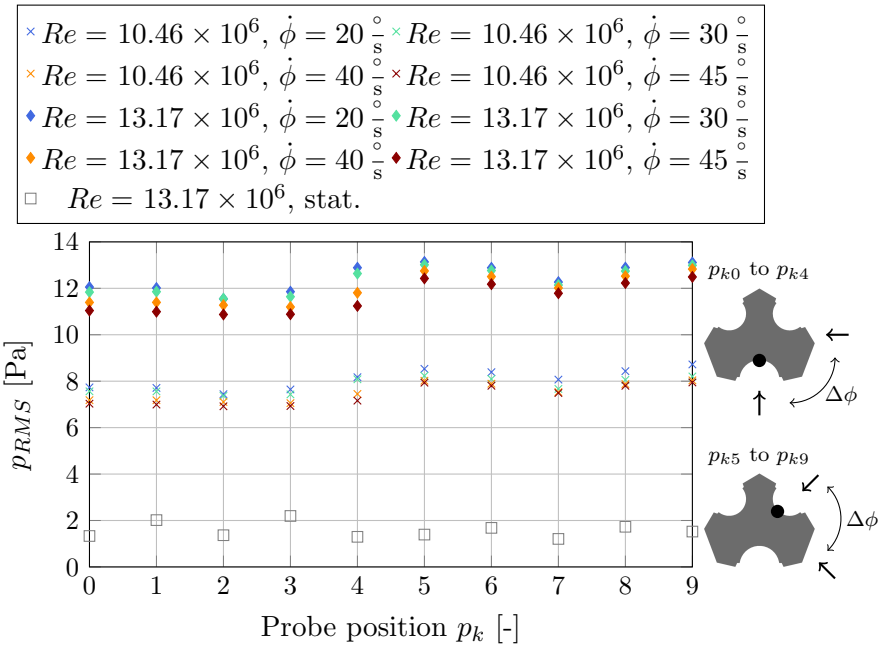

Figure 4.10: Pressure RMS values during a full rotation from head-on to side-wind at each probe position p_k, Re and rotational speed of the model. In addition, the maximum RMS values during constant incident angle flow at a Reynolds number of 13.17×10^6 are displayed.

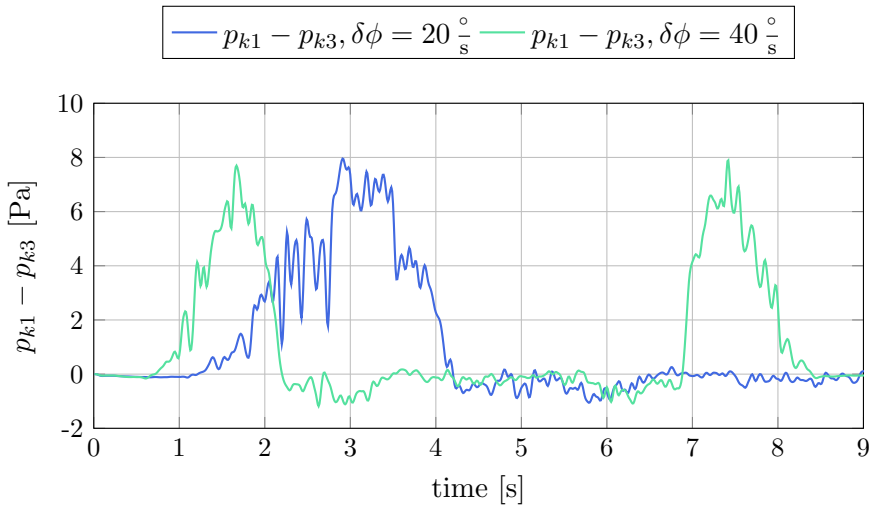

Figure 4.11: Time series of the pressure difference between probe p_{k1} and p_{k3} for a rotation starting at $\phi = 0.0$ at $Re = 13.17 \times 10^6$.

the incident angle range, ranging from $\Delta\phi = 10.0$ to 90.0°. In fig. 4.12 only the cases for an angular velocity of ($20\,\frac{°}{s}$) are presented, as those yield the largest RMS values (cf.

fig. 4.10). The range of change in wind direction, which can be expected during operation at those wind speeds, is highlighted in green. In addition, as the angular range in which the fluctuation occurs affects the result, two cases of different angles around which the rotation takes place (ϕ_{rel} = 45.0 and 90.0°) are displayed. As shown in fig. 4.12, the

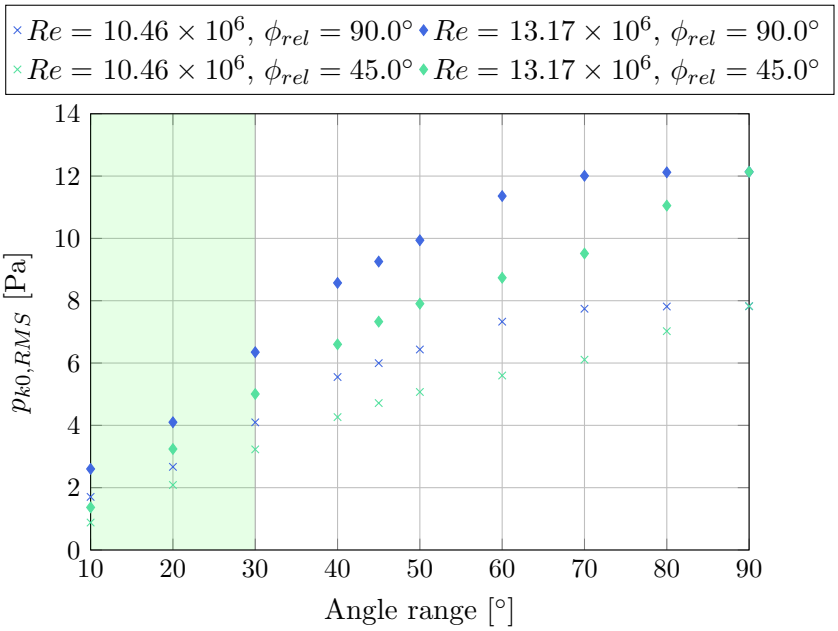

Figure 4.12: Pressure RMS values over the angle range of rotation around an angle of 45.0 and 90.0° relative to the cavity opening at the probe p_{k0} for each Reynolds number and an angular velocity of 20 $\frac{°}{s}$.

RMS values during rotation are strongly dependent on between which angle range the fluctuation takes place. This observation can also be made in fig. 4.9 as the gradient of the mean pressure is steeper in the area of a side-wind condition compared to the head-on flow condition. A fluctuation around a side-wind situation yields larger RMS values than a fluctuation around an angle of 45° relative to the cavity normal axis. For a rotation over a range of 30° the difference accounts for a relatively higher RMS value of 26.9 % for both Reynolds numbers. An increase in the Reynolds number from 10.46×10^6 to 13.17×10^6 results in a relative increase in RMS value of around 55.0 % for both angles of rotation.

In fig. 4.13 the dependency of the pressure RMS value on the Reynolds number for p_{k0} due to the rotation is illustrated. The RMS value is evaluated for different ranges of rotation $\Delta\phi$ of 20, 50 and 90° starting from side-wind conditions ($\phi = 90°$).

As shown in fig. 4.13, the dependency of the RMS value on the Reynolds number during a rotation of the tower can be approximated by second-order polynomial functions. The interpolation is based on the measured values during rotation at Re = 10.46×10^6 and 13.17×10^6 and the differences in mean pressure during stationary flow direction between the start and end position of each rotation at Re = 3.49×10^6. Additionally, this figure

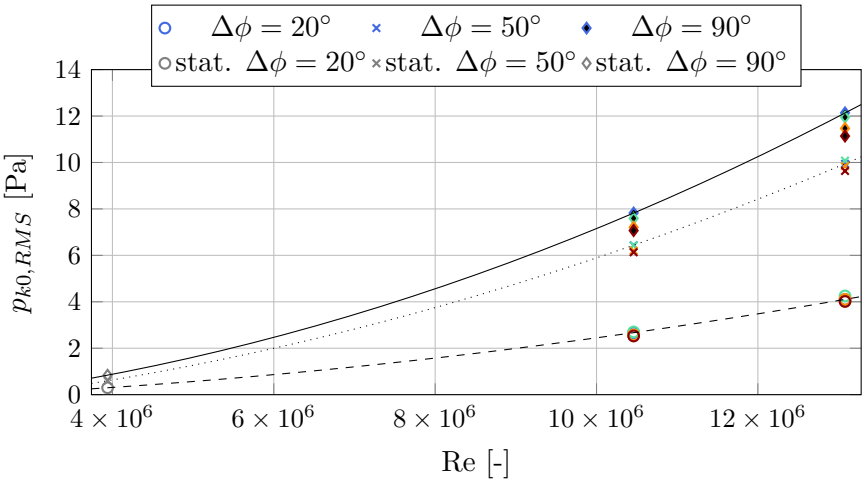

Figure 4.13: Re-Dependency of the pressure RMS value at the probe position p_{k0} during rotation of the model evaluated for different ranges of rotation $\Delta\phi$. Also displayed is the interpolation based on a second order polynomial function. Additionally, the differences in mean pressure during stationary (stat.) flow direction between the start and end position of each rotation for Re = 3.49×10^6 is shown.

confirms the sensitivity of the RMS values under rotation with respect to the range in which the rotation takes place. As stated before, this can also be identified in the gradient of the RMS values in fig. 4.12. Based on the polynomial functions at a Reynolds number of 36.61×10^6 which corresponds to a wind speed of 14 $\frac{\text{m}}{\text{s}}$ pressure RMS values at probe position p_{k0} can be extrapolated. For a range of rotation of 20, 50 and 90° RMS values of 29.28, 71.29 and 89.47 Pa are expected which exceed the extrapolated RMS values which occur under a constant incident angle flow by up to one order of magnitude, as will be presented in fig. 4.30.

This section concludes with the analysis of the pressure differences between different cavities under wind and especially during changes in the incident angles. As the air stream of the separate cavities are merged within the air system of the tower differences in the mean pressure at different cavities may become problematic when they are in the range of the over all pressure drop in the system. In analogy to the representation of local surface pressure fluctuations under varying incident angles in fig. 4.12 the differences between two cavities are analyzed for various ranges of rotation and two relative mean incident angles (45° which represents south-eastern flow and 90° which represents eastern flow). Instead of the local pressure the pressure difference at the cavity centers between the southern cavity and the north-eastern and north-western is considered here.

For the given incident angles, under which the rotation is taking place, the pressure differences between the southern and north-eastern cavity exceed the pressure difference between the southern and north-western cavity because in this configuration the north-western cavity does not experience direct inflow.

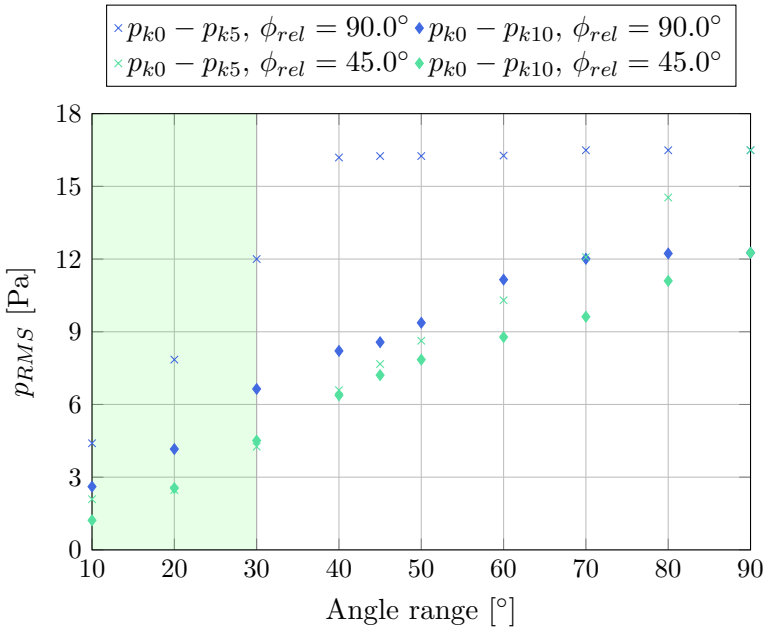

Figure 4.14: Pressure RMS values of the pressure differences $p_{k0} - p_{k5}$ and $p_{k0} - p_{k10}$ over the angle range of rotation around an angle of 45.0 and 90.0° at $Re = 13.17 \times 10^6$ and an angular velocity of 20 $\frac{°}{s}$.

Compared to the local pressure differences displayed in fig. 4.12, the amplitudes in the pressure difference between the southern and north-eastern cavity in fig. 4.14 exceed the local fluctuations significantly for angle ranges $> 20°$. The results emphasize the dependency on the range of rotation but also in which angle range the rotation takes place ($\phi_{rel} = 45$ or 90°), as for example at a rotation around the incident angle of $\phi = 45.0°$ RMS values in the pressure difference of up to 16.5 Pa can be observed.

The results obtained by the experiments are further extrapolated to an increased wind speed of 14 $\frac{m}{s}$ by the change in the dynamic pressure. RMS values in the pressure difference between the southern and north-eastern cavity of up to 129 Pa are expected at $u_\infty = 14 \frac{m}{s}$ following the same dependency on the angle range of rotation as within fig. 4.14 which leads to RMS values of up to 94 Pa for a variation in the incident angle of 30° around side wind conditions ($\phi_{rel} = 90°$). In relation to the over all pressure drop in the hot air stream (approximately 1000 Pa) of the air system this can safely be evaluated as uncritical.

Summary: Surface Pressure Evaluation During Varying Incident Angles

In this part of the experimental campaign the impact of shifts in the wind direction on the surface pressure is evaluated. The model is rotated between a southern and northern incident angle with rotational speeds ranging from 20 to 45 $\frac{°}{s}$ at Reynolds numbers of 10.46×10^6 and 13.17×10^6 (4 and 5 $\frac{m}{s}$ in the real-scale application). A slight decrease in

the RMS value with increasing rotational speed can be observed at all probe positions. The pressure fluctuation is mainly prescribed by the shift in the stagnation pressure on the receiver. For the evaluation of the RMS value during wind direction changes, it is essential to estimate realistic ranges of rotation. As shown in section 3.1 the direction variability decreases with wind speed and an evaluation of fluctuations in the range of 30° is considered sufficient. The RMS value also heavily depends on the angle relative to which the rotation takes places and RMS values of up to 6 Pa are observed in the experiment. As the fluctuation is related to the dynamic pressure, an extrapolation based on a second-degree polynomial function with respect to the Reynolds number can be applied, which leads to RMS up to 47 Pa at 14 $\frac{\mathrm{m}}{\mathrm{s}}$ wind speed.

4.1.3 Passive Countermeasures to Reduce Wind-Induced Pressure Fluctuations

As discussed in section 1.3.4 a variety of measures to reduce convective losses in cavity receivers are investigated in literature. They can be grouped into active and passive measures. The most common active measures are aerowindows (cf. [44], [46]) where air is ejected next to the cavity opening to deflect ambient wind and prevent it from entering the cavity in order to reduce forced convective losses. In terms of passive measures for example quartz windows [45] are a common approach which is only applicable for cavity receiver up to a certain size due to structural restrictions of such windows.

In the experimental part of this work a passive approach has been chosen as the implementation and control of active measures was too complicated within the high-pressure wind tunnel. The tower model has been designed in a modular way, which allows the application of different surface structures next to the cavity opening. Those parts (also referred to as shields) are mounted with screws from the inside of the tower as displayed in the technical sketch of the model in Appendix A. This modular approach allows the investigation of adjusted surface structures in addition to the standard polished aluminum surface. In the left part of fig. 3.7 the tower is shown with one of the adjusted shields, that reach from the top of the cavity opening to the bottom of the receiver. The shields were manufactured via additive manufacturing with the Stereolithography (SLA) method from polymer resin, which was chosen as a cost-effective approach with a high level of design freedom. The two designs which are investigated in addition to the polished aluminum surface are displayed in fig. 4.15. In the upper part the front view on the southern cavity is shown while in the lower part the shields are displayed in detail. The attachments on the side walls are inspired by vortex generators used in aircarft engineering. For example in Lin [121] micro vortex generators are discussed, which are used to prevent boundary layer separation on wings by introducing streamwise vortices inside the boundary layer, which effectively increases the lift on the airfoil and reduces drag. The trapezoid form of the VG configuration is adopted from Lin [121], while the wedge-type configuration CVG is adopted from Holden and Babinsky [122]. In the context of this study those vortex generators are applied in order to alter the flow separation, with the intention of diffusing the flow separation and by that reducing the severity of the pressure fluctuations.

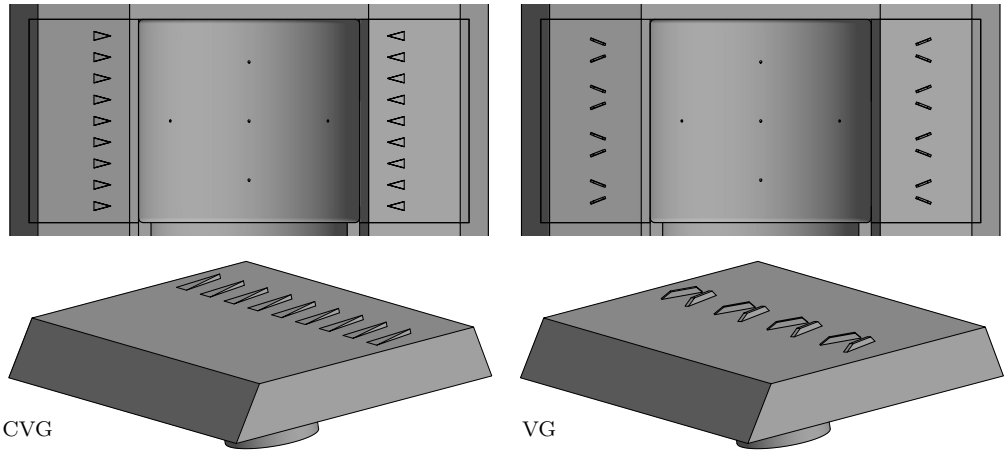

Figure 4.15: Technical sketches of the adjusted shields next to the cavity opening.

The trapezoid attachments on the shields in the VG configuration have a height of 0.5 mm and a length to height ratio of 7. At the wind facing side an inclination angle of 32° is applied while on the other side a steeper angle of 52° is applied. The attachments are tilted by an angle of 58° towards the horizontal axis on the surface. The attachments in the wedge-type configuration CVG have an endpoint height of 0.4 mm and a length to height ratio of 9 which results in an inclination angle of 6°. The trapezoids have a base width of 1.9 mm.

The experiments with the polymer shields revealed deficiencies of the applied manufacturing method and design with regards to the attachment to the tower. A screw joint was directly cut into the polymer material, which in some cases was not able to withstand the dynamic pressure in the wind tunnel leading to a loss of shields. It is assumed that the contact pressure of the screws was to low which, in combination with slight gaps between the polymer shields and the tower due to the lower manufacturing precision of the shields, enabled the flow to lift the shields. Due to those deficiencies no measurement under constant incident angles is available with the VG configuration and only measurements under varying wind directions for the Reynolds number of 10.46×10^6 are available for both configurations.

The exemplary probe positions in fig. 4.16 show that the influence of different side shields is restricted to a narrow incident angle range. For example at p_{k3} the critical angle range in terms of RMS values between 33.8 and 78.8° is not influenced by the application of the shields. At p_{k3} the application of the shield is not beneficial, as it leads to increased RMS values within 90.0° and 123.8° with a significant increase at 123.8° of 127.3 %, without significantly reducing the RMS value at any incident angle. At p_{k9} the reduction potential is similarly low despite at an incident angle of 56.3° (78.7° relative to the cavity normal axis) where the RMS value is reduced by 54.3 %.

In table 4.3 the effect of the CVG shields on the pressure RMS value under constant incident angle flow is shown for cases where the relative difference extends 30 % at a free stream Reynolds number of 13.17×10^6. The absolute and relative difference in the RMS

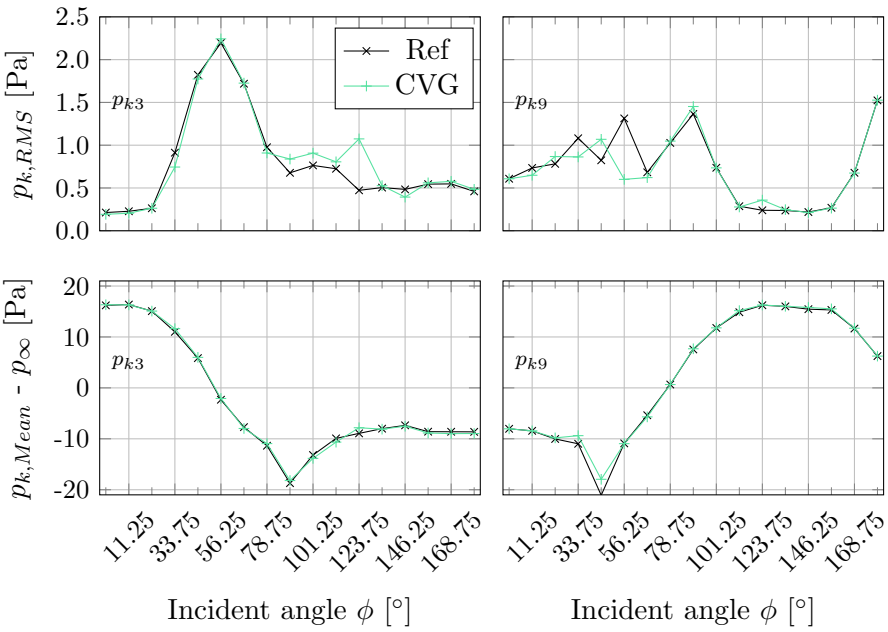

Figure 4.16: Pressure RMS value at p_{k3} within the southern cavity and at p_{k9} within the north-eastern cavity as a function of the incident angle ϕ for $Re = 13.17 \times 10^6$. The results obtained with the reference shields and CVG configuration are shown.

value is shown under the corresponding relative incident angle ϕ_{rel}, which is defined as the incident angle in relation to the cavity normal axis (p_{k0} to p_{k4}: 0° and p_{k5} to p_{k9}: 135°).

It has to be concluded that the application of the shields in the way they are designed does not significantly and systematically reduce the pressure RMS value under constant incident angles. Although incident angles occur under which the RMS is reduced significantly (as shown in table 4.3), this does not apply at all probe positions within the respective cavity and furthermore a slight change in the incident angle can lead to a significant increase in the RMS value. For example at p_{k8} where the RMS value is reduced by 31.6 % at a relative incident angle of 101.2° while at a relative incident angle of 90.0° leads to an increase of 33.4 % compared to the reference case.

In fig. 4.17 the spectral pressure distribution for the cases of 123.8° flow at p_{k3} and 78.8° flow at p_{k9} is visualized, where the application of the CVG shields leads to an increase in the RMS value of 127.3 % and a decrease of −54.3 % respectively (as shown in table 4.3). At p_{k3} it can be observed that the application of the CVG shields leads to an overall higher level in the power spectral density, especially in the low frequency range which agrees with the higher RMS values in that case. In contrast to that, at the relative incident angle of 78.8° at p_{k9} the application of the CVG shields leads to an overall reduction in the power spectral density. In addition to that, the peaks at $St = 0.08$ and 0.44 are significantly reduced for this particular incident angle.

Table 4.3: Relative and absolute difference in the pressure RMS value between the reference and CVG shields for cases where the relative deviation in the RMS value exceeds 30 %.

p_k	ϕ_{rel}	$\frac{p_{RMS,CVG}-p_{RMS,Ref}}{p_{RMS,Ref}}$	$p_{RMS,CVG} - p_{RMS,Ref}$
p_{k6}	101.2°	−30.2 %	−0.35 Pa
p_{k7}	101.2°	−37.2 %	−0.45 Pa
p_{k8}	101.2°	−31.6 %	−0.38 Pa
p_{k5}	90.0°	31.9 %	0.27 Pa
p_{k6}	90.0°	49.8 %	0.33 Pa
p_{k8}	90.0°	33.4 %	0.28 Pa
p_{k9}	78.8°	−54.3 %	−0.71 Pa
p_{k0}	123.8°	129.6 %	0.60 Pa
p_{k1}	123.8°	137.2 %	0.63 Pa
p_{k2}	123.8°	105.8 %	0.52 Pa
p_{k3}	123.8°	127.3 %	0.60 Pa
p_{k4}	123.8°	102.5 %	0.49 Pa

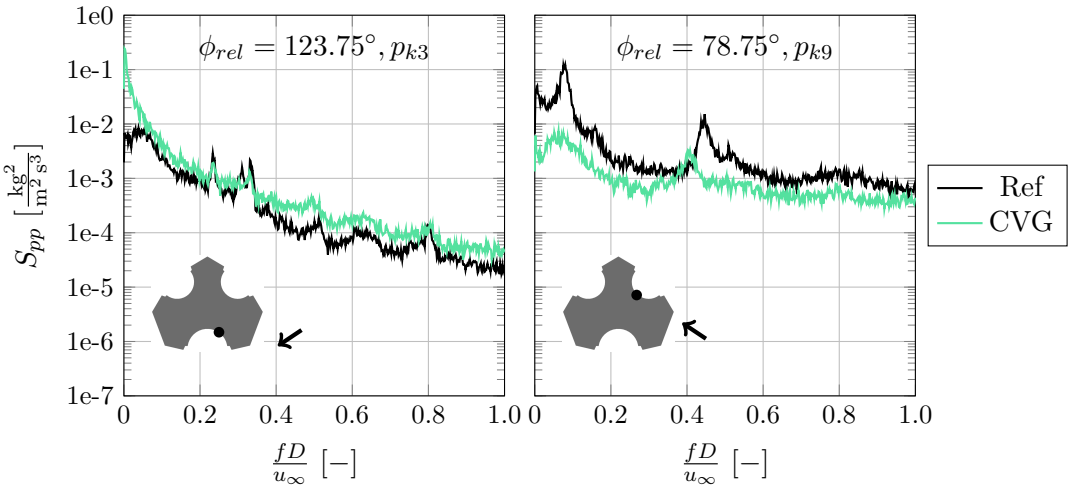

Figure 4.17: Pressure power spectral density S_{pp} for two selected flow situations with and without the application of the CVG shields.

The application of the adjusted polymer shields has also been tested under varying incident angles for a free stream Reynolds number of 10.46×10^6 and its influence on the pressure RMS value in the local surface pressure is evaluated during the rotation of the tower.

In fig. 4.18 the pressure RMS value is visualized during a rotation of the incident angle. As the trends, which can be observed, are independent from the range of rotation the results are shown exemplary for a rotation between $\phi_{rel} = 90° \pm 25°$ at each probe posi-

tion within the southern and north-eastern cavity. The results obtained under different angular velocities are also consistent, so in fig. 4.18 the results obtained under 20 $\frac{°}{s}$ are shown with the reference shields and the polymer shields of the types VG and CVG.

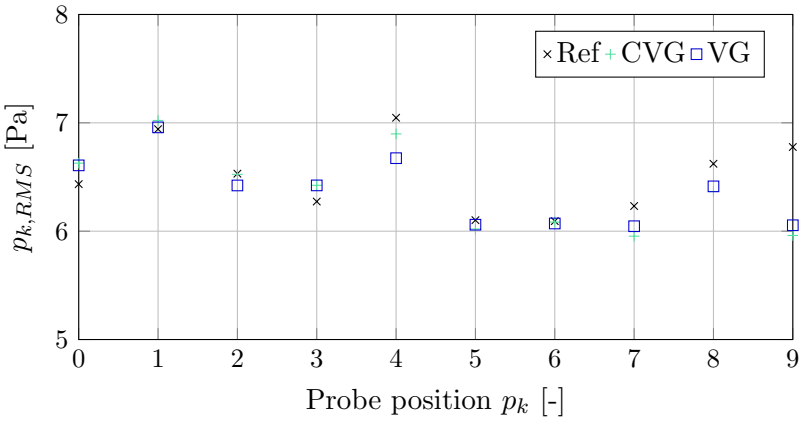

Figure 4.18: Pressure RMS values at each probe position within the southern (p_{k0} to p_{k4}) and north-eastern cavity (p_{k5} to p_{k9}) at $\phi = 90.0°$ during a change of incident angle between $\pm 25°$ at $Re = 10.46 \times 10^6$ and an angular velocity of 20 $\frac{°}{s}$.

The application of the shields can be observed to be most effective at the upper probe within the cavities (p_{k4} and p_{k9}). At p_{k9} a reduction in the RMS value of 0.72 Pa can be observed. At p_{k4} the reduction is less significant with values ranging between 0.15 and 0.25 Pa. For the remaining probe positions there are cases where the application of the polymer shields leads to slightly increased RMS values or no significant difference as at p_{k5} or p_{k6}. It can be concluded that the influence of the adjusted shields on the pressure RMS value due to a variation in the incident angle is not significant at most probe positions and also inconsistent as it leads to a reduction at the upper probe positions but does not significantly reduce the RMS values at the rest of the receiver surface.

Summary: Passive Countermeasures to Reduce Wind-Induced Pressure Fluctuations

The application of attachments at the walls adjacent to the cavity opening and their influence on the surface pressure was tested under constant and varying incident angle flow. The so called shields were designed without and with two different attachements inspired from vortex generators in aircraft engineering with the aim of disturbing the flow separation at the cavity opening to reduce pressure RMS values inside the cavity.

Design-based deficiencies in the attachment of the additive manufactured polymere resin shields could be observed during the experiments. The screw connection between the tower and the shield was not able to withstand the forces in the High Pressure Wind Tunnel, which led to a detachment of shields in some cases. For the remaining experiments it can be summarized that while for certain incident angles the adjusted polymere

shields lead to significant reductions in the RMS value, in the majority of the cases the RMS values are increased by the application of the proposed attachments. It has to be concluded that the application of such surface attachments does not significantly and, what is most important, not systematically reduce the surface pressure RMS values for a wide range of incident angles.

4.2 Numerical Simulations

From a modeling perspective, the numerical simulations in this work can be grouped into two parts. First, the simulation of wind flow around the tower without the consideration of the receiver flow (SE-model) to investigate the surface pressure distribution under wind. Secondly, simulations are conducted with the consideration of the receiver and return air flow under operation with the boundary conditions presented in section 3.3.5 (E-model) in order to extend the evaluation of wind-induced surface pressure fluctuations by the receiver flow and to estimate the impact on the surface pressure under wind. In addition to that, the wind influence on forced convective heat losses in the OVR cavity receiver is investigated numerically for different wind speeds and countermeasures to reduce convective losses are systematically investigated.

At first, a model validation based on a qualitative comparison of surface flow visualizations and on a quantitative comparison of the surface pressure with the experimental results will be presented. For the validation, a case with 4 $\frac{\mathrm{m}}{\mathrm{s}}$ wind speed from a south-eastern incident angle is chosen. In addition a simulation at 14 $\frac{\mathrm{m}}{\mathrm{s}}$ wind speed is conducted to cover higher wind speeds which have to be expected during the operation of the solar tower plant (cf. section 3.1). For the cases without considering the receiver operation a south-eastern wind direction is chosen as this represents the predominant wind direction at the reference location but also poses a situation where the three receiver cavities are subject to three different relative incident angles: partial inflow at the southern cavity with a relative incident angle of $\phi_{rel} = 45°$, flow parallel to the cavity at the north-eastern cavity $\phi_{rel} = 90°$ and a flow situation at the north-western cavity, where the cavity is in the wake of the tower with its central surface normal axis aligned with the flow incident angle.

Within the E-model the receiver and return air flow under design-point conditions are included to extend the evaluation of wind-induced surface pressure fluctuations by that influence. In addition to the impact on the surface pressure, wind induced forced convective heat losses are studied at different wind speeds for the main cavity under lateral wind conditions. The forced convective losses are evaluated for design and off-design conditions and further countermeasures are evaluated based on wind-adjusted return air distributions and windshields which are applied on the irradiation shields adjacent to the cavity opening. Due to the necessity of a higher spatial resolution within the cavity only the main cavity is included (as described in section 3.3.1) under an eastern incident angle.

Table 4.4 gives an overview of the simulations that were conducted including the incident angle, free stream velocity, receiver modeling and turbulence model, which are applied in the respective cases. In the upper part of table 4.4 the cases are named where the whole tower is included in the numerical domain as presented in section 3.3.1. In the middle of table 4.4 the cases with the model, where only the southern cavity is included are shown, which are used in order to evaluate the receiver influence on the surface pressure distribution. In the bottom part of table 4.4 the basic parameters in the investigation of forced convective heat losses at the cavity receiver are summarized, which includes a variety of simulations at 4 and 8 $\frac{\mathrm{m}}{\mathrm{s}}$ wind speed with applied windshields

Table 4.4: Overview of the simulation cases, including the incident angle, Reynolds number, receiver modelling approach, turbulence model and temporal resolution.

case name	ϕ [°]	u_∞ [$\frac{\mathrm{m}}{\mathrm{s}}$]	Re_∞ [−]	Receiver modeled	turbulence model	temporal solution
SE4RANS	45	4	10.46×10^6	no	SA-RANS	steady-state
SE4DDES	45	4	10.46×10^6	no	SA-DDES	transient
SE14RANS	45	14	36.28×10^6	no	SA-RANS	steady-state
SE14DDES	45	14	36.28×10^6	no	SA-DDES	transient
E4DDES	90	4	10.46×10^6	no	SA-DDES	transient
E4DDES	90	4	10.46×10^6	yes	SA-DDES	transient
E0RANS	90	0	0.00	yes	SA-RANS	steady-state
E4RANS	90	4	10.46×10^6	yes	SA-RANS	steady-state
E8RANS	90	8	20.92×10^6	yes	SA-RANS	steady-state
E8DDES	90	8	20.92×10^6	yes	SA-DDES	transient

or variations in the distribution of the externally returned warm air, which is included in the return air concept as presented in section 2.1.1.

4.2.1 Model Validation and Verification

In this section the numerical results obtained with the SE-model will be validated by a comparison with the wind tunnel experiments. The validation is based on a quantitative comparison of the surface pressure regarding the statistical evaluation of pressure RMS and mean values and a comparison in the spectral domain. In addition, a qualitative validation is performed by a comparison of surface flow visualization within the experiment with a visualization of surface streamlines based on the wall shear stress in CFD. In order to evaluate the deficiencies and advantages of the different turbulence modeling approaches the RANS and DES results will be compared. At first the results obtained with the SE4 model will be compared to the wind tunnel measurements at an incident angle of $\phi = 45°$ and free stream velocity u_∞ of $4\,\frac{\mathrm{m}}{\mathrm{s}}$.

As presented in section 3.2.3, the surface oil flow visualization in the experiment was performed by applying a coating to the tower which contains Titanium-Dioxide particles which align along the surface streamlines during the experiment. In CFD the surface flow visualization is realized via an evaluation of the wall shear stress based on the wall normal component of the shear-stress symmetric tensor retrieved from the turbulence model. To visualize the wall shear stress at the tower surface a random sample of streamlines based on the wall shear stress vector field is computed. In fig. 4.19 the comparison between the numerical and experimental surface flow visualization techniques is shown. In the CFD results the surface is colored in the wall shear stress in addition to the stream line visualization. In the upper part of the figure a view angle from the flow direction is displayed and at the lower part of the figure the southern cavity is shown. The CFD simulation is evaluated at the time step corresponding to a simulation time of 133.6 s. In the measurement, the wind tunnel fan was operating for a couple of seconds and the model was immediately ejected from the test section for the documentation.

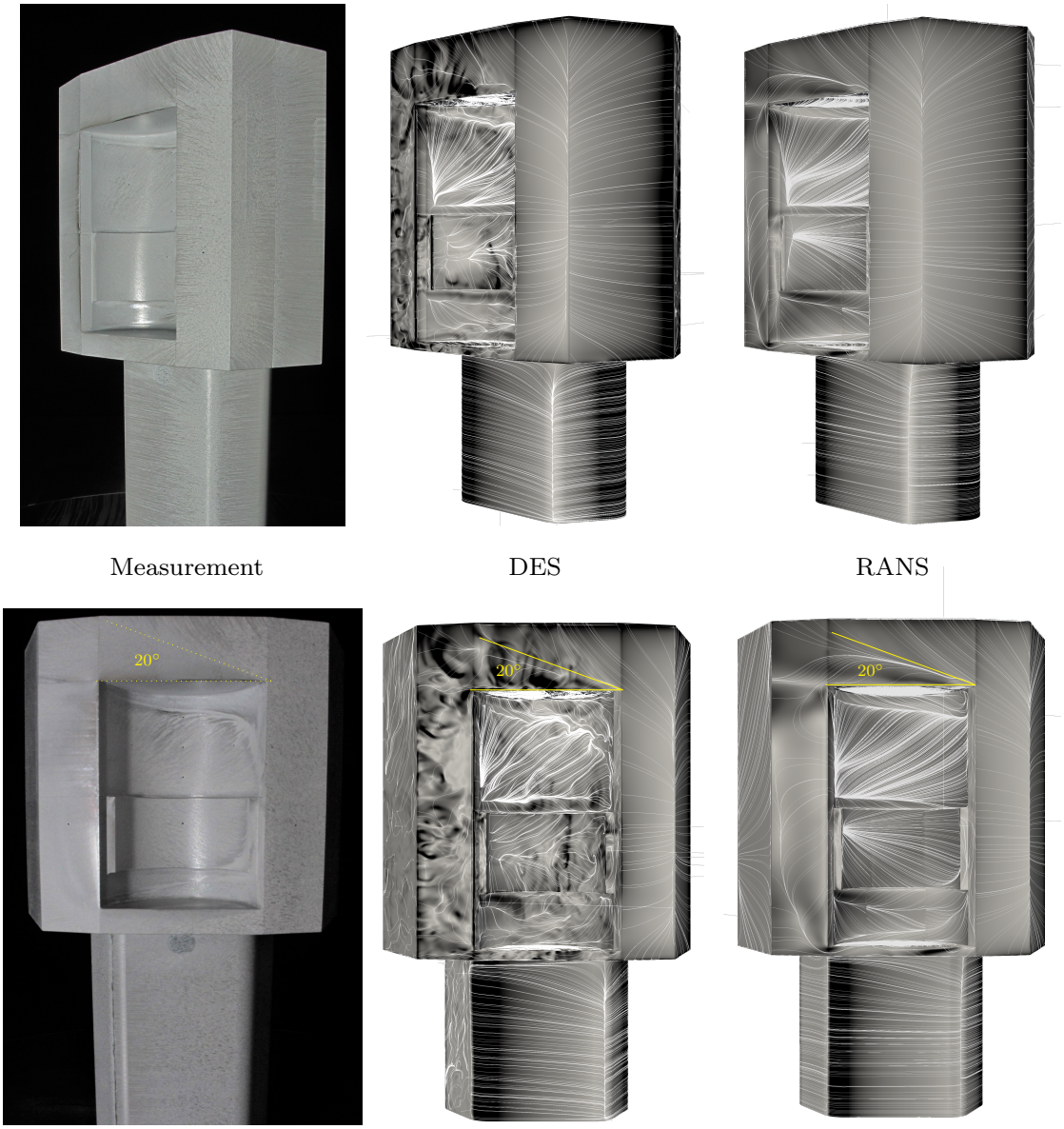

Figure 4.19: Comparison of the experimental surface oil flow visualization (left) and a visualization of the wall shear stress surface vector field calculated by the SE4DDES model (middle) and the SE4RANS model (right). The upper part shows a view from the inflow direction, while the lower part shows the southern cavity.

In the upper part of fig. 4.19 a great level of agreement between the stagnation line and streamlines that originate from there can be observed at the upper and the lower part of the tower, both for the comparison of RANS and DES model with the measurement. This agreement is expected as the DES model operates in RANS mode in the wall-boundary layer and the stagnation area is not subject to heavily separated flow. The differences in the wall shear stress arise in areas of separated flow, like inside the cavity where the separated flow interacts with the receiver surface. The deviations originate from the turbulence modeling as in the RANS model the flow is averaged and does not contain small scale fluctuations.

At the upper edge of the cavity a vortex arises which has a vertical inclination of approximately 20° and can be clearly identified in the DES and RANS visualization. In the measurement this vortex is harder to identify as the contact area at the wall blurs out due to the "averaging" which takes place during the measurement time. Still the vortex can be observed in both the measurement and CFD simulations.

Inside the cavity the qualitative agreement between the surface oil flow visualization in the measurement and especially the visualization in the DES is very high. Especially the vortex which originates at the upper part of the cavity and proceeds along the receiver surface and the streamlines inside the cavity agree fairly well between the measurement and DES.

A comparison, based on the methods presented, works especially well at parts of the tower where predominantly stationary attached boundary layer flow is present or at least the flow characteristics are fairly stationary. In areas of transient turbulent flow separation, the surface oil flow visualization in the measurement gives an impression of the mean flow structure, which partially differs from the snapshots based on the wall shear stress vector field by the CFD simulation. Averaging of multiple simulated time steps could potentially increase the comparability in those areas. Another difficulty in the visualization method in the measurement lies in the process of image making, since the brightness strongly influences the result and reflections may obscure areas of the picture. All in all, this comparison enables a qualitative visual validation of the flow field at least at the surface of the tower in addition to the validation via the surface pressure, which will be discussed in the following part.

In the following part the calculated surface pressure with the SE-model under 4 $\frac{\mathrm{m}}{\mathrm{s}}$ wind will be compared to the experimental data obtained under the same conditions based on the concept of similitude. At first in fig. 4.20 a qualitative comparison of the temporal signals obtained from the measurement and SE4DDES model is shown at the cavity center probe positions p_{k0}, p_{k5} and p_{k10}.

Especially at the southern (p_{k0}) and north-western (p_{k10}) cavity the simulated time series agree fairly well with the measurement. At the north-eastern cavity (p_{k5}) at some points in the time series larger gradients and pressure fluctuations can be observed in the simulation. What becomes visible in the time series data comparison is the discrepancy between the sampling rate in the measurement and the simulation. The measurement data was sampled with a sampling frequency f_s of 1000 Hz, which is fairly high in the model environment but due to the concept of similitude results in a comparatively coarse sampling rate of 0.57 Hz in the full scale of the tower as the sampling rate follows the

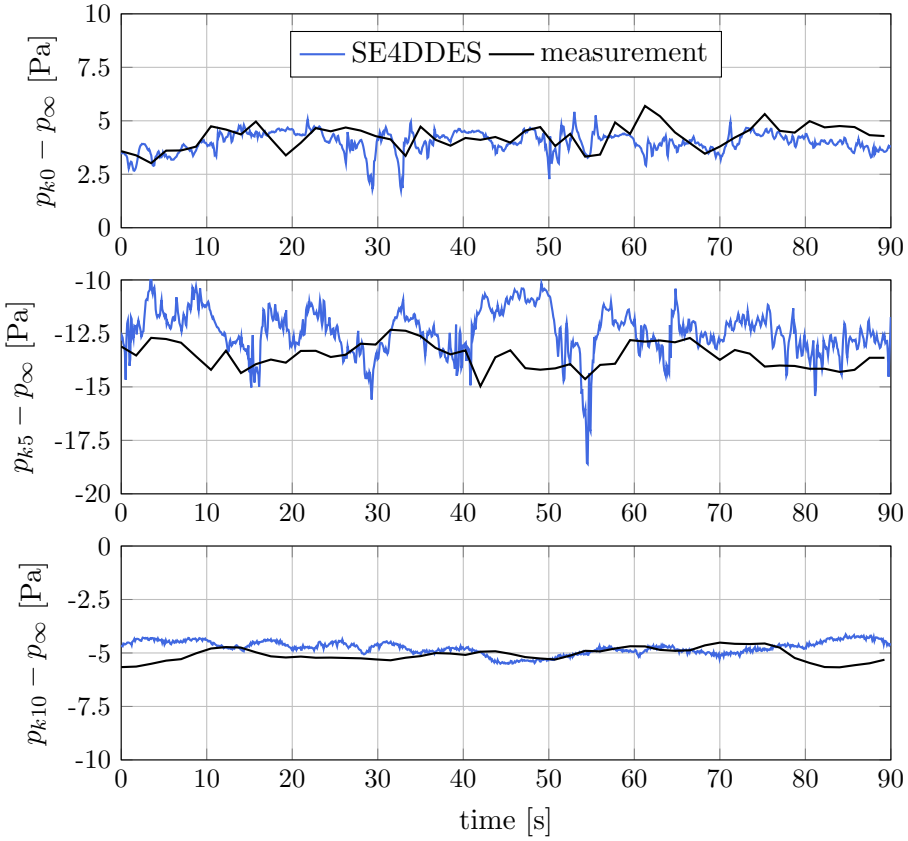

Figure 4.20: Pressure time series calculated by the SE4DDES model and obtained from the measurement, both displayed for the probes at the center of the southern (p_{k0}), north-eastern (p_{k5}) and north-western cavity (p_{k10}).

Strouhal-similitude by eq. (4.1).

$$St = \frac{f_{s,M} D_M}{u_M} = \frac{f_{s,F} D_F}{u_F} \tag{4.1}$$

In fig. 4.21 the comparison of the measured and calculated mean and root mean square (RMS) pressure values at each probe within the cavities is shown. In addition to the results obtained from the transient DDES model, the mean pressure at each probe location obtained by the stationary RANS simulation is added in the lower part of fig. 4.21.

As discussed before, the receiver cavities experience three different relative incident angles, which is also reflected by the level of agreement in the pressure fluctuation, quantified by the RMS value, which is displayed in the upper part of fig. 4.21. The highest agreement in the RMS value with the measurement can be observed in the wake of the tower (north-western cavity) with an average deviation from the measurement of less than 0.1 Pa. As presented in the evaluation of the integral length scale with respect

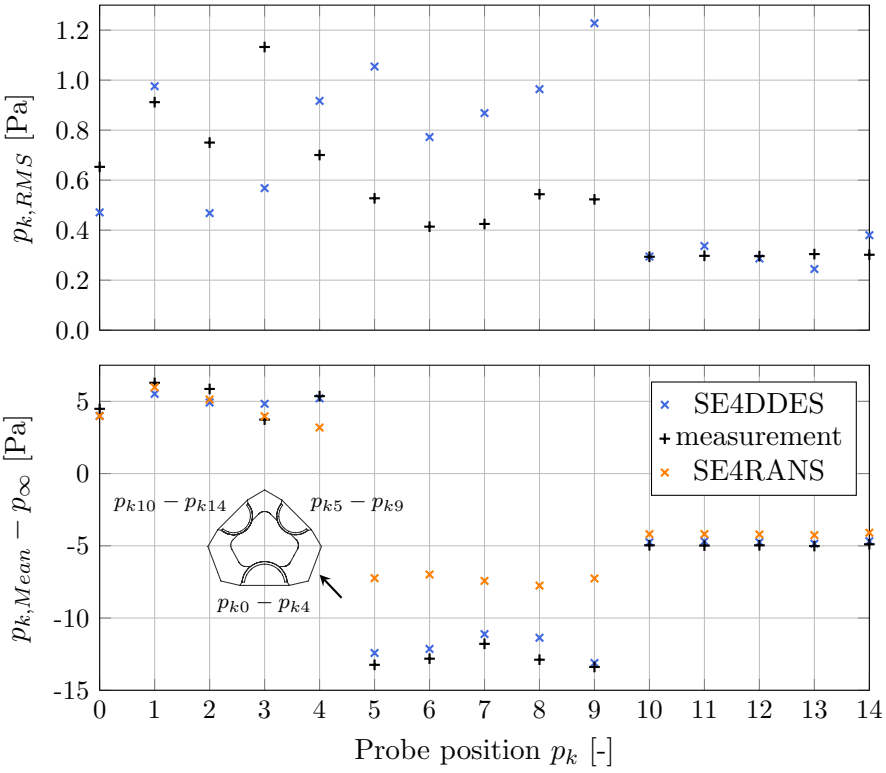

Figure 4.21: Model validation via pressure RMS and mean values for the case of 4 $\frac{\text{m}}{\text{s}}$ wind speed from south-eastern direction. Simulation results calculated by the SE4DDES model (RMS and mean pressure) and the SE4RANS model (mean pressure) are displayed in addition to the measurement data.

to the grid size (cf. fig. 3.15), the grid sizing in the wake cavity allows for the highest resolution of turbulent scales in the spectrum which explains the high level of agreement in the pressure RMS value.

At the southern cavity the deviation from the measurement varies between 0.1 and 0.6 Pa. At the p_{k1} probe, which encounters direct inflow, the agreement is the highest with a deviation of only 0.1 Pa in the RMS value. At p_{k0}, p_{k2} and p_{k3} the CFD model under-predicts the RMS value with the largest deviation at p_{k3} with 0.6 Pa.

At the north-eastern cavity the RMS value calculated by the DDES model is systematically higher then the values obtained from the measurement. Based on the measurement data, which mainly contains the surface pressure and the visualization of the surface flow, it is difficult to interpret the deviation at this cavity. Still two possible hypotheses can be named for the deviation in the pressure fluctuation. The surface pressure fluctuation inside the north-eastern cavity is mainly influenced by the flow separation at the cavity opening and the vortex body interaction with the surface. A possible reason is an over-prediction of the separation induced pressure fluctuations due to the relatively coarse grid spacing. As presented in fig. 3.15 the ratio of the integral length scale with

respect to the grid spacing is comparatively low in the area of flow separation at the north-eastern cavity opening with values of $\frac{l_0}{\Delta}$ of less than 4 which may lead to the observed behavior.

As mentioned before the temporal resolution in the measurement data is comparatively low (cf. fig. 4.20) which leads to the issue, that higher frequency contributions of the signal are not captured by the measurement. As the surface pressure at the north-eastern cavity is heavily influenced by the flow separation at the tower it contains comparatively high frequency contributions which are not captured by the recorded time series of the measurement. This potentially contributes to an under-prediction of the RMS value in the measurement, but the grid spacing is assumed to be the main reason for the observed deviation.

The mean pressure in fig. 4.21 calculated by the DDES model agrees very well with the measured values at each probe. The average deviation from the mean pressure in the wake cavity is 0.2 Pa, at the southern main cavity 0.7 Pa and at the north-eastern cavity 0.8 Pa. The largest deviation from the measurement can be observed in the north-eastern cavity at p_{k8} with an absolute deviation of 1.5 Pa. The SE4DDES case was evaluated over 56000 time steps which corresponds to a simulation time of 96.0 s.

Compared to the transient DDES model the stationary RANS model yields comparable results in the mean pressure at the north-western and southern cavity with an average deviation from the measurement of 0.8 and -0.7 Pa respectively. The RANS model tends to overestimate the mean pressure in the north-eastern cavity by an average of 5.5 Pa which is substantially higher than the mean pressure calculated by the DDES model. The mean pressure in the RANS model was obtained by averaging the latest 3000 iterations.

In order to further understand the deviation in mean pressure between the RANS and DDES model at the north-eastern cavity, the flow field is visualized on horizontal planes at the middle of each cavity. In fig. 4.22 the velocity and pressure are visualized on those horizontal slices.

The slice values are not monitored during the transient DES, so a comparison of the instantaneous values is made here. As quantitatively shown in fig. 4.21 the pressure in the southern and north-western cavity is at a comparable level within the two models. At the north-eastern cavity the reason for the over-prediction in the surface pressure by the RANS model can be identified, which is the failure to adequately model the flow separation at the north-eastern tower edge. In the RANS model the flow is deflected away from the cavity while in the DDES model the eddies originating from the separation point are (partially) resolved due to the DES approach and enter the cavity leading to a local reduction in the surface pressure.

When comparing the results from the RANS to the DDES model, the mean, maximum and minimum velocity magnitude in the cavity is under-predicted by the RANS simulation by approximately 50.0 %. This trend is also visual in the vorticity, which is defined as the curl of the velocity field. To enable a comparison of cases at different wind speeds, the non-dimensional vorticity $\frac{\omega D}{u_\infty}$ is introduced here. In table 4.5 slice values are summarized, only including the flow field that is enclosed inside the cavity. The evaluation of the vorticity reveals that the RANS model calculates a much lower vorticity

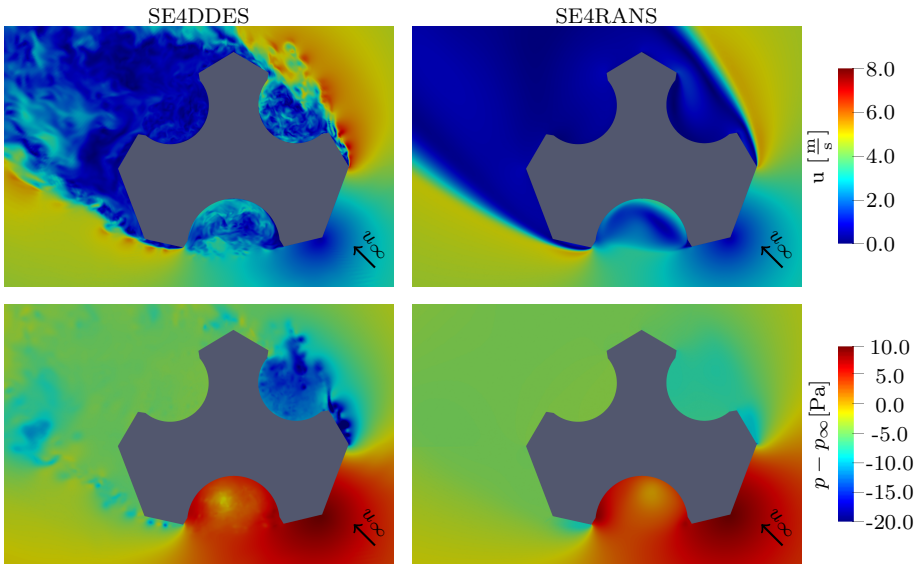

Figure 4.22: Visualization of the instantaneous velocity (upper part) and pressure (lower part) on a horizontal slice at the middle of the receiver under 4 $\frac{\text{m}}{\text{s}}$ wind speed from south-eastern direction. Displayed are the results calculated by the SE4DDES model (left, at $t = 133.6\,\text{s}$) and the SE4RANS model (right, at the final iteration).

in the north-eastern cavity as the separated vortices are not modeled adequately due to the Reynolds-averaging. The spacial averaged vorticity in the north-eastern cavity calculated by the RANS model is 75.2 % lower compared to what is calculated by the DDES model. Compared to the north-eastern cavity, in the north-western and southern cavity the mean vorticity calculated by the RANS model is much closer to the results based on the DDES model but still the vorticity is systematically underestimated by the RANS model. In the SE4DDES model the average magnitude of the vorticity is significantly higher in the north-eastern cavity compared to the other cavities which accounts for the higher RMS values observed in fig. 4.21.

In addition to the pressure evaluation in the temporal domain, an analysis in the frequency domain was undertaken. For this a fast Fourier transform (FFT) of both the measured and simulated pressure signals is performed using Welch's method [123] to calculate the power spectral density of the surface pressure (S_{pp}) and its frequency distribution. The FFT was performed using segments of equal distance, with a Hann windowing function and an overlap of 50.0 %. The Hann windowing function here is used to reduce spectral leakage due to the finite nature of the signal (for a detailed explanation of windowing functions cf. [124]). In fig. 4.23 the power spectral density of the pressure signal at each center of the cavity is shown for the measurement data and the results obtained from the SE4DDES model.

At the southern cavity (p_{k0}) the main peak in the frequency spectrum matches fairly well at a Strouhal number of around 0.31 in the simulation and 0.35 in the measurement.

Table 4.5: Vorticity magnitude $|\omega|$ evaluated on horizontal slices at the middle of each receiver based on the results by the DDES model (at 133.6 s) and the RANS model (at the final iteration).

	S			NE			NW		
case	mean $\|\omega\|$	max $\|\omega\|$	min $\|\omega\|$	mean $\|\omega\|$	max $\|\omega\|$	min $\|\omega\|$	mean $\|\omega\|$	max $\|\omega\|$	min $\|\omega\|$
SE4DDES	13.01 $\frac{1}{s}$	969.82 $\frac{1}{s}$	0.04 $\frac{1}{s}$	18.32 $\frac{1}{s}$	1673.92 $\frac{1}{s}$	0.21 $\frac{1}{s}$	4.61 $\frac{1}{s}$	507.69 $\frac{1}{s}$	0.06 $\frac{1}{s}$
SE4RANS	6.99 $\frac{1}{s}$	425.02 $\frac{1}{s}$	0.06 $\frac{1}{s}$	4.54 $\frac{1}{s}$	303.61 $\frac{1}{s}$	0.06 $\frac{1}{s}$	3.09 $\frac{1}{s}$	167.04 $\frac{1}{s}$	0.04 $\frac{1}{s}$

At the north-eastern cavity (p_{k5}) the agreement in the frequency spectrum is not that satisfactory as expected by the qualitative comparison of the time series data at fig. 4.20. The main peak in the CFD signal at St ≈ 0.61 is not visible in the measurement data. As discussed before the discrepancy might be attributed to the grid spacing in the area of flow separation. The cavity surface in the wake of the tower (p_{k10}) is not directly influenced by vortex shedding, which is the cause for the absence of a dominant peak in the frequency spectrum. The agreement in the slope of the decay of the power spectral density is very similar between the measurement and the simulation, which is the case at all probe positions.

There are systematic differences between the measurement and simulation conditions that make the comparison in the frequency domain difficult in the given case. As mentioned before, the sampling rate in the measurement data compared to the simulation is very coarse which results in a non-dimensional cut-off frequency due to the Nyquist criterion of around $\frac{fD}{u_\infty} \approx 2.5$. The average time step in the SE4DDES simulation corresponds to $\frac{fD}{u_\infty} \approx 5100$, which regarding the Nyquist criterion gives a non-dimensional cut-off frequency of 2550. This is the reason for the higher spectral resolution in the high frequency domain of the CFD spectrum. On the other hand, the measurement time is comparatively large which leads to the high spectral resolution in the low-frequency domain of the spectrum obtained from the measurement. Due to the limitations in the computational resources the simulated time is comparatively short with around 96.0 s, which leads to a coarser resolution in the low-frequency domain of the spectrum. Also, regarding uncertainties in the frequency analysis, the background noise of the wind tunnel and its frequency distribution is unknown. To account for this, a rather large number of 24 windowing segments has been chosen in the FFT of the measurement data whereas for the evaluation of the CFD data two windows were used. Another important issue to be discussed in the context of cut-off frequencies in CFD analysis is the influence of grid resolution. The spatial resolution directly specifies the smallest possible size of the vortices to be resolved, which is indicated by a drop in the frequency spectrum. For example Mockett et al. [33] investigated the flow around a cylinder and compared the results to PIV measurements. In the frequency domain of the simulation a fairly sharp drop off could be seen at non-dimensional frequencies of $St \approx 2$, which is attributed by the authors to either the spatial or temporal filtering of the simulation. The absence of a drop of in the frequency domain by the SE4DDES case indicates a sufficiently fine grid resolution in that regard.

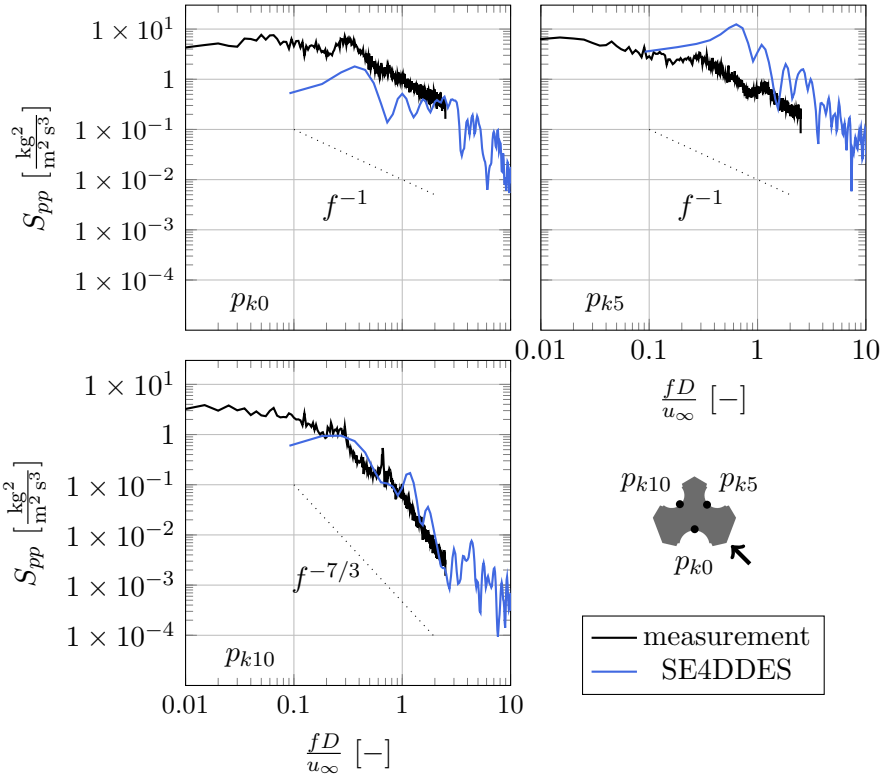

Figure 4.23: Frequency distribution of the power spectral density of the surface pressure S_{pp} at each receiver center probe obtained from the SE4DDES model and the measurement at $Re = 10.46 \times 10^6$ and $\phi = 45°$.

In terms of the grid spacing a study of flow around a generic car side mirror published by Haase et al. [32] revealed that a higher grid resolution does not improve the prediction of the larger, energy-containing structures but rather improve the level of agreement in the high frequency domain of the spectrum. In the study the differences due to varying grid resolutions could be observed at frequencies above $\approx 900\,\mathrm{Hz}$ which is way above the level that is relevant to the open volumetric receiver.

In general, the pressure spectra obtained by the simulation and measurement can be observed to exhibit a similar slope at each probe position which indicates an adequate resolution of the simulation to model the energy containing scales in the spectrum. In the wake of the tower the slope follows the $\sim f^{-7/3}$ scaling as proposed for small-scale turbulence by Kolmogorov [64]. Within the north-eastern and southern cavity the pressure spectra follow a slope $\sim f^{-1}$ within the measurement data and simulations. The deviation from the theroetical isotropic $\sim f^{-7/3}$ behaviour is also observed e.g. by Patwardhan and Ramesh [125] in turbulent boundary layer flow in the proximity of the wall and is explained by shear which leads to a deviation from the isotropic behavior.

In the following part the validation of the E4 model will be presented. The results obtained with the E4 model will be compared to the wind tunnel measurements at an incident angle of $\phi = 90°$ and a free stream velocity u_∞ of $4\,\frac{\mathrm{m}}{\mathrm{s}}$.

In fig. 4.24 the mean and RMS values at the pressure probes obtained with the RANS and DDES with the E-model and from the measurement are visualized. The DDES model is evaluated over a simulation time of 45.1 s. As already discussed in section 3.3.6

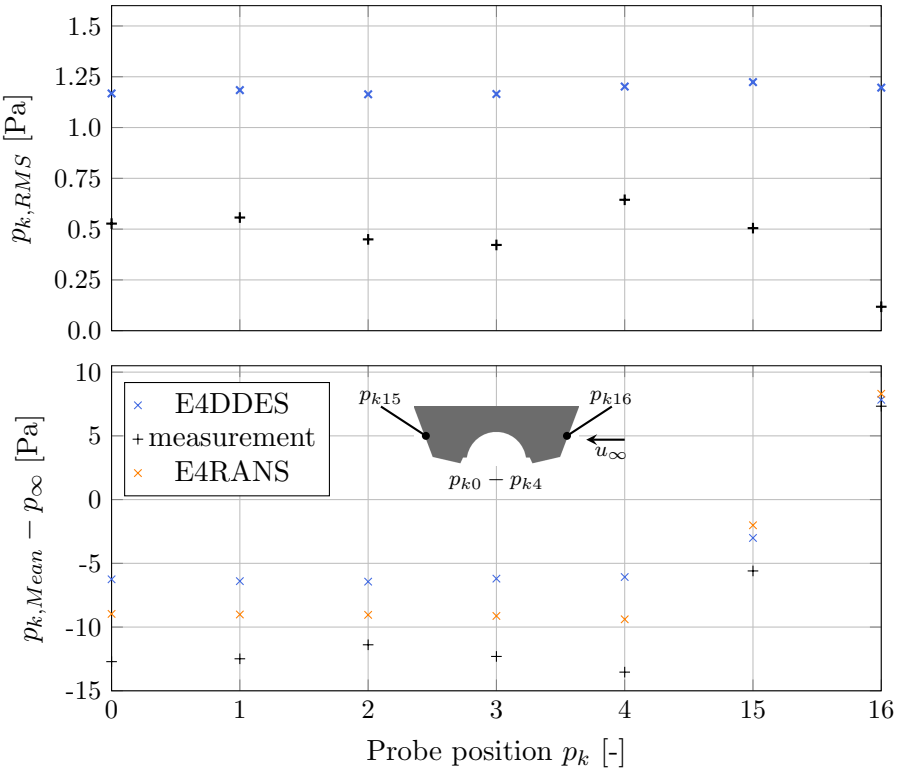

Figure 4.24: Model validation via pressure RMS and mean values for the case of $4\,\frac{\mathrm{m}}{\mathrm{s}}$ wind speed from eastern direction. Simulation results calculated by the E4DDES model (RMS and mean pressure) and the E4RANS model (mean pressure) are displayed.

there are deviations in the pressure field compared to the measurement which are attributed to the assumption of symmetry and an interaction between the symmetry plane and the flow field.

As shown in the lower part of fig. 4.24, the simulation with the DDES model results in an offset of $\approx 6.2\,\mathrm{Pa}$ (average of p_{k0} to p_{k4}) in the mean pressure within the receiver cavity. In the stagnation point of the flow (p_{k16}) that offset is not nearly as pronounced with a difference of $\approx 0.5\,\mathrm{Pa}$. This leads to the conclusion that the difference in the average pressure is caused by the deviation in the aerodynamic resistance of the tower caused by the assumption of symmetry which does not apply to the geometry of the tower but had to be applied in order to reduce the computational costs of the model as

mentioned before. For the RANS model, the deviation in the mean pressure is not as pronounced with an average offset of 3.4 Pa within the cavity.

In addition to the deviation in the mean pressure the pressure signal calculated by the DDES E-model incorporates an overlaying low frequency fluctuation which is not observed within the measurement (as mentioned in section 3.3.6) which accounts for the deviation in the RMS value visualized in the upper part of fig. 4.24. This deviation is present at each pressure probe. Based on the FFT shown in fig. 4.25 the frequency of the overlaying fluctuation can be determined to 0.27 Hz which equates to a dimensionless frequency of 2.33.

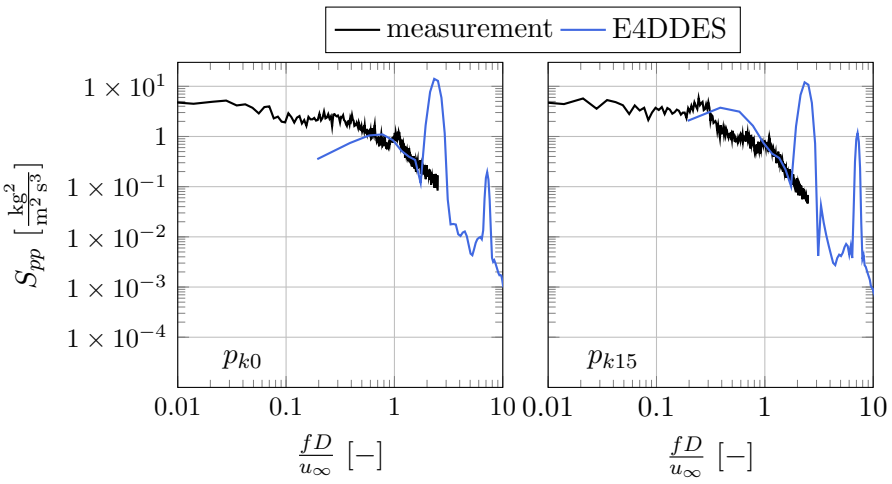

Figure 4.25: Frequency spectra of the surface pressure at p_{k0} and p_{k16} obtained with the E4DDES model. Additionally the pressure spectra obtained from the wind tunnel measurement are displayed at $Re = 10.46 \times 10^6$ and $\phi = 90°$.

An additional test case with a mirrored numerical domain along the symmetry plane and by this omitting the symmetry plane was conducted in order to isolate the influence of the symmetry plane on the flow. The results (as shown in fig. 3.20) reveal that the overlaying fluctuation, which is visual in the peak within fig. 4.25 is caused by the presence of the symmetry plane along the east-western tower axis. Those fluctuations are attributed to the reflective behavior of the symmetry boundary condition and its interaction with the separated flow, which occurs in the transient simulations.

The observations made above highlight the limitations of the numerical model in terms of the applicability of the symmetry plane and the modeling error introduced by the assumption of symmetry along the east-western axis of the tower which effectively alters the aerodynamic resistance and therefore the mean pressure within the receiver cavity. As also remarked in section 3.3.6 those numerical fluctuations naturally do not occur within stationary RANS simulations with the model and therefore the evaluation of the forced convective heat losses is not affected by this. Only the offset in the mean pressure applies to this investigation.

Summary: Model Validation and Verification

The validation is conducted for a case of 4 $\frac{\mathrm{m}}{\mathrm{s}}$ wind speed, without including the receiver flow in the CFD model but instead treating it as a wall, as within the measurement. With the SE-model that includes the whole tower for a case of south-eastern incident flow the model is validated qualitatively and quantitatively. The qualitative validation is based on flow visualization techniques of the near surface flow which shows great agreement in the main eddies and orientation of surface streamlines compared to the measurement. The quantitative validation is based on the surface mean and RMS pressure inside the receiver cavities. The comparison shows excellent agreement in the mean pressure level at all probe positions. The cavities experience different relative incident angles due to their orientation, which is reflected in the level of agreement with the measurements of the pressure fluctuation (quantified by the RMS value). In the wake, the RMS values agree very well, while the RMS values in the cavities exposed to flow separation are slightly overestimated in the simulation. The deviation is attributed to a mesh discretization that is too coarse in these areas. The validation in the frequency domain exhibits comparable slopes in the spectrum, which indicates that the rate of decay in turbulence is captured by the model. The comparability is limited due to the comparatively short simulation times leading to a low spectral resolution in the low-frequency domain.

The E-model is designed to later on include the receiver flow and is therefore more finely discretized. As a compromise, to bring the computational costs to a manageable range, only half of the domain is simulated with the assumption of symmetry along the east-western axis. This does however alter the aerodynamic behavior of the tower, which shows in a shift in the mean pressure. Also this approach shows its limitations as an overlaying low-frequency fluctuation can be observed in the spectral evaluation and also the RMS value of the surface pressure. The overlaying fluctuation is attributed to the flow interaction with the symmetry boundary condition, as a test with a mesh that is mirrored along the symmetry plane does not exhibit those fluctuations.

4.2.2 Evaluation of the Surface Pressure and Flow Field without the Consideration of the Receiver Flow

A major motivation to conduct CFD simulations of the flow around the solar tower in addition to the wind tunnel measurement is, besides the additional information on several quantities regarding the flow field, the possibility to realize higher wind speeds which can be expected during operation of such a solar tower plant. In addition to the case with 4 $\frac{\mathrm{m}}{\mathrm{s}}$ wind from south-eastern direction a case with 14 $\frac{\mathrm{m}}{\mathrm{s}}$ is simulated as well for a simulation time of 39.3 s. In this section the results obtained with the SE-model for both cases of wind speed will be presented and discussed.

At first a flow visualization via the λ_2-criterion (as presented in section 2.3.5) is undertaken for the DDES cases of 4 and 14 $\frac{\mathrm{m}}{\mathrm{s}}$ wind speed. In addition the results obtained with the RANS model at 4 $\frac{\mathrm{m}}{\mathrm{s}}$ wind speed are displayed as well.

In fig. 4.26 λ_2 iso-surfaces are displayed for $\lambda_2 = -0.5$ from a southern perspective on the main cavity. As mentioned in Dong et al. [81], the choice of the λ_2 value influences

the structure of the iso-surfaces and especially the point of vortex breakdown. The value of -0.5 is chosen heuristically and, most importantly, consistently for each case. The iso-surfaces are colored in the non-dimensional vorticity magnitude $|\omega_d| = \frac{|\omega|D}{u_\infty}$. The

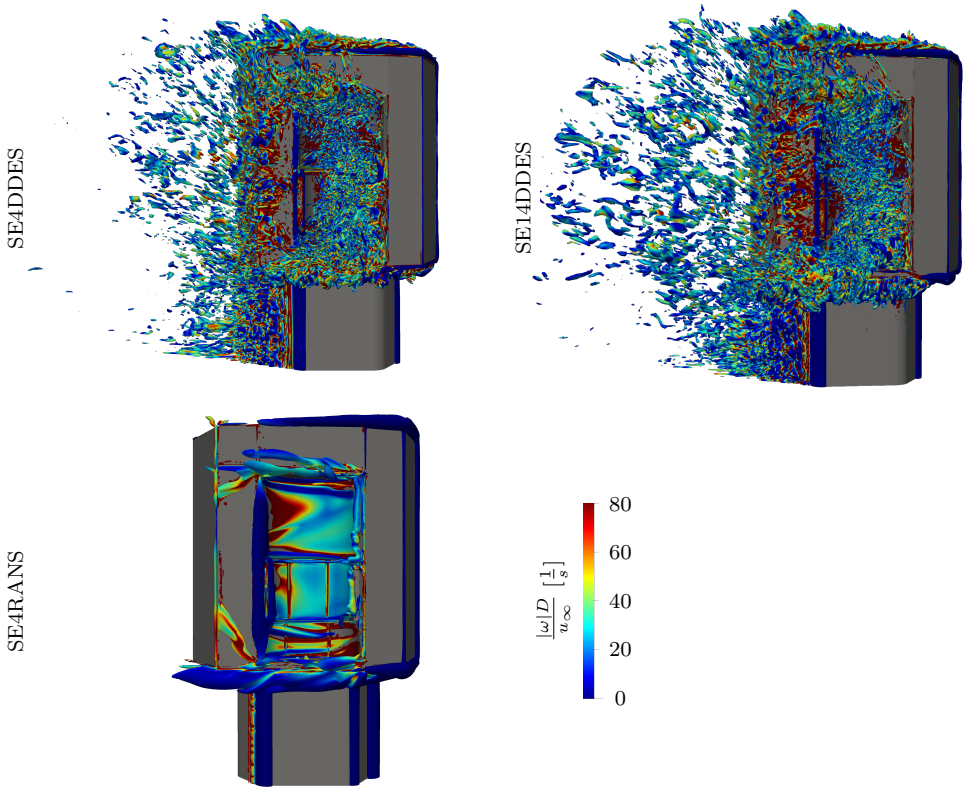

Figure 4.26: Instantaneous λ_2 iso-surfaces ($\lambda_2 = -0.5$) colored in the non-dimensional vorticity magnitude $|\omega_d|$ for the cases SE4DDES (at $t = 133.6\,\mathrm{s}$), SE14DDES (at $t = 39.3\,\mathrm{s}$) and SE4RANS (at the final iteration).

comparison between the SE4RANS and SE4DDES case in fig. 4.26 visually shows the main difference between the flow field calculated by the DDES and the RANS model as the DDES model is able to resolve the small-scale turbulent structures in the flow around the tower whereas this information is lost in the Reynolds-averaging. Nevertheless, similarities between the RANS and DDES model in the location of main vortex cores do exist. For example, the vortices which arise at the top and the bottom of the upper part of the tower are predicted by both models. In the visualization of the RANS results a preliminary vortex breakdown which is attributed to the limitations of the λ_2-method can be seen at the vortex at the roof of the tower. Also, the vortex which arises at the upper part of the cavity opening is predicted by both models as also shown in the surface flow visualization (cf. fig. 4.19). Regarding the DDES cases with different wind speeds, a structurally similar flow field without significant differences in the main vortices can be observed.

To further analyze the differences in the flow field between the two DDES cases, instantaneous snapshots of the non-dimensional vorticity magnitude are evaluated in addition to the λ_2-visualization. In fig. 4.27 the non-dimensional vorticity magnitude is shown for the simulation with 4 (left side) and 14 $\frac{\mathrm{m}}{\mathrm{s}}$ wind speed (right side) at three different horizontal slices. The slices are positioned at the middle of the receiver (s1), middle of the whole cavity (s2) and in the middle of the lower part of the tower (s3). Within the cavities (s1, or s2) fig. 4.27 reveals higher vorticity magnitudes in the north-

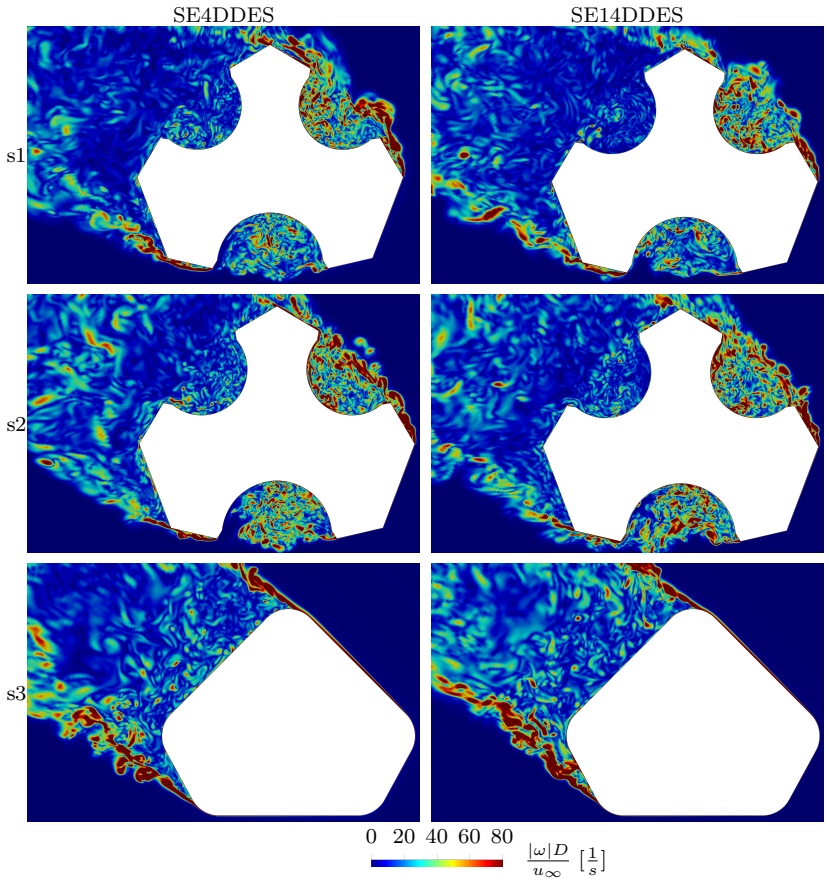

Figure 4.27: Horizontal slices of the instantaneous non-dimensional vorticity magnitude at three different heights: middle of the receiver (s1), middle of the whole cavity (s2) and in the middle of the lower part of the tower (s3). At the left side the results obtained from the SE4DDES model at $t = 133.6\,\mathrm{s}$ and at the right side the results obtained by the SE14DDES model at $t = 39.3\,\mathrm{s}$ are displayed.

eastern cavity in both cases compared to the southern cavity which as mentioned before is the cause for the slightly higher pressure RMS values compared to e.g. the southern cavity. The vortices entering the north-eastern cavity arise from the flow separation at the sharp corner on the eastern side of the tower. In general the non-dimensional vorticity

is very similar for the cases of 4 and 14 $\frac{\mathrm{m}}{\mathrm{s}}$ which indicates the Reynolds-independence of the flow. Also, the separation lines at the tower are Re-independent as the flow separation is defined by the discontinuities in the slope of the tower geometry.

In the following part the surface pressure is evaluated with regards to the mean and RMS values. In order to enable a comparison regarding the surface pressure, in fig. 4.28 the mean and the RMS of the pressure coefficient C_p is visualized for the SE4DDES and SE14DDES case (in analogy to fig. 4.21). The SE4DDES case is evaluated over 56000 time steps which corresponds to a simulation time of 96.0 s while the SE14DDES case is evaluated over 50000 time steps which corresponds to a simulation time of 26.8 s.

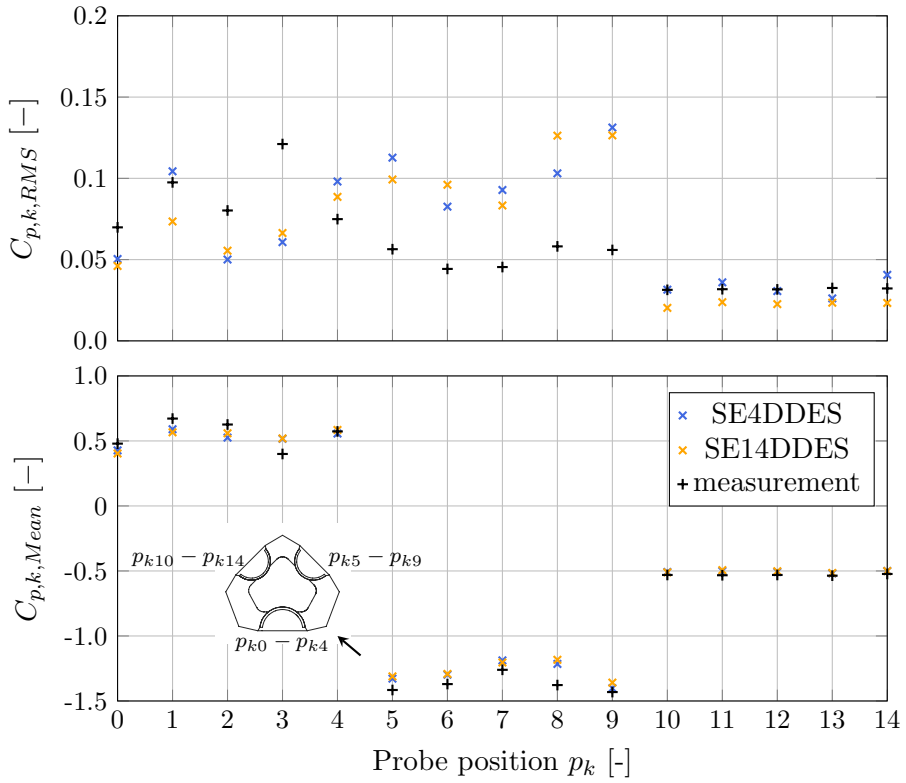

Figure 4.28: RMS and mean pressure coefficient C_p for the case of 4 and 14 $\frac{\mathrm{m}}{\mathrm{s}}$ wind speed from south-eastern direction calculated by the SE4DDES and the SE14DDES model compared to the measurement data at an equivalent wind speed of 4 $\frac{\mathrm{m}}{\mathrm{s}}$.

Regarding the mean pressure coefficient C_p the results obtained by the two models are very similar within the respective cavities with an average relative deviation of 4.2 % in the southern cavity, 1.8 % in the north-eastern cavity and 0.8 % in the north-western cavity between the models. This also applies for the respective deviation from the measurement data which shows that the pressure coefficient is Reynolds-independent within the Re-range and within the uncertainties of the simulation and measurement.

Regarding the RMS value of the pressure coefficient the quantitative agreement between the two models and with the measurement data varies for each cavity. In the southern cavity the relative deviation in the RMS value is very high at the probe at the leeward side of the cavity (p_{k1}) where the RMS value in the SE4DDES case is 42.5 % higher compared to the SE14DDES model. This may be attributed to the difference in the boundary layer and subsequently flow separation at the cavity opening near the southern cavity. The vortices which emerge from that flow separation induce a turbulent flow-structure interaction at the leeward side of the main cavity. It is argued that the difference in pressure RMS value is attributed to a shift in the area where those vortices reach the cavity surface due to the difference in free stream velocity and therefore velocity profile in the boundary layer which separates into the cavity. The relative deviation in the RMS value of C_p lies within 8.5 % for the rest of the probes within the southern cavity. In the north-eastern cavity the scatter in the RMS values between the two cases is the highest with an average relative deviation of 12.3 %. Especially at the leeward side of the north-eastern cavity (p_{k8}) the RMS in the pressure coefficient is relatively increased by 22.5 % at the higher wind speed case which as well as the deviation observed at p_{k1} is attributed to the flow separation at the cavity opening. At the north-western cavity which is in the wake of the tower the RMS value in the pressure coefficient is significantly lower under a free stream velocity of 14 $\frac{\mathrm{m}}{\mathrm{s}}$ with an average relative drop in the RMS value of 31.2 %. The difference in that area can be explained by the lower dimensionless vorticity in the wake cavity as qualitatively seen in the graphical representation in fig. 4.27, as the flow is deviated stronger due to the higher free stream velocity.

In the following part the surface pressure under 4 and 14 $\frac{\mathrm{m}}{\mathrm{s}}$ wind will be compared in the spectral domain by applying a FFT with the same procedure and parameters as presented in the discussion of the results in fig. 4.23. In fig. 4.29 the power spectral density of the pressure signal at the probe positions p_{k1}, p_{k8} and p_{k10} is displayed based on the results with the SE4DDES and SE14DDES model. As expected, higher wind speeds lead to a higher level in the power spectral density in the SE14DDES case compared to the SE4DDES case, which applies to the entire frequency spectrum.

At an incident angle of $\phi = 45°$ the peaks in the frequency spectrum are not nearly as pronounced as for example observed during the measurement at incident angles of 78.8° (relative to the cavity normal axis) as shown in fig. 4.6. In the measurement the low frequency part of the spectrum is resolved with a significantly higher resolution due to the longer evaluation time. Therefore the experimental frequency spectra obtained at the corresponding incident angle are evaluated (cf. fig. C.1) to identify peaks in the spectra and select the probe positions displayed in fig. 4.29. Within the measurement slightly pronounced peaks in the surface pressure spectra at the probe position p_{k3} and p_{k11} can be observed at around $St = 0.19$ and 0.29 respectively. In the north-eastern and the north-western cavity no pronounced peaks in the frequency spectrum can be observed.

The evaluation of the peak frequencies obtained from the simulations is subject to a certain degree of uncertainty due to the comparatively low peak frequencies which require a long simulation time to be resolved in the signal. As visualized in fig. 4.29 at p_{k3} a pronounced peak in the spectrum of the measurement can be observed at $St = 0.19$

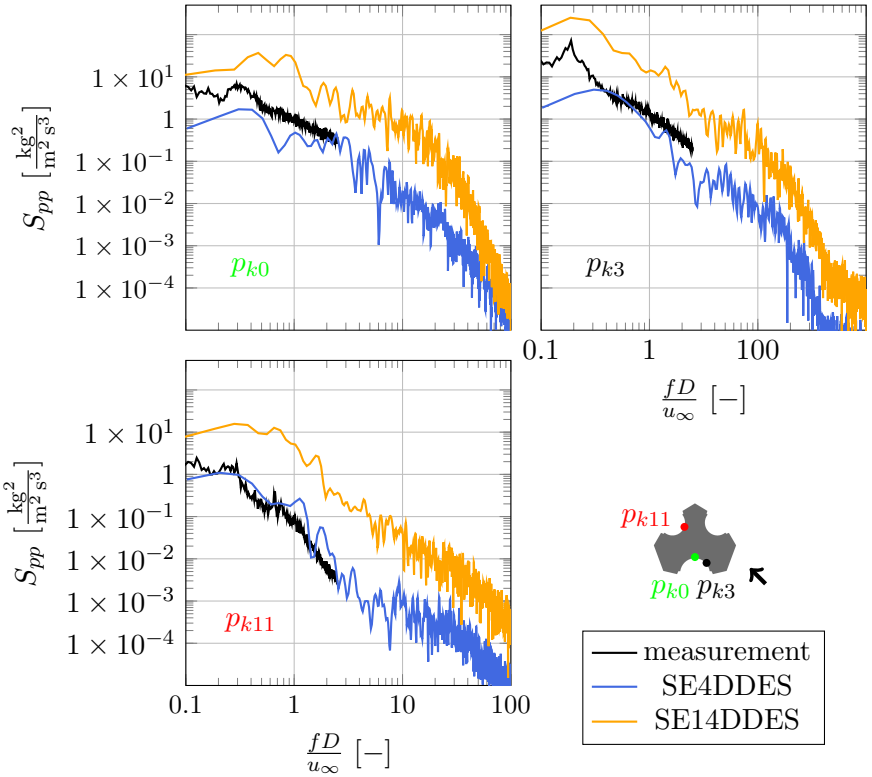

Figure 4.29: Frequency spectra of the surface pressure obtained from the SE4DDES and SE14DDES simulation. Also displayed are the frequency spectra obtained from the wind tunnel measurement for the incident angle and Reynolds number corresponding to the SE4DDES case.

which is not visual within the SE4DDES case but slightly visual in the SE14DDES case. The absence is attributed to the comparatively low spectral resolution in the frequency domain.

At p_{k0} the peak in the measurement matches fairly well with the peak obtained from the SE4DDES case with Strouhal numbers of 0.33 and 0.31 respectively. At 14 $\frac{\mathrm{m}}{\mathrm{s}}$ the peak is also indicated, but cannot be clearly identified due to the low spectral resolution in this frequency range.

The peak in the measurement at p_{k11} at $St = 0.29$ is matched very well at the SE14DDEs case with a non-dimensional frequency of 0.28 while in the SE4DDEs case the peak is not as pronounced.

Within the described uncertainty it can be summarized that the slope in the pressure spectrum matches fairly well. At the given incident angle the north-eastern and north-western cavity does not experience vortex shedding and subsequently no dominant peaks can be observed in the spectrum. At the southern cavity the interaction of shedding vortices with the receiver surface can be observed to some degree e.g. at p_{k3} and even though the peaks are not as pronounced in the simulations as discussed above, the peak

frequencies can be observed to increase with wind speed on average peak frequency in the southern cavity of 0.05 Hz at 4 $\frac{\mathrm{m}}{\mathrm{s}}$ to 0.10 Hz at 14 $\frac{\mathrm{m}}{\mathrm{s}}$.

In fig. 4.30 the dependency of the mean and RMS pressure on the free stream Reynolds number Re at the center of each cavity is shown based on the results by the SE4DDES and SE14DDES model. As shown in the comparison of the results obtained under 4 and 14 $\frac{\mathrm{m}}{\mathrm{s}}$ in fig. 4.28 the mean and RMS of the dimensionless pressure coefficient C_p is Reynolds-independent within the uncertainties of the model which implies a second-degree dependence of the mean and RMS pressure on Re. Therefore in fig. 4.30 an interpolation based on second degree polynomial functions of the RMS and mean pressure obtained from the wind tunnel measurement is shown as well.

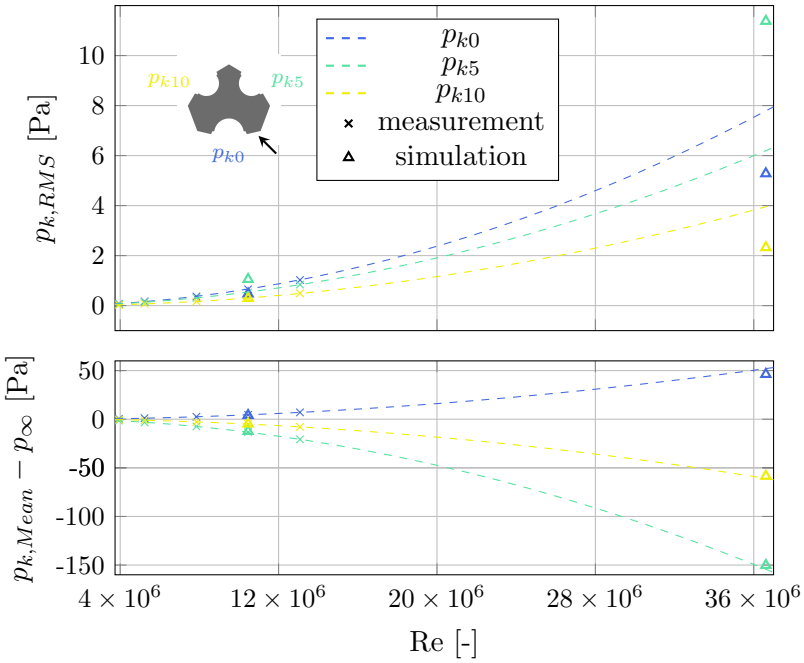

Figure 4.30: Re-dependency of the mean and RMS pressure at the center of each receiver cavity (p_{k0}, p_{k5} and p_{k10}) based on the data obtained from the wind tunnel measurement. Also displayed are the calculated results with the SE4DDES and SE14DDES model.

The agreement of the validation case has already been discussed in section 4.2.1 so at this points the focus will be on the extrapolation for higher wind speeds and the agreement between the simulation and the extrapolated values based on the measurement data. For this comparison, the measurement data has been extrapolated based on a least-square fit second order polynomial function. Regarding the mean pressure the extrapolation for higher wind speeds based on the measurement data is in very good agreement with the simulated results by the SE14DDES model. The deviation from the extrapolated values which were extrapolated solely based on the measurement at Reynolds numbers lower than 13.08×10^6 is lower than 6.0 Pa at each probe with 5.8,

4.1 and 2.4 Pa at the probe locations p_{k0}, p_{k5} and p_{k10} respectively.

The comparison of the RMS values shows a significantly larger deviation between the simulation and the extrapolated measurement in the case of an incident flow at 14 $\frac{\text{m}}{\text{s}}$. Based on the validation case, the agreement between the extrapolated measurement and simulation at 14 $\frac{\text{m}}{\text{s}}$ was expected to be the highest at the north-western cavity. At the southern cavity the level of agreement in the validation case varies along the receiver whereas at the north-eastern cavity the RMS value is systematically overestimated by the simulation compared to the measurement. The deviation between the results obtained by the simulation with 14 $\frac{\text{m}}{\text{s}}$ free stream velocity and the extrapolated measurement agree with what has been shown for the validation case at 4 $\frac{\text{m}}{\text{s}}$ free stream velocity. At the wake cavity (north-west) the simulation underestimates the pressure RMS value slightly with an average deviation of -1.4 Pa. In the southern cavity the simulated RMS value is lower compared to the extrapolated measured value with an average deviation of -2.7 Pa. At the probe position p_{k3} which is positioned on the leeward side of the main cavity the simulated RMS value is -7.2 Pa lower than the extrapolated value. The reason for the discrepancy is assumed to be the shift in the stagnation point of the detached vortices at the higher wind speed compared to the measurement. Due to the increased wind speed the deflection at the south-eastern main cavity edge is stronger which leads to a shift in the stagnation point in the southern cavity. This fact cannot fully be taken into account in the extrapolation solely based on the measurement results. This shift effects the RMS value much stronger than the mean pressure which is less sensitive to the incident angle and more uniform within each cavity in general. At the north-eastern cavity the simulation systematically predicts higher RMS values compared to the extrapolation based on the measurement with an average difference of 6.7 Pa. Nevertheless, the extrapolation allows to quantify the RMS values which have to be expected under increased wind speeds within an acceptable range of uncertainty in order to evaluate the importance in comparison to pressure fluctuations caused by varying incident angles (cf. section 4.1.2) which are significantly higher and more relevant to the operation of the receiver.

Summary: Evaluation of the Surface Pressure and Flow Field without the Consideration of the Receiver Flow

One major purpose of the CFD model is to extend the evaluation of wind-induced surface pressure fluctuations for wind speeds up to 14 $\frac{\text{m}}{\text{s}}$. The results with the SE-model for the cases of 4 and 14 $\frac{\text{m}}{\text{s}}$ exhibit Reynolds-independence in the non-dimensional vorticity in the field and the pressure coefficient at the surface. Also the level of agreement to the measurement in the pressure coefficient is similar for both wind speeds.

In the spectral evaluation it can be observed that the slope in the decay matches fairly well. Within the southern cavity, which is subject to vortex shedding, the peak frequencies can be observed to increase with increasing wind speed (within the aforementioned uncertainty in the spectral resolution of the simulation). At wind speeds of 14 $\frac{\text{m}}{\text{s}}$ the OVR will experience pressure fluctuations, when subject to the flow separation at the tower with an average frequency of 0.102 Hz, while the peak frequencies at 4 $\frac{\text{m}}{\text{s}}$ are lower

at 0.046 Hz on average.

The dependency of the mean and RMS pressure on the Reynolds number can be estimated by a second-degree polynomial function, which despite the uncertainty in in the model, allows an estimate of the severity of pressure fluctuations that the cavity OVR will be subject to under high wind speeds. Based on the extrapolation of the measurement data, RMS values of approximately 8 Pa are to be expected.

4.2.3 Influence of the Receiver Flow and its Interaction with Ambient Wind on the Surface Pressure

In this section the simulation with the E-model where (in addition to the ambient wind) the receiver flow is considered and its influence on the surface pressure fluctuations in the receiver cavity is discussed. As mentioned in section 1.4 it was assumed that surface pressure fluctuations are primarily caused by the ambient wind and that the receiver flow plays a minor role. This hypothesis will be evaluated in the following. Within the E-model the receiver flow is modeled with the agglomerate approach described in section 3.3.5 while ambient wind is considered from an eastern incident angle ($\phi = 90°$) at 4 $\frac{\mathrm{m}}{\mathrm{s}}$.

As the inclusion of the receiver flow was not possible in the experimental set-up, the receiver modeling approach is validated by a comparison to published work by Stadler et al. [49], as discussed in the uncertainty analysis in section 3.3.7. It is concluded that the model in this study yields comparable results in the total air return ratio for the same design point conditions with an absolute deviation in the ARR of 1.2 % which lies within the level of the discretization error in the grid independence study. In the agglomerate approach by Stadler et al. [16] the area ratios between the hot and return air cells corresponds to the ratio within the actual HiTRec geometry and therefore the respective velocities are comparable to the actual geometry. As discussed in section 3.3.7 the pressure fluctuations caused by the receiver flow obtained with this modeling approach pose a conservative estimate due to the coarsening of the return air outlets.

In fig. 4.31 the time series of the surface pressure at each probe position are visualized which are obtained by the simulation with the E4DDES model, that includes the receiver flow and the measurement where the receiver flow is not considered. In the simulation a maximum Courant number of 1 is prescribed which leads to a time step in the order of 0.000248 s.

The pressure at probe p_{k16} in the stagnation area of the flow it not visually influenced by the receiver flow and consequently the average pressure matches very well with the measurement (within the deviation introduced by the symmetry plane, as discussed before). At the beginning of the simulation, the pressure at p_{k15} is about 2.5 Pa above the measurement value but tends to approach the pressure level in the measurement with increasing simulation time. In a qualitative manner the pressure inside the cavity depends on the location within the cavity due to local differences in the impact of the ambient wind and especially the impact of the external return air which is ejected from below the receiver. At p_{k2} which is located about 3.9 m above the external return air

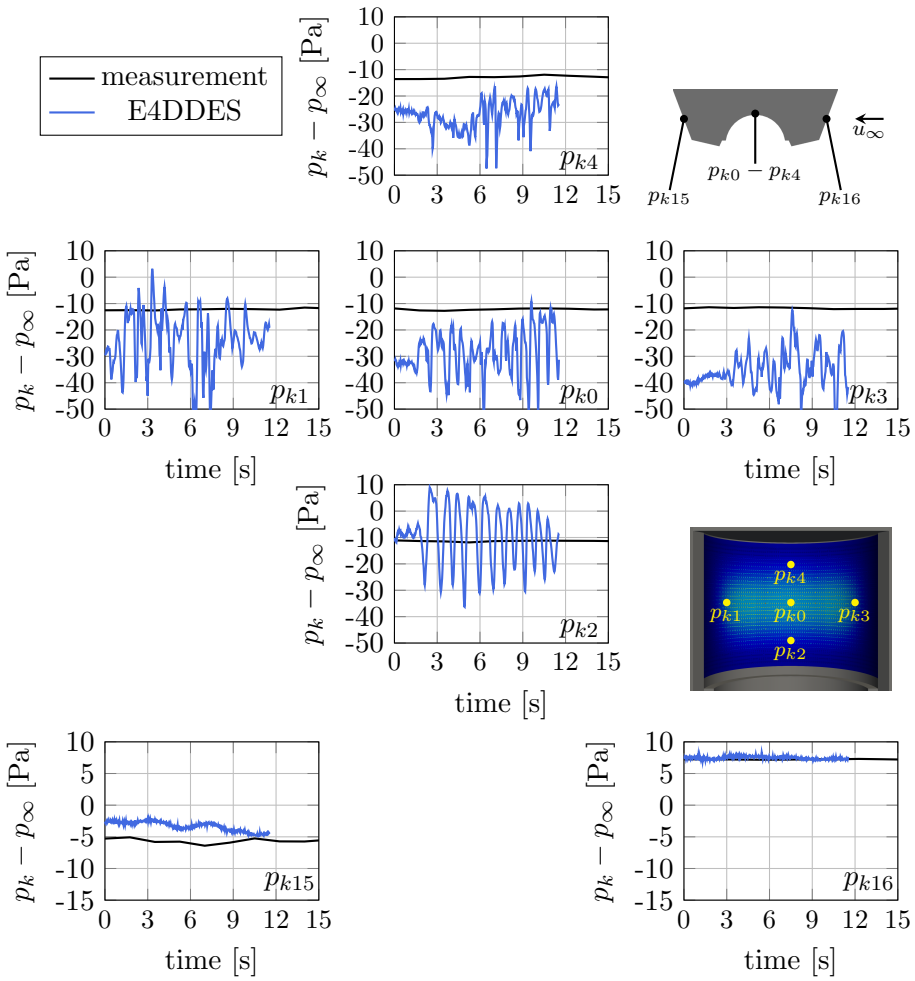

Figure 4.31: Pressure time series obtained from the E4DDES model including the receiver flow and from the measurement data at $\phi = 90°$ and $u_\infty = 4\,\frac{\mathrm{m}}{\mathrm{s}}$ at each probe within the southern cavity (p_{k0} to p_{k4}), at p_{k16} in the stagnation area and at p_{k15} on the wake side of the tower.

outlet surface the flow field and consequently the surface pressure is visually dominated by the external return air flow which shows in the higher average pressure and the qualitatively more periodically fluctuation compared to the other probe positions within the cavity. The external return air enters the numerical domain with a Reynolds number of 1.36×10^5 based on the depth of the external return air outlet and the average outflow velocity. What can already be noted by the time series data is that the pressure fluctuations under wind, when considering the receiver flow significantly exceed those caused by the mere presence of ambient wind at $4\,\frac{\mathrm{m}}{\mathrm{s}}$.

As discussed in the validation of the E-model in section 4.2.1 and the uncertainty analysis in section 3.3.7, the assumption of symmetry along the east-western axis introduces

a modeling error. With the case without considering the receiver flow it could be shown that this assumption leads to a shift in the average pressure within the cavity of $\approx 6.2\,\mathrm{Pa}$ which consequently also has to be assumed to apply to the pressure signals in fig. 4.31, which are additionally superposed by the receiver flow. What is fairly remarkable is that the overlaying pressure fluctuation observed in the E-model without the receiver flow, that is attributed to the flow interaction with the symmetry plane (cf. section 4.2.1) is not present at any probe position in this case. This leads to the conclusion that the presence of the receiver flow hinders the evolution of those numerical fluctuations.

In fig. 4.32 the RMS and mean values obtained from the pressure time series displayed in fig. 4.31 are evaluated. In addition the mean pressure obtained with the precursor RANS simulation is displayed.

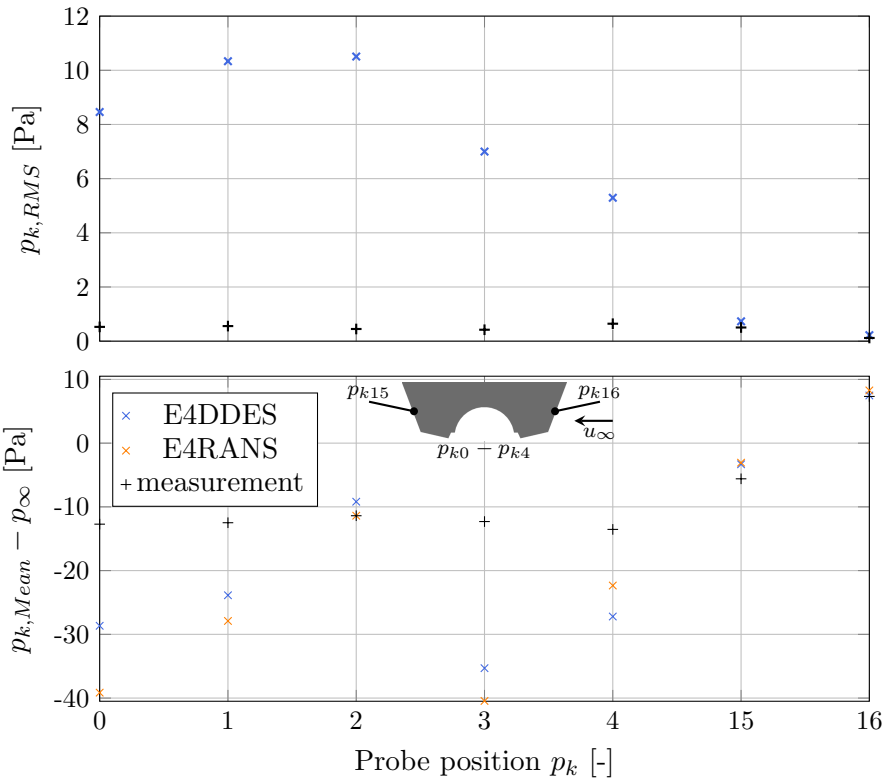

Figure 4.32: Pressure RMS and mean values for the case of $4\,\frac{\mathrm{m}}{\mathrm{s}}$ wind from eastern direction. Simulation results obtained by the E4DDES model including the receiver flow (RMS and mean pressure) and the E4RANS model including the receiver flow (mean pressure) are displayed. In addition the results obtained from the measurement are shown.

As shown in fig. 4.32, the largest RMS values can be observed at p_{k2} with up to 10.5 Pa which is mainly caused by the external return air and its interaction with the receiver flow. At p_{k1}, which is placed on the windward side of the receiver, RMS values of

10.3 Pa are recorded which are caused by the interaction of the separated ambient wind and the receiver flow in that area. In addition to the outflow velocities of the return air the temperature difference between the return air and ambient air induces a convective updraft which further contributes to the velocity and pressure fluctuations in the vicinity of the receiver. Due to the heat transfer within the receiver between the hot and return air stream, which is considered in the outflow temperature of the internal return air (cf. section 3.3.5), the return air outlet temperature is observed to vary between $\approx 280\,°\mathrm{C}$ and $\approx 670\,°\mathrm{C}$. Due to the mass flow distribution at the receiver (cf. fig. 3.19) internal return air outflow velocities range from around $1\,\frac{\mathrm{m}}{\mathrm{s}}$ to $28\,\frac{\mathrm{m}}{\mathrm{s}}$. As visual in fig. 4.32, the presence of the receiver and return air flow lead to a shift in the average pressure of up to $-23.0\,\mathrm{Pa}$ at p_{k3} compared to the measurement without considering the receiver flow. As the return air conditions of the receiver are similar at p_{k1} and p_{k3}, the lower mean pressure at p_{k3} is attributed to the local impact of ambient wind. The probe located in the vicinity of the external return air outlet (p_{k2}) poses an exception to this with a slightly increased average pressure of 2.2 Pa compared to the measurement.

The RMS values at the probe positions which are placed outside the cavity are not significantly increased by the receiver flow with a deviation in the RMS value compared to the measurement of less than 0.2 Pa. Regarding the average pressure at the probe positions outside the cavity the deviation in the stagnation area is very low with 0.2 Pa. Compared to the measurement, the average pressure in the wake (p_{k15}) is about 2.3 Pa above the value obtained from the measurement which is in alignment with the validation case without the receiver flow (cf. fig. 4.24) and as discussed in that context is attributed to the assumption of symmetry which alters the aerodynamic resistance of the tower.

Due to the computational restrictions, the simulation time is relatively short, which does not facilitate a statistically significant analysis in the frequency spectrum, especially in the low-frequency domain, which is why a spectral analysis of the surface pressure under the consideration of the receiver flow is omitted.

Based on the results shown in fig. 4.31 and fig. 4.32 and despite the restrictions observed with the validation case with the E-model a few conclusions can still be drawn. The hypothesis that ambient wind is the dominant influence on the surface pressure within the cavity is disproven, at least under a constant incident angle flow at relatively low wind speeds of $4\,\frac{\mathrm{m}}{\mathrm{s}}$. The RMS values within the cavity due to the flow conditions induced by the momentum of the receiver flow, the convective updraft due to the density difference between the return and ambient air and the lateral wind at $4\,\frac{\mathrm{m}}{\mathrm{s}}$ induce pressure fluctuations in the order of 5.2 to 10.5 Pa quantified by the RMS value which significantly exceed the RMS values under the mere presence of wind, which for this incident angle are way below 1 Pa.

As presented in fig. 4.31 the overlaying low-frequency fluctuation observed in the case without considering the receiver flow cannot be observed when the receiver flow is included in the simulation. What has to considered though is the shift in the average pressure due to the application of the symmetry plane which has to be included in the modeling error of the average pressure. Based on the observations discussed with the E-model without receiver flow, the pressure RMS values in fig. 4.32 should be foreseen with an uncertainty in the order of the observed low-frequency fluctuation (2.3 Pa) of

the E-model validation case.

Summary: Influence of the Receiver Flow and its Interaction with Ambient Wind on the Surface Pressure

With the E-model the receiver flow and return air flow have been included in the evaluation of wind-induced surface pressure fluctuations. The receiver flow through the porous absorbers is modeled with a simplification by treating it as a continuous cylindrical surface instead of resolving the porous structures. Still the discretization inside the cavity and subsequent mesh count prevents a simulation of the whole tower due to the restrictions in computational resources. Therefore only half of the domain is modeled by assuming symmetry along the east-western axis. In the validation case an overlaying low-frequency fluctuation caused by the interaction of ambient wind with the symmetry plane was present. Those fluctuations can not be observed here, as they do not evolve when the receiver flow is present.

The presence of the receiver flow lowers the mean pressure inside the cavity except for the area close to the external return air outlet. In that area the pressure characteristic is prescribed by the external return air flow with a more evenly fluctuation and increased average pressure. It can be summarized that, compared to the receiver flow, wind is not the dominant influence on the surface pressure fluctuations under constant incident angle flow. When the receiver flow is considered in the model, RMS values up to 10.5 Pa occur which extends the maximum observed in the entire measurements without the receiver flow by a factor of 5. The highest fluctuations occur on the leeward part of the cavity where the eddies emerging from the flow separation of ambient wind at the cavity opening interact with the receiver flow and close to the external return air outlet. As expected, the pressure at the probe positions outside the cavity is not influenced by the receiver flow. Due to short simulation times an evaluation in the frequency domain is omitted at this point.

4.2.4 Wind Influence on Forced Convective Heat Losses at the Open Volumetric Cavity Receiver

In this section the focus lies on the investigation of the wind influence on the convective losses during an operation of the cavity receiver. The case of lateral wind on the main receiver has been chosen as presented in section 3.3.1. In contrast to closed-loop surface receivers, which have been the focus in most studies (cf. section 1.3.2), at the OVR the interference of ambient wind with the returned warm air is the mechanism of interest in the discussion of convective losses. The convective losses under wind can be quantified by the air return ratio (ARR) and the receiver inlet temperature.

The boundary conditions and assumptions for the simulations in this section with and without wind are described in detail in section 3.3.5. The air return ratio is calculated by a mass flow weighted average of the return air concentration ξ at the receiver hot air cells. At design point conditions 50 % of the return air is returned externally, which is denoted by the elr factor.

As shown in eq. (2.13), the ARR is defined as the ratio of the returned warm air mass flow in relation to the total returned air mass flow (or hot air mass flow), which consists of internal return air, external return air and ambient air (in case of an incomplete air return). For the receiver-averaged evaluation of the internal (ARR_{ilr}) or external air return ratio (ARR_{elr}) this definition is adjusted in the way that the returned warm air mass flow ($\dot{m}_{ilr,returned}$, or $\dot{m}_{elr,returned}$) is related to the respective return air mass flow ($\dot{m}_{ilr}$, or $\dot{m}_{elr}$) instead of the total returned mass flow.

$$ARR_{ilr} = \frac{\dot{m}_{ilr,returned}}{(1-elr)\dot{m}_h} = \frac{\dot{m}_{ilr,returned}}{\dot{m}_{ilr}} \quad ARR_{elr} = \frac{\dot{m}_{elr,returned}}{(elr)\dot{m}_h} = \frac{\dot{m}_{elr,returned}}{\dot{m}_{elr}} \tag{4.2}$$

In local (zonal) evaluations, this adjustment is not applied, as locally the external and internal return air concentration can reach values up to 100 % (based on eq. (2.13)) when related to the local hot air mass flow. The adjustment in the receiver-averaged values has to be kept in mind when comparing local and receiver-averaged values of the air return ratios.

A constant irradiation at design point conditions is assumed with a total intercepted irradiation of 125.0 MW and an additional 14.4 MW of spillage due to reflection from adjacent walls (cf. visualization of the distribution in fig. 3.19). The amount of spillage has been adopted from the work by Stadler et al. [49]. As mentioned before, at design point conditions the return air mass flow is divided equally between the internal and external return air system.

At first the wind influence on two reference configurations regarding the distribution of externally returned air are investigated at 4 and 8 $\frac{\mathrm{m}}{\mathrm{s}}$ wind speed at design point conditions. The first reference elr distribution (ref_01) constitutes a uniform distribution with an outflow velocity of around 11.9 $\frac{\mathrm{m}}{\mathrm{s}}$, while the second reference distribution (ref_02) is adjusted with a circumferential weight factor to match the vertically integrated receiver mass flow distribution. This results in an external return air distribution as visualized in fig. 4.33 with an increased mass flow in the center on the elr outflow surface.

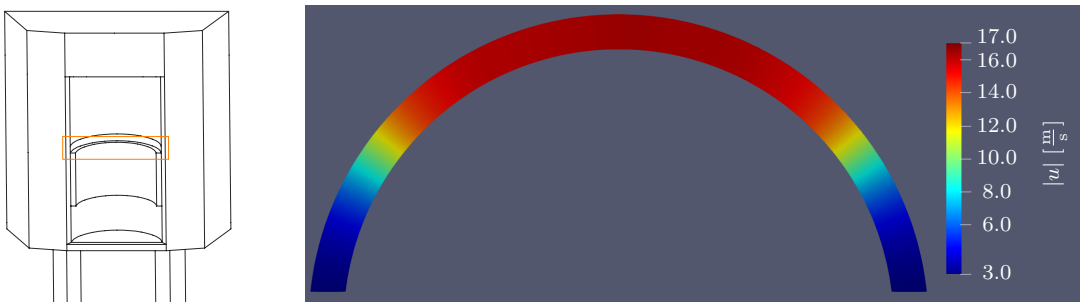

Figure 4.33: Continuous elr distribution with a weight factor based on the vertically averaged receiver mass flow (ref_02).

In addition, off-design conditions are investigated with a case of reduced irradiation (60 %) and a case with a reduced external return air factor (25 %) and therefore increased internally returned mass flow. In the table 4.6 the cases which will be discussed in this

section and the parameters in the model are summarized. The cases under windless con-

Table 4.6: Receiver parameters of the cases, which will be analyzed in terms of the wind influence on convective heat losses.

case name	$\dot{Q}_{inc}$	$T_{h,out}$	elr-factor	elr distribution
ref_01	125 MW	670 °C	50 %	uniform
ref_02	125 MW	670 °C	50 %	cf. fig. 4.33
q60	75 MW	670 °C	50 %	cf. fig. 4.33
elr25	125 MW	670 °C	25 %	cf. fig. 4.33

ditions are all conducted with the set of boundary conditions described in section 3.3.5 which adjust the receiver mass flow in order to establish the given hot air target temperature $T_{h,out}$. In the case of reduced irradiation the intercepted irradiation is globally reduced by 40 % while maintaining the same distribution. Due to the same target hot air temperature this results in a reduced receiver mass flow of approximately 129 $\frac{\text{kg}}{\text{s}}$ and subsequently reduced return air mass flow. The case of reduced elr factor is calculated at the design point intercept which yields a total receiver mass flow of approximately 230 $\frac{\text{kg}}{\text{s}}$ of which 173 $\frac{\text{kg}}{\text{s}}$ are returned internally and 57 $\frac{\text{kg}}{\text{s}}$ externally.

The following parameter study regarding the wind influence on the forced convective losses in the cavity receiver are based on stationary RANS simulations. It is argued that the stationary RANS approach is applicable even if it does not resolve (but model) the turbulent flow interaction between wind and the receiver and return air flow because the quantity of interest here is the average convective loss instead of its instantaneous fluctuations. Furthermore, as the aim here is to conduct a parameter study to compare different configurations, the requirements for accuracy of the absolute values is not as important as the relative difference between the configurations. Additionally, a parameter study of this magnitude would not have been possible with the available computational resources when transient scale resolving simulations were conducted over a statistically significant simulation time.

To further qualify the applicability of the RANS approach the results of a steady-state RANS simulation are compared to a transient DES for a case of 8 $\frac{\text{m}}{\text{s}}$ wind with the uniformly distributed external return air. The transient simulation for this comparison has been conducted for a comparatively short simulation time of 3.5 s and was initialized from the steady state RANS solution. In table 4.7 the receiver-averaged total air return ratio ARR_{tot} and hot air inlet temperature $T_{h,in}$ is displayed for the DES and RANS simulation. The results have been averaged over 1.8 s which corresponds to 11000 iterations while the stationary RANS solution was obtained from the last 5900 iterations. Within the averaging time the ARR_{tot} and $T_{h,in}$ vary as depicted in table 4.7. While the RANS solution reached a converged state with regards to the quantities of interest, the transient DES contains temporal fluctuations which are comparatively high. On average the DDES predicts higher convective losses due the lateral wind compared to the RANS simulation which is also reflected by the averaged inlet temperature. In addition to the

Table 4.7: Receiver-averaged total air return ratio ARR_{tot} and hot air inlet temperature $T_{h,in}$ under 8 $\frac{\mathrm{m}}{\mathrm{s}}$ lateral wind, obtained with RANS and DDES modeling.

case	ARR_{tot}	$T_{h,in}$
RANS	75.5 ±0.1 %	509.0 ±0.3 K
DDES	74.4 ±2.1 %	505.6 ±7.4 K

agreement in the receiver-averaged quantities, it is also important to ensure comparable results in the distribution along the receiver surface regardless of the turbulence modeling approach. In fig. 4.34 the ARR_{tot} and $T_{h,in}$ is evaluated on nine separate zones on the receiver as visualized in the sketch in the upper part of the figure.

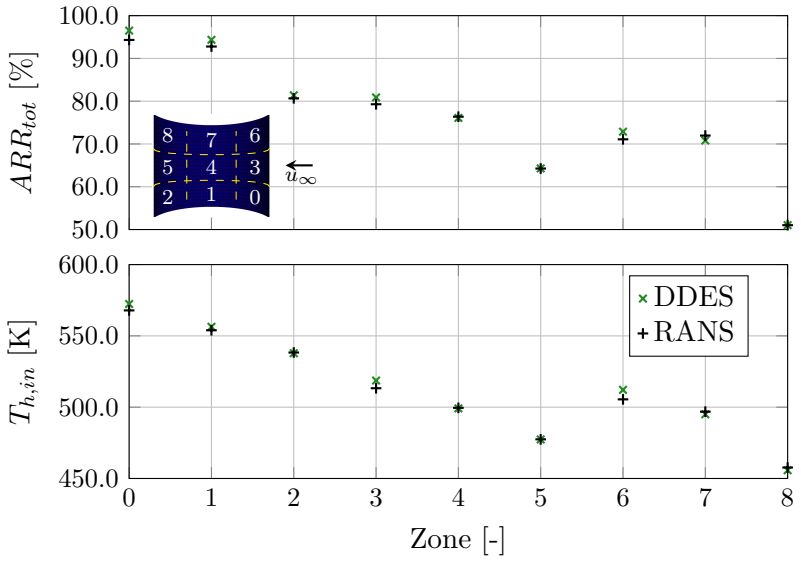

Figure 4.34: Local evaluation of the zonal-averaged total air return ratio ARR_{tot} and receiver inlet temperature $T_{h,in}$ with the ref_02 distribution with the RANS and DDES model under 8 $\frac{\mathrm{m}}{\mathrm{s}}$ lateral wind.

Although differences between the zonal averaged values exist in some areas, the agreement between the RANS and DES model is very high in both quantities shown and also the ranking between the separate zones can be predicted accurately with the RANS model. Based on this comparison, the RANS approach is deemed sufficient for the evaluation of the time-averaged convective losses under wind and will be used for the following parameter study.

In fig. 4.35 the dependency of the receiver-averaged internal, external and total air return ratio on wind speed is evaluated for the cases in table 4.6. As introduced in section 2.3.1, the distinction between the internal and external return air ratio is conducted by separately solving a transport equation for each return air system within the

numerical solution. For all cases shown, the results have been averaged over at least 1000 iterations after a converged stationary state has been reached. A stationary state has been defined by an upper limit in the deviation in the quantity of interest. During the evaluation period the external and internal return air varies by less than 0.07 % (absolute) and the hot air inlet temperature varies by less than 0.2 K compared to the average values.

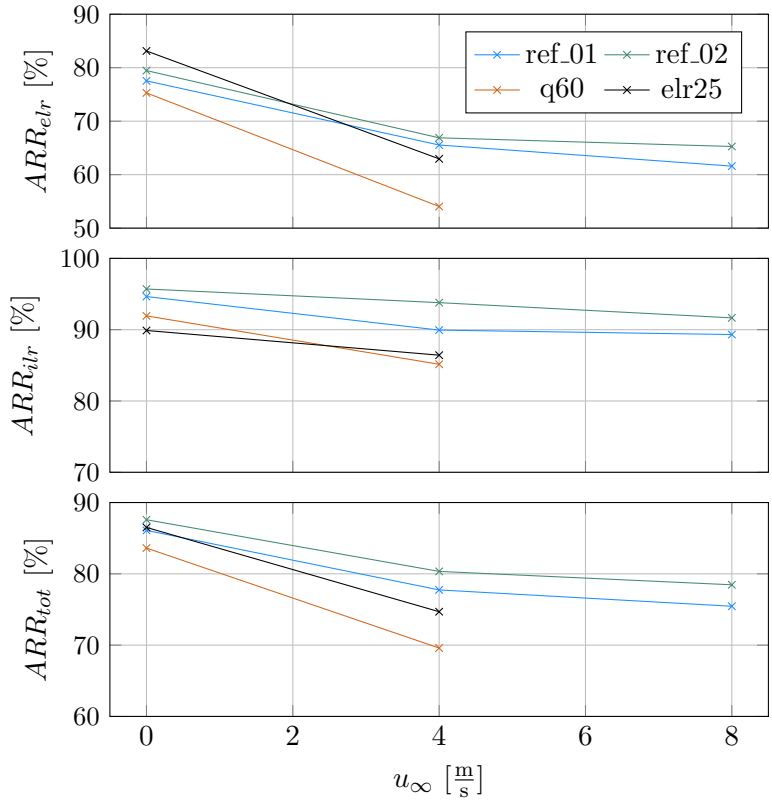

Figure 4.35: Dependency of the receiver-averaged internal ARR_{ilr}, external ARR_{elr} and total air return ratio ARR_{tot} on wind speed for the cases presented in table 4.6.

As shown in fig. 4.35 the mass flow-adapted elr distribution (ref_02) results in higher air return ratios compared to a uniform elr distribution (ref_01) regardless of the wind conditions. Focusing on the ref_02 distribution, the internal air return ratio drops from 95.7 % under windless conditions to 93.8 % under 4 $\frac{m}{s}$ wind and further to 91.7 % under 8 $\frac{m}{s}$ wind. Compared to the ARR_{ilr}, the externally returned air is influenced much stronger by the lateral wind as the ARR_{elr} decreases significantly more. The ARR_{elr} drops from 79.5 % under windless conditions to 66.9 % under 4 $\frac{m}{s}$ wind and further to 65.3 % under 8 $\frac{m}{s}$ wind. Compared to the uniform elr distribution (ref_01), the further increase in the lateral wind speed from 4 to 8 $\frac{m}{s}$ has a lesser effect on the ARR_{elr} in the case with the absorber-mass flow adjusted distribution (ref_02). Compared to

the design point case (ref_02) a 25 % reduction in the external return air mass flow (elr25) leads to a considerable increase in the external air return ratio of 3.6 percentage points under windless condition. In contrast to that, the total air return ratio is slightly lower compared to the reference case (ref_02) with a reduction of 1.1 percentage points. Compared to both design point cases where half of the return air is returned externally a stronger decline in the ARR_{elr} can be observed from 0 to 4 $\frac{\mathrm{m}}{\mathrm{s}}$ which is attributed to the decreased impulse of the externally returned air which makes it more vulnerable to ambient wind.

The part load case with 60 % irradiation yields the lowest total air return ratio which is in agreement with the results published by Stadler et al. [49] as the air return ratio tends to increase with the receiver mass flow. The wind influence in this case of reduced receiver mass flow is comparable to the case with the decreased elr-factor (elr25), which also is attributed to the decreased impulse of the externally returned air.

The evaluation of receiver-averaged values gives a first impression of the importance of a well-designed externally returned air distribution and the vulnerability of the externally returned air to lateral wind as it is way more sensitive to ambient wind than the internally returned air.

A local evaluation of the external air return ratio provides further insight about the wind influence on the receiver flow. For the local evaluation, the receiver is split into nine segments as visualized in the upper part of fig. 4.36 on which the mass flow-averaged external air return ratio is evaluated for the ref_02 distribution. As fig. 4.36 reveals, the external return air is especially disturbed at the leeward side of the receiver by lateral wind. For example in zone 2 the external return air ratio drops from around 64.6 % under windless conditions to 36.5 % at 8 $\frac{\mathrm{m}}{\mathrm{s}}$ wind speed. In the upper zone at the leeward side of the receiver (zone 8) the external air return ratio already reaches its minimum at 4 $\frac{\mathrm{m}}{\mathrm{s}}$ wind speed with a drop from 20.6 % to 8.7 %. A further increase in wind speed only accounts for an additional decrease of 0.4 percentage points in the ARR_{elr}. This can be explained by the impulse of the externally returned air which decreases along the receiver height, as it is drawn in on its way to the top of the receiver. This is why the external air return ratio at the bottom of the receiver decreases less at lower wind speeds compared to at the upper part of the receiver. Furthermore, it can be seen that due to the wind influence the local air return ratio slightly increases at parts of the windward side of the receiver but overall the losses at the leeward side overcompensate these gains.

The flow visualization in fig. 4.37 shows the wind influence on the externally returned air for the cases with the ref_02 elr distribution under 4 and 8 $\frac{\mathrm{m}}{\mathrm{s}}$ wind speed.

In the left part of fig. 4.37 streamlines in a horizontal plane in the middle of the receiver are shown, which are colored in the magnitude of the velocity. In addition, the receiver and tower boundary is colored in the air temperature and internal cells are shown based on a temperature filter ($T \geq 400\,\mathrm{K}$) and colored in the air temperature as well. The flow, which enters the domain on the right side of fig. 4.37, separates at the cavity opening and is party deflected but also enters the leeward side of the cavity. This results in a vertical vortex rotating in the mathematically negative sense inside the cavity. The effect on the returned air is visualized by the temperature-filtered internal field as a deflection of the returned air towards the windward side of the receiver occurs. In the representation of

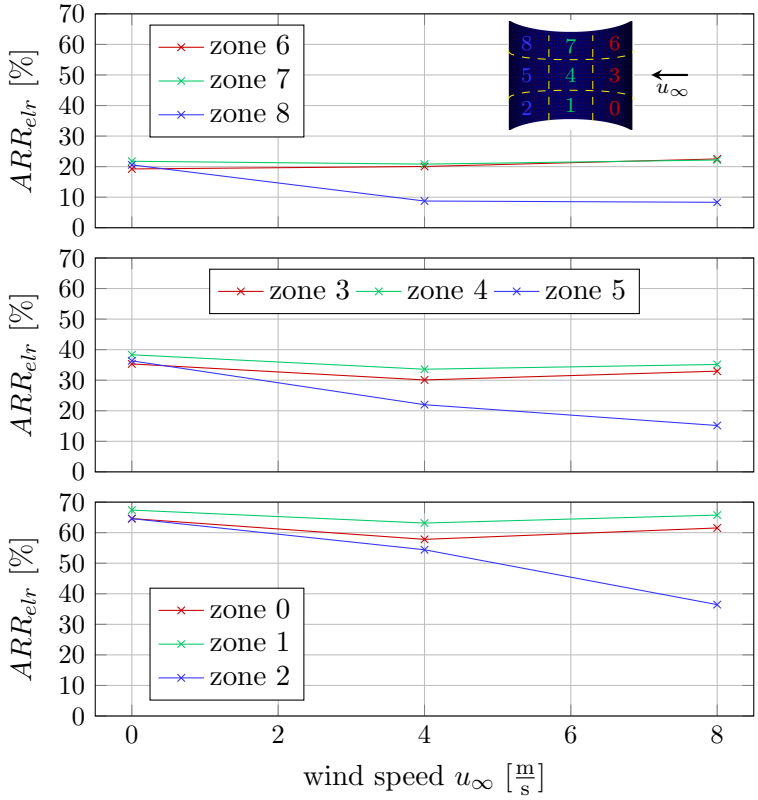

Figure 4.36: Local evaluation of the zonal-averaged external air return concentration ARR_{elr} with the ref_02 distribution under 0, 4 and 8 $\frac{m}{s}$ lateral wind.

the streamlines on the right side, the vortex within the receiver cavity can be identified that occurs under lateral wind. In the cut plane which is colored in the air temperature it can be seen how the vortex at 8 $\frac{m}{s}$ wind leads to a stronger deflection of the externally returned air due to its higher vorticity. The deflection ultimately leads to a higher loss of returned air towards the top and the windward side of the receiver, as visualized by the temperature-colored tower walls.

Summary: Wind Influence on Forced Convective Heat Losses at the Open Volumetric Cavity Receiver

In the previous part the wind influence on forced convective heat losses is investigated, quantified by the loss in return air. The air return ratio (ARR) is evaluated with the E-model without and with 4 and 8 $\frac{m}{s}$ lateral wind. In this evaluation the receiver is operated at design point (100 % intercept) and part load conditions, with a reduced irradiation (60 % intercept). Furthermore, a shift between the evenly distributed external and internal return air mass flow is investigated, where only 25 % of the return air mass flow is returned externally.

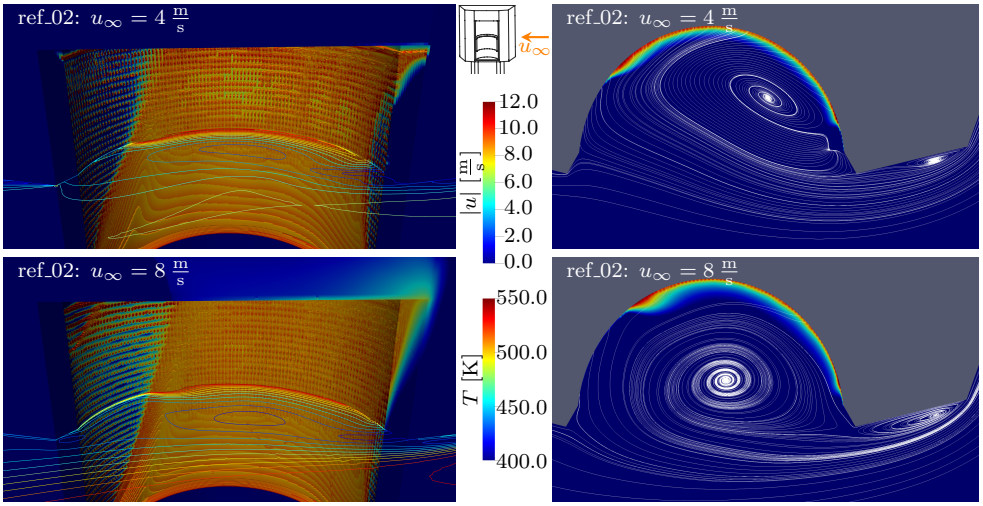

Figure 4.37: Visualization of the flow via streamlines in a horizontal plane in the middle of the receiver. At the left part the tower and receiver boundary is colored in the air temperature and internal cells are visualized based on a temperature filter ($T \geq 400\,\mathrm{K}$). On the right, the slice is colored in the air temperature. In the upper part of the plots the case with $4\ \frac{\mathrm{m}}{\mathrm{s}}$ wind is displayed, while in the lower part the case with $8\ \frac{\mathrm{m}}{\mathrm{s}}$ is displayed, both for the ref_02 distribution.

For the aforementioned cases a receiver averaged evaluation of the air return ratios is conducted. At design point conditions it can be summarized that especially the external air return ratio drops significantly under lateral wind, with a stronger reduction in the low wind speed range. The internal return air is less affected by ambient wind. At part load conditions with reduced irradiation, the overall receiver mass flow is reduced to maintain the target temperature which also leads to reduced return air mass flows. Because of the reduced momentum of the external return air, it is even stronger affected by ambient wind under part load conditions. Furthermore, a zonal evaluation has been conducted, where the receiver is split into nine zones on which the air return ratio is evaluated. The results show that the leeward side of the receiver is especially vulnerable to lateral wind. In that area the separated ambient wind enters the cavity and deflects the return air leading to lower air return ratios. What can also be identified is the influence of the momentum of the externally returned air, which decreases along the way up the receiver. The lower part of the receiver maintains relatively high external air return ratios at lower wind speeds while the upper part is not able to withstand ambient wind at the same wind speed.

Overall, this investigation emphasizes on the vulnerability of externally returned air to ambient wind and the local differences that heavily depend on wind speed and presumably the wind direction.

4.2.5 Active Countermeasures for Forced Convective Heat Losses Reduction

As shown in section 1.3.4, countermeasures to reduce convective losses are the subject of intensive research. While the applications are mostly focused on closed-loop surface receivers, where the loss mechanism is not based on a loss of the heat transfer medium itself, the application of those measures can in theory still be transferred to the open volumetric receiver.

In contrast to e.g. the study by Flesch et al. [46] or Prakash et al. [38], lateral wind does not act as a natural air curtain at the given cavity design of the receiver due to the opening angle of 168° and mainly due to the size of the aperture which allows the air to enter the cavity on the leeward side of the receiver after being deflected at the cavity opening (cf. fig. 4.37).

For the cavity receiver design under investigation, a fully or even partial transparent window is not feasible due to the size of the aperture with a diameter of approximately 21 m. The thermal and especially structural stresses on the material due to the sheer weight of such a window prevent the applicability of this measure.

The investigation of the wind influence on the air return ratio with the reference elr distributions as presented in section 4.2.4 reveals the sensitivity of the externally returned air to lateral wind. In this section potential countermeasures are presented to reduce the wind influence on the receiver flow and on the losses of returned air. The approaches are located in the field of active measures, which in this thesis are distinguished from passive measures like e.g. windows, or adjustments in the structure by the fact that they can be actively adjusted during the operation of the receiver.

Wind-Adjusted External Return Air Distributions

The first approach is based on adjusting the external return air distribution while maintaining the overall design return air mass flow. In order to locally vary the outflow distribution, the outlet surface is split into 12 circumferential segments as visualized in fig. 4.38. As mentioned in section 2.1.1 the receiver in the reference plant concept

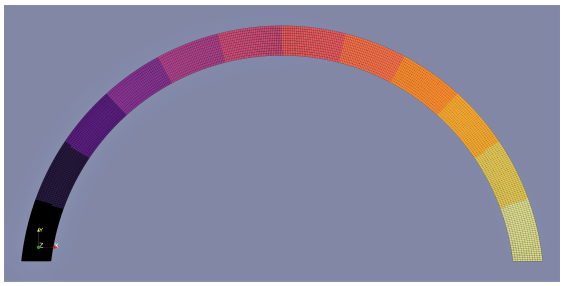

Figure 4.38: Segmentation of the external return air surface in 12 segments for the investigation of adjusted elr distributions under wind.

is segmented into vertical units called subreceivers, whose hot air streams are merged within the air system in the tower. The amount of zones at the elr outlet is chosen to

match the number of subreceiver units of which 12 are foreseen in the receiver design.

In the design of the return air system, segment-wise varying outflow conditions can be achieved by implementing adjustable flaps which partially restrict the cross-sectional outflow area. In order to maintain the prescribed mass flow each segment needs to be equipped with an independent fan and some sort of permanent mass flow measurement to ensure the desired distribution. In the simulation model this is achieved by simply adjusting the velocity outlet conditions on the predefined zones (cf. fig. 4.38).

Within this approach two different concepts with two variants each are investigated, which are visualized in fig. 4.39. In this figure the elr outflow surface is visualized from above and colored in the outflow velocity. The first concept (v_01: upper left

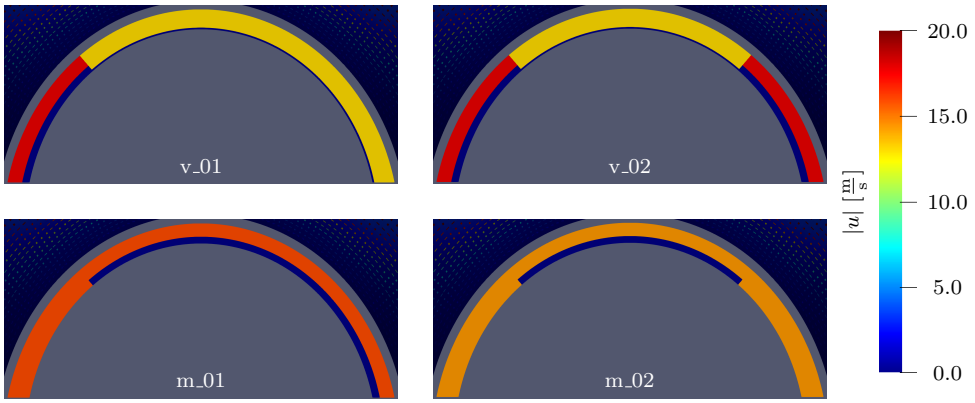

Figure 4.39: Proposed elr outflow distributions colored in the outflow velocity. In this representation, the lateral wind enters the domain from the right side.

and v_02: upper right) is based on prescribing the same mass flow on each segment but adjusting the outflow velocity by partially restricting the cross-sectional outflow area. The v_01 distribution is chosen based on the findings from the investigation of the reference distribution under wind, which showed the interference with the return air flow at the leeward side of the cavity. Therefore, the outflow velocity has been increased in this area to increase the return air impulse. In addition, in the v_02 distribution, this adjustment has also been applied to the windward side of the receiver. In the second concept the outflow velocity is kept constant along the entire outflow area while the segment-wise mass flow is shifted towards the leeward side (m_01: bottom left) or uniformly towards both sides of the receiver (m_02: bottom right). In cases m_01 and m_02, the outflow area in the zones of reduced mass flow is reduced by 23 % compared to the other zones while maintaining a uniform outflow velocity under the constraint of maintaining the total reference elr mass flow. The adjustment is applied on nine (m_01) or six (m_02) segments as visualized in fig. 4.38. In the v_01 and v_02 case the outflow area has been restricted by 23 % in areas of increased outflow velocity which leads to a relative velocity increase in those areas of 37.5 % compared to the unrestricted outflow segments. This restriction is applied on the outer three segments.

Under windless conditions the inverse (v_02 and m_02) and asymmetrical outflow

distributions (v_01 and m_01) presented here are not expected to be favorable compared to the reference distributions, which is why those distributions are only evaluated under wind influence.

A parameter study for the two different wind speeds under investigation (4 and 8 $\frac{\mathrm{m}}{\mathrm{s}}$) with the elr distributions presented above was conducted and evaluated in terms of the air return ratios and mass flow-averaged hot air inlet temperature $T_{h,in}$. The receiver-averaged results are summarized in table 4.8 and table 4.9.

Table 4.8: Receiver-averaged air return ratios and receiver inlet temperature under 4 $\frac{\mathrm{m}}{\mathrm{s}}$ lateral wind.

	ref_01	ref_02	v_01	v_02	m_01	m_02
ARR_{elr}	65.5 %	66.9 %	68.7 %	69.5 %	68.1 %	65.6 %
ARR_{ilr}	89.9 %	93.8 %	89.8 %	89.3 %	88.8 %	89.7 %
ARR_{tot}	77.7 %	80.3 %	79.3 %	79.4 %	78.4 %	77.7 %
$T_{h,in}$	515.5 K	522.6 K	516.2 K	516.4 K	513.8 K	512.5 K
ARR_c	79.9 %	82.2 %	80.2 %	80.2 %	79.2 %	78.8 %

At comparatively low wind speeds of 4 $\frac{\mathrm{m}}{\mathrm{s}}$ the receiver mass flow adjusted elr distribution (ref_02) still provides the highest air return ratios regarding the internal and external air return ratio based on receiver-averaged values. This consequently leads to the highest mass flow-averaged hot air inlet temperature $T_{h,in}$ of 522.6 K. Due to the definition of the caloric air return ratio ARR_c it qualitatively follows the results of the mass-flow averaged inlet temperature $T_{h,in}$ for all cases investigated.

As visually seen in fig. 4.37 and quantitatively shown for the ref_02 distribution in fig. 4.36 the local differences in the wind-induced interference with the receiver flow are significant as especially the leeward side of the receiver is disturbed by the lateral wind. A local evaluation of the cases in table 4.8 is shown in the zonal representation of the external and total air return ratio in fig. 4.40. The zonal evaluation of the cases in fig. 4.40 reveals that the adjusted elr distributions reduce the losses of returned air at the leeward zones of the receiver (2, 5 and 8) significantly. Compared to the reference distribution ref_02 a shift in the mass flow towards the leeward side of the receiver (m_01) yields an increase in the total air return ratio of 8.9, 14.4 and 18.4 percentage points respectively.

On the other hand the air return ratio in the central zones (1, 4 and 7) is reduced by the adjusted elr distributions. Especially in the center of the receiver ARR_{tot} is at 86.3 % with the ref_02 distribution while the adjusted elr distribution yield ARR_{tot} in the range of 70.4 to 76.3 %. For this wind speed the improvement at the leeward side is overcompensated by the decrease in the central zones of the receiver because the receiver mass flow in the center of the receiver is higher than on the edges (cf. fig. 3.19). At the windward side of the receiver an adjustment in the elr distribution does not significantly affect the air return ratio regardless of the distribution.

The fact that the v-configurations yield lower (receiver-averaged) convective losses

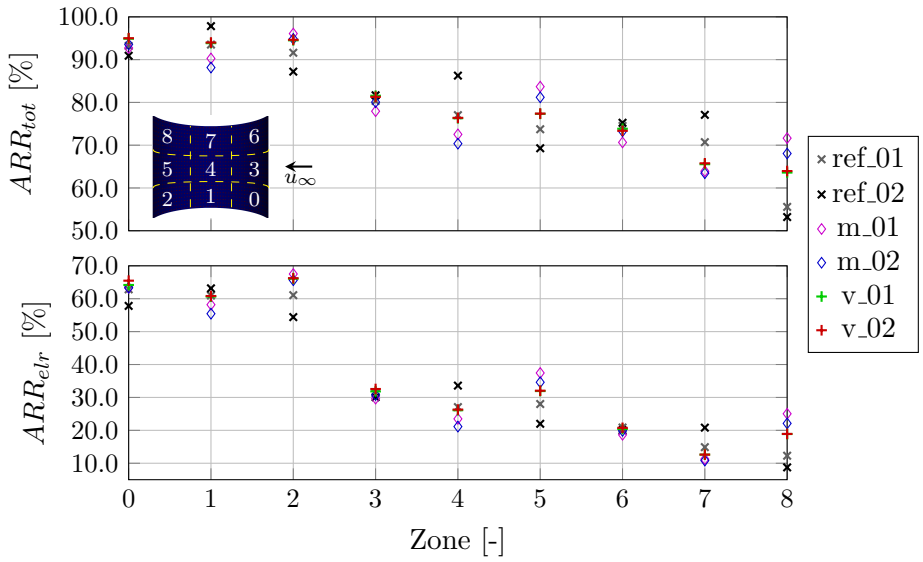

Figure 4.40: Local evaluation of the zonal-averaged total ARR_{tot} and external air return ratio ARR_{elr} for the cases in table 4.8 under 4 $\frac{\text{m}}{\text{s}}$ lateral wind.

compared to the m-configurations can be attributed to the higher air return ratio in the center third of the receiver.

While the adjustments, as shown in fig. 4.40, successfully increase the air return ratio at the leeward side of the receiver, the reference distribution ref_02 still yields the lowest convective losses under 4 $\frac{\text{m}}{\text{s}}$ lateral wind.

The proposed elr distributions have also been investigated under a larger wind speed of 8 $\frac{\text{m}}{\text{s}}$ and the receiver-averaged quantities for those cases are summarized in table 4.9.

Table 4.9: Receiver-averaged air return ratios and receiver inlet temperature under 8 $\frac{\text{m}}{\text{s}}$ lateral wind.

	ref_01	ref_02	v_01	v_02	m_01	m_02
ARR_{elr}	61.6 %	65.3 %	72.2 %	72.4 %	71.9 %	69.8 %
ARR_{ilr}	89.3 %	91.7 %	92.1 %	92.0 %	91.8 %	92.3 %
ARR_{tot}	75.5 %	78.5 %	82.2 %	82.8 %	81.8 %	81.0 %
$T_{h,in}$	509.0 K	517.0 K	525.3 K	524.2 K	522.6 K	521.8 K
ARR_c	77.5 %	80.1 %	83.2 %	83.1 %	82.6 %	82.2 %

Compared to the cases at lower wind speed the reference distribution ref_02 does no longer yield the lowest convective losses indicated by the total air return ratio ARR_{tot} and the averaged receiver inlet temperature. At 8 $\frac{\text{m}}{\text{s}}$ lateral wind, an adjustment of the momentum or mass flow at the leeward side of the external return air outlet significantly improves the overall external air return ratio which in this case leads to higher inlet

temperatures $T_{h,in}$ at the receiver. The v_01 and v_02 distributions account for the lowest convective losses with external air return ratios of 72.2 % and 72.4 % respectively compared to the case with the reference elr distribution ref_02 where the external air return ratio drops to 65.3 %. The higher air return ratio in those cases also contributes to an increase in the average hot air inlet temperature $T_{h,in}$ of 7.8 K compared to the ref_02 case. The difference in the air return ratio between v_01 and v_02 lies within the model uncertainty, which explains the counter-intuitive behavior between the total air return ratio and average hot air inlet temperature. The shift in the mass flow with the m_01 and m_02 distribution also yields a measurable reduction in convective losses with the same tendency observed in the v-configuration where it seems that the shift towards the leeward side is the predominant influence here. But with regards to the model uncertainties in the air return ratio of 0.8 % the differences between m_01 and m_02 should not be overemphasized.

Again, a zonal evaluation gives further inside on what the improvements are accounted for. Similar to fig. 4.40 in fig. 4.41 the ARR_{tot} and ARR_{elr} are evaluated on the predefined zones at the receiver. Similar to the cases at 4 $\frac{\text{m}}{\text{s}}$ lateral wind, an adjustment in

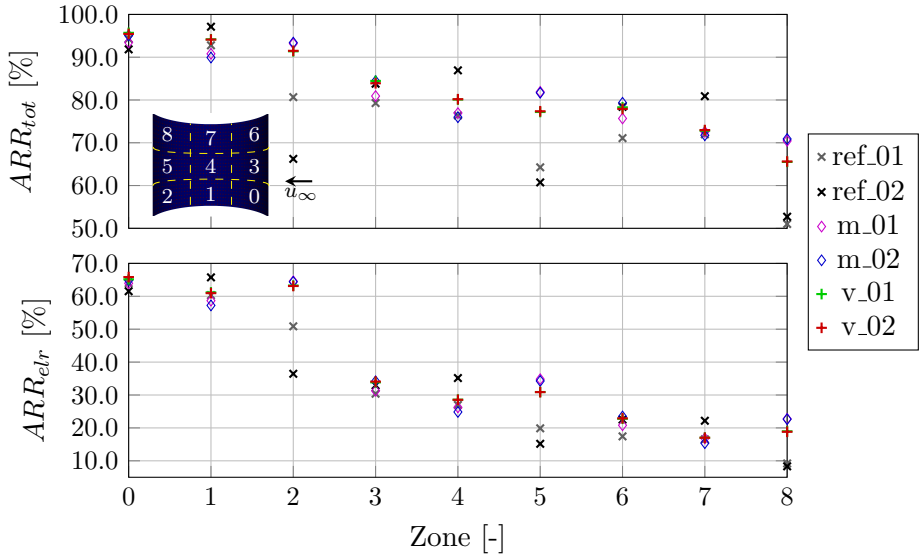

Figure 4.41: Local evaluation of the zonal-averaged total ARR_{tot} and external air return ratio ARR_{elr} for the cases in table 4.9 under 8 $\frac{\text{m}}{\text{s}}$ lateral wind.

the elr distribution results in a negligible impact on the air return ratio at the windward zones (0, 3 and 6) compared to the reference distribution ref_02. The average deviation lies within the model uncertainty at zones 3 and 6 while at zone 0 the total air return ratio could be increased by 3.1 % on average. Due to the higher external return air mass flow in the central zones the reference distribution ref_02 yields the highest air return ratios in that region of the receiver also under 8 $\frac{\text{m}}{\text{s}}$ lateral wind. At the lower central zone 1 the difference accounts for 4.9 percentage points compared to averaged adjusted distributions. At the upper central zones (4 and 7) the ref_2 distribution yields a total

air return ratio which is around 8.5 percentage points higher. The leeward side of the receiver is where the advantage of the adjusted elr distribution becomes visible. With an increase in the lateral wind speed from 4 to 8 $\frac{\mathrm{m}}{\mathrm{s}}$ the ARR_{elr} only drops by 1.0 percentage points at the leeward side of the receiver (mass flow weighted averaged over zones 2,5 and 8) with the v_01 distribution, whereas with the reference distribution ref_02 it drops by 7.2 percentage points. Based on the m_01 distribution an increase in the total air return ratio in the leeward zones 2, 5 and 8 of 27.0, 21.2 and 17.7 percentage points can be achieved compared to the ref_02 distribution. As summarized in table 4.9 the v-configurations account for slightly higher total and external air return ratios which is attributed to the higher air return ratios in the central zone where the mass flow is higher compared to the m-distributions.

A remarkable observation is that the adjusted elr distributions yield a better receiver performance under 8 $\frac{\mathrm{m}}{\mathrm{s}}$ than under 4 $\frac{\mathrm{m}}{\mathrm{s}}$ wind speed. This indicates that there is further room for improvement at the lower wind speed case in regards to the elr distribution and the amount of adjustment in the outflow velocity or mass flow. The shift towards the edges may be too severe in relation to the wind speed at the low wind speed cases.

A flow visualization of the flow field within the cavity with the v_01 distribution under both wind speeds in fig. 4.42 gives further insight on the discussed results.

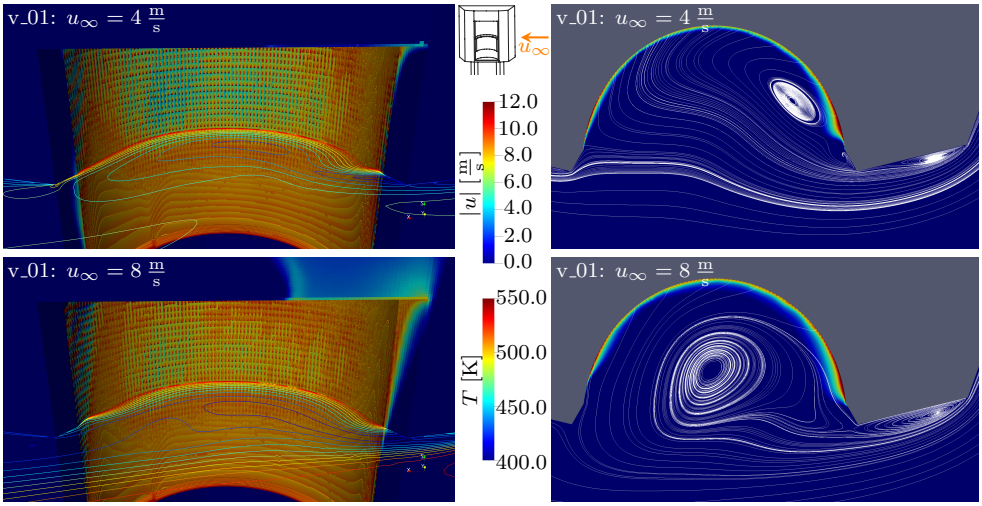

Figure 4.42: Visualization of the flow via streamlines in a horizontal plane in the middle of the receiver. At the left part the tower and receiver boundary is colored in the air temperature and inter cells are visualized based on a temperature filter ($T \geq 400\,\mathrm{K}$). On the right side the slice is colored in the air temperature. In the upper part of the plots the case with 4 $\frac{\mathrm{m}}{\mathrm{s}}$ is displayed, while in the lower part the case with 8 $\frac{\mathrm{m}}{\mathrm{s}}$ is shown, both for the v_01 distribution.

Compared to the reference distribution ref_02 (cf. fig. 4.37) the return air flow is significantly less disturbed and shifted away from the leeward side of the receiver at both 4 and at 8 $\frac{\mathrm{m}}{\mathrm{s}}$ wind speed. Due to the increased momentum of the elr in that region,

the return air flow can withstand the wind influence to a greater extent and the air return ratio in that region is increased. On the other hand, the inlet temperature in the central region is visually lower compared to the reference case (ref_02) which underlines the conflict of interest between high return air ratios in the central part of the receiver where the receiver mass flow is highest and the protection of the lateral receiver surfaces against the wind influence. In all cases it can be observed how a part of the returned air is lost especially in the windward upper corner of the cavity due to a combination of convective updraft and wind influence.

Application of an Aerowindow

In addition to the wind-adjusted external return air distribution, the application of an aerowindow as a second measure to reduce convective losses under wind is numerically investigated. As with the investigation of adjusted elr-distributions, the receiver is operated at design point conditions. RANS simulations are conducted of lateral wind at $4\,\frac{\mathrm{m}}{\mathrm{s}}$ wind speed as the results shown before (cf. section 4.2.4) already yield a significant drop in the total air return ratio at this wind speed from 87.6 to 80.3 %. For this investigation, the reference distribution of externally returned air ref_02 has been chosen as it yields the best performance in terms of air return ratios and convective losses at that wind speed. Based on the previous findings regarding the flow visualization, two possible ways of implementing the aerowindow have been chosen and are visualized in fig. 4.43.

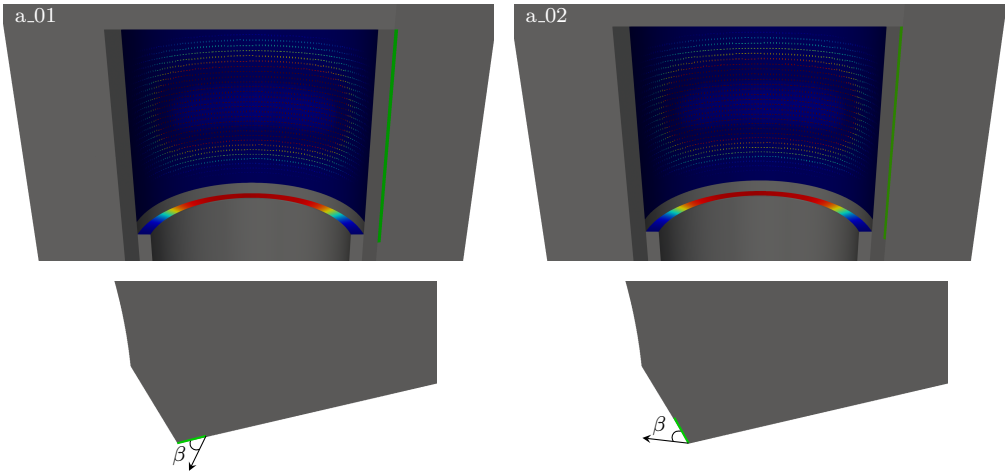

Figure 4.43: Proposed implementations of an aerowindow (a_01 and a_02) at the cavity receiver as a measure to reduce forced convective losses, including the outflow area (green) and definition of the outflow angle β.

The aerowindow is placed adjacent to the windward cavity edge either on the inward or outward facing surface. The boundary conditions applied on the aerowindow area are a Dirichlet boundary condition regarding the velocity with variable outflow angles as defined in the bottom of fig. 4.43. Regarding the pressure a Neumann zero gradient condition is applied while the rest of the variables are defined in agreement with the free stream values which are also prescribed at the ambient inlet ($T = T_\infty$, $\tilde{\nu} = 3\nu(T_\infty)$).

The intention of the aerowindow is to further increase the deflection of ambient wind at the cavity opening in order to prevent inflow into the cavity. In previous studies on aerowindows applied at smaller cavities (cf. [46], [44]) the intention was to seal the cavity opening with the application of an aerowindow. The cavity receiver under investigation has a cavity width of approximately 14 m.

Conceptionally the aerowindow as applied in this model can be described as a turbu-

lent free jet. The theory on turbulent free jets can be utilized to estimate the outflow momentum which would be necessary to seal a cavity of the given size. This approximation is done based on the assumption of a round jet entering a stagnant ambient without the consideration of wind. As described in Pope [63] under such conditions the jet flow can be observed to decay with axial distance to the outlet in terms of a reduction in the centerline velocity while the cross-sectional area of the jet widens with traveling distance. For example in an experimental study by Hussein et al. [126] an axisymmetric jet flow has been captured with Laser-Doppler Anemometry (LDA) to analyze the development of the jet flow emerging into a resting environment. Based on the measurement within the study the decrease of the centerline velocity $u_{jet,c}$ with distance x from the jet outlet can be approximated via eq. (4.3)

$$\frac{u_{jet,c}}{u_{jet,out}} = \frac{B}{(x - x_{jet,out})/d} \tag{4.3}$$

with the jet outlet velocity $u_{jet,out}$, the outlet diameter of the jet d and the virtual origin of the jet $x_{jet,out}$. The decay rate B has been observed to be Reynold-independent (cf. [63]) and the value of 5.8 determined by Hussein et al. [126] is applied here. Based on eq. (4.3) a jet outflow velocity of almost 49 $\frac{\mathrm{m}}{\mathrm{s}}$ would be necessary to maintain a jet velocity of 4 $\frac{\mathrm{m}}{\mathrm{s}}$ at the opposite edge of the cavity, which equals to an aerowindow mass flow of around 144 $\frac{\mathrm{kg}}{\mathrm{s}}$ ($\approx 63\,\%$ of the receiver flow).

The estimate is based on the assumption of an emerging jet into a resting environment. When ambient wind is considered the outflow momentum potentially needs to be further increased in order to withstand the deflection of the aerowindow due to the wind. Compared to prior studies (e.g. [46]) the jet speed that would be necessary to theoretically seal the cavity is way too high to be economically feasible as the jet speed necessary to yield an effective aerowindow increases with aperture size.

Based on this estimation the approach at the cavity design under investigation further is not to actually seal the cavity but instead locally influence the flow separation at the cavity opening to at least partly prevent inflow and the consequent disturbance of the receiver flow.

The jet velocity and outflow angle as the relevant parameters of the aerowindow are varied within a parameter study whose variations are summarized in table 4.10.

An evaluation of the receiver-averaged air return ratios reveals that the application of an aerowindow in the proposed way in the cavity design under investigation does not reduce the forced convective losses (with regards to the model uncertainty) for any of the investigated outflow angles and velocities under 4 $\frac{\mathrm{m}}{\mathrm{s}}$ side wind. In table 4.11 the receiver-averaged quantities are summarized, which are obtained by the stationary RANS simulations.

Compared to the reference case without an aerowindow (ref_02) not a single case with an aerowindow leads to an increase in the air return ratio above the model uncertainty. The aerowindow of type a_02 and type a_01 with an outflow angle of 90 or 135° even lead to a significant decrease in the total air return ratio of more than 6 percentage points. The aerowindows of type a_01 with an outflow angle of 45° and an outlet jet velocity

Table 4.10: Parameter variations regarding the outflow angle β and velocity $u_{jet,out}$ of the aerowindows applied in the cavity receiver design.

type	β	$u_{jet,out}$	$\dot{m}_{jet}$
a_01	45°	4.0 $\frac{\mathrm{m}}{\mathrm{s}}$	11.7 $\frac{\mathrm{kg}}{\mathrm{s}}$
a_01	45°	16.0 $\frac{\mathrm{m}}{\mathrm{s}}$	46.9 $\frac{\mathrm{kg}}{\mathrm{s}}$
a_01	45°	30.0 $\frac{\mathrm{m}}{\mathrm{s}}$	88.0 $\frac{\mathrm{kg}}{\mathrm{s}}$
a_01	45°	40.0 $\frac{\mathrm{m}}{\mathrm{s}}$	117.3 $\frac{\mathrm{kg}}{\mathrm{s}}$
a_01	90°	16.0 $\frac{\mathrm{m}}{\mathrm{s}}$	46.9 $\frac{\mathrm{kg}}{\mathrm{s}}$
a_01	135°	16.0 $\frac{\mathrm{m}}{\mathrm{s}}$	46.9 $\frac{\mathrm{kg}}{\mathrm{s}}$
a_02	90°	16.0 $\frac{\mathrm{m}}{\mathrm{s}}$	46.9 $\frac{\mathrm{kg}}{\mathrm{s}}$

Table 4.11: Receiver-averaged air return ratio with the application of aerowindows under 4 $\frac{\mathrm{m}}{\mathrm{s}}$ lateral wind. The case name indicates the type, outflow angle β and outflow velocity $u_{jet,out}$ of the aerowindow.

	ref_02	a01_45_4	a01_45_16	a01_45_30	a01_45_40	a01_90_16	a01_135_16	a02_90_16
ARR_{elr}	66.9 %	67.3 %	67.1 %	64.8 %	59.2 %	61.2 %	61.0 %	61.6 %
ARR_{ilr}	93.8 %	93.8 %	93.8 %	93.4 %	85.9 %	86.3 %	86.2 %	86.4 %
ARR_{tot}	80.3 %	80.6 %	80.4 %	79.1 %	72.5 %	73.8 %	73.6 %	74.0 %

of $\leq 16\,\frac{\mathrm{m}}{\mathrm{s}}$ yield results comparable to the reference case within the model uncertainty in the air return ratio. A further increase in the outlet velocity of the jet leads to a significant reduction in the air return ratios.

In fig. 4.44 the flow is visualized for the cases with the a_01 aerowindow with an outflow angle of 45 and 90° and an outflow velocity of 16 $\frac{\mathrm{m}}{\mathrm{s}}$. A cut plane which is placed in the middle of the receiver and colored in the air temperature is visualized in addition to the streamlines in that plane.

In this representation it can be seen how the aerowindow locally deflects the separated boundary layer flow at the outer cavity side wall but is not able to prevent the ambient wind from entering the cavity regardless of the outlet angle. On the contrary, the aerowindow further enhances the vortex within the cavity which leads to the increase of convective losses with increasing jet outlet velocity. Based on the quantitative results in table 4.11 and the flow visualization in fig. 4.44 it can be concluded that the application of an aerowindow is not a feasible measure to reduce forced convective losses in the proposed cavity design under lateral wind. Due to the size of the cavity the impulse of the aerowindow necessary to seal the cavity is too large to be achievable and a local deflection of the incoming lateral wind does not effectively reduce forced convective losses.

The potential of this measure is considered to be limited in this application due to the size of the aperture area as discussed above. The effectiveness of the aerowindow for incident angles that vary from the investigated lateral wind can be assumed to be

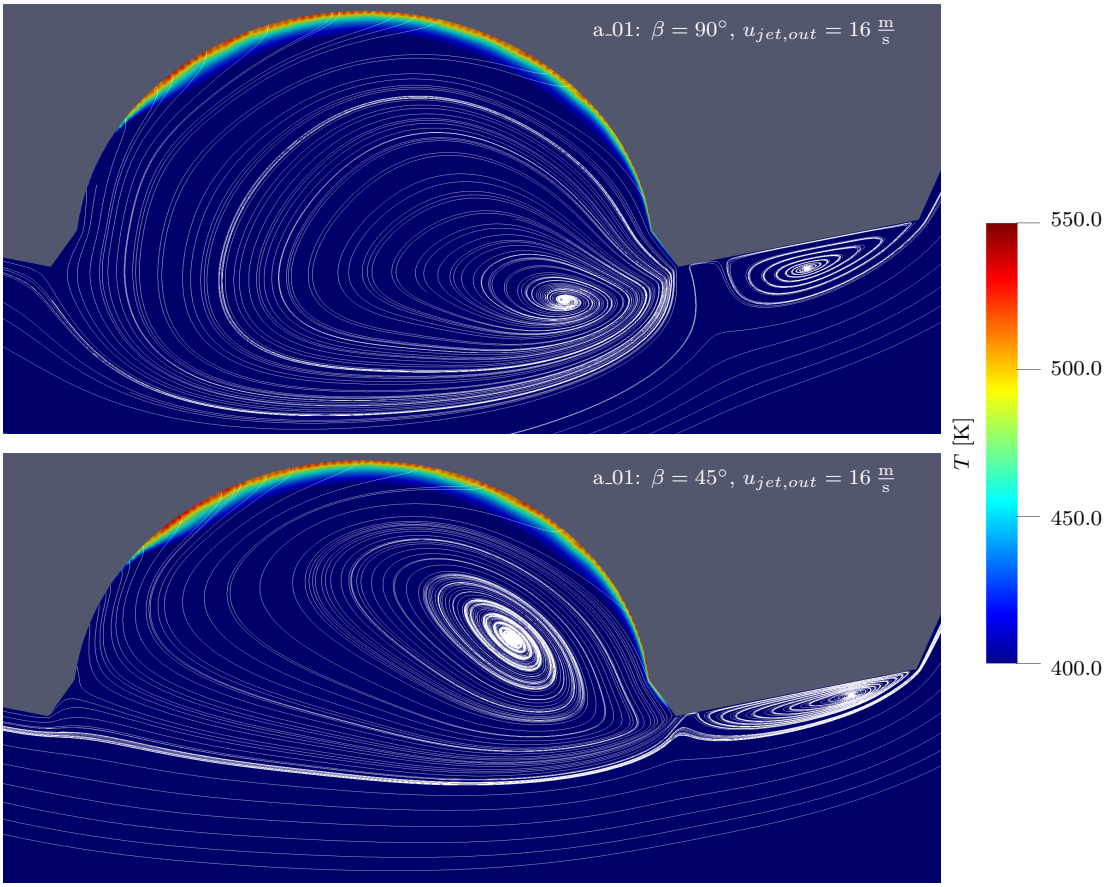

Figure 4.44: Visualization of the flow via streamlines in a horizontal plane in the middle of the receiver. The cut plane is colored in the temperature. In the upper part of the plot the case with an aerowindow with an outflow angle of 90° is shown while in the lower part the case with an outflow angle of 45° is shown, both for the type a_01 and a jet outflow velocity of 16 $\frac{m}{s}$.

equally low as the incoming wind will deflect the aerowindow especially in those areas where the jet momentum has decayed along the path of the jet. In those cases, similar situations may occur where the cold air emerging from the aerowindow is deflected into the receiver and return air flow, leading to increased convective losses in that area of the receiver.

Summary: Active Countermeasures for Forced Convective Heat Losses Reduction

Based on the findings before, the application of actively controllable countermeasures to reduce the wind-influence on the return air losses are investigated. In first approach an adjustable external return air outlet is foreseen in terms of its mass flow and/or velocity distribution. For this, the external return air outlet is segmented in zones and

four different distributions are tested under wind. In the first concept, the mass flow is shifted to the sides of the elr outlet, in the other concept the mass flow distribution remains constant, but the outflow velocity is altered but restricting the outflow area. The investigation reveals a central conflict of interest between shielding the edges of the receiver against the lateral wind and maintaining a high air return ratio in the center of the receiver, where it matters the most due to the higher receiver hot air mass flow in that area. Due to this effect an adjustment in the elr distribution is not effective at low wind speeds, but at higher wind speeds especially the concept of increasing the outflow velocity at the edges leads to significantly reduced convective losses. This parameter study shows that the effectiveness of measures to reduces the wind influence on convective losses is highly dependent on the wind conditions, which suggests the use of controllable measures with adjustable components.

The second approach includes the application of an aerowindow which is placed on the wall adjacent to the cavity opening on the windward side of the tower. The outlet extends over the height of the receiver, where air is ejected at ambient temperature with varying mass flows and outlet angles. The intention of the aerowindow usually is to seal the cavity opening and deflect incoming ambient wind. Due to the size of the cavity in this receiver concept, sealing the cavity is not realistic, as the necessary aerowindow mass flows would be too high. Nevertheless, the application and the ability to redirect ambient wind were examined. The results show that for all cases the cold air from the aerowindow is deflected into the cavity, leading to increased convective losses, which leads to the conclusion that an aerowindow is not applicable in the given receiver design.

5 Discussion

In this section the main findings which are presented in chapter 4 will be highlighted and discussed. Conclusions are drawn and the findings will be related to the current state in literature where possible and the significance and limitations of the findings will be evaluated.

5.1 Applicability of the DES Model Evaluated by the Comparison to the Measurement

For the model validation, a case of south-eastern wind with a wind speed of $4\,\frac{\mathrm{m}}{\mathrm{s}}$ is compared to the results obtained from the measurement. An excellent agreement in the time-averaged surface pressure at each probe can be observed with the SE-model, which includes the whole tower, with deviations of less than 0.2 Pa in the wake cavity and less than 0.8 Pa in the other cavities. The difference is attributed to the spatial discretization in relation to the integral length scale of turbulence. The agreement in the pressure fluctuation quantified by the RMS value is excellent in the wake cavity with a deviation of less than 0.1 Pa while the level of agreement in the other cavities varies. At the north-eastern cavity, which experiences lateral wind, the RMS value is systematically over-predicted in the simulation which is attributed to the grid spacing within the cavity and at the edge where the flow separates. A local grid refinement is assumed to increase the level of agreement. Overall it can be concluded that an unstructured meshing approach which allows an easier application of locally adjusted grid densities is presumed to be favorable in such a complex geometry, which experiences locally varying length scales of turbulence that require different levels of spatial discretization as shown in fig. 3.15.

The visualization of the surface flow via surface oil measurements compared to instantaneous wall shear stress streamlines in the simulation reveals that the main features of the near-surface flow are captured by the CFD model. The main characteristics show a great level of agreement within the limits of comparability as the measurement visualized a time average near surface field while in CFD only instantaneous representations are available. The streamlines emerging at the wind-facing part of the tower and the main vortices emerging at the cavity opening are represented both in the simulation and measurement.

The comparison in the spectral domain has a limited comparability due to insufficient simulation times in order to resolve the low-frequency spectrum with a higher resolution. Furthermore the sampling frequency in the measurement of 1000 Hz results in a cut-off in the spectrum at $St = 2.5$ which is a lot lower than the cut-off frequency in the simulations due to the strict requirements on the time step. Nevertheless, it can be

observed that the slope of the pressure spectrum and the decay in the power spectral density matches very well at each cavity which gives confidence that the inertial range is captured by the simulation.

In general, the flow around the solar tower is a very applicable case for the DES modeling approach due to the massively separated flow and prescribed separation lines due to the non-continuous geometry of the tower.

The second model (E-model) is created in order to include the receiver flow in the discussion of surface pressure fluctuations and further evaluate the wind influence on forced convective heat losses in the cavity receiver. In order to model the receiver flow, a higher spatial resolution within the receiver cavity is applied which made it necessary to reduce the size of the domain in order to keep computational costs within a manageable limit. Therefore, the size of the domain has been reduced by the application of a symmetry plane along the east-western tower axis which introduces a modeling error. The east-western tower axis does not represent an actual symmetry axis in the geometrical sense which causes a modification of the aerodynamic resistance of the tower, that can be observed in an offset in the average pressure inside the cavity of $\approx 6\,\mathrm{Pa}$. As discussed in section 3.3.6 the presence of the symmetry plane and the interaction with lateral wind introduces an overlying low-frequency pressure fluctuation with a dominant frequency of $0.27\,\mathrm{Hz}$ and an average amplitude of $2.3\,\mathrm{Pa}$ which is not observed in the experimental results. In a test case, where the mesh is mirrored along the symmetry plane and by that omitting the symmetry condition, this fluctuation is not observed. This leads to the conclusion that it originates from the flow interaction with the symmetry plane. This observation emphasizes that caution needs to be exercised when applying symmetry boundary conditions in the vicinity of strongly separated flow.

Within the simulation where the receiver flow is included those low-frequency fluctuations are not observed anywhere inside the domain which leads to the conclusion that the presence of the receiver flow suppresses the evolution of those fluctuations.

Furthermore, the evaluation of the forced convective heat losses via the air return ratio is not influenced by the fluctuations observed in the validation case with the E-model as those transient fluctuations naturally do not occur during the stationary RANS approach. It is argued that even though the symmetry plane introduces a slight deviation in the average pressure, the evaluation of the air return ratio under wind is not affected by the modeling error, as the relative differences in the air return ratio caused by increases in wind speed and or the application of countermeasures are more relevant than the absolute values itself. Furthermore the offset in the average pressure of $6\,\mathrm{Pa}$ can safely be assumed to not significantly alter the receiver flow within the cavity.

5.2 Influence of Wind Speed and Wind Direction on the Surface Pressure Distribution in the Receiver under Constant Incident Angles

In the measurement critical incident angles can be identified in terms of the pressure RMS value, with the largest RMS values occurring under incidence angles of 45 to 80°

relative to the cavity center normal axis. Within each cavity, large deviations in the local pressure RMS value are observed where the lateral parts of the receiver are subject to stronger fluctuations due to the interaction with the eddies emerging from the flow separation at the cavity opening. For example in the southern cavity the pressure RMS values at the windward probe position exceed the cavity-averaged RMS value by 65 % at a critical angle of 56.3° (cf. fig. 4.4).

The RMS values show a second-degree polynomial dependency on the Reynolds number or free stream velocity ranging from 0.1 Pa at wind speeds of 1.3 $\frac{\mathrm{m}}{\mathrm{s}}$ to 2.2 Pa at 5 $\frac{\mathrm{m}}{\mathrm{s}}$ (at the leeward side of the southern cavity under an incident angle of 56° to the cavity normal axis). Depending on the incident angle the RMS values increase by a factor of 9.5 (at $\phi = 180.0°$) to 16.1 (at $\phi = 56.3°$) within the Reynolds number range, which is covered in the measurement.

At particular incident angles periodic vortex shedding can be observed on the receiver surface by means of a spectral analysis with a FFT. For example at an incident angle of 78.8° relative to the cavity center normal axis periodic vortex shedding can be observed at $St \approx 0.4$ for all Reynolds numbers. According to the Strouhal number which only decreases slightly with Re in that case the peak frequency in the surface pressure fluctuation increases almost linearly with the free stream velocity from 0.016 to 0.056 Hz within the investigated Reynolds number range.

Regarding the extrapolation to larger wind speeds a range up to 14 $\frac{\mathrm{m}}{\mathrm{s}}$ wind speed is expected to cover the relevant range for the operation of such a scaled up receiver at the reference plant site as evaluated in section 3.1. Based on existing literature on the Re-regimes in bluff body flow (cf. section 1.3.1) the Strouhal number is expected to remain constant, or only slightly increase for higher Reynolds numbers and the frequency is further expected to increase linearly. As mentioned before the RMS values under constant incident angles are observed to follow a second-order degree polynomial function with respect to the Reynolds number which leads to extrapolated RMS values of up to ≈ 8 Pa for the most critical incident angles at the lateral parts of the receiver. Based on those results, the impact on the receiver mass flow and thermal stresses during operation can be assumed negligible, as will be evaluated in detail in section 5.4.

5.3 Influence of Varying Incident Angles on the Surface Pressure Distribution in the Cavity Receiver

During changes in the incident angle the average surface pressure at the receiver varies due to the shift in the stagnation point. A varying incident angle is observed to cause significantly higher RMS values than the cases of constant incident angles. Under a full rotation from head-on to side-wind the highest local pressure RMS value with values up to 13.1 Pa are observed within the Reynolds number range in the experiments. Under realistic wind conditions, the wind direction variability decreases strongly with increasing wind speed (as shown in fig. 3.4) which needs to be considered in the evaluation of the results. A reduction in the range of rotation naturally decreases the surface pressure fluctuation during such rotation. Furthermore, the RMS values during rotation are

strongly dependent on between which angle range the fluctuation takes place as the gradient of the mean pressure is observed to be steeper around side-wind conditions compared to head-on flow conditions. For the realistic assumption of a range of rotation of 30° around a lateral incident angle pressure RMS values up to 6.3 Pa at 5 $\frac{\mathrm{m}}{\mathrm{s}}$ free stream velocity are expected. The RMS value under those conditions is observed to increase based on a second-degree polynomial function (cf. fig. 4.13) which leads to RMS values of up to 46.7 Pa at a free stream velocity of 14 $\frac{\mathrm{m}}{\mathrm{s}}$. For a range of rotation of 50° at 5 and 14 $\frac{\mathrm{m}}{\mathrm{s}}$ those values increase to 9.9 and 71.3 Pa respectively, which underlines the importance of the knowledge about the wind direction variability at a potential power plant location. Regarding the characterization within the frequency domain the dominant frequency in the pressure fluctuation is directly prescribed by the change in the incident angle which is prescribed by the rotational speed in the measurement and in the real application depends on the short-term wind characteristics.

5.4 Estimation of the Impact of Wind Induced Surface Pressure Fluctuations on the Operation of the Open Volumetric Cavity Receiver

As introduced in section 1.4, pressure fluctuations at the receiver surface are a relevant parameter with regards to a safe operation of the OVR. Especially at highly irradiated areas of the receiver the operating mass flow is necessary to prevent overheating of the structure which is why it is desired to maintain a constant receiver mass flow under irradiation. Due to the open process, surface pressure fluctuations locally influence the receiver mass flow and an estimation of the severity is especially necessary for the proposed scaled-up cavity receiver design, where the influence of ambient wind is higher compared to smaller towers.

In order to evaluate the impact of wind induced pressure fluctuations on the receiver operation and namely the receiver mass flow, the correlation between the receiver inlet velocity and pressure difference in the system (cf. eq. (3.23)) is applied. For this estimation a pressure drop in the hot air stream under design point conditions of ≈ 1000 Pa is assumed a realistic design value. In order to set the mass flow distribution along the receiver surface as shown in fig. 3.19 differently sized orifices are foreseen in the pipe system behind the absorber modules with pressure drop coefficients in the range of 2000 to 240000 (based on the dimensioning in [17]). Because the air streams are merged together, every absorber module (cf. fig. 2.2, including the downstream orifice) within the receiver experiences the same total pressure drop and changes in the ambient pressure result in the same relative deviation from the design point mass flow independent of the individual pressure drop coefficient.

The evaluation has to distinguish between cases of constant incident angle flow and situations of varying incident angles, which results in different amplitudes and characteristic frequencies in the surface pressure fluctuations as mentioned before. For this estimation wind speeds up to 14 $\frac{\mathrm{m}}{\mathrm{s}}$ are considered.

Flow under constant incident angles leads to pressure fluctuations caused by the flow

separation at the tower geometry as those emerging vortices induce fluctuations in the velocity and pressure field. It was shown in the evaluation of the measurements (section 4.1.1) and based on the extrapolation up to 14 $\frac{\mathrm{m}}{\mathrm{s}}$ that pressure RMS values of up to $\approx 8.0\,\mathrm{Pa}$ are to be expected under constant incident angles. The pressure fluctuations induced by the receiver flow itself were numerically investigated and presented in section 4.2.3. The results show that the receiver flow itself introduces pressure fluctuations in the same order of magnitude as the extrapolated wind induced pressure fluctuations observed under constant incident angle flow without receiver operation in the experiments (cf. section 4.1.1). The RMS values due to the receiver flow reach RMS values of up to $\approx 10.5\,\mathrm{Pa}$. Assuming a sinusoidal pattern, the amplitude can be derived with a factor of $\sqrt{2}$.

Based on the correlation of the receiver inlet velocity in eq. (3.23) a pressure fluctuation with an amplitude of 14.8 Pa (calculated from the RMS value) leads to a relative deviation in the receiver mass flow of 0.7 % which can safely be assumed negligible for the operation of the receiver.

Compared to flow under constant incident angles, changing wind directions potentially lead to significantly higher surface pressure fluctuations due to the shift in the stagnation point and corresponding surface pressure. The amplitudes depend on the relative incident angle and angle range of rotation. As discussed in section 3.1, the wind direction variability significantly decreases with wind speed. An evaluation of secondly data at the STJ agrees with this observations and further revealed that based on five measurement days with varying wind speeds, the secondly variation in the incident angles is below 20° between consecutive measurement points 92 % of the time. For the estimation of the impact on the air system a limit of 20° in the incident angle change is deemed sufficient. Furthermore, it was observed that the angle, around which the change in the incident angles takes place, significantly influences the RMS value with lateral wind conditions being the most relevant.

For angle range of rotation of 20°, around a lateral incident angle, at wind speeds exceeding 8.2 $\frac{\mathrm{m}}{\mathrm{s}}$ wind becomes the relevant influence on the pressure fluctuations compared to the receiver flow induced fluctuations. For a 20° angle range and under 14 $\frac{\mathrm{m}}{\mathrm{s}}$ wind, RMS values of up to 29.3 Pa are expected based on the extrapolation of measurement data presented in fig. 4.13. The RMS value can again be transferred to an amplitude assuming a sinusoidal pattern by a factor of $\sqrt{2}$ which gives amplitudes of up to 41.4 Pa Based on the correlation of the receiver inlet velocity this leads to a relative deviation in the receiver mass flow of 1.9 % which still can be assumed irrelevant in terms of a safe operation of the receiver.

What needs to be considered in this evaluation are part load conditions of the receiver. During periods of reduced irradiation (e.g. during off design conditions in the morning) the receiver mass flow is typically reduced to maintain the target temperature, which is achieved by reducing the fan induced pressure difference in the system. Due to the lower pressure drop in the system under part load, fluctuations in the ambient pressure become more relevant. During part load conditions with a mass flow reduction of 75 % a pressure drop within the air system of 66 Pa results, which leads to wind-induced mass flow drop of 39.0 % based on the approach applied above for varying incident angles with

an angle range of rotation of 20°.

Based on the knowledge of how much the mass flow is affected by ambient wind, it is possible to estimate the impact on the maximum temperature in the porous structure with a fluid-structure model. For a simple estimate of the maximum temperature in the HiTRec absorber, the stationary 1D continuum model developed by Broeske et al. [13] is applied. Within the model, the flow inside a channel of the HiTRec absorber and the solid body is discretized in 1D, including heat convection via Nusselt correlations and conduction within both phases. The solar irradiation is derived from ray tracing results and thermal irradiation is considered by a surface to surface radiation model (cf. [13] for a detailed explanation).

With this 1D-model part load cases are simulated and evaluated in terms of the maximum occurring temperature in the absorber structure. The boundary conditions are derived from the flux density and mass flow distribution shown in fig. 3.19, assuming a flux density and mass flow distribution which is globally reduced by 75 % during part load. Two different variants regarding the inlet temperature are considered with a case of an air return ratio of 60 % and a relatively low return air temperature of 120 °C and a second case with an air return ratio of 80 % and a relatively high return air temperature of 270 °C. Based on the caloric approach of calculating the air return ratio (cf. eq. (2.3)) this results in inlet fluid temperatures of 82 and 221 °C, respectively.

For the estimation, three characteristic absorber modules at the receiver are evaluated, that cover a broad range with respect to the intercepted irradiation and mass flow density and inlet temperatures that can be expected. This gives confidence in the results representative nature. One absorber module is placed in the center with the highest intercepted irradiation $\dot{Q}_{inc}$, one is laterally shifted towards the edge of the receiver at around 1/4 of the chord length with a lower irradiation and mass flow and a third module represents average conditions regarding the mass flow and irradiation under part load. The parameters and the resulting maximum absorber temperatures $T_{abs,max}$ obtained by the 1D continuum model are summarized in table 5.1.

Table 5.1: Maximum absorber temperature $T_{abs,max}$ in the HiTRec absorber calculated with the 1D continuum model by Broeske et al. [13] under wind-induced mass flow drops at part load conditions.

			No wind		Wind	
Position	$\frac{\dot{Q}_{inc}}{A_{rec}}$ $[\frac{\mathrm{kW}}{\mathrm{m}^2}]$	T_{in} [°C]	$\frac{\dot{m}}{A}$ $[\frac{\mathrm{kg}}{\mathrm{s\,m}^2}]$	$T_{abs,max}$ [°C]	$\frac{\dot{m}}{A}$ $[\frac{\mathrm{kg}}{\mathrm{s\,m}^2}]$	$T_{abs,max}$ [°C]
Center	250	82.0	0.437	508.8	0.267	693.5
	250	221.0	0.437	613.7	0.267	715.9
Side	80	82.0	0.147	445.3	0.09	560.6
	80	221.0	0.147	530.6	0.09	618.1
Average	129	82.0	0.185	542.3	0.113	680.4
	129	221.0	0.185	623.7	0.113	733.3

The mass flow densities $\frac{\dot{m}}{A}$ in table 5.1 refer to the hot air mass flow at each absorber cup with respect to the cup frontal surface area. For the cases under wind, the mass flow is reduced by the aforementioned 39.0 %, which leads to an increase of the maximum absorber temperature of 88 to 185 K to up to 733.3 °C, which is still way below the material limits of approximately 1200 °C (cf. [5]). What is not included in the 1D-model is the return air stream within an absorber module, which in the application further reduces the solid structure temperatures. Therefore, the estimate with the 1D-channel model poses a conservative estimate with regards to the maximum absorber temperature and based on this simple approach it can be concluded that the material limits in the absorber temperature are not expected to be reached due to wind-induced receiver mass flow drops.

What can not be evaluated with this application of the steady-state 1D model are the temperature gradients occurring during those mass flow drops. In addition to the maximum temperature, the temperature gradients are relevant as well in terms of thermal stresses inside the porous structure. In order to evaluate the temperature gradients within the absorber structure, a transient absorber model has to be applied, which is able to model the thermal behaviour of the absorber and the transient chatacteristics of the air in the air system, which is out of scope of this thesis.

5.5 Passive Countermeasures to Reduce Surface Pressure Fluctuations in Large-Scale Open Volumetric Receivers

Passive measures in terms of adjustments to the tower geometry, such as the curvature of the outer shell of the tower or the application of geometric features have the potential to alter the aerodynamic behavior and local flow conditions at the solar tower. Within the experiments in this work, attachments on the tower walls next to the cavity opening are applied in order to influence the flow separation at the cavity opening and subsequently the pressure fluctuations induced by flow separation. The idea was based on an earlier flow separation at the attachments and consequent diffusion of the eddies which enter the cavity. As shown in section 4.1.3 the application of the attachments fails to consistently reduce the pressure RMS values within the cavity and no significant reduction in the RMS value under (near) side wind conditions can be observed. Those results prove the inapplicability of the intended effect but also underline the main difficulty of such measures which is a restricted effectiveness in terms of the wind incident angle. This is also observed, for example, in the work of Siegrist [47], as discussed in section 1.3.4. In order to increase the effectiveness of such measures in general, it is evident that knowledge of the local weather conditions at a potential power plant site is necessary in order to customize the passive measures to the specific application. As shown in the investigation of active countermeasures to reduce convective losses in section 4.2.5, the effectiveness decreases with the size of the aperture which can also be expected to apply to passive measures as their influence on the flow field diminishes along the flow path. An approach which could be applied on the tower design in this study is an overall reshape of the outer shell of the tower in order to alter the aerodynamic behavior of the

tower and deflect the flow at particular incident angles.

5.6 Wind Influence on Forced Convective Losses in the Open Volumetric Cavity Receiver

Until now the air return ratio in the OVR cavity design has only been evaluated under windless conditions (cf. [49]). Based on the results in this work, this evaluation is extended to the effects of lateral wind on the main cavity of the proposed cavity receiver design.

In contrast to the observations by Prakash et al. [38] and for some cases in Tan et al. [44], lateral wind does not act as a shielding barrier on the cavity receiver in this study as the ARR decreases with increasing wind speed. This is attributed to the different design of the cavity which has an opening angle of around 168° and a larger aperture area which allows ambient wind to interfere with the leeward side of the cavity as shown in a flow visualization (cf. fig. 4.37). It can be shown that lateral wind separates at the cavity opening, enters the cavity at the leeward side of the receiver and deflects the return air in that region. Due to the wind flow around the cavity a vortex is present in the cavity whose vorticity increases with wind speed leading to a stronger deflection of especially the externally returned air. This leads to a drop in the receiver-averaged total air return ratio from 87.6 % to 80.3 % and further to 78.5 % at 0, 4 and 8 $\frac{\mathrm{m}}{\mathrm{s}}$ wind speed respectively (with the external return air distribution that is adapted to the receiver mass flow). The decrease of the ARR is steeper in the low velocity range ($\leq 4\,\frac{\mathrm{m}}{\mathrm{s}}$) and flattens for larger wind speeds, which is in qualitative alignment with the observations by Maldonado Quinto [43] at a single and a cluster of four vertically placed HiTRec absorber modules.

A local evaluation of the air return ratios (internal and external) reveals that the external return air is especially vulnerable to lateral wind as the ARR_{elr} drops comparatively stronger especially at the leeward side of the receiver. The vulnerability of the external return air in the lateral regions of the receiver is attributed to the lower impulse (due to the mass flow distribution of the elr with an increased mass flow in the center of the receiver). The impulse further decreases with traveling distance of the returned air leading to a stronger deflection in the upper part of the receiver.

In addition to the evaluation under design point conditions, simulations of lateral wind with the receiver operating under off-design conditions are conducted. This investigation reveals an overall decreased air return ratio under part load (60 % intercept) and a stronger decrease in the external air return ratio which is attributed to the decreased momentum of externally returned air as the return air mass flow is reduced under part load conditions.

5.7 Evaluation of Countermeasures to Reduce Forced Convective Losses in the Open Volumetric Cavity Receiver

Based on the evaluation of forced convective losses under wind, a local adjustment of the external return air distribution is proposed as a measure to reduce those losses. To enable local adjustments in the outflow properties, the elr outflow surface is split into segments. In the proposed countermeasure the idea is to shield the regions which are affected by ambient wind, namely the edges of the receiver by shifting the mass flow or increasing the outflow velocity in those regions. The implementation of different outflow distributions is investigated, which reveals that under relatively low wind speeds of $4\,\frac{\mathrm{m}}{\mathrm{s}}$ a receiver mass flow adjusted elr distribution, which does not shield the lateral areas of the receiver overall yields the highest air return ratios. This emphasizes a constraint on the proposed measure as the ARR in the center of the receiver is more important due to the larger receiver mass flow in that area. This can lead to the situation where an improvement in the ARR at the edges of the receiver is overcompensated by the decreased ARR in the center of the receiver.

At increased wind speeds of $8\,\frac{\mathrm{m}}{\mathrm{s}}$, especially the adjusted elr distributions based on changing the outlet velocity by restricting the outflow area yield a significant improvement in ARR_{elr}, leading to an increase in the receiver-averaged inlet temperature of $\approx 8\,\mathrm{K}$. Especially at the leeward third of the receiver the ARR_{elr} can be increased by approximately 16.7 percentage points compared to the reference distribution which is a significant improvement with respect to the model uncertainties.

The dependency of the effectiveness on wind speed shows that actively controllable measures are more promising than passive adjustments which cannot be altered depending on the ambient wind conditions.

The elr distributions presented in this work do not claim to be optimal in terms of the reduction in convective losses as for example the convective losses could not be reduced at the low wind speed case at $4\,\frac{\mathrm{m}}{\mathrm{s}}$. In order to find an optimal elr distribution a feedback controller that adjusts the segment-wise outflow conditions based on the evaluation of the air return ratio or the receiver inlet temperature could be applied in the simulation model. Nevertheless, the investigation demonstrates the potential of a wind-adjusted elr distribution as an effective measure to reduce wind-induced convective losses with significant improvements at higher wind speeds.

In addition to the adjusted elr distribution the application of an aerowindow adjacent to the cavity opening is proposed in order to further shield the cavity against lateral wind. Regardless of the outflow angle and velocity, the aerowindow could not be shown to reduce the forced convective losses by at least deflecting ambient wind at the cavity opening. Due to the size of the aperture, aerowindow mass flows would be required that are not feasible in order to seal the cavity, or effectively deflect ambient wind. The effectiveness can further be assumed to depend on the wind incident angle as the outflow impulse needs to be large enough to withstand e.g. partial or full inflow into the cavity.

The evaluation of the potential of the proposed countermeasures is limited in the fact that only lateral wind was investigated. It can be expected that incident angles ranging

from lateral to head-on wind are relevant in terms of wind-induced convective losses. The investigated cases still demonstrate that ambient wind has a relevant impact on the air return ratio in the cavity OVR and that an adjusted external return air distribution has the potential to increase the ARR significantly. Nevertheless, those measures are not able to fully neglect the wind influence on a cavity receiver of this scale as a reduction in the ARR compared to windless conditions cannot be prevented. The application of an aerowindow should be considered for cavity receivers with smaller aperture areas as in those cases the required outflow impulse to seal the cavity decreases with the required traveling distance of the jet (as shown in [39] or [44]).

5.8 Recommendations for the Design of Large-Scale Open Volumetric Receivers

In general, the orientation of the receiver is prescribed by the orientation towards the sun and consequently the efficiency of the heliostat field. The optical efficiency of the heliostat field has a high priority in the receiver design as the heliostats contribute to about 40 to 50 % of the total costs according to Pfahl et al. [84]. This poses a significant restriction on the freedom of design regarding the receiver.

In addition to the countermeasures applied in this work, an adjustment in the tower geometry itself is a potential measure to reduce the wind influence on the forced convective losses. The cavity design has proven to increase the receiver efficiency in terms of reduced radiation losses and increased air return ratios compared to a convex receiver surface (e.g. STJ) as shown in Stadler et al. [49]. The outer shell of the tower could be further optimized under the consideration of ambient wind as well, which could also be incorporated in the design process under consideration of the predominant wind directions at the site location. Based on the experiences on the effectiveness of geometric adjustments being limited to certain incident angles (cf. section 4.1.3 or [47]), the knowledge of the meteorological conditions at the potential power plant site is essential in that process. Especially the predominant incident angle and its variability is a relevant parameter as varying incident angles account for the highest wind-induced pressure fluctuations.

As shown by Stadler et al. [16], it is advisable to partially return the warm air externally through outlets located adjacent to the receiver surface as this has the potential to significantly reduce parasitic losses by reducing the internally returned mass flow, which causes a relatively high pressure drop compared to the external return air flow path. Based on the evaluation of forced convective heat losses in the cavity design, it is advisable to incorporate locally controllable outlets of the externally returned air as this allows a response on changing wind conditions and can be incorporated in the overall control strategy of the receiver. The external return air outlet should be segmented into multiple separate outlets which allows a local adjustment of the outflow conditions with controllable flaps. Besides monitoring the overall hot air temperature after the sub-receiver air streams are merged, a measurement of the sub-receiver outlet temperatures should be included to incorporate the local information within the control strategy.

The application of an aerowindow should only be considered for smaller OVRs as an additional measure to reduce the wind influence on the receiver operation. The effectiveness of the aerowindow increases with decreasing traveling distance of the aerowindow jet, which offers the potential of sealing the cavity against ambient wind.

6 Summary

In this dissertation the wind influence on the operation of the open volumetric receiver (OVR) is modeled and evaluated, with the focus on a particular design incorporating cavity shaped receivers in a 240 MWth solar tower.

Unlike, for example, in molten salt tube receivers, the OVR employs an open process where ambient air is drawn into the receiver as the heat transfer medium. The openness of the process introduces additional questions and potential issues when ambient wind is present. Due to flow separation at the solar tower and changes in the wind direction, the surface pressure at the receiver varies during operation. These changes cause fluctuations in the receiver mass flow, as it is prescribed by the difference between the ambient pressure and the suction pressure set by fans in the air system. Sudden drops in the receiver mass flow can cause overheating and potential damage to the absorber structure. In addition to that, the wind influence on forced convective heat losses has been investigated in this thesis. To increase the over all system efficiency, in this concept the air is returned to the front of the absorbers after the heat exchange to the subsequent process. The aim of returning the air is using the remaining exergy and by that increasing the inlet air temperature at the receiver. Convective losses occur due to an incomplete air return by losses of return air to the ambient, which is enhanced in the presence of ambient wind. In this dissertation, these phenomena are evaluated for a scaled-up solar tower with a tower height of about 200 m, which includes three cavity-shaped open volumetric receivers. Due to the natural increase of wind speeds with height, ambient wind becomes a more relevant parameter for scaled-up designs. The results provide an indication of the severity of the wind influence on the operational safety in terms of overheating due to mass flow fluctuations and the convective losses under wind for cavity OVRs and the effectiveness of countermeasures.

The applied methods to evaluate these phenomena include CFD simulations with OpenFOAM and experiments in a wind tunnel. For the investigation of wind-induced surface pressure fluctuations, transient Detached-eddy simulations are performed, accompanied by wind tunnel experiments with a model of the tower (scale 1:290) in the High-pressure wind tunnel in Göttingen. In the experiments, Reynolds numbers up to 13.17×10^6 were reached, which correspond to wind speeds up to $5\,\frac{\mathrm{m}}{\mathrm{s}}$ in the real scale application based on the concept of similitude. The surface pressure obtained from the measurements is evaluated under constant incident angle flow from various directions and also during changes in the incident angle. With the CFD model, higher wind speeds up to $14\,\frac{\mathrm{m}}{\mathrm{s}}$ are evaluated and the receiver flow is included in the discussion, as both could not be captured by the experiments. The CFD model is validated by a comparison between the measurement and simulation based on a qualitative comparison of surface flow visualizations and a quantitative comparison of the mean and RMS value of

the pressure and its spectral distribution at probe positions inside the receiver cavities. Excellent agreement is shown for the mean pressure and the slopes in the frequency spectrum. The agreement in the RMS value varies depending on the flow characteristics, highlighting the need for locally adjusted mesh densities to capture the varying scales of turbulence. The validation is based on the simulations without considering the receiver flow. Ambient wind was assumed to be the dominant influence on the surface pressure compared to the receiver flow. Based on the results obtained, this assumption has proven to be valid for pressure fluctuations induced by changes in the wind direction but not for constant incident angle wind. In order to include the receiver flow in the CFD model, the mesh density, especially inside the cavities, had to be increased significantly. In order to keep the computational resources manageable for the transient DES, it was decided to simulate half of the tower focusing on the main cavity. Therefore, symmetry was assumed along the east-western axis of the tower, which geometrically does not pose a symmetry plane. This assumption introduces a shift in the aerodynamic resistance of the tower shown in the mean pressure and further introduced numerical instabilities that could be assigned to the interaction with the symmetry plane. Due to these unforeseen issues, the transient investigation with the receiver flow is limited to a case at $4\,\frac{\mathrm{m}}{\mathrm{s}}$ with simulation times that do not enable a spectral analysis. However, some conclusions can be drawn. Areas where ambient wind interacts with the receiver flow cause pressure fluctuations up to 10 Pa. Areas near the external return air outlet experience a more periodic pressure fluctuation with amplitudes of the same order.

For a constant incident angle flow, the pressure fluctuation depends on the incident angle as the physical cause is the flow-surface interaction of the separated vortices. The fluctuations caused by changes in the incident angle are, in addition to the flow separation, caused by the change in the dynamic pressure on the receiver surface. Therefore, they are highly dependent on the angle range or angle variability, which decreases with wind speed based on weather data evaluation. An angle range of 20° has been evaluated as an conservative estimate at high wind speeds. The expected RMS values in relation to the wind speed can be extrapolated by second-degree polynomial functions. Based on those assumptions, varying incident angles at $14\,\frac{\mathrm{m}}{\mathrm{s}}$ wind cause RMS values up to 29 Pa, significantly exceeding those under constant incident angle flow at the same wind speed. As evaluated in chapter 5, the impact on the absorber mass flow and consequently the material temperatures is particularly high under part load conditions due to the reduced pressure drop in the system. The resulting material temperatures in the porous structure are estimated with a 1D model. The maximum temperatures due to mass flow drops under wind are well below the material limits and therefore do not indicate any risk to the operation of the the OVR in this regard.

The evaluation of forced convective heat losses is performed with stationary RANS simulations, since the target value is the area- and time-averaged rate of successfully returned air (air return ratio, ARR). This approach does not allow the evaluation of fluctuations in the ARR, but enables an extensive parameter study and a numerical evaluation of countermeasures. The model is successfully verified by a comparison with previously published simulations of a similarly shaped cavity receiver under windless conditions. The investigation of forced convective heat losses covers 4 and $8\,\frac{\mathrm{m}}{\mathrm{s}}$ lateral

wind in addition to windless conditions. The results reveal a high local dependence of the air return ratio depending on where the wind enters the cavity and interacts with the receiver and return air flow. The momentum of the return air is also relevant, as it determines how well the return air can resist deflection by the ambient wind. Significant reductions in the air return ratio can be observed, especially for return air which is ejected from external outlets and not from between the absorber modules. The total receiver-averaged air return ratio drops from 87.6 %, to 80.3 % and further to 78.5 % at 0, 4 and 8 $\frac{\mathrm{m}}{\mathrm{s}}$ lateral wind, respectively. Based on these observations, countermeasures are numerically investigated, including the application of an aerowindow to deflect the incoming wind and an adjustable external return air distribution to locally alter the return air mass flow or outlet velocity. The application of an aerowindow adjacent to the cavity opening is investigated for various outlet angles and mass flows. In smaller cavity receivers, aerowindows are applied to seal the cavity against wind, which is not applicable in the given concept due to the size of the aperture. Because of the natural decrease in the outflow momentum of the aerowindow, the mass flows that would be necessary to seal the cavity would be too large. Therefore the aim was a deflection of incoming wind rather that sealing the cavity. With all configurations tested, it was not possible to deflect incoming wind effectively, as the cold air emerging from the aerowindow was drawn into the cavity, resulting in even increased convective losses.

As a second countermeasure, adjustable external return air distributions are investigated. The outlet is divided into segments, where the outlet mass flow or velocity can be adjusted individually while maintaining the total return air mass flow. The idea is to shift the return air mass flow or increase the return momentum in the lateral areas of the receiver, which have been shown to be most sensitive to lateral wind. The results of the low wind speed case (4 $\frac{\mathrm{m}}{\mathrm{s}}$ wind) highlight a constraint to this approach, as the adjustments successfully increase the air return ratio in the lateral parts of the receiver, but simultaneously reduce the air return ratio in the center of the receiver. Due to the receiver mass flow distribution with higher receiver mass flows in the center, large air return ratios in that area are more important for the overall efficiency of the return air system. At higher wind speeds (8 $\frac{\mathrm{m}}{\mathrm{s}}$), a significant improvement in the local return ratios and also the receiver-averaged air return ratio can be achieved with the adjusted distributions, leading to an increase in the averaged receiver inlet temperature of approximately 8 K (total receiver mass flow weighted average) compared to the reference case. Although the proposed distributions do not claim to be optimal, they indicate that locally adjustable return air distributions are an effective measure to reduce convective losses in the presence of wind and should be incorporated into the receiver control strategy.

7 Outlook

In terms of the wind-induced pressure fluctuations, the effect on the air system is only evaluated in relation to the design pressure drop within the air system. In order to evaluate the dynamic response of the air system in more detail the whole system and its components like pipes, vessels, fans etc. need to be discretized and modeled in detail. Such a model needs to be able to represent the transient behavior of the air in the system, the thermal behavior of the receiver structure and the surface pressure fluctuations obtained from the measurements and simulation can be utilized as input data in the boundary conditions. As under part load conditions, the mass flow within the receiver and subsequently the pressure drop in the system is reduced, part load poses a critical condition which has to be included in such an investigation. As shown in chapter 5 in a stationary approach, the material limit temperatures are not expected to be reached. What should be evaluated additionally, are the temperature gradients within the porous structure under given wind-induced pressure fluctuations. For this evaluation, a transient absorber model has to be applied, ideally including the downstream components of the air system, as they are expected to influence the inertia of the system, which prescribes how the system reacts on transient pressure conditions. Also the evaluation depends on the exact technical layout of the system which is out of scope of this thesis. Most importantly, the thermo-mechanical behavior of the porous absorber structure and the dynamics in the air system have to be modeled with high accuracy, ideally validated with experimental results. With such an investigation critical ambient conditions with regards to the structural integrity of the absorber material and potential measures to ensure a safe operation can be tested.

The evaluation of wind-induced pressure fluctuations with the transient DES approach showed the limitations of the method due to the high requirements on the level of discretization and the simulation times in order to obtain statistically significant results. Even with the application of the agglomerate approach to simplify the receiver modeling, the simulations where the receiver flow is considered reached the limitations of computational resources available in this work. The application of a symmetry plane in order to reduce the computational costs further introduced numerical instabilities due to the interaction of the separated flow with the boundary condition which emphasizes that caution needs to be taken in the dimensioning of numerical domains and with the application of symmetry planes in transient DES, especially in the vicinity of massively separated flow. In order to overcome the limitations in computational resources, an unstructured meshing approach, which allows a local refinement of the computational grid where necessary could be applied. This is expected to allow a modeling of the entire tower while ensuring dimensions of the domain which prevent contributions to the modeling error due to unintended interactions between the flow around the tower and

the ambient boundary conditions.

With such a meshing approach, the investigation regarding the forced convective heat losses could be extended as well, as the simulations in this work were limited to lateral wind. The results already showed the potential of countermeasures to reduced forced convective heat losses due to air return losses by applying a wind-adjusted external return air distribution. The evaluation should be expanded for further incident angles within the range of lateral to head-on wind in order to also capture partial or fully inflow which can be expected to be relevant in terms of forced convective losses. In order to identify optimal wind-dependent distributions of externally returned air, the simulation model could be expanded to incorporate a feedback controller that adjusts the segment-wise outflow conditions during the simulation based on the evaluation of the air return ratio or the receiver inlet temperature at the receiver. The control strategy should include locally evaluated air return ratios as well as the target hot air temperature.

Also, an investigation of the proposed countermeasures under part load conditions should be included. As the receiver and the return air mass flow will be reduced under part load conditions, the return air is more vulnerable to ambient wind due to the reduced impulse. It could be investigated how an adjustment in the return air distribution or even a shift in the total mass flow between the internally and the externally returned air is beneficial, while still maintaining the internal return air mass flow which is necessary to cool the internal structure.

Bibliography

[1] Tamme, R., Laing, D., Steinmann, W.-D., and Bauer, T. "Thermal Energy Storage". In: *Solar thermal energy*. Ed. by Alexopoulos, S. O. and Kalogirou, S. A. Encyclopedia of Sustainability Science and Technology Series. New York, NY, U.S.A.: Springer, 2022, pp. 285–313. DOI: 10.1007/978-1-0716-1422-8_684.

[2] Alexopoulos, S. and Hoffschmidt, B. "Concentrating Receiver Systems (Solar Power Tower)". In: *Solar Thermal Energy*. Springer, New York, NY, 2022, pp. 63–110. DOI: 10.1007/978-1-0716-1422-8_677.

[3] Mehos, M., Turchi, C., Vidal, J., Wagner, M., Ma, Z., Ho, C., Kolb, W., Andraka, C., and Kruizenga, A. *Concentrating Solar Power Gen3 Demonstration Roadmap*. Tech. rep. NREL/TP-5500-67464. 2017. DOI: 10.2172/1338899.

[4] Ho, C. K. "A review of high-temperature particle receivers for concentrating solar power". In: *Applied Thermal Engineering* 109 (2016), pp. 958–969. ISSN: 1359-4311. DOI: 10.1016/j.applthermaleng.2016.04.103.

[5] Ávila-Marín, A. L. "Volumetric receivers in Solar Thermal Power Plants with Central Receiver System technology: A review". In: *Solar Energy* 85.5 (2011), pp. 891–910. ISSN: 0038-092X. DOI: 10.1016/j.solener.2011.02.002.

[6] Hoffschmidt, B. "Vergleichende Bewertung verschiedener Konzepte volumetrischer Strahlungsempfaenger". PhD thesis. DLR, 1996. URL: https://elib.dlr.de/31097/.

[7] Fricker, H. W. "Tests with a small volumetric wire receiver". In: *Proceedings of the Third International Workshop on Solar Thermal Central Receiver Systems, Springer-Verlag, Konstanz, Berlin, Heidelberg, New York*. 1986.

[8] Pitz-Paal, R. "Solartechnik". Lecture Script. RWTH Aachen University, WS 2017/2018. 2017.

[9] Hoffschmidt, B., Fernandez, F., Hennecke, K., Romero, M., Stobbe, P., and Tellez, F. "Development of Ceramic Volumetric Receiver Technology". In: *5th Cologne Solar Symposium, Cologne, 21.06.01*. 2001. URL: https://elib.dlr.de/1960/.

[10] Téllez, F., Romero, M., Heller, P., Valverde, A., Dibowski, G., and Ulmer, S. "Thermal Performance of "SolAir 3000 kWth" Ceramic Volumetric Solar Receiver". In: *12th International Symposium Solar Power and Chemical Energy Systems, October 6 - 8, 2004, Oaxaca, Mexico*. Ed. by Ramos, C. and Huacuz, J. Vol. 12. SolarPACES International Symposium. Instituo de Investigaciones Electricas, 2004. URL: https://elib.dlr.de/2961/.

[11] Koll, G., Schwarzbözl, P., Hennecke, K., Hartz, T., Schmitz, M., and Hoffschmidt, B. "The Solar Tower Jülich - A Research and Demonstration Plant for Central Receiver Systems". In: *SolarPACES 2009*. 2009. URL: https://elib.dlr.de/60306/.

[12] Capuano, R. "Design of Advanced Porous Geometry for Open Volumetric Solar Receivers Based on Numerical Predictions". PhD thesis. RWTH Aachen University, 2017. DOI: 10.18154/RWTH-2017-07248.

[13] Broeske, R. T., Schwarzbözl, P., and Hoffschmidt, B. "A new partitioned 1D LTNE continuum model for the simulation of 3D-shaped honeycomb absorbers". In: *Solar Energy* 236 (2022), pp. 533–547. DOI: 10.1016/j.solener.2022.02.024.

[14] Stadler, H., Maldonado, D., Offergeld, M., Schwarzbözl, P., and Trautner, J. "CFD model for the performance estimation of open volumetric receivers and comparison with experimental data". In: *Solar Energy* 177 (2019), pp. 634–641. DOI: 10.1016/j.solener.2018.11.068.

[15] Tiddens, A., Röger, M., Stadler, H., and Hoffschmidt, B. "Air return ratio measurements at the solar tower Jülich using a tracer gas method". In: *Solar Energy* 146 (2017), pp. 351–358. ISSN: 0038-092X. DOI: 10.1016/j.solener.2017.02.027.

[16] Stadler, H., Tiddens, A., Schwarzbözl, P., Göhring, F., Baumann, T., and Trautner, J. "Improved performance of open volumetric receivers by employing an external air return system". In: *Solar Energy* 155 (2017), pp. 1157–1164. ISSN: 0038-092X. DOI: 10.1016/j.solener.2017.07.050.

[17] Schwager, C., Teixeira Boura, C., Göhring, F., Schwarzbözl, P., Uhlig, R., and Giuliano, S. *VORWAiRTS - Volumetrischer Receiver mit hoher Luftrückführrate zur Verbesserung des Systemwirkungsgrads: Schlussbericht: Berichtszeitraum: 01.09.2016 - 30.11.2019*. Tech. rep. Kraftanlagen München GmbH , Deutsches Zentrum für Luft- und Raumfahrt , Solar-Institut, Jülich, 2020. DOI: 10.2314/KXP:174916471X.

[18] Roshko, A. "Perspectives on bluff body aerodynamics". In: *Journal of Wind Engineering and Industrial Aerodynamics* 49.1-3 (1993), pp. 79–100. ISSN: 0167-6105. DOI: 10.1016/0167-6105(93)90007-B.

[19] Mockett, C. "A comprehensive study of detached-eddy simulation". PhD thesis. Technische Universität Berlin, 2009. DOI: 10.14279/depositonce-2305.

[20] Schewe, G. "On the force fluctuations acting on a circular cylinder in crossflow from subcritical up to transcritical Reynolds number". In: *Journal of Fluid Mechanics* 133 (Aug. 1983), pp. 265–285. DOI: 10.1017/S0022112083001913.

[21] Achenbach, E. "Distribution of local pressure and skin friction around a circular cylinder in cross-flow up to Re = 5 x 10^6". In: *Journal of Fluid Mechanics* 34.4 (1968), pp. 625–639. DOI: 10.1017/S0022112068002120.

[22] Schröder, W. *Fluidmechanik*. 4., korrigierte Auflage. Vol. 16. Aachener Beiträge zur Strömungsmechanik. Aachen: Wissenschaftsverlag Mainz, 2018. ISBN: 978395-8862210.

[23] Gölling, B. "Experimentelle Untersuchungen des laminar-turbulenten Überganges der Zylindergrenzschichtströmung". Dissertation. Georg-August-Universität Göttingen, 2001. DOI: 10.53846/goediss-2720.

[24] Roshko, A. "On the Wake and Drag of Bluff Bodies". In: *Journal of the Aeronautical Sciences* 22.2 (1955), pp. 124–132. DOI: 10.2514/8.3286.

[25] Bearman, P. and Morel, T. "Effect of free stream turbulence on the flow around bluff bodies". In: *Progress in Aerospace Sciences* 20.2 (1983), pp. 97–123. ISSN: 0376-0421. DOI: 10.1016/0376-0421(83)90002-7.

[26] Mittal, R. and Balachandar, S. "Effect of three–dimensionality on the lift and drag of nominally two–dimensional cylinders". In: *Physics of Fluids* 7.8 (1995), pp. 1841–1865. ISSN: 1070-6631. DOI: 10.1063/1.868500.

[27] Jordan, S. A. and Ragab, S. A. "A Large-Eddy Simulation of the Near Wake of a Circular Cylinder". In: *Journal of Fluids Engineering* 120.2 (1998), pp. 243–252. ISSN: 0098-2202. DOI: 10.1115/1.2820640.

[28] Spalart, P. "Strategies for turbulence modelling and simulations". In: *International Journal of Heat and Fluid Flow* 21.3 (2000), pp. 252–263. ISSN: 0142-727X. DOI: 10.1016/S0142-727X(00)00007-2.

[29] Ashton, N., West, A., Lardeau, S., and Revell, A. "Assessment of RANS and DES methods for realistic automotive models". In: *Computers & Fluids* 128 (2016), pp. 1–15. ISSN: 0045-7930. DOI: 10.1016/j.compfluid.2016.01.008.

[30] Spalart, P. R., Jou, W.-H., Strelets, M., and Allmaras, S. R. "Comments on the Feasibility of LES for Wings and on the Hybrid RANS/LES Approach". In: *Proceedings of the First AFOSR International Conference on DNS/LES*. Advances in DNS/LES. 1997, pp. 137–148. ISBN: 1570743657.

[31] Haase, W., Aupoix, B., Bunge, U., and Schwamborn, D., eds. *FLOMANIA — A European Initiative on Flow Physics Modelling: Results of the European-Union funded project, 2002 – 2004*. Vol. 94. SpringerLink Bücher. Berlin, Heidelberg: Springer Berlin Heidelberg, 2006. ISBN: 9783540395072. DOI: 10.1007/978-3-540-39507-2.

[32] Haase, W., Braza, M., and Revell, A., eds. *DESider – A European Effort on Hybrid RANS-LES Modelling: Results of the European-Union Funded Project, 2004–2007*. Vol. 103. SpringerLink Bücher. Berlin, Heidelberg: Springer Berlin Heidelberg, 2009. DOI: 10.1007/978-3-540-92773-0.

[33] Mockett, C., Perrin, R., Reimann, T., Braza, M., and Thiele, F. "Analysis of Detached-Eddy Simulation for the Flow Around a Circular Cylinder with Reference to PIV Data". In: *Flow, Turbulence and Combustion* 85 (2010), pp. 167–180. DOI: 10.1007/s10494-009-9243-x.

[34] Squires, K. D., Krishnan, V., and Forsythe, J. R. "Prediction of the flow over a circular cylinder at high Reynolds number using detached-eddy simulation". In: *Journal of Wind Engineering and Industrial Aerodynamics* 96.10 (2008), pp. 1528–1536. ISSN: 0167-6105. DOI: 10.1016/j.jweia.2008.02.053.

[35] Spalart, P. R., Deck, S., Shur, M. L., Squires, K. D., Strelets, M. K., and Travin, A. "A New Version of Detached-eddy Simulation, Resistant to Ambiguous Grid Densities". In: *Theoretical and Computational Fluid Dynamics* 20.3 (2006), pp. 181–195. ISSN: 0935-4964. DOI: 10.1007/s00162-006-0015-0.

[36] Wolmarans, J. R. and J., R. K. "One-way fluid-structure interaction of a medium-sized heliostat using scale-resolving CFD simulation". In: *Solar Energy* 191 (2019), pp. 84–99. ISSN: 0038-092X. DOI: 10.1016/j.solener.2019.08.068.

[37] Clausing, A. "An analysis of convective losses from cavity solar central receivers". In: *Solar Energy* 27.4 (1981), pp. 295–300. ISSN: 0038-092X. DOI: 10.1016/0038-092X(81)90062-1.

[38] Prakash, M., Kedare, S., and Nayak, J. "Investigations on heat losses from a solar cavity receiver". In: *Solar Energy* 83.2 (2009), pp. 157–170. ISSN: 0038-092X. DOI: 10.1016/j.solener.2008.07.011.

[39] Flesch, R., Stadler, H., Uhlig, R., and Hoffschmidt, B. "On the influence of wind on cavity receivers for solar power towers: An experimental analysis". In: *Applied Thermal Engineering* 87 (2015), pp. 724–735. ISSN: 1359-4311. DOI: 10.1016/j.applthermaleng.2015.05.059.

[40] Siegrist, S., Stadler, H., and Hoffschmidt, B. "Measurements of the forced convective heat loss from open cylindrical cavities of multi-MW scale solar central receiver systems". In: *AIP Conference Proceedings* 2033.1 (2018), p. 040036. ISSN: 0094-243X. DOI: 10.1063/1.5067072.

[41] Marcos, M., Romero, M., and Palero, S. "Analysis of air return alternatives for CRS-type open volumetric reciever". In: *Energy* 29.5-6 (2004), pp. 677–686. ISSN: 0360-5442. DOI: 10.1016/S0360-5442(03)00176-2.

[42] Roldán, M. I., Fernández-Reche, J., and Ballestrín, J. "Computational fluid dynamics evaluation of the operating conditions for a volumetric receiver installed in a solar tower". In: *Energy* 94 (2016), pp. 844–856. ISSN: 0360-5442. DOI: 10.1016/j.energy.2015.11.035.

[43] Maldonado Quinto, D. "Konvektive Verluste an offenen volumetrischen Solarstrahlungsempfängern". PhD thesis. RWTH Aachen University, 2016. URL: https://elib.dlr.de/109026/.

[44] Tan, T., Chen, Y., Chen, Z., Siegel, N., and Kolb, G. J. "Wind effect on the performance of solid particle solar receivers with and without the protection of an aerowindow". In: *Solar Energy* 83.10 (2009), pp. 1815–1827. ISSN: 0038-092X. DOI: 10.1016/j.solener.2009.06.014.

[45] Amsbeck, L., Helsch, G., Röger, M., and Uhlig, R. "Development of a Broadband Antireflection Coated Transparent Silica Window for a Solar-Hybrid Microturbine System". In: *SolarPACES 2009*. SolarPACES, Sept. 2009. URL: https://elib.dlr.de/61593/.

[46] Flesch, R., Grobbel, J., Stadler, H., Uhlig, R., and Hoffschmidt, B. "Reducing the convective losses of cavity receivers". In: *AIP Conference Proceedings* 1734.1 (2016), p. 030014. ISSN: 0094-243X. DOI: 10.1063/1.4949066.

[47] Siegrist, S. "Forced convective heat loss from cavities of multi-megawatt scale solar receivers". Dissertation. Aachen: RWTH Aachen University, 2018. DOI: 10.18154/RWTH-2018-231862.

[48] Schwarzbözl, P., Giuliano, S., Noureldin, K., Doerbeck, T., Rosselló, A., and Schrüfer, J. "Annual performance assessment of a 50 MWe commercial solar tower plant with improved open volumetric receiver". In: *SolarPACES 2020: 26th International Conference on Concentrating Solar Power and Chemical Energy Systems*. AIP Conference Proceedings. AIP Publishing, 2020, p. 030021. DOI: 10.1063/5.0085758.

[49] Stadler, H., Schwarzbözl, P., Maldonado, D., Broeske, R., Andlauer, F., Trautner, J., and Schrüfer, J. "Performance assessment of an improved open volumetric receiver design with 240 MWth". In: *SolarPACES 2018: International Conference on Concentrating Solar Power and Chemical Energy Systems*. AIP Conference Proceedings. AIP Publishing, 2019, p. 030057. DOI: 10.1063/1.5117569.

[50] Belhomme, B., Pitz-Paal, R., Schwarzbözl, P., and Ulmer, S. "A New Fast Ray Tracing Tool for High-Precision Simulation of Heliostat Fields". In: *Journal of Solar Energy Engineering* 131.3 (2009). ISSN: 0199-6231. DOI: 10.1115/1.3139139.

[51] Drexelius, M., Schwarzbözl, P., and Pitz-Paal, R. "Experimental evaluation of wind induced pressure fluctuations in cavity shaped open volumetric air receivers". In: *Solar Energy* 247 (2022), pp. 146–157. ISSN: 0038-092X. DOI: 10.1016/j.solener.2022.10.003.

[52] Hoffschmidt, B., Téllez, F. M., Valverde, A., Fernández, J., and Fernández, V. "Performance Evaluation of the 200-kWth HiTRec-II Open Volumetric Air Receiver". In: *Journal of Solar Energy Engineering* 125.1 (2003), pp. 87–94. DOI: 10.1115/1.1530627.

[53] Buckingham, E. "On Physically Similar Systems; Illustrations of the Use of Dimensional Equations". In: *Physical Review* 4.4 (1914), pp. 345–376. ISSN: 0031-899X. DOI: 10.1103/PhysRev.4.345.

[54] Wolowicz, C. H., Brown, J. S., and Gilbert, W. P. "Similitude Requirements and Scaling Relationships as Applied to Model Testing". In: 1979.

[55] Kline, S. J. *Similitude and Approximation Theory*. Berlin, Heidelberg: Springer Berlin / Heidelberg, 1986. ISBN: 9783642616389.

[56] Büttgenbach, S., Constantinou, I., Dietzel, A., and Leester-Schädel, M. "Piezoresistive Pressure Sensors". In: *Case Studies in Micromechatronics*. Springer, Berlin, Heidelberg, 2020, pp. 21–85. DOI: 10.1007/978-3-662-61320-7_2.

[57] Ferziger, J. H. and Perić, M. *Numerische Strömungsmechanik*. 2., aktual. Aufl. 2020. Berlin, Heidelberg: Springer Berlin Heidelberg, 2020. ISBN: 9783662465448. URL: http://nbn-resolving.org/urn:nbn:de:bsz:31-epflicht-1813599.

[58] Hirsch, C. *Fundamentals of numerical discretization*. Reprinted. Vol. Vol. 1. Wiley series in numerical methods in engineering. Chichester: Wiley, 2001. ISBN: 0471917621.

[59] Courant, R., Friedrichs, K., and Lewy, H. "Über die partiellen Differenzengleichungen der mathematischen Physik". In: *Mathematische Annalen* 100.1 (1928), pp. 32–74. ISSN: 0025-5831. DOI: 10.1007/BF01448839.

[60] Choi, H. and Moin, P. "Effects of the Computational Time Step on Numerical Solutions of Turbulent Flow". In: *Journal of Computational Physics* 113.1 (1994), pp. 1–4. ISSN: 0021-9991. DOI: 10.1006/jcph.1994.1112.

[61] Spalart, P. R. and Streett, C. *Young-Person's Guide to Detached-Eddy Simulation Grids*. Tech. rep. 2001. URL: https://ntrs.nasa.gov/citations/20010080473.

[62] Richardson, L. F. "Weather prediction by numerical process". In: *Cambridge: Cambridge University Press* (1922). DOI: 10.1017/CBO9780511618291.

[63] Pope, S. B. *Turbulent flows*. 1. publ., 12. print. Cambridge: Cambridge Univ. Press, 2000. DOI: 10.1017/CBO9780511840531.

[64] Kolmogorov, A. N. "The local structure of turbulence in incompressible viscous fluid for very large Reynolds numbers". In: *Proceedings of the Royal Society of London. Series A: Mathematical and Physical Sciences* 434.1890 (1991), pp. 9–13. DOI: 10.1098/rspa.1991.0075.

[65] Wilcox, D. C. *Turbulence modeling for CFD*. 3. ed., 2. print. La Cañada, Calif., DCW Industries, 2006. ISBN: 9781928729082.

[66] Comte-Bellot, G. and Corrsin, S. "Simple Eulerian time correlation of full-and narrow-band velocity signals in grid-generated, 'isotropic' turbulence". In: *Journal of Fluid Mechanics* 48 (1971), pp. 273–337. DOI: 10.1017/S0022112071001599.

[67] Reynolds, O. "On the dynamical theory of incompressible viscous fluids and the determination of the criterion". In: *Philosophical Transactions of the Royal Society of London, Series A* 186 (1895), pp. 123–164. DOI: 10.1098/rsta.1895.0004.

[68] Boussinesq, J. *Essai sur la théorie des eaux courantes*. Memoires presentes par divers savants a l'Academie des Sciences de l'Institut National de France, Tome XXIII, No 1. Imprimerie Nationale, Paris, 1877.

[69] Prandtl, L. "7. Bericht über Untersuchungen zur ausgebildeten Turbulenz". In: *ZAMM - Journal of Applied Mathematics and Mechanics / Zeitschrift für Angewandte Mathematik und Mechanik* 5.2 (1925), pp. 136–139. DOI: 10.1002/zamm.19250050212.

[70] Spalart, P. R. and Allmaras, S. R. "A one-equation turbulence model for aerodynamic flows". In: *30th Aerospace Sciences Meeting and Exhibit*. 1992. DOI: 10.2514/6.1992-439.

[71] Boris, J. P., Grinstein, F. F., Oran, E. S., and Kolbe, R. L. "New insights into large eddy simulation". In: *Fluid Dynamics Research* 10.4-6 (1992), pp. 199–228. ISSN: 0169-5983. DOI: 10.1016/0169-5983(92)90023-P.

[72] Leonard, A. "Energy Cascade in Large Eddy Simulations of Turbulent Fluid Flow". In: *Adv. Geophys.* 18A (Jan. 1974), pp. 237–248. DOI: 10.1016/S0065-2687(08)60464-1.

[73] Deardorff, J. W. "A numerical study of three-dimensional turbulent channel flow at large Reynolds numbers". In: *Journal of Fluid Mechanics* 41.2 (1970), pp. 453–480. DOI: 10.1017/S0022112070000691.

[74] Lund, T. S. "The use of explicit filters in large eddy simulation". In: *Computers & Mathematics with Applications* 46.4 (2003), pp. 603–616. DOI: 10.1016/S0898-1221(03)90019-8.

[75] Smagorinsky, J. "General Circulation Experiments with the Primitive Equations". In: *Monthly Weather Review* 91.3 (1963), pp. 99–164. DOI: 10.1175/1520-0493(1963)091<0099:GCEWTP>2.3.CO;2.

[76] Deck, S. "Zonal-Detached-Eddy Simulation of the Flow Around a High-Lift Configuration". In: *AIAA Journal* 43.11 (2005), pp. 2372–2384. DOI: 10.2514/1.16810.

[77] Piomelli, U., Balaras, E., Pasinato, H., Squires, K. D., and Spalart, P. R. "The inner–outer layer interface in large-eddy simulations with wall-layer models". In: *International Journal of Heat and Fluid Flow* 24.4 (2003), pp. 538–550. DOI: 10.1016/S0142-727X(03)00048-1.

[78] Chapman, D. R. "Computational Aerodynamics Development and Outlook". In: *AIAA Journal* 17.12 (1979), pp. 1293–1313. DOI: 10.2514/3.61311.

[79] Versteeg, H. K. and Malalasekera, W. *An introduction to computational fluid dynamics: The finite volume method*. Pearson education, 2007.

[80] Schlichting, H. and Gersten, K. *Boundary-Layer Theory*. 9th ed. 2017. Springer eBook Collection Engineering. Berlin, Heidelberg: Springer, 2017. DOI: 10.1007/978-3-662-52919-5.

[81] Dong, Y., Yan, Y., and Liu, C. "New visualization method for vortex structure in turbulence by lambda2 and vortex filaments". In: *Applied Mathematical Modelling* 40.1 (2016), pp. 500–509. ISSN: 0307-904X. DOI: 10.1016/j.apm.2015.04.059.

[82] Jeong, J. and Hussain, F. "On the identification of a vortex". In: *Journal of Fluid Mechanics* 285 (1995), pp. 69–94. DOI: 10.1017/S0022112095000462.

[83] ISO 2008. *Guide to the expression of uncertainty in measurement (GUM:1995)*. Tech. rep. International Organization for Standardization, 2008.

[84] Pfahl, A., Coventry, J., Röger, M., Wolfertstetter, F., Vásquez-Arango, J. F., Gross, F., Arjomandi, M., Schwarzbözl, P., Geiger, M., and Liedke, P. "Progress in heliostat development". In: *Solar Energy* 152 (2017), pp. 3–37. DOI: 10.1016/j.solener.2017.03.029.

[85] Brooks, M. J., Du Clou, S., van Niekerk, W. L., Gauche, P., Leonard, C., Mouzouris, M. J., Meyer, R., van der Westhuizen, N., van Dyk, E. E., and Vorster, F. J. "SAURAN : a new resource for solar radiometric data in Southern Africa". In: *2413-3051* (2015). ISSN: 2413-3051. URL: https://scholar.sun.ac.za/handle/10019.1/99705.

[86] Kent, C. W., Grimmond, C., Gatey, D., and Barlow, J. F. "Assessing methods to extrapolate the vertical wind-speed profile from surface observations in a city centre during strong winds". In: *Journal of Wind Engineering and Industrial Aerodynamics* 173 (2018), pp. 100–111. ISSN: 0167-6105. DOI: 10.1016/j.jweia.2017.09.007.

[87] Augsburger, G. "Thermo-economic optimisation of large solar tower power plants". PhD thesis. EPFL, 2013. DOI: 10.5075/epfl-thesis-5648.

[88] Saucier, W. J. and Brundidge, K. C. "Variability of Wind Direction in Relation to Wind Speed". In: *Bulletin of the American Meteorological Society* 37.9 (1956), pp. 462–464. ISSN: 1520-0477. DOI: 10.1175/1520-0477-37.9.462.

[89] Mahrt, L. "Surface Wind Direction Variability". In: *Journal of Applied Meteorology and Climatology* 50.1 (2011), pp. 144–152. ISSN: 1558-8432. DOI: 10.1175/2010JAMC2560.1.

[90] Joffre, S. M. and Laurila, T. "Standard Deviations of Wind Speed and Direction from Observations over a Smooth Surface". In: *Journal of Applied Meteorology* 27.5 (1988), pp. 550–561. ISSN: 0894-8763. DOI: 10.1175/1520-0450(1988)027<0550:SDOWSA>2.0.CO;2.

[91] van Hinsberg, N. P. "The Reynolds number dependency of the steady and unsteady loading on a slightly rough circular cylinder: From subcritical up to high transcritical flow state". In: *Journal of Fluids and Structures* 55 (2015), pp. 526–539. DOI: 10.1016/j.jfluidstructs.2015.04.002.

[92] van Hinsberg, N. P., Schewe, G., and Jacobs, M. "Experimental investigation on the combined effects of surface roughness and corner radius for square cylinders at high Reynolds numbers up to 107". In: *Journal of Wind Engineering and Industrial Aerodynamics* 173 (2018), pp. 14–27. DOI: 10.1016/j.jweia.2017.12.003.

[93] Günter Schewe. "Force and Moment Measurements in Aerodynamics and Aeroelasticity using Piezoelectric Transducers". In: *Springer handbook of experimental fluid mechanics*. Ed. by Tropea, C., Yarin, A. L., and Foss, J. F. Springer handbooks. Berlin: Springer, 2007, pp. 596–616. ISBN: 978-3-540-25141-5.

[94] Tamura, Y. and Fujii, K. "Visualization for computational fluid dynamics and the comparison with experiments". In: *Flight Simulation Technologies Conference and Exhibit*. 1990, p. 3031. DOI: https://dx.doi.org/10.2514/6.1990-3031.

[95] Moffat, R. J. "Describing the uncertainties in experimental results". In: *Experimental Thermal and Fluid Science* 1.1 (1988), pp. 3–17. DOI: 10.1016/0894-1777(88)90043-X.

[96] Braune, M. "Identifizierung eines Flattermechanismus an einem superkritischen Profil unter laminarer Strömung". PhD thesis. Georg-August-Universität Göttingen, 2021. DOI: 10.53846/goediss-8675.

[97] Allen, H. J. and Vincenti, W. G. "Wall interference in a two-dimensional-flow wind tunnel, with consideration of the effect of compressibility". In: *Annual Report of the National Advisory Committee for Aeronautics* 268 (1944), p. 155.

[98] Roshko, A. "Experiments on the flow past a circular cylinder at very high Reynolds number". In: *Journal of Fluid Mechanics* 10 (1961), pp. 345–356. DOI: 10.1017/S0022112061000950.

[99] Ansys. *ICEM CFD, Release 2020 R2, Help System, ANSYS ICEM CFD User's Manual, ANSYS, Inc.* 2022.

[100] Poulain, P., Craig, K. J., and Meyer, J. P. "Transient simulation of an atmospheric boundary layer flow past a heliostat using the Scale-Adaptive Simulation turbulence model". In: *Journal of Wind Engineering and Industrial Aerodynamics* 218 (2021), p. 104740. ISSN: 0167-6105. DOI: 10.1016/j.jweia.2021.104740.

[101] Liu, F. "A thorough description of how wall functions are implemented in OpenFOAM". In: *Proceedings of CFD with OpenSource Software, Edited by Nilsson. H.* 2016.

[102] Popovac, M. and Hanjalic, K. "Compound Wall Treatment for RANS Computation of Complex Turbulent Flows and Heat Transfer". In: *Flow, Turbulence and Combustion* 78.2 (2007), pp. 177–202. ISSN: 1573-1987. DOI: 10.1007/s10494-006-9067-x.

[103] The OpenFOAM Foundation. *OpenFOAM — Free CFD Software — The OpenFOAM Foundation*. https://openfoam.org/. Accessed: 19.11.2022. 2022.

[104] Patankar, S. and Spalding, D. "A calculation procedure for heat, mass and momentum transfer in three-dimensional parabolic flows". In: *International Journal of Heat and Mass Transfer* 15.10 (1972), pp. 1787–1806. ISSN: 0017-9310. DOI: 10.1016/0017-9310(72)90054-3.

[105] Issa, R. I. "Solution of the implicitly discretised fluid flow equations by operator-splitting". In: *Journal of Computational Physics* 62.1 (1986), pp. 40–65. DOI: 10.1016/0021-9991(86)90099-9.

[106] Patankar, S. V. *Numerical heat transfer and fluid flow*. Series in computational methods in mechanics and thermal sciences. Washington: Hemisphere Pub. Corp. and New York McGraw-Hill, 1980. ISBN: 0070487405.

[107] Shur, M. L., Spalart, P. R., Strelets, M. K., and Travin, A. K. "An Enhanced Version of DES with Rapid Transition from RANS to LES in Separated Flows". In: *Flow, Turbulence and Combustion* 95.4 (2015), pp. 709–737. ISSN: 1573-1987. DOI: 10.1007/s10494-015-9618-0.

[108] Yan, J., Mockett, C., and Thiele, F. "Investigation of Alternative Length Scale Substitutions in Detached-Eddy Simulation". In: *Flow, Turbulence and Combustion* 74.1 (2005), pp. 85–102. ISSN: 1573-1987. DOI: 10.1007/s10494-005-6916-y.

[109] Stephan, P., Kabelac, S., Kind, M., Martin, H., Mewes, D., and Schaber, K. *VDI-Wärmeatlas*. Berlin, Heidelberg: Springer, 2013. DOI: 10.1007/978-3-642-19981-3.

[110] Allmaras, S. R., Johnson, F. T., and Spalart, P. R. "Modifications and clarifications for the implementation of the Spalart-Allmaras turbulence model". In: *Seventh international conference on computational fluid dynamics (ICCFD7)*. Vol. 1902. Big Island, HI. 2012.

[111] Ahlbrink, N., Belhomme, B., and Pitz-Paal, R. "Transient Simulation of Solar Tower power Plant with Open Volumetric Air Receiver". In: *SolarPACES 2009*. 2009. URL: https://elib.dlr.de/78438/.

[112] Ahlbrink, N., Andersson, J., Diehl, M., and Pitz-Paal, R. "Optimization of the Mass Flow Rate Distribution of an Open Volumetric Air Receiver". In: *Journal of Solar Energy Engineering* 135.4 (2013). ISSN: 0199-6231. DOI: 10.1115/1.4024245.

[113] Ferziger, J. H. and Perić, M. "Further discussion of numerical errors in CFD". In: *International Journal for Numerical Methods in Fluids* 23.12 (1996), pp. 1263–1274. ISSN: 0271-2091. DOI: 10.1002/(SICI)1097-0363(19961230)23:12<1263::AID-FLD478>3.0.CO;2-V.

[114] Celik, I., Ghia, U., Roache, P. J., Freitas, C. J., Coloman, H., and Raad, P. E. "Procedure for Estimation and Reporting of Uncertainty Due to Discretization in CFD Applications". In: *Journal of Fluids Engineering* 130.7 (2008), p. 078001. ISSN: 0098-2202. DOI: 10.1115/1.2960953.

[115] Meana-Fernández, A., Fernández Oro, J. M., Argüelles Díaz, K. M., Galdo-Vega, M., and Velarde-Suárez, S. "Application of Richardson extrapolation method to the CFD simulation of vertical-axis wind turbines and analysis of the flow field". In: *Engineering Applications of Computational Fluid Mechanics* 13.1 (2019), 359–376. ISSN: 1994-2060. DOI: 10.1080/19942060.2019.1596160.

[116] Meloni, S., Di Marco, A., Mancinelli, M., and Camussi, R. "Experimental investigation of jet-induced wall pressure fluctuations over a tangential flat plate at two Reynolds numbers". In: *Scientific Reports* 10.1 (2020), p. 9140. ISSN: 2045-2322. DOI: 10.1038/s41598-020-66037-2.

[117] Drexelius, M., Schwarzbözl, P., and Pitz-Paal, R. "Numerical analysis of wind-induced convective heat losses in large-scale open volumetric cavity receivers and the evaluation of countermeasures". In: *Solar Energy* 267 (2024). DOI: https://doi.org/10.1016/j.solener.2023.112233.

[118] Drexelius, M. and Schwarzbözl, P. "Numerical and Experimental Investigation of the Wind Influence on Scaled-Up Open Volumetric Cavity Receivers". In: vol. ASME 2024 18th International Conference on Energy Sustainability. Energy Sustainability. July 2024, V001T05A003. DOI: 10.1115/ES2024-130498.

[119] Jones, G., Cincotta, J., and Walker, R. "Aerodynamic Forces on a Stationary and Oscillating Circular Cylinder at High Reynolds Numbers". In: (1969).

[120] Savitzky, A. and Golay, M. J. E. "Smoothing and Differentiation of Data by Simplified Least Squares Procedures". In: *Analytical Chemistry* 36.8 (1964), pp. 1627–1639. ISSN: 0003-2700. DOI: 10.1021/ac60214a047.

[121] Lin, J. "Control of turbulent boundary-layer separation using micro-vortex generators". In: *30th Fluid Dynamics Conference*. Reston, Virigina: American Institute of Aeronautics and Astronautics, 6281999. DOI: 10.2514/6.1999-3404.

[122] Holden, H. and Babinsky, H. "Effect of Microvortex Generators On Seperated Normal Shock/ Boundary Layer Interactions". In: *Journal of Aircraft* 44.1 (2007), pp. 170–174. ISSN: 0021-8669. DOI: 10.2514/1.22770.

[123] Welch, P. "The use of fast Fourier transform for the estimation of power spectra: A method based on time averaging over short, modified periodograms". In: *IEEE Transactions on Audio and Electroacoustics* 15.2 (1967), pp. 70–73. DOI: 10.1109/TAU.1967.1161901.

[124] Harris, F. "On the use of windows for harmonic analysis with the discrete Fourier transform". In: *Proceedings of the IEEE* 66.1 (1978), pp. 51–83. DOI: 10.1109/PROC.1978.10837.

[125] Patwardhan, S. S. and Ramesh, O. N. "Scaling of pressure spectrum in turbulent boundary layers". In: *Journal of Physics: Conference Series* 506 (2014), p. 012011. DOI: 10.1088/1742-6596/506/1/012011.

[126] Hussein, H. J., Capp, S. P., and George, W. K. "Velocity measurements in a high-Reynolds-number, momentum-conserving, axisymmetric, turbulent jet". In: *Journal of Fluid Mechanics* 258 (1994), pp. 31–75. ISSN: 0022-1120. DOI: 10.1017/S002211209400323X.

[127] Meyer, M. *Signalverarbeitung: Analoge und digitale Signale, Systeme und Filter*. 7., verb. Aufl. 2014. SpringerLink Bücher. Wiesbaden: Springer Vieweg, 2014. ISBN: 9783658026127. DOI: 10.1007/978-3-658-02612-7.

[128] Yoshizawa, A. "Statistical theory for compressible turbulent shear flows, with the application to subgrid modeling". In: *The Physics of Fluids* 29.7 (1986), pp. 2152–2164. DOI: 10.1063/1.865552.

[129] Saad, T., Cline, D., Stoll, R., and Sutherland, J. C. "Scalable Tools for Generating Synthetic Isotropic Turbulence with Arbitrary Spectra". In: *AIAA Journal* 55.1 (2017), pp. 327–331. DOI: 10.2514/1.J055230.

Appendix

A Technical Sketch of the Wind Tunnel Model

In fig. A.1 an exploded view of the wind tunnel model is shown, including all the main parts of the tower except the screws and pins used for the attachment. As shown in fig. A.1, the side shields adjacent to the receiver cavities are attached from the inside. At the entire upper part, outward facing screws were avoided within the construction besides the top and bottom plates, which are attached by screws and pins. The model is mounted on the force balance, which is located outside of the tower side wall and is not visual in this sketch.

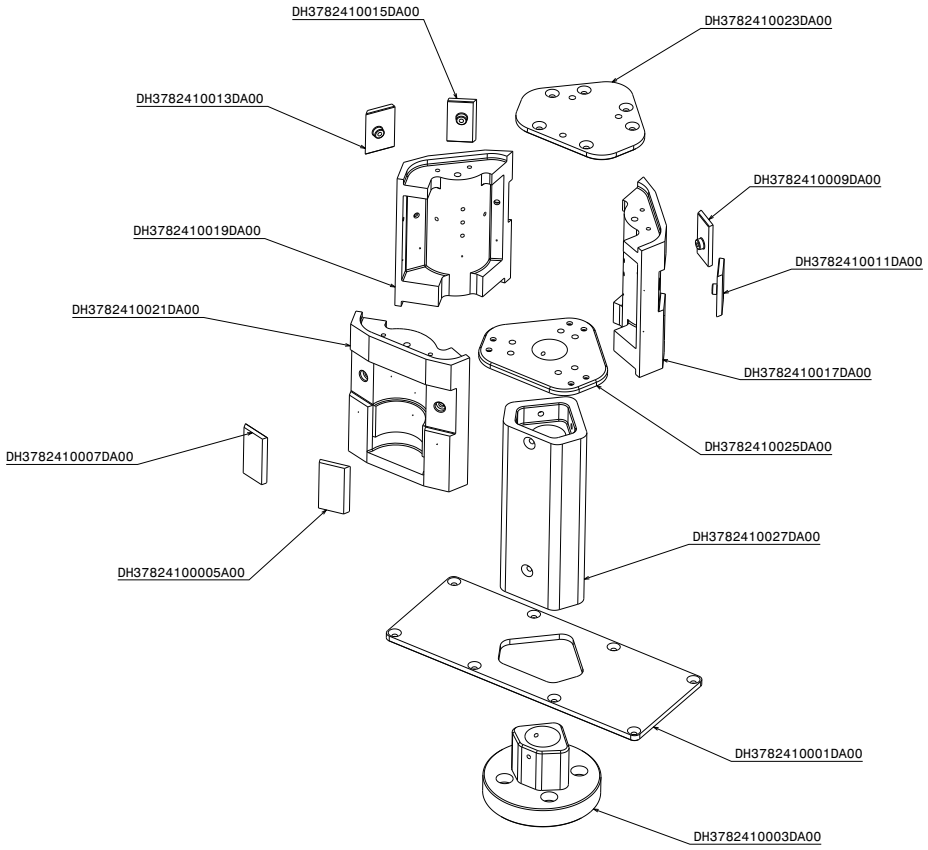

Figure A.1: Technical sketch of the solar tower model in an exploded view including the interface to the wind tunnel side wall.

B Applied Fourier Transform

To analyze data signals in the frequency domain, a Fourier transform can be applied to convert the time signal into a frequency signal. For further reading, the reader is referred to Meyer [127] where the fundamentals of signal processing are derived and described in detail. In the most basic sense a Fourier transform is defined for a periodic signal $x(t)$ with the oscillation period T that can be decomposed into a series of harmonic oscillations. Using Euler's formula (c.f. [127]) the function $x(t)$ can be written in the complex form as in eq. (B.1)

$$x(t) = \sum_{k=-\infty}^{\infty} \hat{c}_k \exp(ik\omega t) \quad \text{with} \quad \hat{c}_k = \frac{1}{T}\int_0^T x(t)\exp(-ik\omega t)dt \tag{B.1}$$

with the Fourier coefficients $\hat{c}_k$.

For aperiodic signals, the Fourier transform can be applied by striving the period T towards ∞, which results in the mathematical definition of the Fourier transform $X(i\omega)$ in the frequency domain as in eq. (B.2).

$$X(i\omega) = \frac{1}{2\pi}\int_{-\infty}^{\infty} x(t)\exp(-i\omega t)dt \tag{B.2}$$

In measurements and simulations, a continuous signal $x(t)$ is sampled at a sampling rate $f_s = \frac{1}{T}$ which results in time discrete signals of the form $x[n]$. For those signals a discrete Fourier transform (DFT) or fast Fourier transform (FFT) can be applied. In general, the signals are finite, containing N discrete values obtained over the time period NT with the interval length T.

The DFT writes as in eq. (B.3)

$$X[m] = \sum_{n=0}^{N-1} x[n]\exp(-i2\pi\frac{mn}{N}) \tag{B.3}$$

with n sampling points and the frequency f which obtained from $f = \frac{m}{NT}$.

The fast Fourier Transform (FFT) is an algorithm based on the DFT which utilizes the periodicity of the trigonometric functions behind the DFT to effectively reduce the computational costs while maintaining the same result as with the DFT (c.f. [127]).

In this study, Welch's method of the FFT presented in [123] is applied to obtained the frequency distribution and the power spectral density (S_{xx}) of the measurement and simulation data. In Welch's method, the discrete signal $x[n]$) is divided into L segments of N data points each. Each segment in the time domain is multiplied with a windowing function $w[n]$) before a DFT is applied. The results obtained from each segment are

then averaged as a final step. The windowing function is applied to reduce the so-called leakage effect that occurs due to the finiteness of the signal. The Hann windowing function is used in this work, which writes as in eq. (B.4).

$$w\left[n\right] = \frac{1}{2}\left(1 - cos\left(\frac{2\pi n}{N}\right)\right) \tag{B.4}$$

The windowing function fades to zero at the edges of the time series ($n \to 0$ and $n \to N$). For a detailed explanation of windowing functions the reader is referred to Harris [124]).

The power spectral density (S_{xx}) at each frequency bin is computed via eq. (B.5)

$$S_{xx}\left[m\right] = S_A \frac{1}{L} \sum_{l=1}^{L} \left|X_{w,l}\left[m\right]\right|^2 \tag{B.5}$$

where $X_{w,l}\left[m\right]$ denotes the DFT of the discrete signal multiplied with the windowing function for each interval l.

$$X_{w,l}\left[m\right] = \sum_{n=0}^{N-1} x\left[n\right] w\left[n\right] \exp(-i2\pi \frac{mn}{N}) \tag{B.6}$$

The parameter S_A in eq. (B.5) denotes a correction factor for the amplitude in each segment, which is set to 1 in this work.

C Additional Wind Tunnel Measurement Data

In this section, additional data obtained from the wind tunnel experiments described in section 4.1 are presented as a reference. Furthermore, the procedure for obtaining the data samples for the test series of varying incident angles is described.

C.1 Power Spectrum of the Surface Pressure at a South-Eastern Incident Angle

In fig. C.1 the power spectral density of the surface pressure S_{pp} obtained at an incident angle of $\phi = 45°$ is displayed for all probe positions inside the cavities. The incident angle corresponds to the incident angle at which the DDES simulations with the SE-model have been conducted, the results of which are discussed in section 4.2.2.

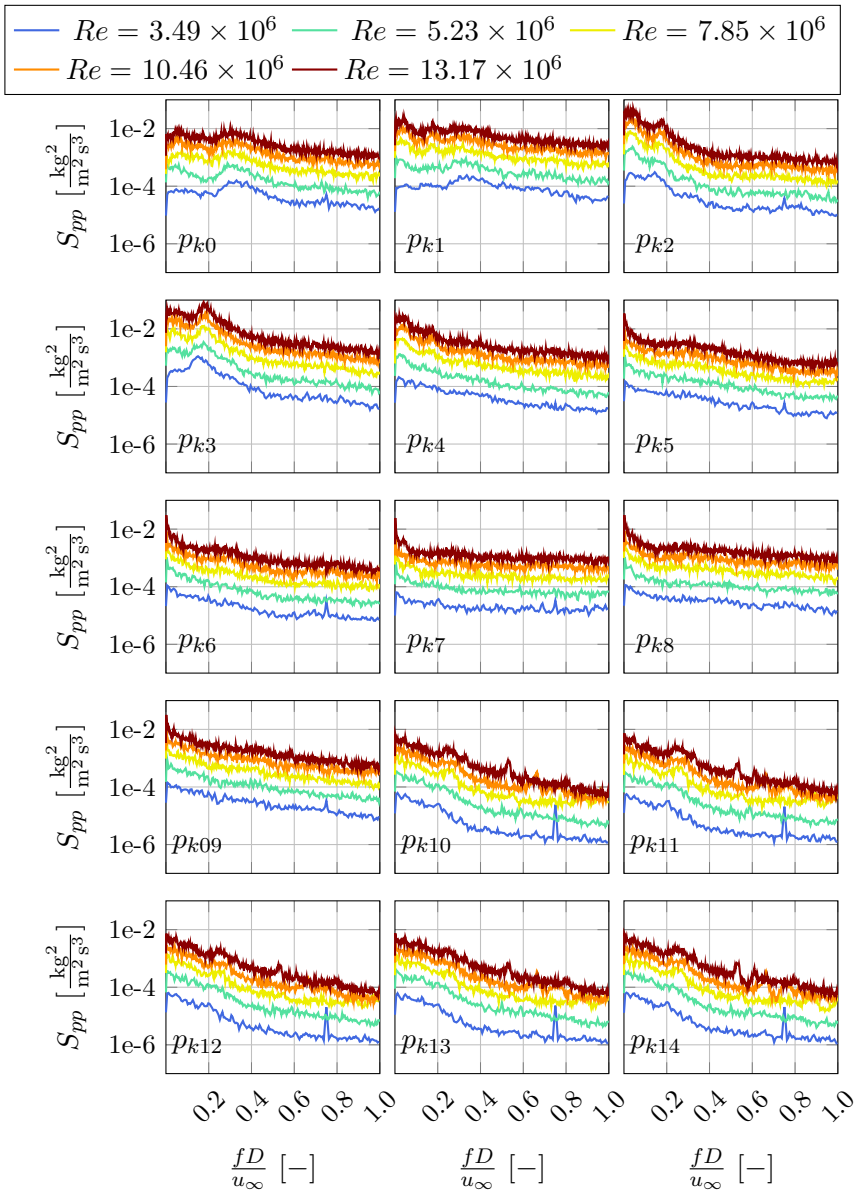

Figure C.1: Power spectral density of the pressure S_{pp} as a function of the dimensionless frequency $\frac{fD}{u_\infty}$ based on the free stream velocity u_∞ and the tower width D, for an incident angle of $\phi = 45°$ each cavity probe and Reynolds number.

C.2 Identification of the Time Samples in Test Series of Varying Incident Angles

In contrast to the first test series within the measurements (constant flow direction), the data processing of the second test series of varying incident angles is more complex due to the measurement procedure. As described in section 3.2.2 the tower had to be rotated back and forth in order to avoid torsion and damage to the instrumentation of the measurement equipment. Between each rotation the tower was rested to avoid hysteresis and as the start had to be manually initiated by the operator the rest time is not uniform. For the pressure evaluation, a synthetic time series was created in a post-processing step, which excludes the times when the tower was rested between each rotation. To identify the start and end of each rotation, the pitch moment is analyzed, which is calculated from the forces recorded by the piezoelectric force balance (cf. section 3.2.3).

As can be seen in fig. C.2, the beginning and end of each rotation can be identified by a local search of the extrema in the pitch moment. To facilitate the automatic identification of the local extrema in the pitch moment, the signal is filtered with a Savitzky-Golay filter (cf. [120]) to reduce the noise in the signal. In principal, the algorithm uses a polynomial window-wise regression to smooth the signal. In this case the filter window length was chosen to be 0.7 s and the data in each window was fitted by a second order polynomial function. Based on the given rotational speed the start of the rotation can

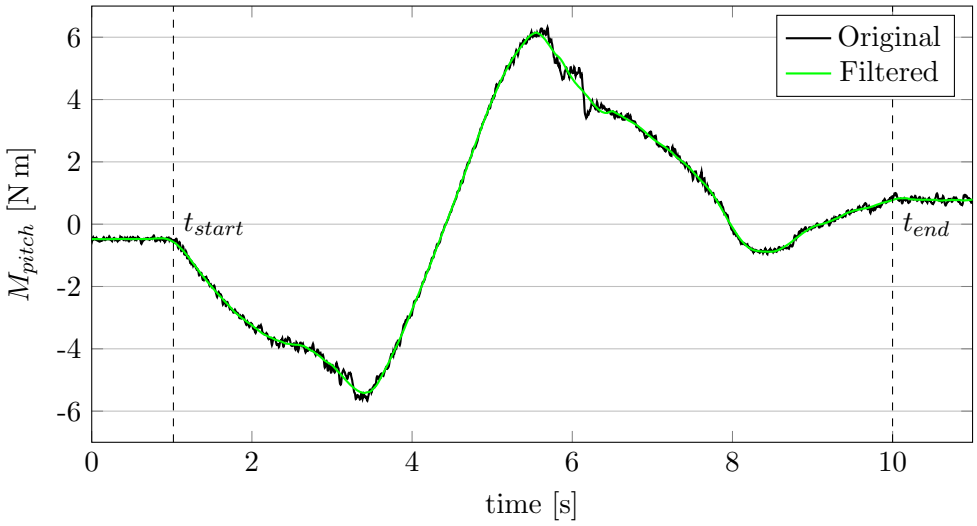

Figure C.2: Original and filtered time series of the measured pitch moment M_{pitch} during a rotation from $\phi = 0°$ to 180° with an angular velocity of 20 $\frac{°}{s}$ and Reynolds number of 10.46×10^6.

be traced back from the local minimum in the filtered pitch moment.

D SA-turbulence Model

In this section the full set of model equations of the Spalart-Allmaras RANS (SA-RANS) turbulence model are presented as it is applied within the simulations in this thesis. Furthermore, the definition of the DES length scale used within the Spalart-Allmaras (Delayed) Detached-eddy simulation (SA-(D)DES) model is presented, followed by the calibration process of the model constant C_{DES} within the (D)DES model which is based on a case of decaying isotropic turbulence (DIT).

D.1 SA-RANS Model

The SA-RANS model presented by Spalart and Allmaras [70] is a one-equation model for the modified SA-eddy viscosity $\tilde{\nu}$, which is obtained by the following transport equation

$$\frac{\partial(\tilde{\nu})}{\partial t} + \nabla \cdot (u\tilde{\nu}) = c_{b1}\rho\tilde{S}\tilde{\nu} - c_{w1}f_w\rho\frac{\tilde{\nu}^2}{d^2} + \frac{1}{\sigma}[\nabla((\nu+\tilde{\nu})\nabla\tilde{\nu}) + c_{b2}(\nabla\tilde{\nu})^2] \tag{D.1}$$

with $\tilde{S}$ defined as

$$\tilde{S} \equiv \Omega + \frac{\tilde{\nu}}{\kappa^2 d^2} f_{v2} \tag{D.2}$$

with Ω as the magnitude of the vorticity, d as the distance to the wall and κ as the thermal conductivity. The function f_{v2} is defined as in eq. (D.3).

$$f_{v2} = 1 - \frac{\chi}{1+\chi f_{v1}} \quad \text{with} \quad \chi = \frac{\tilde{\nu}}{\nu} \quad \text{and} \quad f_{v1} = \frac{\chi^3}{\chi^3 + c_{v1}^3} \tag{D.3}$$

The function f_w in the destruction term of eq. (D.1) is determined by

$$f_w = g\left(\frac{1+c_{w3}^6}{g^6 + c_{w3}^6}\right) \quad \text{with} \quad g = r + c_{w2}(r^6 - r) \quad \text{and} \quad r \equiv \frac{\nu_t}{S\kappa^2 d^2} \tag{D.4}$$

The eddy viscosity ν_t needed to close the Navier-Stokes equations is calculated via

$$\nu_t = \tilde{\nu} f_{v1} \tag{D.5}$$

The model parameters are summarized in table D.1.

Table D.1: SA-RANS model parameters used in this work.

σ	c_{b1}	c_{b2}	c_{w1}	c_{w2}	c_{w3}	c_{v1}	c_s
2/3	0.1355	0.622	$\left(\frac{c_{b1}}{\kappa^2} + \frac{1+c_{b2}}{\sigma}\right)$	0.3	2	7.1	0.3

D.2 Formulation of the DES Length Scale in the SA-DDES Model

Within the SA-DDES model [35] the DES length scale $\tilde{d}$ is adjusted compared to the SA-DES model [30] to prevent modelled stress depletion (MSD). In OpenFOAM version 6 [103] the DES length scale $\tilde{d}$ is redefined as in eq. (D.6).

$$\tilde{d} \equiv d - f_d \, max(0, d - C_{DES}\Delta) \tag{D.6}$$

When the delay function f_d is set to 0 the model yields the RANS formulation and when f_d is set to 1 it yields the LES mode formulation (cf. eq. (3.18)). The delay function f_d is defined as in eq. (D.7) with the model parameters $c_{d1} = 8$ and $c_{d2} = 3$.

$$f_d = 1 - tanh\left[(c_{d1} r_d)^{c_{d2}}\right] \tag{D.7}$$

The parameter r_d is given by eq. (D.8).

$$r_d = min\left(\frac{\nu_{eff}}{|\nabla \mathbf{u}| \kappa^2 d^2}, 10\right) \tag{D.8}$$

Compared to the SA-DES model, the DES length scale no longer solely depends on the mesh (cf. eq. (3.18)) but also on the effective dynamic viscosity ν_{eff} which is time-dependent.

D.3 SA-(D)DES Model: Parameter Calibration

The decay of isentropic turbulence is a canonical test case commonly used to calibrate turbulence models by comparison with DNS or experimental data. In the DIT test case, a transient simulation of the decay of isentropic turbulence in a cubical computational domain is conducted. The obtained turbulent kinetic energy spectrum obtained by the simulation is qualitatively compared to measurement data by Comte-Bellot and Corrsin [66]. In this way it is possible to gain insight on the performance of the numerical settings and also the inherent level of dissipation within the solver. Within the applications of the SA-DES models, the DIT case is a common way to calibrate the DES model parameter C_{DES} (cf. [108]). In this section, the results obtained with the DES model are also compared to a LES turbulence model using the k-equation SGS model (proposed by Yoshizawa [128]) with low dissipative numerical schemes to gain further insight on the applicability of the selected numerical discretization and interpolation schemes. In the LES test case, second order central-differences schemes are chosen for the discretization of gradients. The DES in this study uses the Linear-Upwind Stabilised Transport (LUST) scheme for the discretization of the velocity gradient, which is a flux blending scheme of central-differences (75 %) and linear-upwind (25 %) to stabilize the solutions while maintaining second order accuracy. The geometry of all test cases is a cube with an edge length of $2\pi 0.09\,\mathrm{m}$. The cube is discretized with a uniformly spaced hexahedral mesh of 128 elements in each direction. For the transient solution the PIMPLE solver in PISO mode is chosen for all test cases and the time step fulfils the requirement of a Courant number ≤ 0.1. Regarding the boundary conditions, the cube sides are treated as periodic boundaries for the variables $\mathbf{u}$, p, ν_t and the turbulence quantities $\tilde{\nu}$ or k depending on the turbulence model. The initial internal field values are obtained from the measurement at $t = 0$ by Comte-Bellot and Corrsin [66] with an inverse Fourier transform based on the procedure proposed by Saad et al. [129] with the tool createBoxTurb from the OpenFOAM release v2206. In fig. D.1 the numerical results are compared to the experimental data by Comte-Bellot and Corrsin [66].

The level of agreement with the measurement is evaluated based on the agreement of the energy distribution across the length scales, as well as the rate of decay of that energy. In the energy spectrum it can be seen that the SA-DDES model slightly overpredicts the energy in the wavenumber range between 90 and 250. Compared to the measurement, at $t = 0.285$ the energy decays more strongly for wavenumbers greater than 250 in both the SA-DDES and the kEqn model. At $t = 0.656$ the qualitative agreement with the measurement is higher for the SA-DDES model. Based on this test case the model parameter $C_{DES} = 0.65$ and the numerical schemes were evaluated as suitable for this study.

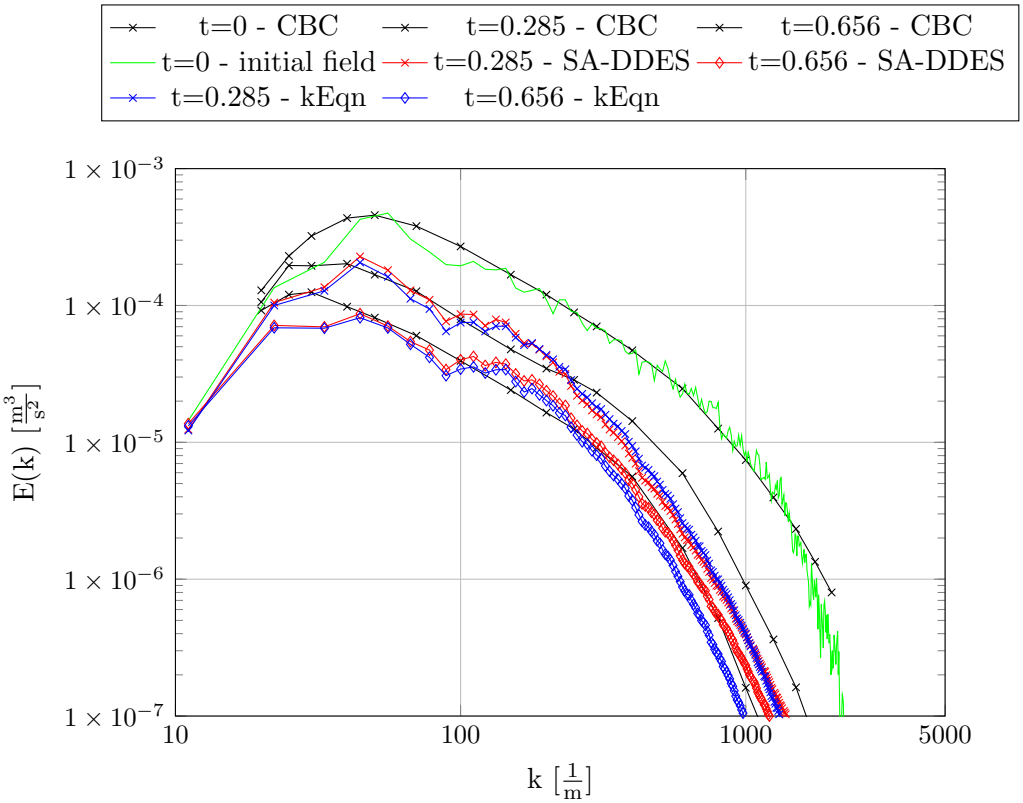

Figure D.1: Turbulent kinetic energy spectrum of the DIT cases. Displayed are the spectral results obtained by the measurement data by Comte-Bellot and Corrsin [66] (in black) and by CFD simulations with the kEqn LES model (blue) and the SA-DDES model (red). Shown are the spectra at two time steps of decay t after 0.285 and 0.656 s. Additionally the energy spectrum of the initial velocity field is displayed (green).

E Thermophysical Properties

The models for the thermophysical properties are defined differently in the models where the receiver flow is considered (E-model) in comparison to the models where the receiver is treated as a wall with the general assumption of incompressibility (SE-model). Regardless of the model, the air properties are based on tabulated data of dry air from [109]. In the SE-model, a constant density ρ and dynamic viscosity μ at 298.15 K is assumed.

In the E-model the air properties are modeled temperature dependent. The density is calculated based on the assumption of an ideal gas, as presented in section 2.3.1. The dynamic viscosity μ and the heat conductivity κ are determined by fourth order polynomial functions with respect to the temperature T as in eq. (E.1).

$$c_0 + c_1 T + c_2 T^2 + c_3 T^3 + c_4 T^4 \tag{E.1}$$

For the specific heat capacity c_p and the specific enthalpy h the JANAF model as implemented in OpenFOAM v6 [103] is used. Within the JANAF model the temperature range is divided into a low and a high temperature range, which are approximated with different coefficients. The thermophysical properties are determined within the temperature range between 273.15 and 1273.15 K, which is split in the JANAF model at 773.15 K. The coefficients, which are used in the least squares fit based on the data by Stephan et al. [109] are summarized in table E.1.

Table E.1: Polynomial coefficients used in the polynomial least squares fit based on the data of dry air by Stephan et al. [109] to calculate the thermophysical properties in the E-model.

property	c_0	c_1	c_2	c_3	c_4
μ	9.7853×10^{-7}	7.1511×10^{-8}	-5.1260×10^{-11}	2.8814×10^{-14}	-6.7665×10^{-18}
κ	3.8794×10^{-4}	1.0211×10^{-4}	-6.1020×10^{-8}	3.4103×10^{-11}	-7.9033×10^{-15}
$c_p(T < 773.15\,\mathrm{K})$	1.0359	-2.2607×10^{-4}	3.7417×10^{-7}	2.7706×10^{-10}	-3.3550×10^{-13}
$c_p(T \geq 773.15\,\mathrm{K})$	1.2381	-1.1464×10^{-3}	2.1578×10^{-6}	-1.4560×10^{-9}	3.4767×10^{-13}

F Numerical Schemes and Solver Settings

This section summarises the numerical schemes and solver settings used in RANS and DES with the SE- and E-models. As described in section 2.3.1, the two models differ in terms of the governing equations and underlying assumptions, as the SE-model assumes incompressible flow and does not include the receiver and return air flow.

F.1 Numerical Schemes and Solver Settings in the SE-RANS Model

Numerical schemes:

```
/*--------------------------------*- C++ -*----------------------------------*\
| =========                      |                                            |
|
| \\      /  F ield              | OpenFOAM: The Open Source CFD Toolbox
|
|  \\    /   O peration          | Version:  2.1.1
|
|   \\  /    A nd                | Web:      www.OpenFOAM.org
|
|    \\/     M anipulation       |
|
\*---------------------------------------------------------------------------*/
FoamFile
{
    version     2.0;
    format      ascii;
    class       dictionary;
    object      fvSchemes;
}
// * * * * * * * * * * * * * * * * * * * * * * * * * * * * * * * * * * * * * //

ddtSchemes
{
    default          bounded steadyState;
}
gradSchemes
{
    default          cellLimited Gauss linear 1;
}
divSchemes
{
    default          none;
    div(phi,U)       bounded Gauss linearUpwindV grad(U);
    div(phi,nuTilda) bounded Gauss limitedLinear 0.2;
    div((nuEff*dev2(T(grad(U))))) Gauss linear;
}
laplacianSchemes
{
    default          Gauss linear limited 0.5;
}
interpolationSchemes
{
    default          linear;
}
snGradSchemes
{
    default          corrected;
}
wallDist
{
    method meshWave;
}
```

```
fluxRequired
{
    default         no;
    p_rgh;
}

// ************************************************************************* //
```

Solver settings:

```
/*--------------------------------*- C++ -*----------------------------------*\
| =========                 |                                                 |
| \\      /  F ield         | OpenFOAM: The Open Source CFD Toolbox           |
|  \\    /   O peration     | Version:  6                                     |
|   \\  /    A nd           | Web:      www.OpenFOAM.org                      |
|    \\/     M anipulation  |                                                 |
\*---------------------------------------------------------------------------*/
FoamFile
{
    version     2.0;
    format      ascii;
    class       dictionary;
    object      fvSolution;
}
// * * * * * * * * * * * * * * * * * * * * * * * * * * * * * * * * * * * * * //

solvers
{
    p
    {
        solver           GAMG;
        tolerance        1e-7;
        relTol           0.01;
        smoother         DICGaussSeidel;
        nPreSweeps       0;
        nPostSweeps      2;
        cacheAgglomeration on;
        agglomerator     faceAreaPair;
        nCellsInCoarsestLevel 500;
        mergeLevels      1;
    }

    U
    {
        solver          GAMG;
        tolerance       1e-09;
        relTol          0.001;
        smoother        DILUGaussSeidel;
        cacheAgglomeration true;
        nCellsInCoarsestLevel 500;
        agglomerator    faceAreaPair;
        mergeLevels     1;
        maxIter         50;
    }
    nuTilda
    {
        $U;
        tolerance       1e-05;
    }
}
SIMPLE
{
    nNonOrthogonalCorrectors 2;
    pRefCell 0;
    pRefValue 85543.199;
    residualControl
    {
        p_rgh 1e-6;
        U 1e-8;
        nuTilda 1e-4;
    }
}
relaxationFactors
{
    fields
    {
        p               0.4;
    }
    equations
    {
        U               0.6;
        nuTilda         0.8;
    }
}
cache
{
    grad(U);
```

```
}
// ************************************************************************* //
```

F.2 Numerical Schemes and Solver Settings in the SE-DDES Model

Numerical schemes:

```
/*--------------------------------*- C++ -*----------------------------------*\
| =========                 |                                                 |
| \\      /  F ield         | OpenFOAM: The Open Source CFD Toolbox           |
|  \\    /   O peration     | Version:  6                                     |
|   \\  /    A nd           | Web:      www.OpenFOAM.org                      |
|    \\/     M anipulation  |                                                 |
\*---------------------------------------------------------------------------*/
FoamFile
{
    version     2.0;
    format      ascii;
    class       dictionary;
    object      fvSchemes;
}
// * * * * * * * * * * * * * * * * * * * * * * * * * * * * * * * * * * * * * //

ddtSchemes
{
    default backward;
}
gradSchemes
{
    default          Gauss linear;
    grad(nuTilda)    cellLimited Gauss linear 1;
    grad(U)          cellLimited Gauss linear 1;
}
divSchemes
{
    default          none;
    div(phi,U)       Gauss LUST unlimitedGrad(U);
    div(phi,nuTilda) Gauss upwind;
    div((nuEff*dev2(T(grad(U))))) Gauss linear;
}
laplacianSchemes
{
    default          Gauss linear limited corrected 0.33;
}
interpolationSchemes
{
    default          linear;
}
snGradSchemes
{
    default          limited corrected 0.33;
}
wallDist
{
    method meshWave;
}
fluxRequired
{
    default          no;
    p_rgh;
}

// ************************************************************************* //
```

Solver settings:

```
/*--------------------------------*- C++ -*----------------------------------*\
| =========                      |                                            |
|
| \\      /  F ield              | OpenFOAM: The Open Source CFD Toolbox
|
|  \\    /   O peration          | Version:  6
|
|   \\  /    A nd                | Web:      www.OpenFOAM.org
|
|    \\/     M anipulation       |
|
\*---------------------------------------------------------------------------*/
FoamFile
{
    version     2.0;
    format      ascii;
    class       dictionary;
    object      fvSolution;
}
// * * * * * * * * * * * * * * * * * * * * * * * * * * * * * * * * * * * * * //

solvers
{
    p
    {
        solver           GAMG;
        tolerance        1e-7;
        relTol           0.05;
        smoother         DICGaussSeidel;
        nPreSweeps       2;
        nPostSweeps      2;
        cacheAgglomeration on;
        agglomerator     faceAreaPair;
        nCellsInCoarsestLevel 500;
        mergeLevels      1;
    }
    U
    {
        solver          GAMG;
        tolerance       1e-9;
        relTol          0.05;
        smoother        DILUGaussSeidel;
        cacheAgglomeration true;
        nCellsInCoarsestLevel 500;
        agglomerator    faceAreaPair;
        mergeLevels     1;
        maxIter         20;
    }
    nuTilda
    {
        $U;
        tolerance       1e-5;
    }
    pFinal
    {
        $p;
        relTol          0;
    }
    UFinal
    {
        $U;
        relTol          0;
    }
    nuTildaFinal
    {
        $nuTilda
        relTol          0;
    }
}
PIMPLE
{
    nNonOrthogonalCorrectors 2;
    nOuterCorrectors    50;
    nCorrectors         1;
    momentumPredictor   yes;
    residualControl
     {
        p { relTol 0;  tolerance 1e-6; }
        U { relTol 0; tolerance 1e-8; }
        nuTilda { relTol 0; tolerance 1e-4; }
     }
}
```

```
relaxationFactors
{
    fields
    {
        p               0.4;
        pFinal          1;
    }
    equations
    {
        U               0.6;
        nuTilda         0.8;
        "(U|nuTilda)Final"  1;
    }
}
cache
{
    grad(U);
}

// ************************************************************************* //
```

F.3 Numerical Schemes and Solver Settings in the E-RANS Model

Numerical schemes:

```
/*--------------------------------*- C++ -*----------------------------------*\
| =========                      |                                            |
|
| \\      /  F ield              | OpenFOAM: The Open Source CFD Toolbox
|
|  \\    /   O peration          | Version:  2.1.1
|
|   \\  /    A nd                | Web:      www.OpenFOAM.org
|
|    \\/     M anipulation       |
|
\*---------------------------------------------------------------------------*/
FoamFile
{
    version     2.0;
    format      ascii;
    class       dictionary;
    object      fvSchemes;
}
// * * * * * * * * * * * * * * * * * * * * * * * * * * * * * * * * * * * * * //

ddtSchemes
{
    default       bounded steadyState;
}

gradSchemes
{
    default          cellLimited Gauss linear 1;
}

divSchemes
{
    default          none;
    div(phi,U)       bounded Gauss linearUpwindV grad(U);
    div(phi,K)       bounded Gauss limitedLinear 0.2;
    div(phi,h)       bounded Gauss limitedLinear 0.2;
    div(phi,nuTilda) bounded Gauss limitedLinear 0.2;
    div((nuEff*dev2(T(grad(U))))) Gauss linear;
    div(((rho*nuEff)*dev2(T(grad(U))))) Gauss linear;
    div(phi,ARRilr)     bounded Gauss upwind;
    div(phi,ARRelr)     bounded Gauss upwind;
}
laplacianSchemes
{
    default          Gauss linear limited 0.5;
}
interpolationSchemes
{
    default          linear;
}
snGradSchemes
{
    default           corrected;
}
wallDist
{
    method meshWave;
}
fluxRequired
{
    default          no;
    p_rgh;
}

// ************************************************************************* //
```

Solver settings:

```
/*--------------------------------*- C++ -*----------------------------------*\
| =========                      |                                           |
|
| \\      /  F ield              | OpenFOAM: The Open Source CFD Toolbox
|
|  \\    /   O peration          | Version:  6
|
|   \\  /    A nd                | Web:      www.OpenFOAM.org
|
|    \\/     M anipulation       |
|
\*---------------------------------------------------------------------------*/
FoamFile
{
    version     2.0;
    format      ascii;
    class       dictionary;
    object      fvSolution;
}
// * * * * * * * * * * * * * * * * * * * * * * * * * * * * * * * * * * * * * //

solvers
{
    p_rgh
    {
        solver           GAMG;
        tolerance        1e-7;
        relTol           0.01;
        smoother         DICGaussSeidel;
        nPreSweeps       0;
        nPostSweeps      2;
        cacheAgglomeration on;
        agglomerator     faceAreaPair;
        nCellsInCoarsestLevel 500;
        mergeLevels      1;
    }

    "(ARRelr|ARRilr)"
    {
        solver          GAMG;
        tolerance       1e-07;
        relTol          0.01;
        smoother        DILUGaussSeidel;
        cacheAgglomeration true;
        nCellsInCoarsestLevel 500;
        agglomerator    faceAreaPair;
        mergeLevels     1;
        minIter         3;
        maxIter         20;
    }
    U
    {
        solver          GAMG;
        tolerance       1e-08;
        relTol          0.001;
        smoother        DILUGaussSeidel;
        cacheAgglomeration true;
        nCellsInCoarsestLevel 500;
        agglomerator    faceAreaPair;
        mergeLevels     1;
        maxIter         20;
    }
    "(h|nuTilda)"
    {
        $U;
        tolerance       1e-05;
    }

SIMPLE
{
    nNonOrthogonalCorrectors 1;
    pRefCell 0;
    pRefValue 100000;
    residualControl
    {
        "ARR.*" 1e-6;
        p_rgh 1e-6;
        U 1e-8;
        "(h|nuTilda)" 1e-4;
    }
}
relaxationFactors
```

```
{
    fields
    {
        p_rgh                   0.4;
        p_rghFinal              1;
    }
    equations
    {
        U                   0.6;
        h                   0.8;
        omega               0.8;
        nuTilda             0.8;
        "(U|k|omega|nuTilda|h)Final"   1;
    }
}
cache
{
    grad(U);
}

// ************************************************************************* //
```

F.4 Numerical Schemes and Solver Settings in the E-DDES Model

Numerical schemes:

```
/*--------------------------------*- C++ -*----------------------------------*\
| =========                 |                                                 |
|
| \\      /  F ield         | OpenFOAM: The Open Source CFD Toolbox
|
|  \\    /   O peration     | Version:  6
|
|   \\  /    A nd           | Web:      www.OpenFOAM.org
|
|    \\/     M anipulation  |
|
\*---------------------------------------------------------------------------*/
FoamFile
{
    version     2.0;
    format      ascii;
    class       dictionary;
    object      fvSchemes;
}
// * * * * * * * * * * * * * * * * * * * * * * * * * * * * * * * * * * * * * //

ddtSchemes
{
    default        backward;

}
gradSchemes
{
    default          Gauss linear;
    grad(nuTilda)    cellLimited Gauss linear 1;
    grad(U)          cellLimited Gauss linear 1;
}
divSchemes
{
    default          none;
    div(phi,U)       Gauss LUST unlimitedGrad(U);
    div(phi,K)       Gauss upwind;
    div(phi,h)       Gauss upwind;
    div(phi,nuTilda) Gauss upwind;
    div((nuEff*dev2(T(grad(U))))) Gauss linear;
    div(((rho*nuEff)*dev2(T(grad(U))))) Gauss linear;
    div(phi,ARRilr)     Gauss upwind;
    div(phi,ARRelr)     Gauss upwind;
}
laplacianSchemes
{
    default          Gauss linear limited corrected 0.33;
}
interpolationSchemes
{
    default          linear;
}
snGradSchemes
{
    default           limited corrected 0.33;
}
wallDist
{
    method meshWave;
}
fluxRequired
{
    default          no;
    p_rgh;
}

// ************************************************************************* //
```

Solver settings:

```
/*--------------------------------*- C++ -*----------------------------------*\
| =========                      |                                            |
| \\      /  F ield              | OpenFOAM: The Open Source CFD Toolbox      |
|  \\    /   O peration          | Version:  6                                |
|   \\  /    A nd                | Web:      www.OpenFOAM.org                 |
|    \\/     M anipulation       |                                            |
\*---------------------------------------------------------------------------*/
FoamFile
{
    version     2.0;
    format      ascii;
    class       dictionary;
    object      fvSolution;
}
// * * * * * * * * * * * * * * * * * * * * * * * * * * * * * * * * * * * * * //

solvers
{
    p_rgh
    {
        solver           GAMG;
        tolerance        1e-7;
        relTol           0.05;
        smoother         DICGaussSeidel;
        nPreSweeps       0;
        nPostSweeps      2;
        cacheAgglomeration on;
        agglomerator     faceAreaPair;
        nCellsInCoarsestLevel 500;
        mergeLevels      1;
    }
    p_rghFinal
    {
        $p_rgh;
        relTol          0;
    }
    "(ARRelr|ARRilr)"
    {
        solver          GAMG;
        tolerance       1e-07;
        relTol          0.05;
        smoother        DILUGaussSeidel;
        cacheAgglomeration true;
        nCellsInCoarsestLevel 500;
        agglomerator    faceAreaPair;
        mergeLevels     1;
        minIter         3;
        maxIter         20;
    }
    U
    {
        solver          GAMG;
        tolerance       1e-09;
        relTol          0.05;
        smoother        DILUGaussSeidel;
        cacheAgglomeration true;
        nCellsInCoarsestLevel 500;
        agglomerator    faceAreaPair;
        mergeLevels     1;
        maxIter         20;
    }
    "(h|nuTilda)"
    {
        solver          GAMG;
        tolerance       1e-05;
        relTol          0.05;
        smoother        DILUGaussSeidel;
        cacheAgglomeration true;
        nCellsInCoarsestLevel 500;
        agglomerator    faceAreaPair;
        mergeLevels     1;
        maxIter         20;
    }
    UFinal
    {
        $U;
        relTol      0;
```

```
    }
    hFinal
    {
        $h
        relTol       0;
    }
    nuTildaFinal
    {
        $nuTilda
        relTol       0;
    }
    ARRilrFinal
    {
        $ARRilr
        relTol       0;
    }
    ARRelrFinal
    {
        $ARRelr
        relTol       0;
    }
}
PIMPLE
{
    nNonOrthogonalCorrectors 1;
    nOuterCorrectors     50;
    nCorrectors          1;
    momentumPredictor    yes;
    residualControl
    {
        "ARR.*" { relTol 0; tolerance 1e-6; }
        U { relTol 0; tolerance 1e-8; }
        p_rgh { relTol 0;  tolerance 1e-6; }
        "(h|nuTilda)" { relTol 0; tolerance 1e-4;}
    }
}

relaxationFactors
{
    fields
    {
        p_rgh                0.4;
        p_rghFinal           1;
    }
    equations
    {
        U                0.6;
        h                0.8;
        nuTilda          0.8;
        "(U|k|omega|nuTilda|h)Final"   1;
    }
}

cache
{
    grad(U);
}

// ************************************************************************* //
```